# Optogenetic-fUSI reveals brain-wide neural pathways downstream of specific cell-types

## ARNAU SANS DUBLANC

Supervisor:

Prof. Karl Farrow

Chair: Prof. Sander Govers

Members of the Examination Committee:

Prof. Alan Urban

Prof. Lieve Moons

Prof. Wim Vanduffel

Prof. Emilie Macé

Dissertation presented in partial fulfilment of the requirements for the degree of Doctor of Science.

**April 2022**

# SUMMARY

How visual information is processed by the brain to orient our attention and guide behavior is central to our understanding of sensory – motor transformations. Transgenic mouse models together with molecular and genetic tools and high-throughput recording techniques have allowed us to start to understand how local brain circuits and their direct projections are organized to integrate sensory information and guide behavior. However, these approaches, as currently applied, have fostered a reductionist conceptualization of these processes, identifying specific pathways as necessary and sufficient for a particular behavior. We believe that continuing in this direction will limit our understanding of the neural basis of these behaviors; creating observational biases where the field increasingly focuses attention where it is easiest to look and ignoring the role of potentially critical unobserved cell-populations, pathways, and the interactions between them.

Here we present an experimental solution to this problem that combines optogenetics, to manipulate specific cell-types, and functional ultrasound imaging (fUSI) to observe the brain-wide consequence of manipulating these cell-types with high spatiotemporal resolution (~100µm$^3$, 100ms). We use this framework to investigate the contribution of distinct cell-types in the mouse superior colliculus to behavior and map the brain-wide neural activity they produce in awake mice. This approach allowed us to identify new brain areas involved in colliculus-driven behaviors and demonstrate that each cell-types mediates behavior via a broad yet distinct downstream network of brain regions.

The superior colliculus is part of the network of brain areas involved in implementing the motor consequences of attention; playing a central role in directing attention and triggering the motor outputs that orient us toward objects of interest, or away from threats. In addition, dysfunction of the superior colliculus and its downstream partners has been associated with psychiatric and developmental disorders including anxiety, post-traumatic stress disorders, autism, and schizophrenia. In mice, there is evidence of a strong relationship between individual cell-types and orienting, hunting and defensive behaviors. We use this relationship to delineate the cell-type specific brain-wide functional networks that lie downstream of the superior colliculus. We first establish that optogenetic activation of 4 different cell populations each trigger a distinct behavior. Subsequently, we map out the brain-wide neuronal activity in 264 brain regions that occurs as a consequence of optogenetically activating these populations. These recordings allowed us to unravel the different spatial and temporal functional networks that lie downstream of each cell-type and link these to differences in the evoked behaviors. The results of this work highlighted that each cell-type of the colliculus is functionally connected to at least 82 brain areas, forming a large brain-wide network that acts to guide a distinct behavior.

Critically, fUSI allowed us to inspect the brain-wide activity of awake animals in an unbiased manner. This revealed brain areas that had not previously been considered as part of these networks. A selection of these were targeted for electrophysiological recordings and chemogenetic manipulations. Our electrophysiological recordings supported the fUSI findings and demonstrated that neurons in the downstream nuclei preferentially respond to ecologically relevant visual stimuli. Chemogenetic manipulation of an area identified with opto-fUSI, the posterior paralaminar nuclei of the thalamus (PPnT), illustrated the role it plays in mediating habituation to repeated input from the superior colliculus.

Finally, using the recently developed volumetric fUSI, that allows simultaneous imaging of the entire brain, combined with optogenetics (opto-vfUSI), we obtained results consistent with opto-fUSI, with

a fraction of the time and stimulations. Importantly, this allowed us to identify the neural pathways downstream of an additional cell-type that is very sensitive to adaptation, and thus to repeated stimulations.

We believe this is an important step towards understanding the role of the superior colliculus. Although the superior colliculus has been implicated in the coordination of attention and orienting behaviors, the results of this study demonstrate that this is accomplished through a set of downstream networks that are far broader than the individual pathways recent manipulations have highlighted. This has implications for understanding all functions of the superior colliculus including how it directs the brains attention to objects of interest, triggers defensive behaviors and the unconscious processing of fear. Being able to systematically investigate the causal link between specific cell-types and brain-wide neuronal activity is critical for comprehending the role the superior colliculus plays in these processes and how its dysfunction could contribute to psychiatric disorders.

This experimental framework is versatile enough to be applied to many small brain mammals including mice, Peromyscus, rats and marmosets. We believe that the combination of optogenetics and functional ultrasound imaging (fUSI and vfUSI) bridges the gap between precise circuits manipulations and brain-wide activity measurements and provides an opportunity to gain a mechanistic understanding of how neural activity in specific cell-types causally relates to brain-wide activity and behavior.

# SAMENVATTING

Hoe visuele informatie door de hersenen wordt verwerkt om onze aandacht te oriënteren en gedrag te sturen, staat centraal in ons begrip van sensorisch-motorische transformaties. Transgene muismodellen samen met moleculaire en genetische hulpmiddelen en opnametechnieken met hoge doorvoer hebben ons in staat gesteld te begrijpen hoe lokale hersencircuits en hun directe projecties zijn georganiseerd om sensorische informatie te integreren en gedrag te sturen. Deze benaderingen, zoals ze momenteel worden toegepast, hebben echter geleid tot een reductionistische conceptualisering van deze processen, waarbij specifieke paden zijn geïdentificeerd als noodzakelijk en voldoende voor een bepaald gedrag. We zijn van mening dat het doorgaan in deze richting ons begrip van de neurale basis van dit gedrag zal beperken; het creëren van observationele vooroordelen waarbij het veld in toenemende mate de aandacht vestigt waar het het gemakkelijkst is om te kijken en de rol van potentieel kritische niet-geobserveerde celpopulaties, paden en de interacties daartussen te negeren.

Hier presenteren we een experimentele oplossing voor dit probleem die optogenetica combineert, om specifieke celtypes te manipuleren, en functionele ultrasone beeldvorming (fUSI) om de hersenbrede consequentie te observeren van het manipuleren van deze celtypes met een hoge spatiotemporele resolutie (~100µm3, 100ms). We gebruiken dit raamwerk om de bijdrage van verschillende celtypen in de superieure colliculus van de muis aan gedrag te onderzoeken en de hersenbrede neurale activiteit die ze produceren in wakkere muizen in kaart te brengen. Deze benadering stelde ons in staat om nieuwe hersengebieden te identificeren die betrokken zijn bij colliculus-gestuurd gedrag en om aan te tonen dat elk celtype gedrag bemiddelt via een breed maar duidelijk stroomafwaarts netwerk van hersengebieden.

De superieure colliculus maakt deel uit van het netwerk van hersengebieden die betrokken zijn bij het implementeren van de motorische gevolgen van aandacht; een centrale rol spelen bij het richten van de aandacht en het activeren van de motoruitgangen die ons oriënteren op interessante objecten of weg van bedreigingen. Bovendien is disfunctie van de superieure colliculus en zijn stroomafwaartse partners in verband gebracht met psychiatrische en ontwikkelingsstoornissen, waaronder angst, posttraumatische stressstoornissen, autisme en schizofrenie. Bij muizen zijn er aanwijzingen voor een sterke relatie tussen individuele celtypes en oriëntatie-, jacht- en defensief gedrag. We gebruiken deze relatie om de celtype-specifieke hersenbrede functionele netwerken af te bakenen die stroomafwaarts van de superieure colliculus liggen. We stellen eerst vast dat optogenetische activering van 4 verschillende celpopulaties elk een ander gedrag veroorzaken. Vervolgens brengen we de hersenbrede neuronale activiteit in 264 hersengebieden in kaart die optreedt als gevolg van het optogenetisch activeren van deze populaties. Met deze opnames konden we de verschillende ruimtelijke en temporele functionele netwerken ontrafelen die stroomafwaarts van elk celtype liggen en deze koppelen aan verschillen in het opgeroepen gedrag. De resultaten van dit werk benadrukten dat elk celtype van de colliculus functioneel verbonden is met ten minste 82 hersengebieden, en een groot hersenbreed netwerk vormt dat een duidelijk gedrag stuurt.

Van cruciaal belang was dat fUSI ons in staat stelde om de hersenbrede activiteit van wakkere dieren op een onbevooroordeelde manier te inspecteren. Dit onthulde hersengebieden die voorheen niet als onderdeel van deze netwerken werden beschouwd. Een selectie hiervan was bedoeld voor elektrofysiologische opnames en chemogenetische manipulaties. Onze elektrofysiologische opnames ondersteunden de bevindingen en toonden aan dat neuronen in de stroomafwaartse kernen bij voorkeur reageren op ecologisch relevante visuele stimuli. Chemogenetische manipulatie van een

zijn geïdentificeerd met opto-fUSI, de posterieure paralaminarnuclei van de thalamus (PPnT), illustreerde de rol die het speelt bij het mediëren van gewenning aan herhaalde input van de superieure colliculus.

Ten slotte hebben we met behulp van de recent ontwikkelde volumetrische fUSI, die gelijktijdige beeldvorming van de hele hersenen mogelijk maakt, gecombineerd met optogenetica (opto-vfUSI), resultaten verkregen die consistent zijn met opto-fUSI, met een fractie van de tijd en stimulaties. Belangrijk is dat we hierdoor de neurale paden stroomafwaarts van een extra celtype konden identificeren dat erg gevoelig is voor aanpassing, en dus voor herhaalde stimulaties.

Wij geloven dat dit een belangrijke stap is om de rol van de superieure colliculus te begrijpen. Hoewel de superieure colliculus betrokken is geweest bij de coördinatie van aandacht en oriënterend gedrag, tonen de resultaten van deze studie aan dat dit wordt bereikt via een reeks stroomafwaartse netwerken die veel breder zijn dan de individuele paden die recente manipulaties hebben benadrukt. Dit heeft implicaties voor het begrijpen van alle functies van de superieure colliculus, inclusief hoe het de aandacht van de hersenen richt op interessante objecten, defensief gedrag op gang brengt en de onbewuste verwerking van angst. Het systematisch kunnen onderzoeken van het causale verband tussen specifieke celtypen en hersenbrede neuronale activiteit is van cruciaal belang voor het begrijpen van de rol die de superieure colliculus speelt in deze processen en hoe de disfunctie ervan zou kunnen bijdragen aan psychiatrische stoornissen.

Dit experimentele raamwerk is veelzijdig genoeg om te worden toegepast op veel kleine hersenzoogdieren, waaronder muizen, Peromyscus, ratten en zijdeaapjes. Wij zijn van mening dat de combinatie van optogenetica en functionele ultrasone beeldvorming (fUSI en vfUSI) de kloof overbrugt tussen precieze circuitmanipulaties en hersenbrede activiteitsmetingen en een mogelijkheid biedt om een mechanisch begrip te krijgen van hoe neurale activiteit in specifieke celtypen causaal verband houdt met hersenbrede activiteit en gedrag.

# Acknowledgements

This Thesis has been a long journey, and as with any journey, I have met many people along the way that have left their mark, directly or indirectly, in this work. First of all, Karl Farrow, who gave me the opportunity to start this project under his supervision and mentoring. I feel honestly lucky to have ended in his lab. First, because instead of teaching me how to perform the project he had envisioned (kind of envisioned), he made sure we adapted that project to my skills and interests until I was able to lead it and make it my own. Second, and most important, because Karl has shown an honest interest in becoming a better mentor every year. Not better for him, but better for all that work for him. He has been proactive to adapt his way of mentoring to the needs of every individual as best as he can, and just witnessing that, makes one feel better. Karl is not perfect. One of the critical skills to learn in his lab is to filter his input that can vary and go in complete opposite directions from one week to another. But once one learns to navigate his thoughts, his passion becomes a sail on which to ride forward. Finally, I think one of the main reasons I have enjoyed this project until the end (let's forget about the first-year drama) is how approachable Karl has been. Having our morning coffee on an almost daily basis, going for lunch and talking about trivialities, or joining randomly for dinner because he happened to pass-by the restaurant where me and Laia where about to eat. These little things have made a difference.

From Karl's lab; Ania, drama queen of drama queens, always ready for the worst and yet an unstoppable force. The more hardship she faces, the more effort she puts. She has been an inspiration, truly. I am still not sure of whether she hates or loves behavior, but her contribution in its analysis, and writing of the main manuscript were critical for the project. Katja, the soon to be PI, and not just because she will actually be a PI soon, but that has been the permanent feeling since I met her. Clear of thought, organized, leader attitude 100%. I hope to be a PI one day, she has showed me how to get it done. She also had the patience to show me how to do the Neuropixels recordings (a couple of times due to my terrible notes and memory), analysed the electrophysiology data and wrote the corresponding section in the manuscript. Dani, the best master student EVER. She learnt everything quickly, understood what she was doing and why, and did not kill me for my bad jokes that sometimes cost her a bit of extra stress. She did an excellent work with the chemogenetic experiments. Bram, always ready to help. He probably has one of the longest, if not the longest, to do list unrelated to his project. Because he is all curiosity and doesn't know how to say "no". Thanks to that, instead of working on his project as he should, he helped analyze head-fixed and freely moving behavior for the manuscript. Chen, as much a colleague as a friend. Her cheerful presence, unrelenting working spirit, cheesecakes, brunches, scientific, political, and personal discussions, all of it, has helped my PhD move forward. Dr. Kühn, colleague, friend and a much better scientist and person than she will ever admit, excellent at seeing other people strengths, but not always her own. Discussing with her is the perfect way to uncover a new and insightful perspective. She is the best way to realize how wrong I am. Joana, she is stressed, but you wouldn't know it. Do you need soothing? You go to her. Not like she is going to tell you anything magical, her presence is enough, she feels like 'everything is going to be ok', and that, in a PhD, is GOLD. Adrien, making all the stuff that someone, someday will (probably) use to do great science. Also, my best way to disconnect from work, talking about making video games, making boardgames, writing books, and the certain collapse of modern society. Those parentheses were and are life saving. Subash, an example of determination and fight against the struggles of a PhD. Daniel, in his silent corner, who helped me get through the struggles of my first year. Fred, making everyone's life better, first in the operation's team and now in the lab (and outside the lab, including Dutch

translations). Finally, the master's and bachelor's students that have taught me how to and how not to mentor; Ioannis, Adrien (Again), Ania (Again), Sergi, Dani (not really, that was too easy), Benjamin and Jana.

This project started a collaboration between Alan Urban lab and the Farrow lab. Without their help and contributions this project would not have even been conceived. First of all, Gabriel. Pessimistic? Yes. Genius? That too. You need an experiment to work? He is the man. Do you need the project to move forward quickly? He is probably going to have a heart attack. Gabriel taught me how to perform fUSI experiments, was key at troubleshooting the first opto-fUSI experiments, developed data processing pipelines, taught me how to do basic fUSI analysis, helped set up optogenetic experiments, and has kept improving the fUSI technology every year (including the development of 3D fUSI!). Alan has been an inspiring presence in this project. With very different approach strategies to Karl, it has provided me of an alternative perspective on how to do great science. Always positive, hands on, and motivating. Théo, who contributed to setting up head-fixed behavioral experiments. His critical thinking, and different perspectives due to his mathematical background, have made discussions with him always exciting. I learned something every time I talked to him. Micheline, who has struggled with me to make those damn craniotomies nice, pretty, and durable. I started as the "teacher", but I ended learning from her. Patient, humble, resilient, and always ready to smile. A pleasure to work with. Clément, who taught me my first craniotomies. Yun-An, in the background, trying to make fUSI analysis easy even for a computer ignorant like me.

The Bonin lab, with our weekly lab meetings, their input on presentations, constructive discussions, and transfer of knowledge. With special thanks to Vincent, Joao, Cagatai, and Shahriar. The operation team without whom NERF would be a total mess: Ethel, Ilse, Sophie, Elly, Antonella, Sandra, and Giuliano. Finally, all the Nerfling community, who contribute to a breathable atmosphere at NERF.

Of course, a PhD is not only possible due to what happens within the workspace, but also because of the lifebuoys made up of family and friends that keep you afloat outside of work. Thus, first and foremost, a special thanks to my friends Jordi, Ester and Gerard, for that wonderful feeling that time has not passed, every time I meet them. Also, Egdar, Barbara, Mireia, Salom, my sisters, Marina and Júlia, and even Borja! with whom, although with difficulty, keeping in touch these years has been a treasure for me.

Thanks to Laia, for enduring with me the hard times and putting up with me now, with patience and the best laughs.

Me being able to do a PhD at all, has been partly due to the privileged environment in which I grew up. Thus, also special thanks to my parents for their struggles to create that environment, and for supporting me throughout this journey.

Thanks to the jury members and chair of this thesis for spending their time reading and evaluating this work: Lieve Moons, Wim Vanduffel, Emilie Macé, Alan Urban and Sander Govers.

# Table of Contents

Table of Contents

# LIST OF ABBREVIATIONS

| | |
|---|---|
| AAV | Adeno-associated virus |
| BOLD | Blood oxygen level dependent signals |
| CaMKII | Calcium/calmodulin-dependent protein kinase II |
| CBV | Cerebral blood volume |
| ChR2 | Channelrhodopsin 2 |
| CNO | Clozapine-N-oxide |
| Cre | Cre recombinase |
| DREADDs | Designer receptors specifically activated by designer drugs |
| fMRI | Functional magnetic resonance imaging |
| fUSI | Functional ultrasound imaging |
| GABA | Gamma-Aminobutyric acid |
| Gad2 | Gene encoding for Glutamate decarboxylase isoform of 65 kDa |
| GAD67 | Glutamate decarboxylase isoform of 67 kDa |
| GRP | Gastrin-releasing peptide |
| hM4Di | Modified form of the human M4 muscarinic (hM4) inhibitory receptor |
| IEGs | Immediate early genes |
| LFP | Local field potentials |
| LGN | Lateral geniculate nucleus |
| LP | Lateral posterior nucleus of the thalamus (Pulvinar in primates) |
| mRNA | Messenger ribonucleic acid |
| NTSR | Neurotensin Receptor |
| PBG | Parabigeminal nucleus |
| PAG | Periaqueductal gray |
| PET | Positron emission tomography |
| PV | Parvalbumin |
| YFP | Yellow fluorescent protein |
| SAI | Stratum album intermediate |
| SAP | Stratum album profundum |
| SC | Superior colliculus |

SGI                Stratum griseum intermedium

SGS               Stratum griseum superficiale

SGP               Stratum griseum profundum

SO                 Stratum opticum

SZ                 Stratum zonale

STN               Subthalamic nucleus

vfUSI             Volumetric functional ultrasound imaging

# CHAPTER 1

# Introduction

# 1.1 Neural Circuit Function: from spirits to neurons and brain-wide networks

Today's understanding of the brain, neural circuits and behavior is derived from a long history of evolving theories that, at each point in time, have been greatly determined by the experimental and analytical tools available, and the understanding of fundamental physics and chemistry. Because the goal of this project is to provide a new tool to study brain functions and thus a new perspective on the brain, it is important to understand how technology and neuroscience have paralleled each other.

The first accounts of the brain as being the center of thought and sensation appear as early as the 5th century BC by Alcmaeon of Croton (Adelman, 1987). For the 2400 years that followed, knowledge of brain function originated mainly from clinical observations of brain damage and lesion experiments. From Galenus' descriptions of the function of several cranial nerves in the 2nd century BC (Gross, 2013),  to the fathers of neuropsychology in the 19th century. It was then that doctors such as Harlow (famous after the case of Phineas Gage, (Barker, 1995)), Dax (Roe and Finger, 1996) and Broca (Cowie, 2000) used the brain damage of patients to analyze the relationship between injury in specific areas and the corresponding psychological impairment. During most of that period, it was accepted that the mechanisms by which the brain guided behavior involved "animal spirits". That idea had been introduced by Galenus and was only disputed after the discovery of electrical conductance by Stephen Gray at the beginning of 18th century and the work of Galvani in 1791. Galvani proposed "intrinsic animal electricity" to be the source of muscular contraction and nerve transmission (Corrigan, 1924; McDonald, 2005; Piccolino, 2008).

It was also in the 19th century, accompanied by great advances in optics and the design of microscopes, that new theories started to emerge regarding the composition of the brain, with the first observations and drawings of neurons. Gabriel Valentin, student of Purkinje, was first to describe the cell body and nucleus of neurons in 1834. Purkinje himself did the first descriptions of cerebellar cells and the fiber-like processes around them that seemed specific to the brain, and Remak introduced the structure of nerve fibers and was able to differentiate between myelinated and unmyelinated fibers (Chvátal, 2015). In parallel, in the early 1820s, Pierre Flourens developed the method of surgical ablation and observed that he could remove large cortical sections without observing loss of function in birds and rabbits. If more was removed, all functions gradually disappeared (Pearce, 2009). This led him to propose that the brain acted as a whole to generate perception and thought. During the second half of the century, von Gerlach put together the anatomical work of Valentin, Purkinje, and Remak, the observations of Flourens, and the discovery of "nerve currents" by Bernstein in 1868 (Seyfarth, 2006), to propose a new theory of brain function. In that theory, the brain was composed of a giant net of filaments through which electric signals where transmitted (Stahnisch, 2015). The so called "reticular doctrine" dominated how the brain was understood for more than two decades and Camillo Golgi, who received the Nobel prize in 1906, was still convinced at the reception of the prize of the accuracy of that theory.

The discovery of electricity as the agent transmitting the brain's signals, inspired Hitzig and Fritsch to use electrical stimulations in the cortex of dogs. In doing so, they realized that the brain had topography and functional specialization (Hagner, 2012; Fan and Markram, 2019). David Ferrier confirmed and extended the work of Hitzig and Fritsch by using both ablation and electrical stimulation to delineate sensory and motor areas in several species (Pearce, 2003; Sandrone and Zanin, 2014). However, their discoveries, and the contemporary clinical descriptions of the brain's

topography by Broca, were met with strong opposition due to the variability of results, the low resolution, lack of specificity and because it antagonized the established holistic view of the brain that Flourens had established with his ablation studies. Interestingly, it was Golgi, one of the most fervent defenders of the reticular doctrine, who condemned it when he invented the Golgi staining (1873) (Galliano, Mazzarello and D'Angelo, 2010), a method that allowed the observation of the fine structure of neurons. In the decade following the invention, and owing to the new Golgi staining method, increasing doubts were shed on the reticular nature of the brain by proposing that nerve units touched each other instead of being fused. For instance, Nansen, with his work on the nervous system of marine invertebrates (Haas, 2003), Forel in his degeneration studies (Osiro *et al.*, 2012), and His in his publications on embryological development of the human brain (Dupont, 2018). However, it was not until Ramon y Cajal published his detailed observations and drawings in the late 1880s (Llinás, 2003; Sotelo, 2003) and drew the attention of important figures such as Kölliker and Waldeyer that the new theory started to get traction. Yet, the individuality of neurons was not confirmed until the invention of the electron microscope (Knoll and Ruska, 1932) and the subsequent work of Palay, who was the first to observe the structure of neurons using this new tool (Palay and Palade, 1955; Palay, 1956).

The "neuron doctrine", introduced by Waldeyer in 1891, and based on the work of Nansen, Forel, His and Ramon y Cajal, regards the neuron as the functional and structural unit of the brain (Fodstad, 2001) and it is still considered valid today. Nonetheless, it has not been immune to evolution and technological breakthroughs. In the late 1800s and early 1900s, Ramon y Cajal, Sherrington and Adrian made the first attempts to describe the organization and function of neural circuits. For example, Ramon y Cajal in his diagrams of the visual system of frogs proposed the retinotopic organization of the retinal projections into the tectum, the commissural crossing of retino-tectal fibers and the subsequent crossing in the spinal cord as a means to correct for the visual inversion of the retina (Figure 1.1A). Moreover, he proposed the remodeling of dendrites and axons based on usage as a mechanism for learning. He also was the first to postulate that neurons had directionality, with the currents flowing from dendrites to soma, then the axon and out to the postsynaptic neuron (Ramon y Cajal, 1899; Llinás, 2003). Sherrington introduced the term "synapse", sensory and motor integration, and the concept of receptive fields and neuronal inhibition (Burke, 2007; Molnár and Brown, 2010). Edward Adrian first described the refractory period, and the all-or-none principle, which states that the intensity of a neural response is independent of the stimulus strength. He popularized the use in neurophysiology of the recently developed thermionic vacuum tube (1904), a tool used at the time for amplifying and intercepting coded messages and with it revealed the importance of the firing frequency as a means for neural coding (Garson, 2015; Pearce, 2018). From this collective work the first models were proposed that tried to explain neural network functions and computations and how they could be organized to generate behavior (McCulloch and Pitts, 1943; Hebb, 1949).

The new focus on the individual neuron also inspired the development of microelectrodes to record single-cell activity (Hubel, 1957). This finally allowed one to demonstrate unequivocally the topographic organization of the brain (Mountcastle, 1957), and the functional specialization of neurons. It also sparked new ideas, although some were met with more skepticism than others depending on how well they fit the new collective expectations. For example, in 1959, two key observations of functional specialization were presented regarding visual processing. At the time, it was thought that the retina was a mere light detector that relayed the distribution of light reaching the retina that was to be interpreted further downstream in the brain. However, how such downstream areas could use and transform the retinal signals into percepts was purely theoretical at

the time.  Although some studies had recorded the size of receptive field of neurons in primary visual cortex (Talbot and Marshall, 1941), Hubel and Wiesel (Hubel and Wiesel, 1959) where the first to describe how different neurons in the primary visual cortex preferentially responded to different orientations, shapes and directions of movement. Additionally, they showed that by combining spots of light in the preferred orientation of a neuron they could drive those neurons as effectively as with oriented slights of light. These experiments provided some of the first observations of functional specificity and the mechanism by which the visual properties of neurons in the cortex could be inherited from retinal inputs. Thus, it was the first observation of sensory transformations that could lead to perception. This was exciting news for the community and as Wurtz described it later (Wurtz, 2009), "Their names became such a brand name that H&W rolled off the tongue as easily in the lab as A&W root beer did at lunch."

In the same year (1959), Lettvin provided a different perspective. In his studies with frogs, Lettvin recorded visual responses to different objects, in the retinal fibers innervating the brain. What he found was that the retina, rather than relaying a version of the world made of a mosaic of responses capturing the local distributions of light, it was already capable of "interpreting the world". He found that the retina already responded to different features (described as contrast, moving-edge, dimming and convexity detectors) and sent this information in parallel streams to the brain (Lettvin *et al.*, 1959). This idea collided with the current dogma and was transgressive enough that he was laughed off the stage at the American Physiology Society in Atlantic City. The NIH threatened cutting his funding and he had to publish his findings in the "Proceedings of the Institute of Radio Engineers". Only when he received a surprise visit to his lab by a group of skeptical scientists and conducted the experiments in front of them, they started to take the idea seriously (Myhrvold, 2013). In the following decades, an explosion of single cell recordings highlighted the potential of individual neurons as important players in perception (Maturana *et al.*, 1960; Barlow, Hill and Levick, 1964; Talbot *et al.*, 1968; Wurtz, 1969; O'Keefe and Dostrovsky, 1971; Tolhurst and Movshon, 1975; Desimone *et al.*, 1984). With the neurons' growing popularity, Horace Barlow proposed that "the activities of neurons, quite simply, are thought processes" and that 1000 neurons would be enough to represent a visual scene (Barlow, 1972).

More than 100 years after the neuron doctrine was postulated, it is clear that the brain is composed of individual neurons and understanding their activity is fundamental to explain sensory processing and behavior. However, by shying from the previous holistic view of brain function it has also fostered a rigid and narrow view of how neural networks guide behavior. It is important to note that although crude, Flourens' experiments in the 1820s showed that many brain functions can be maintained after sustaining large cortical loss. Although the topography of the brain today is unquestionable, those results already pointed at the possibility that brain functions could be shared or coordinated by multiple areas. In the last 50 years, slowly but steadily, a new set of technological advances have allowed for these old ideas to be revived and have started to be integrated with the current theoretical and experimental frameworks.

During the 70s and 80s new methods that allowed for the accurate description of interareal connectivity started to appear in quick succession and these methods are being continuously improved upon to this date. Starting from the autoradiographic axonal tract tracing and horseradish peroxidase (HRP)(LaVail and LaVail, 1972), to Cholera toxin (Stoeckel, Schwab and Thoenen, 1977), Fluoro-Gold (Schmued and Fallon, 1986), and the use viral vectors such as herpes virus (Kristensson, Ghetti and Wiśniewski, 1974), adeno associated viruses (Chamberlin *et al.*, 1998), or rabies (Astic *et al.*, 1993). In addition, the development of genetic tools has enabled the targeting of specific subpopulations of neurons or even single cells. These methods include conditional expression

systems (Tsien *et al.*, 1996) and high-throughput DNA sequencing of genetically barcoded neurons (MAPseq) (Kebschull *et al.*, 2016). New histochemical and imaging processing tools, such as CLARITY (Chung *et al.*, 2013) or 3DISCO (Ertürk *et al.*, 2012), now allow for the imaging of fluorescent cells and imaging of the entire structurally intact brain. Together, these techniques have transformed our view of the brain's connectivity. From Ramon y Cajal's linear circuits of visual and auditory processing (Figure 1.1A-B), that he imagined by observing a multitude of separated single neurons stained with the Golgi method, to maps of hundreds or thousands of interconnected cells of, for instance the full connectome of the nematode *C. elegans* (White *et al.*, 1986; cook *et al.*, 2019), and partial reconstructions of the fruit fly and mouse brains (Scheffer *et al.*, 2020; Yin *et al.*, 2020). Also, the colossal work of the MouseLight project (Winnubst *et al.*, 2019) has mapped more than 1000 neurons using serial two-photon tomography on optically cleared brains. Similarly, the Allen brain connectivity project (Oh *et al.*, 2014; Harris *et al.*, 2019) has done systematic tracing of up to 3000 injections of viral tracers in different transgenic mouse lines.
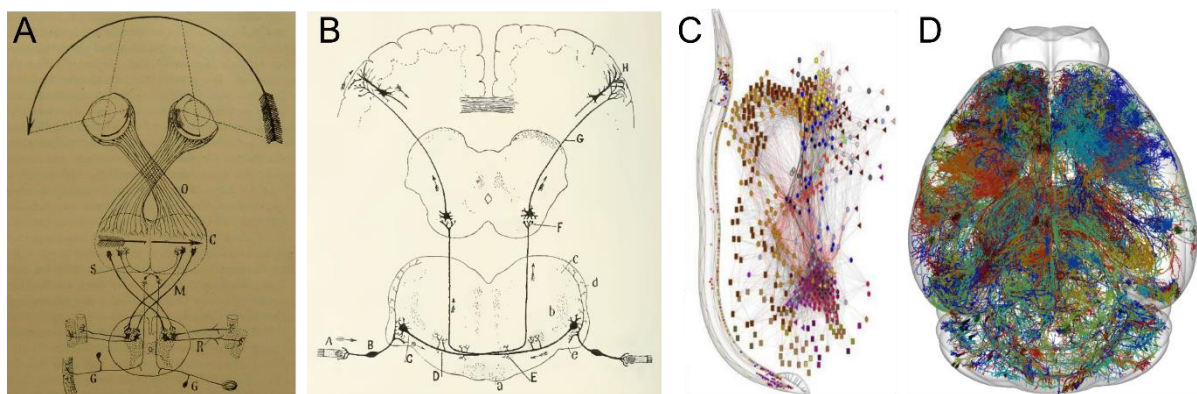


**Figure 1.1. Evolution of the anatomical knowledge of neural circuits.** From Ramón y Cajal's drawings to the 3D reconstruction of more than thousand neurons of the mouse brain. **A**. Ramón y Cajal, 1899; Representation of visual information flow from the retina to motor neurons of the spinal cord. **B.** Ramón y Cajal, 1911; Representation of auditory information flow from mechanosensory hair cells of the organ of Corti to the cortex. **C.** Circuit diagram of the entire nematode connectome. Adapted from Cook et al., 2019. **D.** 3D reconstruction of >300 individually traced neurons from the Mouselight project (Winnubst et al., 2019).

*A. Extracted and adapted from https://archive.org/details/b22384753/page/24/mode/2up B. Extracted and adapted from https://www.biodiversitylibrary.org/item/103261#page/5/mode/1up D. Extracted and adapted from http://ml-neuronbrowser.janelia.org/*

The influence of Cajal's work can still be seen in studies that on many occasions define circuits in a simplified and isolated manner. For example, to describe the generation of behaviors such as predation (Han *et al.*, 2017; Y. Li *et al.*, 2018; Hoy, Bishop and Niell, 2019), evasion (Wei *et al.*, 2015; Huang *et al.*, 2017; L. Li *et al.*, 2018; Salay, Ishiko and Huberman, 2018; Shang *et al.*, 2018; Zhou *et al.*, 2019), or feeding (Krashes *et al.*, 2014; Stachniak, Ghosh and Sternson, 2014), only a few projections are deemed critical. However, the current anatomical data show that (1) Each brain area receives and sends information to and from a large number of areas (Oh *et al.*, 2014), and (2) individual neurons also tend to receive and broadcast information through multiple pathways (Winnubst *et al.*, 2019), making the concept of linear functional pathways unlikely to be the only way the brain processes information and mediates behavior.

Yet, the study of isolated circuits has seen a great expansion in recent years due to one of the greatest inventions that has revolutionized the study of neural circuits. That is, the ability to selectively manipulate the activity of genetically defined cell-types. Two major methods have been developed in parallel for that purpose; (1) Optogenetics, in which light-gated ion channels alter the

expressing cell's membrane potentials to either hyperpolarize or depolarize them in response to specific wavelengths of light (Boyden *et al.*, 2005; Zhang *et al.*, 2007), and (2) Chemogenetics, where designer G-coupled receptors enable the manipulation of Gq, Gi, and Gs protein signal transduction pathways by selectively responding to small molecule exogenous ligands, like clozapine-n-oxide (CNO), that are otherwise inert (Armbruster *et al.*, 2007; Alexander *et al.*, 2009; Rogan and Roth, 2011a). Until the arrival of these new tools, the interrogation of the causal role of particular brain areas or neural pathways had been limited to permanent ablations, pharmacological manipulations, cortical cooling or electrical stimulation. These techniques lack temporal resolution, or cell-type and pathway specificity and therefore made the assignment of circuit function challenging. Optogenetics and chemogenetics, combined with the increasingly available genetic tools for the expression of conditional systems through viral vectors and transgenic animals, have allowed the interrogation of cell-type and projection specific circuits in a reversible manner and started a new era of functional circuit dissection.

These new approaches have focused mainly on both the sufficiency and necessity of a subpopulation of neurons for a given function or behavior. These studies have uncovered the relationship between a great number of individual pathways or cell-types and behavior, such as circuit-specific mechanisms of aggression (Lin *et al.*, 2011), depression (Chaudhury *et al.*, 2013), anxiety (Tye *et al.*, 2011), feeding (Stachniak, Ghosh and Sternson, 2014; Stamatakis *et al.*, 2016; Sweeney and Yang, 2016), nest-building (Li *et al.*, 2019), and innate orienting and defensive behaviors (Wei *et al.*, 2015; Evans *et al.*, 2018; Shang *et al.*, 2018; Hoy, Bishop and Niell, 2019) in mice and working memory, decision making (Oyama *et al.*, 2021), motor and visual behavior (Cavanaugh *et al.*, 2012; Gerits *et al.*, 2012; Chernov *et al.*, 2018; Ebina *et al.*, 2019) in non-human primates, among many others. However, these approaches have also fostered an atomistic conceptualization of behaviors focused on describing specialized circuits that govern particular behaviors (Headley *et al.*, 2019; Pessoa, 2019). This can create observational biases where the field increasingly focuses attention where it is easiest to look and ignores the role of potentially critical unobserved cell-populations, pathways, and the interactions between them.

Studying brain functions and behavior one circuit at a time is an understandable approach as by studying them in isolation, we might be able to decompose behaviors and functions into the individual pieces that contribute to them. However, this is only valid under the assumption that the functional units or "pieces" are made up of individual neurons or isolated pathways. Current anatomical and physiological evidence suggests that most functions can be governed by multiple pathways simultaneously, and that the functional unit might be in the local or global network activity. Already Hebb in his "The Organization Of Behaviour" in 1949 proposed that some brain functions such as brain states and memories, instead of working through an input-output linear pathway, could arise from the recurrent activity reverberating in closed loops circuits. Only with the ability to record from multiple neurons and multiple brain regions simultaneously have we been able to address the possibility that neural functions not only depend on the information encoded by individual neurons, but in the interactions within local groups of neurons (ensembles) and across brain wide networks (Yuste, 2015).

Starting with the invention of the multi-electrode recordings (McNaughton, O'Keefe and Barnes, 1983), and the subsequent development of techniques such as functional magnetic resonance imaging (fMRI), calcium imaging, and functional ultrasound imaging (fUSI), the ability to record from multiple neurons and brain areas simultaneously has not stopped growing (these techniques are discussed in detail below, in the section "Large-scale monitoring of neural networks"). This has reached the point where it is currently possible to record from hundreds of individual neurons across

a few brain areas (Steinmetz *et al.*, 2021), or from dozens of brain areas at a 100 µm$^3$ resolution across the whole brain of small mammals (Macé *et al.*, 2018). In the field of memory encoding and retrieval, this new ability to record from large populations of neurons has had a great impact and has helped reshape our understanding of neural encoding of information. For example, it has been shown that orderly activation of neuronal ensembles in the hippocampus can be used to define positions in space, and the replay of those sequences can be used for memory consolidation and planning (Ólafsdóttir, Bush and Barry, 2018). Re-activation of ensembles in multiple regions can trigger memories (Liu *et al.*, 2012; Tayler *et al.*, 2013) or create false memories (Ramirez *et al.*, 2013). Information about specific memories could be encoded across dozens of areas (Vetere *et al.*, 2017; Roy *et al.*, 2019). Additionally, synchronous periodic activity within and across brain areas (neural oscillations) has been proposed as a means for the functional segregation of neural ensembles (Buzsáki and Watson, 2012), and to play roles in supporting inter-areal communication, input selection, plasticity, consolidation and combination of memories.

Large-scale recordings have changed how we approach and understand a plethora of brain functions. For example, regarding visual perception, it has been demonstrated that the activity of cortical ensembles plays a causal role in visually guided behavior and could correspond to the internal representation of perceptual states (Carrillo-Reid *et al.*, 2019). The representation of semantic maps across the human brain have been demonstrated to be far more extensive than previously thought (Huth *et al.*, 2016). Also, in mice, the encoding of choice or actions could be computed across the entire brain (Steinmetz *et al.*, 2019). Taken together, these studies have determined that many brain functions can only be understood when taking into account both the activity of individual neurons and the collective activity of both local and global networks. However, large scale recordings alone that use the correlation between the observed activity and concurrent behavior to infer the relationship between the two, cannot resolve the causal role of any concrete responses regarding the behaviors being studied. In order to bridge the limitations of both neuron-centric and holistic methods, it is necessary to combine local manipulations with both local and global examinations of circuit function. To date, two main strategies have been developed to combine local manipulations and large-scale recordings simultaneously.

One of the first attempts at studying cell-type specific manipulations together with global interactions consisted of the combination of optogenetics and fMRI (ofMRI) (Lee *et al.*, 2010; Gerits *et al.*, 2012). Although fMRI has relatively low temporal (in the order of seconds) and spatial (~1mm$^3$) resolution, when combined with optogenetic manipulations it revealed how different stimulation patterns (frequencies) can have different brain-wide effects (Weitz *et al.*, 2015). This suggests that populations of neurons that have multiple projections could use different firing patterns as a mechanism for biasing the activation of different pathways without the need of anatomical segregation. In a different study, by looking at the brain-wide effects of activating either D1 or D2 medium spiny neurons of the caudateputamen using ofMRI (Bernal-Casas *et al.*, 2017), they confirmed the long debated classical feedforward model of basal ganglia circuit function. In this model, opposing effects of the direct and indirect pathways on the thalamocortical loop (Albin, Young and Penney, 1989) are predicted, but it had not been tested.

A second strategy used to record the effect of local activations to large networks is the combination of optogenetics and two photon calcium imaging. Calcium imaging has cellular resolution in the expense of a limited field of view and depth. However, it allows the observation of the activity of tens to thousands of neurons simultaneously. In vivo, it has showed that the optogenetic activation of single place-cells in the hippocampus could affect groups of other place-cells that had been actived at the same time. This was one of the first observations that demonstrated that interactions

between cells, such as the synchrony of firing, could have a functional role in shaping firing fields (Rickgauer, Deisseroth and Tank, 2014). More recently, this approach was used to test the functional role of cortical ensembles (Carrillo-Reid *et al.*, 2019) and they found that the artificial activation of visual cortical ensembles is sufficient to trigger visually guided behavior even in the absence of visual stimuli. This further suggests that neuronal ensembles, rather than individual neurons, could constitute a functional unit of the brain. The same strategy has also been rapidly adapted to be performed in smaller models such as the fruit fly (Drosophila), C. elegans (Shipley *et al.*, 2014; Gengyo-Ando *et al.*, 2017) and larval zebrafish (Förster *et al.*, 2017). For instance, in the fly, it has been used to map functional connections of circuits mediating behaviors such as grooming (Hampel *et al.*, 2015), courtship (Zhou *et al.*, 2015) and aggression (Hoopfer *et al.*, 2015).

Large-scale recordings of brain activity, and the combination of cell-type specific manipulations with the imaging of large neuronal networks, have shown that information can be present not only in individual neurons but also in the interactions within local and across brain-wide networks. Thus, in order to understand brain function and behavior a new paradigm has been proposed, where the focus relies on the study of the neural interactions from both local and global perspectives (Yuste, 2015). The combination of optogenetics and fMRI and simultaneous single-cell optical perturbations and Ca2+ imaging offer opportunities to understand such interactions, but the trade-offs between the whole-brain and single-cell resolutions make it necessary to find alternatives that complement and make up for some of their limitations. Functional ultrasound imaging is a novel technique that, similar to fMRI, measures hemodynamic changes as an indirect measure of neural activity. It does not have cellular resolution, but it can be performed in awake and behaving mice, and its sensitivity, temporal (0.1s), and spatial (~100µm$^3$) resolutions makes it a great candidate to complement these techniques in the study of brain-wide neural interactions. For that purpose, in this project, we developed the optogenetic fUSI (opto-fUSI) and thus expanded the availability of tools for studying the interaction between local and global brain wide networks in awake and behaving small mammals in an unbiased manner. To demonstrate the potential of this method, we used it to investigate the contribution of distinct cell-types in the mouse superior colliculus to behavior and map the brain-wide neural activity they produce in awake mice. This approach allowed us to identify new brain areas involved in colliculus-driven behaviors and demonstrate that each cell-type mediates behavior via a broad, partially overlapping and yet distinct downstream network of brain regions.

In the following sections of the Introduction, to provide further context, the superior colliculus and techniques used in this project are described in detail.

# 1.2 The superior colliculus

## 1.2.1 The superior colliculus functions: eye, head, body orienting and more

The superior colliculus (SC) is a brain area in the midbrain, involved in a variety of functions including multimodal sensory integration, sensory to motor transformations, attention and decision making. In 1872 Adamük showed that the SC is involved in the control of eye movements (Apter, 1946), and in the following decades, Bellonci, Wlassak, and Cajal, confirmed that the SC receives direct inputs from the retina. In 1899, Cajal proposed that the distribution of the retinal fibers was topographically organized, mapping the visual world onto its surface (Keating and Gaze, 1970; Llinás, 2003) (Figure 1.1A). Together with its connectivity to contralateral motor centers of the brainstem he drew one of the first diagrams of a circuit for sensory to motor transformations (Llinás, 2003).

Julia Apter, in the 1940s, provided functional evidence of the relationship between visual stimuli and the corresponding motor changes in the colliculus of cats. Combining flashes of light and localized chemical neuronal sensitization (using strychninization), she showed that eye movements evoked by stimulating different points of the SC were directed towards specific locations in the visual field. Additionally, she observed that the target locations of such eye movements corresponded well with the organization of the retinal inputs mapped onto the SC, further suggesting that the SC could be a key node for sensory to motor transformations (Apter, 1946). In the 1970s, Schiller and Stryker found the same relationship in monkeys (Schiller and Stryker, 1972).

The first evidence that the colliculus did more than execute motor commands came from Goldberg and Wurtz. They showed that in the colliculus of macaques, responses could precede eye movements, be enhanced if a visual stimulus was trained to be the target of a saccade, and that responses would decrease if the animal was trained not to respond to a stimulus (Wurtz and Goldberg, 1971, 1972; Goldberg and Wurtz, 1972). This suggested that beyond eye movements, the colliculus could be involved in higher cognitive functions such as guiding spatial attention. In parallel, experiments in freely moving animals (primarily cats and rodents) showed that the colliculus was not only able to trigger eye movements but could also trigger head and body orienting (Sprague and Meikle, 1965; Schaefer, 1970; Syka and Radil-Weiss, 1971) or even defensive behaviors (Dean, Redgrave and Westby, 1989). Additionally, somatosensory and auditory maps were found in deeper layers of the colliculus with similar topographical organizations to the overlaying visual maps (Dräger and Hubel, 1975; Stein, Magalhães-Castro and Kruger, 1976). Overall, these studies led to the idea that the colliculus is responsible for guiding the eye, head and body towards or away from salient stimuli located and encoded within the overlayed somatosensory, auditory, and visual maps.

More than 50 year later, the SC has been characterized in great detail in terms of input and output connectivity, and the neural cell-types of its retinorecipient layers, based on morphology, genetic markers, and response properties. Functionally, it is now well established that beyond gaze shifts, the colliculus mediates innate responses to salient stimuli triggering defensive behaviors such as freezing or escape (Branco and Redgrave, 2020), but also reaching movements (Werner, Hoffmann and Dannenberg, 1997; Stuphorn, Hoffmann and Miller, 1999; Stuphorn, Bauswein and Hoffmann, 2000), or even hunting (Furigo *et al.*, 2010; Hoy, Bishop and Niell, 2019; Shang *et al.*, 2019; Förster *et al.*, 2020). Optogenetic stimulation and chemogenetic inhibition of subpopulations of the colliculus suggest there is a strong relationship between cell-types and particular behaviors (Wei *et al.*, 2015; Shang *et al.*, 2018; Hoy, Bishop and Niell, 2019). Additionally, manipulations of the colliculus during tasks that require spatial attention and target selection confirmed that the colliculus has an active role beyond executing motor commands dictated by the cortex, selecting the goals for the triggered orienting movements (in mice (Wang *et al.*, 2020); in non-human primate (Carello and Krauzlis, 2004; McPeek and Keller, 2004; Dorris, Olivier and Munoz, 2007; Lovejoy and Krauzlis, 2010; Jun *et al.*, 2021)).

In humans, fMRI studies have found that the SC is activated by reaching movements (Linzenbold and Himmelbach, 2012; Himmelbach, Linzenbold and Ilg, 2013), saccade preparation and execution (Furlan, Smith and Walker, 2015; Savjani *et al.*, 2018), and responses to aversive or threatening visual stimuli (Almeida, Soares and Castelo-Branco, 2015; Wang *et al.*, 2020; Kragel *et al.*, 2021). This suggests that the human colliculus could play similar roles as in other animal models, highlighting the translational potential of this area. Importantly, that also hinted the SC could be involved in psychiatric and neurodegenerative disorders where maladaptive visuomotor coordination, attention, decision making, or defensive responses are observed. Consistent with this idea, in recent years, fMRI studies have found abnormal collicular activity in patients with Parkinson's disease

(Pretegiani *et al.*, 2019; Moro *et al.*, 2020) and post-traumatic stress disorders (Olivé *et al.*, 2018; Terpou *et al.*, 2019), and collicular deficits have been proposed in attention deficit hyperactivity disorders and autism (Overton, 2008; Jure, 2018). However, until recently, mechanistic understanding of collicular functions has been limited by the lack of specificity, resolution, or low throughput of the available tools. In the last decade, with the improvements in high-density electrophysiology probes, calcium imaging, statistical analysis and modelling, and the development of optogenetic and chemogenetic tools, collicular research has regained great popularity. These new tools have allowed for the first insights into the causal relationship between the different cell-types of the SC and behavior (Wei *et al.*, 2015; Shang *et al.*, 2018; Hoy, Bishop and Niell, 2019), and into the computations behind collicular saliency signaling (Franceschi and Solomon, 2020; Lee *et al.*, 2020) and decision making (Evans *et al.*, 2018; Jun *et al.*, 2021). However, the relationship between specific cell-types, behaviors, and the multi-synaptic downstream networks involved in the process, is still poorly understood.

## 1.2.2 Collicular structure and connectivity, from cell-types to networks

### A layered structure
The superior colliculus is a conserved structure that can roughly be divided in three main layers across all vertebrates (mammals: superficial, intermediate and deep; non-mammals: superficial, central and periventricular), and is often further subdivided into up to 15 layers depending on the species. Over a 100 years ago, Ramon y Cajal was the first to describe the organization of the colliculus (Ramon y Cajal, 1899) and Huber and Crosby (Huber and Crosby, 1933) made the first attempts at integrating the nomenclature across vertebrate fila. In the 70s, studies in the tree shrew (Casagrande *et al.*, 1972) provided the first evidence that superficial and deep layers could be functionally segregated into visual (superficial) and motor (deep) layers. The superficial layers process visual information and, in mammals, include the stratum zonale (SZ), the stratum griseum superficiale (SGS) and the stratum opticum (SO). Each layer has been shown to contain different genetically identified subpopulations (Gale and Murphy, 2014; Byun *et al.*, 2016), with different morphologies and visual properties (Gale and Murphy, 2014, 2016, 2018). The SO is the entry point of retinal fibers in all vertebrates. In mammals, it is located at the division between the superficial and intermediate layers and although it contains cells, it is dominated by the entering fibers. From there, retinal axons are orderly distributed among the superficial layers, with different retinal ganglion cells providing inputs to specific strata (Hofbauer and Dräger, 1985; Kuljis and Karten, 1988; Yamagata *et al.*, 2006; Hong, Kim and Sanes, 2011; Robles, Filosa and Baier, 2013). Over the SO rests the SGS, which is often further subdivided into two or three sublamina and contains the largest number of cells of the superficial layers. The SZ is the thinnest and outermost layer, characterized by the almost complete absence of cells.

In the superficial layers, the orderly distribution of retinal terminals can also create functional layers. For instance, direction selectivity in the SC has been shown to be inherited directly from the retina (Shi *et al.*, 2017). Consistent with the retinal axonal distribution of direction selective cells (Kim *et al.*, 2010; Kay *et al.*, 2011), in a recent study, Inayat et al. found that in the most superficial layers, up to 80% showed direction selectivity (Inayat *et al.*, 2015). Additionally, in another study, Reinhard et al., 2019 showed that functional segregation of different collicular subpopulations, defined by their projections, could be traced to the different sets of retinal ganglion cells that provide input to them. Non-retinal inputs from areas such as primary and secondary visual cortex or somatosensory cortex have also been shown to be laminae and topographically specific, adding potential layers of functional segregation (Wang and Burkhalter, 2013; Benavidez *et al.*, 2021) (Figure 1.2).

The intermediate layers contain a variety of unimodal and multimodal neurons that respond to visual, auditory and somatosensory stimuli, following a similar topographical organization to the overlaying visual maps (Dräger and Hubel, 1975; Rees, 1996; Wallace, Wilkinson and Stein, 1996). They are generally subdivided into the stratum griseum intermediale (SGI), with an upper and more cellular sub-lamina and a lower sub-lamina dominated by fibers. Below these, fibers running mediolaterally from the stratum album intermediale (SAI) and serve as a border between intermediate and deep layers. Finally, the deep layers are commonly divided into the cellular layer, stratum griseum profundum (SGP), and a narrow white layer, the stratum album profundum (SAP), adjacent to the periaqueductal gray (PAG). Intermediate and deep layers send projections to multiple motor regions and therefore are thought to be the main effector pathway for the motor commands mediated by the colliculus (Sparks and Hartwich-Young, 1989), as well as computing saliency (Lee *et al.*, 2020) or choices (McPeek and Keller, 2004; Evans *et al.*, 2018).
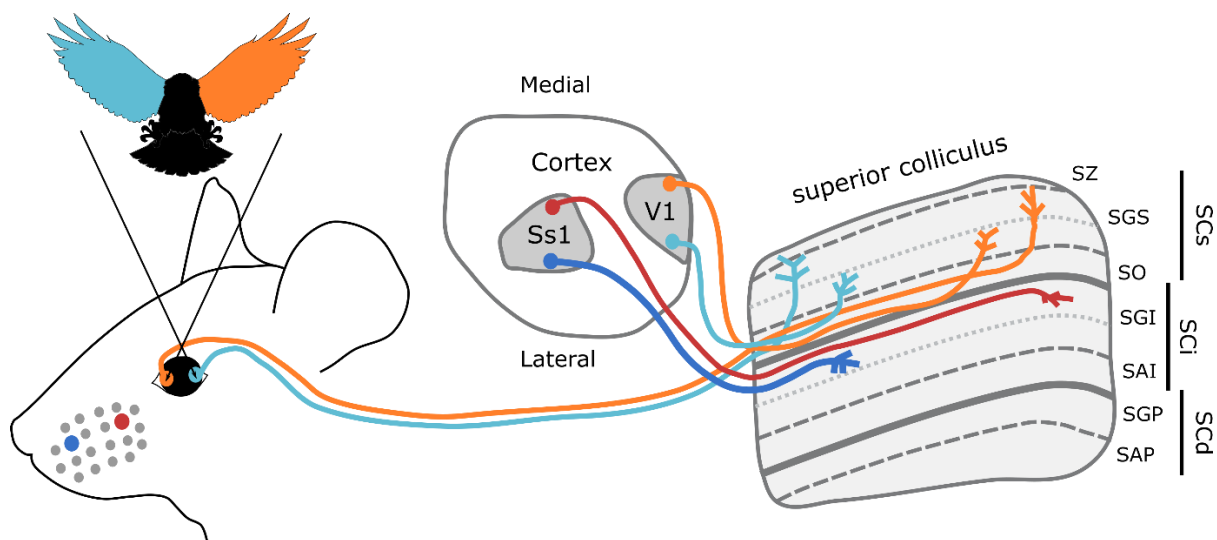


**Figure 1.2. Schematic showing the lamination and alignment of visual and somatosensory inputs in the superior colliculus**. Ss1: Primary somatosensory cortex; V1: Primary visual cortex; SCs: Superior colliculus, superficial layers; SCi: Superior colliculus, intermediate layers; SCd: Superior colliculus, deep layers; SZ: Stratum zonale; SGS: Stratum griseum superficiale; SO: Stratum opticum; SGI: stratum griseum intemediale; SAI: Stratum albicum intermediale; SGP: Stratum griseum profundum; SAP: Stratum albicum profundum. Light gray dotted lines indicate division between upper and lower SGS and SGI.

## Cell-types

Neuronal cell-types are, on a fundamental level, groups of neurons that carry out a specific function (Masland, 2004). From the first drawings of Cajal, it was already clear that neurons come in a wide variety of morphologies and connectivity patterns. Nowadays, these features are used together with response properties, and molecular profiles to group cells in a reproducible manner and study their function (Zeng and Sanes, 2017). In the superficial layers of the superior colliculus, studies in the 70s and 80s identified three major morphological cell types with different projection patterns that could be consistently found in different animal models (Langer and Lund, 1974; Graham and Casagrande, 1980; Laemle, 1983; Sugita *et al.*, 1983; May, 2006); horizontal cells, wide-field cells, and narrow-field cells. In the mouse, there is a growing number of cell-types being characterized in the colliculus that include narrow-field, wide-field and horizontal cells, but also stellate cells (Gale and Murphy, 2014, 2018), heterogeneous populations of interneurons (Endo *et al.*, 2003; Whyland, Slusarczyk and Bickford, 2020), and parvalbumin expressing cells (Villalobos *et al.*, 2018) (Figure 1.3). In the following paragraphs the collicular cell-types present in mice, are described in more detail.

**Horizontal cells** are inhibitory neurons found primarily in the stratum griseum superficiale (Endo *et al.*, 2003; Gale and Murphy, 2014; Whyland, Slusarczyk and Bickford, 2020). They are characterized by their horizontally extended dendrites, large receptive fields, their responses to either large stationary or fast-moving stimuli, and their projections to the lateral geniculate, parabigeminal nucleus and pretectal nuclei (Gale and Murphy, 2014, 2018). Additionally, Gale and Murphy found that horizontal cells can be selectively labelled using transgenic mice in which cre recombinase is expressed under the control of the Gad2 promoter (gad2: an isoform of the gene encoding the enzyme responsible for GABA biosynthesis). Other collicular GABAergic cell-types have been described based on morphology, molecular identity, and connectivity (Mize, 1992; Endo *et al.*, 2003; Villalobos *et al.*, 2018; Whyland, Slusarczyk and Bickford, 2020), but horizontal cells that project outside of the colliculus, do not seem to overlap with other GABAergic subpopulations (Whyland, Slusarczyk and Bickford, 2020). Although gad2 interneurons exist (Gale and Murphy, 2014, 2018), whether they are a major or minor differentiated cell-type has not yet been clarified. To date, the role of horizontal neurons remains largely unexplored.

**Wide-field neurons** are excitatory cells with cell bodies typically located in the stratum opticum. Their most characteristic feature is the large dendritic trees that ascend towards the surface of the SC covering large areas of the visual field. Consistent with their extensive dendritic trees, these neurons have large receptive fields (Gale and Murphy, 2014, 2018). They respond to small, slow-moving objects but also to expanding discs (Wei *et al.*, 2015; Shang *et al.*, 2018). Wide-field neurons have been shown to send projections to a single area, the lateral posterior nucleus of the thalamus (called pulvinar in human and non-human primates) and can be selectively targeted using transgenic mice that express cre under the promotor of the neurotensin receptor 1 (NTSR). SC projections to the pulvinar have been shown to mediate freezing behavior (Wei *et al.*, 2015; Shang *et al.*, 2018) and some aspects of hunting behavior, such as the detection of prey (Hoy, Bishop and Niell, 2019). However, although the experiments that tested hunting behavior used NSTR-cre mice, the defensive role of pulvinar projecting neurons was studied by activating either CaMKII+ neurons (Wei *et al.*, 2015) or parvalbumin+ neurons (PV) (Shang *et al.*, 2018) with similar results. Although wide-field neurons are the only cell-type known to project to the pulvinar, to what degree NTSR, CaMKII and PV neurons overlap and form a homogeneous or heterogeneous population still needs to be clarified.

**Narrow-field cell** bodies are generally found in the lower part of the stratum griseum superficiale. These are also excitatory neurons with narrow dendritic trees that extend both upwards and downward from the soma. Narrow-field neurons have small receptive fields, they are often direction selective, and prefer small stimuli. Interestingly, they send projections to the parabigeminal nucleus but also to the deeper layers of the SC, making them the ideal candidate of collicular visuomotor transformations. In 2014, Gale and Murphy showed that cre recombinase is expressed in Narrow-field neurons of the gastrin releasing peptide (GRP)-Cre mouse line. However, to date, a single study has addressed the role of narrow field neurons. In this study, Hoy, Bishop and Niell, 2019 inhibited this subpopulation of neurons during a hunting test and found that it could be involved in the proper orienting and pursuit of prey. Whether activation of these neurons would promote hunting or other behavioral responses such as reaching, eye movements or defensive behaviors has not been explored.

**Stellate cells** are the smallest cell-type that has been characterized in the superficial layers of the SC. They are typically found in the stratum griseum superficiale and stratum zonale and are characterized by their small size and radial dendritic trees, extending in all the possible directions. In the stratum zonale, they have been proposed to include marginal cells that extend their dendrites

downwards, as it is the only directions their dendrites can go. Similar to Narrow-field cells, stellate cells have small receptive field and prefer small stimuli. They are mostly excitatory neurons (~90%) that provide input to all other cell-types of the superficial layers and to the parabigeminal and LGN nuclei. Recently, it was shown that cre is expressed in stellate cells of Rorb-Cre knock in mouse line (Gale and Murphy, 2018). However, more than 50% of the neurons labelled by this mouse line were interneurons. It is unclear whether locally connected stellate cells and long-range projecting cells are the same or different subpopulations. Thus, although it would be possible to study stellate cells projecting to the parabigeminal and LGN nuclei using retrograde viral vectors, if locally connected stellate cells are a segregated population, it will be a challenge to study their function independently from interneurons. Currently, our knowledge of stellate cells is limited to the morphology and visual response properties.

**Parvalbumin expressing cells** are a heterogeneous population that includes both excitatory (~80%) and inhibitory cells (Villalobos *et al.*, 2018; Whyland, Slusarczyk and Bickford, 2020). The cell bodies of these neurons are generally located in the stratum griseum superficiale, with little presence in the stratum zonale and stratum opticum (Shang *et al.*, 2015, 2018; Villalobos *et al.*, 2018). They have been shown to have a variety of morphologies and electrophysiological properties resembling predominantly stellate cells, but also narrow field, horizontal and wide field neurons. However, no direct immunohistochemical comparison has been performed to assess the degree of overlap between these different cell-types. PV neurons send projections preferentially to LGN, parabigeminal and Pontine nucleus, but also to the pulvinar and respond to looming stimuli, but not to objects moving in other directions (Shang *et al.*, 2015). Additionally, it has been shown that projections to the parabigeminal nucleus promote escape behavior whereas the small projection to the pulvinar contributes to freezing (Shang *et al.*, 2018).

**Interneurons** in the SC have been shown to receive direct input from the retina and primary visual cortex (Zingg *et al.*, 2017; Whyland, Slusarczyk and Bickford, 2020). GABAergic neurons constitute a ~30% of neurons in the superficial layers, including somatostatin, vasopressin, and parvalbumin expressing neurons (Shang *et al.*, 2015; Whyland, Slusarczyk and Bickford, 2020). Using other molecular markers, other studies have divided local interneurons into 4 different groups (GABA+ only = 30%; GAD67+ GABA+ = 45%; GAD67+ GABA+PV+ = 15%; and GABA+PV+ = 10%). Additionally, they have been shown to exhibit a variety of morphological and electrophysiological properties (Mize, 1992; Endo *et al.*, 2003; Gale and Murphy, 2014, 2016; Masterson *et al.*, 2019). However, what are the contributions of these different subpopulations to the different collicular functions is still largely unexplored.
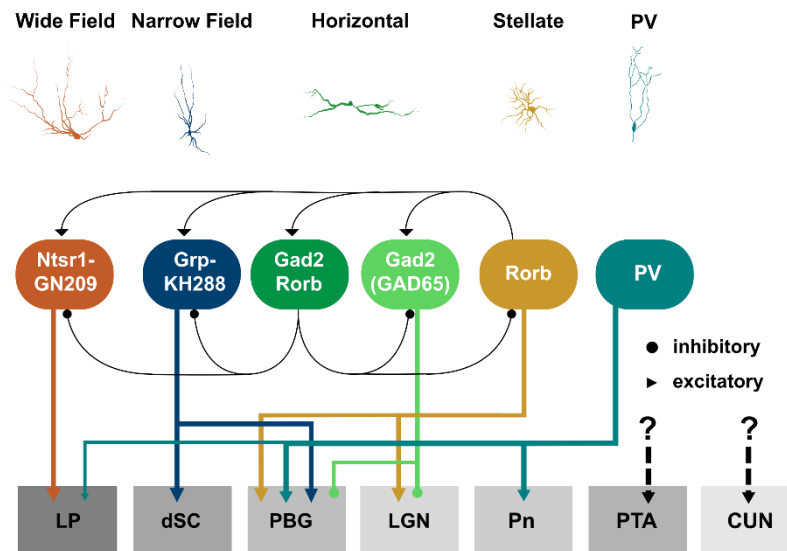
**Figure 1.3. Overview of superior colliculus cell-types and projections.** From Top to bottom: cell-type names, example morphologies, genetic markers, and the projections of the superficial layers of the colliculus. Dashed arrows represent anatomically described projections of the superficial layers of the colliculus that do not belong to any known cell-type.

**Other cells-types** are likely to exist in the superficial layers of the colliculus. For example, a recent molecular characterization of the colliculus found that at least 10 different subpopulations can be differentiated (Byun *et al.*, 2016). Additionally, although it is known that the superficial layers project to the cuneiform nucleus (Mitchell, Dean and Redgrave, 1988; Redgrave *et al.*, 1988; Zingg *et al.*, 2017), and pretectal areas (May, 2006), none of the described genetically defined subpopulations has been shown to project there. Thus, in the coming years, with the renewed interest in collicular function, it is to be expected that the current cell-types will be further divided into more refined subpopulations and that additional cell-types will arise based on new molecular, morphological and functional characterizations.

### 1.2.3 The superior colliculus as a node of brain wide networks

The superior colliculus receives input from areas across the entire brain (May, 2006; Oh *et al.*, 2014; Benavidez *et al.*, 2021). In the superficial layers the major inputs are provided by the contralateral retina, and primary and secondary visual areas (Wang and Burkhalter, 2013), although it also receives inputs from a variety of brain regions including, the ipsilateral retina (Godement, Salaün and Imbert, 1984; Haustead *et al.*, 2008), somatosensory and auditory cortical areas, the hypothalamus, or the hippocampal formation (Oh *et al.*, 2014). Additionally, it has reciprocal connections with its projection targets such as the parabigeminal, lateral geniculate nucleus, pretectal areas, or pulvinar (May, 2006; Oh *et al.*, 2014). However, beyond the mono-synaptic inputs and projections of the colliculus, little is known about the organization and function of collicular downstream pathways. Nonetheless, based on anatomical studies, single-cell recordings, and manipulations, several brain wide circuit models have been proposed where the superior colliculus plays a central role.

#### Circuits for the control of eye movements.

One of the best-known downstream networks of the colliculus is the one in charge of mediating eye movements (Moschovakis, Scudder and Highstein, 1996; Sparks, 2002; May, 2006) (Figure 1.4), and is largely based on the visual system of the cat and non-human primate.

Visual inputs arriving to the superficial layers can be routed to the deeper motor layers of the colliculus through direct connections (May, 2006). From there, different pathways are used to trigger horizontal and vertical movements.

For horizontal eye movements (Figure 1.4), intermediate and deep layers of the colliculus provide excitatory input to the contralateral pontine reticular formation where long-lead burst neurons (LLPNs) and excitatory burst neurons (EBNs) reside (Sparks, 2002). LLPN and EBN neurons have been shown to fire before and during saccades (Strassman, Highstein and McCrea, 1986; Scudder *et al.*, 1996). EBN neurons send projections to the III (oculomotor) and VI (abducents) cranial nerve nuclei than in turn control muscles connected to the left and right of the eyes (Moschovakis, Scudder and Highstein, 1996; Bohlen, Warren and May, 2016). Importantly, EBN neurons also project to neurons in the prepositus hypoglossus and vestibular nuclei, which generate burst-tonic firing patterns that allow to the eye to maintain the new position (McFarland and Fuchs, 1992; Sparks, 2002). In order to coordinate left and right eyes, EBN also project to inhibitory burst neurons (IBNs) located in the caudal part of the reticular formation (Yoshida *et al.*, 1982; Scudder, Fuchs and Langer, 1988; Moschovakis, Scudder and Highstein, 1996). IBNs synapse onto contralateral populations of IBNs, EBNs and motor neurons of the cranial nerves silencing their activity. Between saccades, omnipause neurons in the nucleus raphe interpositus provide tonic inhibition to both EBNs and IBNs to avoid movement (Cohen and Henn, 1972; Langer and Kaneko, 1990; Optican, 2008). The activity of omnipause neurons is regulated by inhibitory inputs from the central mesencephalic reticular formation (midbrain reticular nucleus in mice), that in turn receive strong excitatory inputs from the SC (Wang *et al.*, 2013).
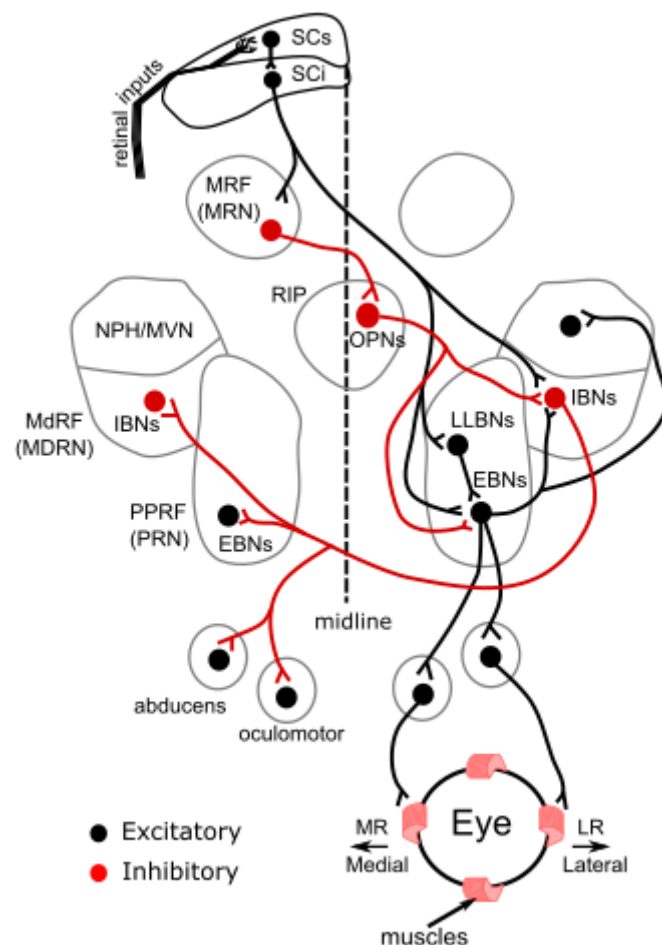
**Figure 1.4. Circuit diagram of the main contributors to horizontal eye movements.** SCs: superior colliculus, superficial layers. SCi: superior colliculus, intermediate layers. MRF: mesencephalic reticular formation. MRN: mdibrain reticular formation (in mice); RIP: raphe interpositus. NPH: nucleus prepositus hypoglossus MVN: medial vestibular nucleus; MdRF: medullar reticular formation; MDRN: medullar reticular nucleus (in mice); PPRF: Paramedian pontine reticular formation; PRN: pontine reticular formation (in mice); OPNs: omnipause neurons; LLBNs: long-lead burst neurons; EBNs: Excitatory burst neurons; IBNs: Inhibitory burst neurons. MR: medial rectus muscle; LR: lateral rectus muscle.

To generate vertical eye movements, the motor layers of the SC send bilateral projections to the rostral part of the medial longitudinal fasciculus (mlf), below and adjacent to the PAG. The mlf contains burst neurons that generate vertical and torsional eye movements (Büttner, Büttner-Ennever and Henn, 1977; King and Fuchs, 1979; Sparks, 2002). Burst neurons of the mlf send direct projections to motor neurons of the oculomotor and trochlear nuclei that control the vertical muscles. Mlf also sends projections to the interstitial nucleus of Cajal (INC), that contain neurons that show burst-tonic firing patterns and allow the maintenance of vertical eye positions (Helmchen, Rambold and Büttner, 1996; Helmchen *et al.*, 1998). Omnipause neurons of the raphe interpositus also receive inputs from the INC (Langer and Kaneko, 1990) and provide tonic inhibition to vertical motor neurons to halt movement between saccades.

Similar pathways have been described for the control of neck and head movements where different pathways downstream of the motor layers of the colliculus control vertical and horizontal head movements (Isa and Sasaki, 2002). For instance, horizontal head movement is controlled by contralateral reticulospinal neurons in the pons and vertical movement by neurons in the Forel's field projecting to the contralateral spinal cord.

The oculomotor network described here is largely based on anatomical and single-cell neural recordings in cats and non-human primates. However, orienting movements have been shown to be mediated by the colliculus across multiple species, including lamprey, the oldest living vertebrates (Suzuki *et al.*, 2019). In mice, the lack of fovea could suggest that mice do not need to direct the eyes towards stimuli or make saccades to explore the visual scene. Accordingly, studies have shown that most eye movements in mice are compensatory to head movements, to stabilize the visual scene. These stabilizing saccades, named optokinetic and vestibuloocular reflexes, do not require the colliculus (Simpson, 1984). For instance, optokinetic reflex relies on retinal projections to the nucleus of the optic tract (NOT) and the dorsal terminal nucleus for horizontal movements (Hoffmann and Fischer, 2001; Osterhout *et al.*, 2015), and medial terminal nucleus for vertical movements (Simpson, 1984; Sun *et al.*, 2015). These nuclei have direct projection to motor nuclei in the brainstem. For example, NOT projects to the medial vestibular nucleus (MVN) and nucleus prepositus hypoglossi (NPH), that in turn, project to motor neurons in the abducens to drive horizontal movements (Simpson, 1984; Kodama and Lac, 2016). Nevertheless, the colliculus is also known for driving head and body orienting movements that follow similar pathways to those described for eye movements, and are more common in mice (Gandhi and Katnani, 2011). Also, it was recently found that the intermediate layers of the colliculus of mice have been shown to contain a cell-type that drives head movements according to a motor map (Masullo *et al.*, 2019), but no similar cell-type has been found driving eye movements. However, the mouse SC contains all the necessary anatomical connections for directed eye movements (May, 2006), and recent studies have demonstrated that freely moving (Michaiel, Abe and Niell, 2020) and head-fixed (Zahler *et al.*, 2021) mice generate directed eye movements using the colliculus. What these eye movements are used for and to what degree they are mediated through the same pathways as in cat or non-human primates is still to be defined.

## Motor control through subcortical loops.

The basal ganglia (striatum, pallidum, substantia nigra (SN) and subthalamic nucleus (STN)), have been implicated in a wide variety of functions, including motor control (Takakusaki *et al.*, 2004), action selection (McHaffie *et al.*, 2005; Fisher and Reynolds, 2014) and reinforcement learning (Redgrave, Vautrelle and Reynolds, 2011). The superior colliculus has both direct and indirect anatomical downstream connections with the basal ganglia and receives inputs back from the substantia nigra.

The proposed subcortical loops start in the superficial layers of the colliculus. The SC send input to the pulvinar that, in turn, can relay the visual information to the caudal part of the striatum. The striatum then projects directly to the substantia nigra (Deniau, Menetrey and Charpier, 1996; Deniau *et al.*, 2007), which closes the loop sending its projections back to the SC (May and Hall, 1984; Redgrave, Marrow and Dean, 1992). Other loops with the basal ganglia originating in the SC include the collicular projections to the intralaminar nuclei of the thalamus (McHaffie *et al.*, 2005) that in turn project to all territories of the striatum and STN (Takada *et al.*, 1985; Féger, Bevan and Crossman, 1994), and direct collicular projections to the STN (Coizet *et al.*, 2009), the substantia nigra (Comoli *et al.*, 2003; May *et al.*, 2009; Shang *et al.*, 2019; Huang *et al.*, 2021) and ventral tegmental area (Comoli *et al.*, 2003; Dommett *et al.*, 2005) (Figure 1.5).

Functionally, the basal ganglia loops have been proposed to help the colliculus select the right target before performing an orienting movement, based on current contextual and sensory information (Mink, 1996; Redgrave, Prescott and Gurney, 1999). The substantia nigra provides tonic inhibition to the colliculus, and before a saccade is performed, nigro-tectal neurons interrupt their inhibition, but only if the saccade is volitional, not spontaneous (Chevalier *et al.*, 1981; Hikosaka and Wurtz, 1983; Chevalier, Vacher and Deniau, 1984), suggesting a role in target selection.
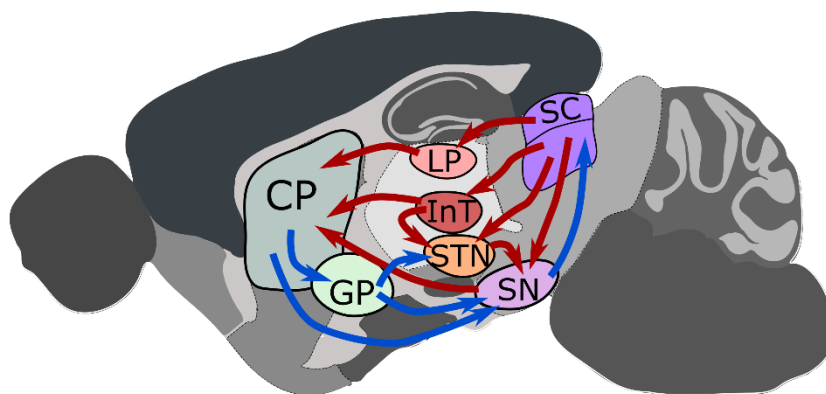


**Figure 1.5. Potential collicular subcortical loops for motor control.** Red arrows depict projections that are predominantly excitarory. Blue arrows depict projections that are predominantly inhibitory. CP: Caudateputamen; GP: Globus pallidum; InT: Intralaminar thalamus; LP: Lateral posterior nucleus of the thalamus; SC: Superior colliculus; SN: Substantia nigra; STN: Subthalamic nucleus. Adapted from (McHaffie *et al.*, 2005; Coizet *et al.*, 2009; Redgrave *et al.*, 2010; Shang *et al.*, 2019)

The activity of nigral neurons is modulated by inhibitory and excitatory inputs from the caudate and STN, respectively. Whereas STN has been shown to be necessary to interrupt ongoing actions or behaviors (Fife *et al.*, 2017), caudate inhibitory projections have similar properties to those found in the substantia nigra, and their activity is highly dependent on behavioral context, such as attentional state, memory requirements, or motivational state (Hikosaka, Sakamoto and Usui, 1989a, 1989b;

Hikosaka, Nakamura and Nakahara, 2006). Additionally, in the cat, stimulation of the caudate evokes both saccades and head turning, further supporting the idea that the caudate provides the orienting-relevant information to the substantia nigra (Laursen, 1962; Kitama *et al.*, 1991). However, although the evidence suggest that the models contain all the necessary components, functional or anatomical proof of the multi-synaptic relationship between these areas is still very limited. The different loops between the basal ganglia and the colliculus are based on both anatomical mono-synaptic studies and electrophysiology recordings in individual areas. It is important to note though, that each of the areas involved in the proposed loops project to multiple other regions. Therefore, although the anatomical connections necessary for the loop might be present, it is also possible that the cells receiving the inputs and the neurons sending the outputs are not the same. For example, the pulvinar is known to send projections not only to the caudate, but also to the visual primary and secondary areas and the lateral amygdala (Zhou *et al.*, 2017, 2018). Thus, collicular neurons projecting to the pulvinar, instead of providing input to caudate-projecting neurons, they might provide only input to amygdala-projecting neurons (Wei *et al.*, 2015) or visual cortex (Bennett *et al.*, 2019). The visual information might therefore be provided by the visual cortex or through the intralaminar projections. Additionally, although silencing, activation and recordings of individual areas have provided compelling evidence of the individual participation of basal ganglia nuclei in orienting behaviors, the precise relationship between these areas and the different cortical and subcortical pathways, or to what extent these are dependent or independent of each other is still largely unexplored.

### Circuit for detection of visual threats.

The superior colliculus has long been known to mediate responses to threatening stimuli (Dean, Redgrave and Westby, 1989). In recent years, collicular functions and the mechanisms for the detection and response to visual threats have gained renewed popularity and have started to be dissected (Figure 1.6). For example, in mice, visual threats such as an approaching object, have been shown to be detected already in the retina by retinal ganglion cells (Münch *et al.*, 2009; Wang *et al.*, 2021) and amacrine cells (Kim *et al.*, 2020). Visual information is sent to the superficial layers of the colliculus, where it is distributed selectively through specific subpopulations of neurons (Reinhard *et al.*, 2019). At this stage, collicular activity is also influenced by cortical inputs that modulate, for example, the magnitude of the response to looming stimuli (Zhao, Liu and Cang, 2014). From the superficial layers of the colliculus, optogenetic activation of pulvinar-projecting neurons has been shown to be sufficient to trigger freezing, possibly through its projection to the lateral amygdala (Wei *et al.*, 2015), which is a structure implicated in conditioned fearful responses (Maren and Quirk, 2004). Alternatively, activation of PV+ neurons projecting to the parabigeminal nucleus triggers escape behavior followed by freezing (Shang *et al.*, 2015, 2018). The parabigeminal nucleus projects to the central amygdala, which can drive freezing, but its role in mediating escape is less clear. The central amygdala is the main output of the amygdalar complex and its projections to the dorsal and ventral periaqueductal gray have been shown to play differential roles in freezing, escape and nociception (Deng, Xiao and Wang, 2016; Tovote *et al.*, 2016; Li and Sheets, 2018). The deep layers of the colliculus have also been shown to trigger escape behavior through its projections to the dorsal part of the periaqueductal gray (Evans *et al.*, 2018). The deep layers of the colliculus receive information directly from the superficial layers, but also from feedback projections from several targets of the superficial layers such as the parabigeminal nucleus, the ventral part of the LGN, the pretectum, or the cuneiform (May, 2006). Some of these areas also project directly to the periaqueductal gray, or are interconnected with each other, but in most cases, the contributions of these different connections have not yet been investigated (Figure 1.6). Feedback projections from the ventral part of the LGN have been recently shown to modulate different aspects of defensive

behaviors. For instance, changing the threshold for triggering escape behaviors in response to threats (Fratzl *et al.*, 2021) or changing the duration of such responses (Salay and Huberman, 2021). Finally, the periaqueductal gray is thought to mediate defensive behaviors through its direct input to the brainstem, medulla or cuneifrom (Lovick, 1993; Cameron *et al.*, 1995; Schenberg *et al.*, 2005), but the precise circuits that would mediate such responses are largely unknown. Overall, with the current anatomical and functional evidence it is clear that the circuits for detection of visual threats have just started to be elucidated. However, with the growing availability of genetic tools such as transgenic mouse lines and transsynaptic viral vectors, that allow the manipulation of ever more refined populations of neurons makes the dissection of collicular function a challenge, rather than a seemingly impossible goal.

Altogether, current anatomical and functional evidence suggests that collicular functions are mediated through brain-wide networks. The extensive anatomical interconnectivity of the different collicular downstream pathways poses the question of to what degree the different collicular-driven behaviors are evoked by independent hardwired pathways or through indistinguishable global networks. Visual information from the retina is segregated in a projection-specific manner, but to what degree or for how long that is maintained is still an open question.
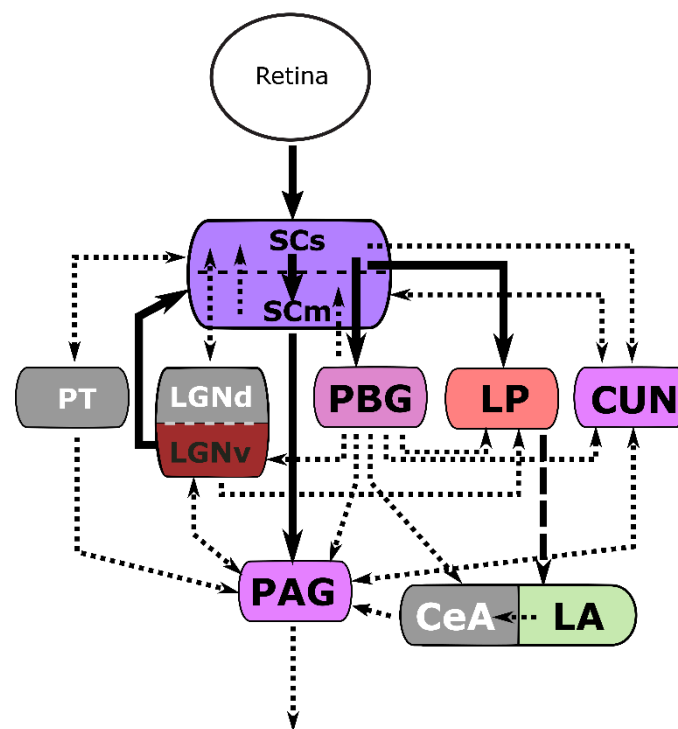


**Figure 1.6. Diagram of connectivity of the superficial layers of the colliculus and its mono-synaptic targets**. Colored regions indicate they have been shown to trigger or regulate collicular-driven defensive behaviors. Gray areas have not been demonstrated to mediate collicular-driven behaviors. Black filled arrows indicate projections that have been shown to participate in defensive behaviors. Dashed line indicates functional and anatomical connection confirmed, but no causal demonstration. Doted lines indicate anatomical connections that have not been shown to be di-synaptically connected to the superficial layers of the SC and have not been specifically targeted to trigger defensive behaviors. SCs: superior colliculus, superficial layers; SCm: Superior colliculus, motor layers; PT: pretectal areas; LGNd: lateral geniculate nucleus, dorsal part; LGNv: lateral geniculate nucleus, ventral part; PBG: parabigeminal nucleus; LP: lateral posterior nucleus of the thalamus; CUN: cuneiform nucleus; PAG: periaqueductal gray; CeA: central amygdala; LA: lateral amygdala. This diagram is based on: (Baleydier and Magnin, 1979; Korte *et al.*, 1992; Monavarfeshani, Sabbagh and Fox, 2017; Zhou *et al.*, 2017; Benavidez *et al.*, 2021)

# 1.3 Large-scale monitoring of neural networks

In order to understand how information is distributed across the brain it is necessary, not surprisingly, to record from large portions of the brain or the whole brain. The study of neural circuits from a brain-wide perspective has gained momentum with the appearance of different alternative tools to examine neural function in large scales. From molecular tools such as the use of immediate early genes, to multi-electrode probes, functional magnetic resonance imaging (fMRI), and more recently *in vivo* $Ca^{2+}$ imaging and fUSI. Each of these techniques offers a unique perspective on the function of neural circuits with its own advantages and disadvantages. In order to better understand why we chose to develop opto-fUSI for the study of neural networks I will describe here in more detail these different set of tools with its advantages and disadvantages and compare them to the fUSI.

## 1.3.1 Functional ultrasound imaging (fUSI) of the brain

fUS imaging is one of the youngest modalities developed to study brain-wide functional networks (Montaldo *et al.*, 2009; Macé *et al.*, 2011). Even though it is a new imaging modality, it is based on the Doppler effect, which is far from a new concept. The Doppler effect is named after Christian Andreas Doppler who first described this effect in 1842 by studying the colored light of binary stars (Coman, 2005). He demonstrated that the relative motion between stars and the earth, resulted in either a red shift or blue shift in the light's frequency. This shift in the frequencies of waves coming from moving objects is what is known as the Doppler effect and that principle also applies to sound waves. For example, in figure 1.7A is shown how, when sound is emitted from a static object (e.g. parked ambulance), the waves travel evenly in all directions and the sound can be perceived equally from any direction. If instead, the sound is emitted from a moving object, the waves get closer to each other in front of the object, increasing the frequency of the wave, and more spaced behind the object, decreasing the frequency. For a passer-by, that results in hearing a higher pitched noise if the object is moving in their direction, or a lower pitched noise if the object is moving away (Figure 1.7A, Bottom). For ultrasound imaging, very short pulses of ultrasound waves (15MHz) are sent in quick succession into the brain (at least 0.5 KHz and up to 20 KHz). When ultrasound waves hit tissue or moving particles they are back scattered, and the echoes are assessed again. If the waves hit a static object such as an axon, or neural soma, there will be no change in the frequency of the backscattered wave. However, if the waves hit an erythrocyte circulating through a blood vessel, depending on the direction of the movement, this will shift the waves towards higher or lower frequencies (Figure 1.7B). Movement of the tissue itself can also cause frequency shifts but these happen within frequency ranges that can generally be filtered (Demené *et al.*, 2015). To measure such frequency shifts, fUS resorts to indirect measures. By emitting a fast (KHz) sequence of ultrasound pulses and measuring their echoes, it can detect shifts in the timing of the receiving echoes caused by the movement of blood cells. Such shifts are equivalent to the Doppler frequency shifts (Edelman and Macé, 2021). By integrating all the non-tissue frequency shifts, a value proportional to the number of circulating cells is obtained (Power Doppler; (Rubin *et al.*, 1994, 1995)), and therefore a measure proportional to the cerebral blood volume (CBV: volume of blood in a given amount of brain tissue). This is not to be confused with cerebral blood flow, which corresponds to the rate of blood being delivered to a given amount of brain tissue, thus blood per minute.

The closest equivalent to CBV measured with fUSI are CBV fMRI measurements. For instance, MRI contrast agents (such as dextran-coated iron oxide agents; MION) injected into the blood stream are used to measure flood flow and volume. In this case, increases and decreases of the concentration of the contrast agent are associated with the corresponding changes in blood volume that follow neural activation (Mandeville *et al.,*1998; Vanduffel *et al.,*2001). Alternatively, CBV measurements in fMRI can be obtained using the vascular space occupancy (VASO) technique. This is done by using a MRI sequence that nulls the blood signal while keeping that of the tissue. Thus, in this context, when there are increases in blood volume due neural activity, the tissue signal decreases proportionally to the increase in CBV (Lua and van Zijl, 2012). Recent studies have shown that in resting state conditions, CBV changes measured with fMRI can be found in the absence of neural activity (Winder *et al.*, 2017). Therefore it is likely that, similarly, the fUSI signal will not always correspond to neural activity and it should be combined with other techniques that allow for direct measurements of neural activity.

By measuring the CBV at very high frequencies (kHz), and combining images obtained by sending waves at different angles (a process called compounding), fUSI can detect the subtle changes in blood volume induced by the neurovascular coupling. Such changes are an indirect measure of neural activity. However, in order to be able to send and record the backscattered echoes, since ultrasound is greatly attenuated and reflected by bone, invasive craniotomies have to be performed. Although, fUSI has been also performed transcranially, in such cases it cannot clearly discern signals much deeper than 2-3 mm into the brain (Tiran *et al.*, 2017). Injecting contrast agents into the bloodstream can amplify the signal, but current methods rely on continuous intravenous injection of micro-bubbles to keep the concentration constant, limiting the conditions in which it is applicable (Errico *et al.*, 2016; Maresca *et al.*, 2020).
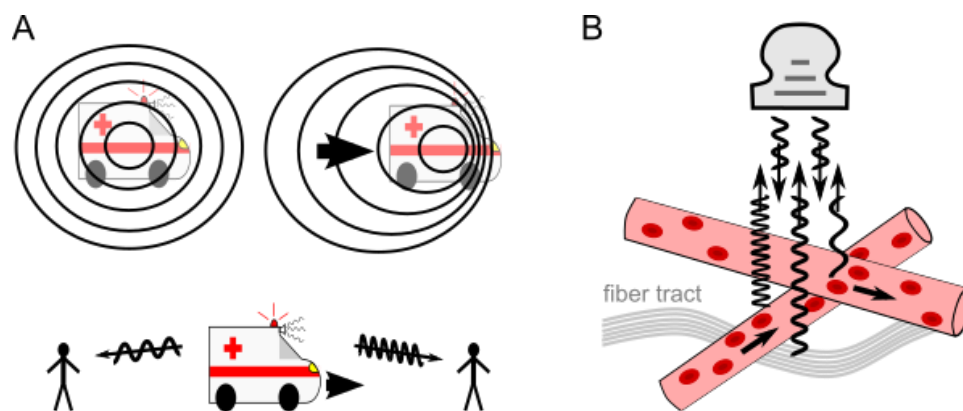


**Figure 1.7. schematic representation of the Doppler effect and fUSI measurements. A.** Top left: static ambulance emitting sound (black circles). Top right: ambulance in motion emitting sound. Bottom: ambulance in motion emitting sound and sound waves. On each side individuals receive the emitted waves. Left: ambulance is moving away from the individual and thus receives lower frequency (low pitch) waves. Right: ambulance is moving towards the individual and thus receives high frequency (high pitch) waves. **B.** Ultrasound transducer emits ultrasound waves at a specific wavelength. If those wavelengths hit a static object (fiber tract), they return a wave of the same wavelength. If ultrasound waves rebound against moving objects (erythrocytes), the returning waves will be shifted to either lower or higher frequencies depending on the direction of the moving object.

Only recently, simultaneous whole brain functional ultrasound imaging has been developed (vfUSI, (Rabut *et al.*, 2019; Brunner *et al.*, 2020)), so the most used modality still consists in imaging the brain through a stepped sequence of parallel plains. Sequential fUSI experiments require long imaging sessions (~3-4h) to obtain enough repetitions to average at each plane. With vfUSI, session

times can be reduced dramatically (30min -1h) while increasing the averaging, and therefore obtaining better signal to noise ratios and sensitivity of the fUSI.

In a typical fUSI experiment, spatial resolution is 100 x 100μm in the imaging plane and 200-250μm across planes. The main reasons for that are; 1) the duration of the ultrasound pulse determines the spatial resolution. High frequency pulses produce better resolution (up to 50 μm resolution with 40-60 MHz frequency; (Foster *et al.*, 2000)), but such short pulses have also less penetration. Thus, in order to image the whole brain of small mammals such as mice, rats or marmosets, a 15 MHz pulses are typically used, which provides a penetration of 1-2cm and a 100 x 100μm in-plane resolution (Urban *et al.*, 2017). 2) On the other hand, the 200-250 μm resolution across planes is mainly limited by the size of the ultrasound beam and the acoustic lens that confines the ultrasound beam within a particular plane. Similar to optical lenses, the acoustic lens is optimized for a specific focal distance and resolution is diminished below and above. The numerical aperture of the fUSI lens has been optimized to allow high resolution (~200-250 μm) across a wide area (~1 cm). Increasing the numerical aperture could increase the resolution but would reduce the imaging area. For volumetric fUSI, no physical lens is used which could allow for more flexibility in applying different focal points and higher cross plane resolution. However, the resolution across planes is 300 μm and this is due to the distance between the components of the transducer. Since this is a very new imaging modality, very few laboratories are participating in its technological development and thus the main limitation is on the industrial and manufacturing side. Therefore, it is likely that in the coming years, while fUSI gets popularized, improvements will be made on this axis (Edelman and Macé, 2021). 3) Finally, CBV changes induced by the neurovascular coupling have an inherent anatomical spatial resolution that has been reported to be of at least 300-700 μm (Berwick *et al.*, 2008; O'Herron *et al.*, 2016; Bimbard *et al.*, 2018; Blaize *et al.*, 2020; Fukuda, Poplawsky and Kim, 2021), meaning that a greater resolution obtained with an ultrasound probe is not likely to translate into a much greater functional resolution.

In terms of temporal resolution, fUSI sends waves at a KHz rate (typically 1-10 KHz) but combines images from waves emitted at different angles to increase the sensitivity and contrast. By increasing or decreasing either the number of angles at which ultrasound waves are emitted (typically: 5-9 angles for functional acquisitions and 15 angles for higher resolution anatomical scans), or the averaging of images at each angle (typically 3), the sampling rate can be adjusted (100-600ms) (Tiran *et al.*, 2017; Bimbard *et al.*, 2018; Macé *et al.*, 2018; Edelman *et al.*, 2021). Hemodynamic responses induced by the neurovascular coupling have been reported to lag by approximately 2 seconds after stimulus onset (Berwick *et al.*, 2008; Aydin *et al.*, 2020; Nunez-Elizalde *et al.*, 2022). Although the onset can start already after ~300ms (Hirano, Stefanovic and Silva, 2011). Recently, Bergel et al.(Bergel *et al.*, 2018), showed that, in rats, the delays between the hemodynamic responses of distant areas ranges between 0.8 and 1.6s, and can be used to study the dynamic sequences following stereotyped behaviors. Therefore, although increasing the sampling rate of fUSI can have advantages regarding the processing of the signals (e.g., noise filtering), in terms of functional resolution, fUSI is already within the relevant physiological timescale of the vascular responses.

One of the greatest advantages of fUSI is the fact that it can be used in freely moving rodents (Sieu *et al.*, 2015; Urban *et al.*, 2015; Bergel *et al.*, 2018; Rabut *et al.*, 2020) and in head-fixed setups were awake mice, ferrets or small primates can behave or perform tasks (Bimbard *et al.*, 2018; Macé *et al.*, 2018; Dizeux *et al.*, 2019; Blaize *et al.*, 2020; Brunner *et al.*, 2020; Ferrier *et al.*, 2020). However, these also poses one of the greatest challenges for fUSI since certain movements have been shown to generate artifacts that can partially mask the neural responses (Brunner *et al.*, 2020; Landemard *et al.*, 2021).

To date, fUSI imaging has been shown to be able to detect and map sensory responses across the brain, including single whisker stimulations (Macé *et al.*, 2011; Brunner *et al.*, 2020), hindlimb (Urban *et al.*, 2014), olfactory (Osmanski *et al.*, 2014a; 2014b; Boido *et al.*, 2019), auditory (Bimbard *et al.*, 2018; Landemard *et al.*, 2021) and visual responses (Gesnik *et al.*, 2017; Rau *et al.*, 2018; Blaize *et al.*, 2020). Additionally, it has been used to study intrinsic functional networks that are thought to represent different brain states, in the context of sleep (Bergel *et al.*, 2018), default mode network (Ferrier *et al.*, 2020), pharmacologically-induced changes (Rabut *et al.*, 2020), and disease models (Macé *et al.*, 2018; Rahal *et al.*, 2020). Also, because of the compact size of the fUSI probe, it has been already combined with other imaging and recording modalities that can greatly increase the interpretation and relevance of such experiments. For instance, fUSI has been combined with simultaneous electrophysiology recordings to show that the fUSI signal correlates well with local neural activity (Nunez-Elizalde *et al.*, 2022), and to study the functional correlates of brain wide neural oscillations (Sieu *et al.*, 2015; Bergel *et al.*, 2018, 2020). It has also been successfully combined with two photon $Ca^{2+}$ imaging to study vascular responses to odours (Boido *et al.*, 2019), and the hemodynamic effects caused by increasing temperatures in response to light stimulation (Rungta *et al.*, 2017). Other examples of combination of fUSI with other techniques include positron emission tomography–computed tomography (PET–CT) (Provost *et al.*, 2018), fMRI (Boido *et al.*, 2019), deep brain electrical stimulation (Nayak *et al.*, 2021) and light stimulation (Rungta *et al.*, 2017; Edelman *et al.*, 2021).

All in all, fUSI provides a unique perspective to map and study brain wide networks involved in a plethora of behaviors. Its spatiotemporal resolution, sensitivity, and portability, complements and fills a gap left between local single-cell resolution techniques such as high-density electrode probes and two-photon calcium imaging, and less sensitive or lower resolution global brain imaging tools such as fMRI or PET. If combined with cell-type specific manipulations and cellular recordings, it has the potential to become an indispensable tool to understand the mechanisms by which neural networks interact and coordinate to govern behavior.

## 1.3.2 Functional magnetic resonance imaging (fMRI)

fMRI was the first tool developed that was able to image brain wide activity in the human brain. fMRI typically detects brain activity indirectly by measuring changes in blood oxygen level dependent (BOLD) signals. The neurovascular coupling is inferred in this case through the complex interactions between oxygenated and deoxygenated hemoglobin as a result of the changes in blood flow ($\uparrow$ activity = $\uparrow$ flow = $\uparrow$oxy-/$\downarrow$deoxy-) and local oxygen metabolism ($\uparrow$ activity = $\uparrow$ $O_2$ metabolism = $\downarrow$oxy-/$\uparrow$deoxy-). Although, the exact relationship between BOLD signals and neural activity are still under debate (Drew, 2019), a number of studies have found that BOLD signal, rather that reflecting local spiking activity, it might correlate better with local field potentials (LFP) (Logothetis *et al.*, 2001; Logothetis and Wandell, 2004; Viswanathan and Freeman, 2007; Rauch, Rainer and Logothetis, 2008; Zhang, Pan and Keilholz, 2020). The composition of LFPs is still under investigation but is generally thought to represent a complex interplay between post-synaptic and pre-synaptic activity (Logothetis, 2003; Herreras, 2016). This complicates the relationship between BOLD and LFPs because it implies that although LFPs reflect neural activity, the main contributing source may not be local but remote. Consistent with that idea, in areas such as the striatum (Shih *et al.*, 2009, 2011), prefrontal cortex (Huo, Smith and Drew, 2014), visual cortex (Sirotin and Das, 2009), or hippocampus (Angenstein, Kammerer and Scheich, 2009), the relationship between the BOLD signal and LFPs was found to be anticorrelated or not correlated at all.

Given that functionally relevant BOLD signals are generally small (<5%), contrast agents such as ultrasmall superparamagnetic iron oxide nanoparticles (USPIO) have been used in non-human primates to enhance the sensitivity of fMRI (Gkagkanasiou *et al.*, 2016). USPIOs provide enhanced measures of cerebral blood volume (CBV) that increase both sensitivity and spatial resolution (Kim *et al.*, 2013). However, since BOLD sensitivity increases with higher magnetic fields, and magnetization of iron oxides saturates (Shen *et al.*, 1993), the improved sensitivity decreases at higher magnetic fields (improved sensitivity: at 2T = x6 ; 3T = x3 ; 4.7T = x1.5-2 ; 9.4T = x1.2-1.5; (Kim *et al.*, 2013)). Additionally, regarding the origin of CBV, it has been shown that although behaviorally and sensory driven neural activity evokes CBV changes, spontaneous hemodynamic fluctuations can also be found in the absence of local neural activity (Winder *et al.*, 2017). This cautions about the interpretability of the BOLD and CBV signals, especially regarding intrinsic functional maps (e.g. default mode network) obtained in resting periods and therefore in the absence of a task or stimulus related activity.

Regardless of the origin of the BOLD and CBV signals, fMRI is still currently the only tool capable of studying the whole brain dynamics of humans and non-human primates. fMRI, has provided insights into many psychiatric disorders, including Alzheimer (E.-S. Lee *et al.*, 2016; Ahmadi, Fatemizadeh and Motie-Nasrabadi, 2020), autism (Rafiee *et al.*, 2021), Parkinsons (Filippi *et al.*, 2018; Rispoli, Schreglmann and Bhatia, 2018; Goelman *et al.*, 2021), or post-traumatic stress disorder (Shin, Rauch and Pitman, 2006; van Rooij *et al.*, 2021) among many others that would have not been possible using other techniques or animal models. Additionally, it has provided a better understanding of the human and its close relatives normal brain function, from fundamental visual responses and oculomotor tasks such as mapping the networks involved in saccades (Baker *et al.*, 2006), color sensitivity (Morita *et al.*, 2004; Parkes *et al.*, 2009) or motion selectivity (Vanduffel *et al.*, 2001; Nelissen, Vanduffel and Orban, 2006), to the processing of complex features such as recognition of objects or shapes (Malach *et al.*, 1995; Pasupathy and Connor, 2001; Denys *et al.*, 2004; Bognár and Vogels, 2021), faces (Kanwisher, McDermott and Chun, 1997; Moeller, Freiwald and Tsao, 2008), body parts (Pinsk *et al.*, 2009; Popivanov *et al.*, 2012; Knights *et al.*, 2021) or scenes (Nasr *et al.*, 2011; Kornblith *et al.*, 2013; McCormick and Maguire, 2021). As well as a plethora of functions otherwise difficult to interpret or translate from other animal models such as attention (Corbetta and Shulman, 2002), memory formation and recall (Miyamoto *et al.*, 2013; Sestieri, Shulman and Corbetta, 2017; Kim, 2019) perceptual learning (Gilbert, Sigman and Crist, 2001), language (Grodzinsky, Pieperhoff and Thompson, 2021), decision making (O'Doherty, Hampton and Kim, 2007), knowledge (Jefferies *et al.*, 2020) or consciousness (Hesselmann, 2013; Calabrò *et al.*, 2015). Finally, analyses of the spontaneous activity in the absence of task or stimulus have been used to describe intrinsic functional networks (van den Heuvel and Hulshoff Pol, 2010; Smitha *et al.*, 2017), such as the motor network, the visual network, or the so-called default mode network, that have proved to be useful for the diagnostic and prognosis of psychiatric disorders (Soddu *et al.*, 2011; Mohan *et al.*, 2016; Sheffield and Barch, 2016; Wolters *et al.*, 2019).

During the last decade, with the growing availability of ultra-high field MR scanners (Dumoulin *et al.*, 2018; van der Zwaag *et al.*, 2018) and new acquisition techniques to reach subsecond temporal resolution (Feinberg *et al.*, 2010; Moeller *et al.*, 2010; Lewis *et al.*, 2016; Bollmann and Barth, 2021), fMRI has expanded to smaller mammals such as rodents that allow for complex genetic manipulations otherwise limited in monkeys and humans. Thus, in recent years, rodent fMRI has started to catch up in mapping the visual system (Niranjan *et al.*, 2016), intrinsic networks (Grandjean *et al.*, 2017), disease models (Lichtman *et al.*, 2021) and awake imaging (Desjardins *et al.*,

2019) to study reward (Cover *et al.*, 2021), memory (Harris *et al.*, 2015) or stress (Dopfel and Zhang, 2018).

One of the limitations of many fMRI studies has been their correlational or descriptive nature, due to the lack of causal manipulations (Ramsey *et al.*, 2010). In order to address that, many labs have combined different stimulation techniques with fMRI to uncover the causal relationship of fMRI signals and specific brain functions. For instance, transcranial magnetic stimulation has been used to study the organization of visual areas (McKeefry *et al.*, 2009), the role of the medial-superior-temporal area in self-perception (Schmitt *et al.*, 2020) or the role of the dorsal intraparietal sulcus in visual attention (Leitão *et al.*, 2015). Additionally fMRI has been combined with optogenetics, both in monkeys (Gerits *et al.*, 2012; Ohayon *et al.*, 2013; Stauffer *et al.*, 2016) and rodents (Lee *et al.*, 2010; Desai *et al.*, 2011; H. J. Lee *et al.*, 2016), and chemogenetics, in rodents (Giorgi *et al.*, 2017; Zerbi *et al.*, 2019), to study the causal role of particular subpopulations of neurons and their interactions with brain wide networks.

Another limitation of fMRI, although mostly for smaller mammals due to the small size of their brains, is the spatial and temporal resolutions. To acquire the data for an fMRI brain volume, a series of 2D slices is imaged covering the whole brain sequentially and repeatedly. Therefore, the time taken to create a full brain volume is what defines the temporal resolution of the experiment. Because higher spatial resolution means increased number of voxels and planes processed to create a volume, there is a general trade-off between the spatial and temporal resolution. That is why, although it is currently possible to obtain sub-second (Feinberg *et al.*, 2010; Moeller *et al.*, 2010) or sub-millimeter resolutions (Fukuda, Poplawsky and Kim, 2016; Polimeni *et al.*, 2018), obtaining both is still challenging, rarely seen (Hendriks *et al.*, 2020), and requires imaging smaller fields of view.

fMRI has no competitor regarding the human and non-human primate brain imaging. However, although fUSI has low penetration into tissue (~2cm), for imaging smaller mammals such as marmosets or rodents, it can provide whole brain measurements at higher temporal and spatial resolution and higher sensitivity (Boido *et al.*, 2019; Edelman *et al.*, 2021). Finally, compared to fMRI, the fUSI compact size makes it easy to add to standard set ups and laboratories and at a much more affordable price.

## 1.3.3 Molecular maps of neural activity

One of the first methods that was developed to study brain-wide functional networks appeared in the 1970s (Kennedy *et al.*, 1975; Sokoloff *et al.*, 1977). It was based on the use of 2-deoxy-D-glucose (2-DG) as a tracer for measuring glucose consumption in the brain. 2-DG was injected intravenously and incorporated in brain areas with higher energy consumption, serving as an activity marker. At the time, functional maps were obtained by collecting electrophysiological data from many recoding sites, which was very time consuming, required a lot of interpolations, and the potential information obtained from each animal was relatively low (Tootell *et al.*, 1982). Therefore, molecular maps offered, for the first time, the opportunity to differentiate functionally segregated regions across the brain and even within brain structures. For example, in some of the first demonstrations of this new technique, they were able to observe the dominance ocular columns (Kennedy *et al.*, 1976), orientation columns (Hubel, Wiesel and Stryker, 1977) and precise retinotopies (Figure 1.8A, (Tootell *et al.*, 1982)) across large sections of visual cortex of macaques. However, the 2-DG method lacked both cellular and temporal (30-45 min) resolution.

During the following decade, in a series of *in vitro* and *in vivo* experiments, it was found that neural stimulation could induce the transient transcription of genes for the expression of proteins such as *cfos* and actin (Greenberg, Ziff and Greene, 1986; Dragunow and Robertson, 1987; Morgan *et al.*, 1987). By performing either immunocytochemistry against the *cfos* protein or in situ hybridization histochemistry against the coding mRNA, they were able to obtain the first functional maps with cellular resolution (Sagar, Sharp and Curran, 1988). Since then, many other so called immediate early genes (IEGs) such as *Arc, Egr-1(Zif268), fosb* and *npas4,* have been found and used to identify neural populations activated in response to a variety of stimuli and conditions (Zhang *et al.*, 1994; Tischmeyer and Grimm, 1999; Ewing, Porr and Pratt, 2013; Heroux *et al.*, 2018), across the entire brain (Figure 1.8B; (Kim *et al.*, 2015)). The underlying assumption regarding this method is that the stimulus or task under study will activate more neurons than the corresponding control in those areas that are involved in the specific process of interest. However, it is also possible that two different behaviors or experiences are processed by a similar number of neurons in a particular area, but via different subpopulations or cell-types (Johnson *et al.*, 2010; Lammel *et al.*, 2012; Beyeler *et al.*, 2016; Ye *et al.*, 2016). In order to disambiguate such situations, different methods have been developed that allow for testing multiple conditions or stimuli in the same animal.
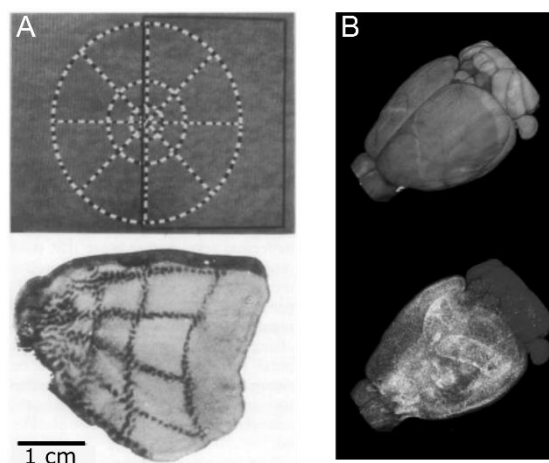


**Figure 1.8. Molecular maps then and now. A.** Top: stimulus that was flashed in front of a macaque to evoke neural activity in the cortex. Bottom: Pattern of brain activation produced by the visual stimulus shown in (A). as revealed by 2DG. (Adapted from Tootel *et al*., 1982). **B.** C-fos exression across the entire brain in response to social behavior. Top: 3D reconstructed mouse brain scanned with serial two-photon tomography. Bottom: overlayed cfos+ neurons (GFP+) (Adapted from Kim *et al*., 2015).

The first strategy developed to assess whether two different neuronal ensembles were activated by different stimuli in a particular area was the dual-epoch mapping. Dual-epoch mapping takes advantage of either the different kinetics of mRNA and protein synthesis or the changes in subcellular distribution of mRNA over time. The first to take advantage of the mRNA and protein kinetics were Chaudhuri and colleagues (Chaudhuri *et al.*, 1997; Zangenehpour and Chaudhuri, 2001). Taking advantage of the fact that mRNA expression of IEGs peaks 30min after induction, but protein accumulation peaks after 1.5-2h, they showed that by spacing the presentation of different stimuli the activated ensembles could be identified using immunohistochemistry against *Zif268* proteins and fluorescent in situ hybridization of its mRNA (I-FISH). Using the same principle, Xiu et al. used the time delay between mRNA and protein production of *cfos* to study the neural populations activated by appetitive and aversive stimuli (Xiu *et al.*, 2014; Zhang *et al.*, 2018). Alternatively, Guzowski et al. (Guzowski *et al.*, 1999; Guzowski and Worley, 2001) used the kinetics of mRNA to develop a technique called cellular compartment analysis of temporal activity by fluorescence in situ hybridization (CatFISH). CatFISH relied on the changes in subcellular distribution of the inducible

expression of *Arc* mRNA. After 20min of *Arc* induction, the mRNA is completely transported to the cytoplasm. Before that, *Arc* mRNA can be found in the nucleus already 5min after induction. Therefore, in CatFISH, animals are exposed to two different environments or stimuli separated by a ~20min interval. Animals are sacrificed 5 min after the second stimulus and then brain slices are analysed using fluorescence in situ hybridization of the *Arc* mRNA. By looking at the neurons with mRNA in either the soma, the nucleus or both, it can be assessed whether the same or different ensembles were activated by each environment or stimulus. A similar method but using *cfos* mRNA localization has also been used to identify the different neural populations activated by fighting and mating (Lin *et al.*, 2011). An apparent limitation of these methods is the fact that after the second stimulus, when mRNA arrives at the transcription peak, animals have to be sacrificed, so it is not possible to carry out other studies on the same animal. However, more recently, to circumvent this limitation they imaged IEG expression using two-photon imaging on *cfos*-GFP transgenic mice, and they were able to identify different populations of cells activated by separated events in the retrosplenial cortex *in vivo* (Meenakshi, Kumar and Balaji, 2021).

Conventional IEG labelling and histochemistry is only able to identify the cell bodies of the activated neurons. In order to be able to track the circuits associated to those neurons, yet another set of transgenic mice, viral constructs and imaging techniques were developed. On the one side, in order to visualize axonal projections of activated cells, transgenic approaches were developed in which the expression of β-galactosidase or a fluorescent protein is regulated by the promoter of an IEG (Wilson *et al.*, 2002; Barth, Gerkin and Dean, 2004). To reduce unspecific expression of the IEGs, two-tiered systems such as TetTag (Reijmers *et al.*, 2007), TRAP (Guenthner *et al.*, 2013) or CANE (Sakurai *et al.*, 2016), ensure that the expression of the IEG is only possible while in the absence or presence of a primary effector (TetTag: doxycycline (Dox); TRAP: tamoxifen; CANE: pseudo-viral vehicles coated with EnvA). These primary effectors can be delivered in the drinking water, food, or injected and therefore allow for time control, even if broad (hours or days), of IEG expression. This has been combined with conditional expression of light-gated ion channels to gain control over populations of neurons activated during a specific experience. By using this technique, they were able recreate fearful behaviors in neutral environments by reactivating ensembles encoding fearful memories (Ramirez *et al.*, 2013). On the other side, different techniques have been developed to allow the visualization of axons across the brain. These include special solutions that make the brains transparent such as 3DISCO (Ertürk *et al.*, 2012), ClearT2 (Kuwajima *et al.*, 2013), CLARITY (Jensen and Berg, 2017), CUBIC (Tainaka *et al.*, 2014), iDISCO (Renier *et al.*, 2014), and PACT (Yang *et al.*, 2014). To do so, the lipids of the tissues are dissolved while preserving the rest of the structure including neural somas and their projections. Once cleared, brains can be imaged using light-sheet microscopes to generate a single whole brain stack (Ye *et al.*, 2016), or serial two-photon tomography (Ragan *et al.*, 2012), which images overlapping brain sections that are sequentially sliced to allow the subsequent reconstruction of the full brain volume.

Despite the spread use of IEGs as activity markers, it must be noted that they are not universal markers of neural activity. Their functions within the cell are generally associated with synaptic plasticity, and circuit maturation (Okuno, 2011). Therefore, it is likely that certain activity thresholds must be passed before IEGs are induced, and that these vary depending on the baseline activity of the area or cell-type. For example, in the substantia nigra, which is known to provide tonic inhibition to the brainstem (Grillner and Robertson, 2016), neural activity does not correlate well with *cfos* expression (Labiner *et al.*, 1993; Applegate, Pretel and Piekut, 1995; Kovács, 1998; Sgambato *et al.*, 1999). In contrast, in other cases, basal expression of IEGs have been shown to be high (i.e., striatum and cortex) (Bhat and Baraban, 1992; Ishida *et al.*, 2000), which makes specific labelling challenging.

Additionally, each IEG serves a specific function and is differently expressed by different cell-types and brain regions (Nguyen *et al.*, 1992; Grimm and Tischmeyer, 1997; Guzowski *et al.*, 2001; Barry, Coogan and Commins, 2016), following even sub-region specific rules (Gonzales *et al.*, 2020). For instance, in cortical areas, IEGs are generally expressed in excitatory neurons rather than inhibitory (Chaudhuri, Matsubara and Cynader, 1995) but, in the olfactory bulb, it is inhibitory cells that preferentially express *cfos* and *Arc* (Guenthner *et al.*, 2013).

Overall, IEG-dependent tools, allow for whole brain mapping of activated ensembles, and even allow for the control of such ensembles to study their causal effects. Although IEG induction has low temporal resolution, it can allow for the identification of multiple ensembles activated by different experiences. However, the low temporal resolution and differential expression by different cell-types and brain areas make it difficult to predict to what degree IEGs represent the full picture of the process under study and needs to be either confirmed using multiple IEGs simultaneously or combined with other techniques. In this regard, fUSI, represents a complementary tool with high sensitivity for neural activation and higher temporal resolution, allowing the study of brain wide circuits dynamically. Although it is unclear what is the exact relationship between the neurovascular coupling and different cell-types (Anenberg *et al.*, 2015; Lacroix *et al.*, 2015; Uhlirova *et al.*, 2016; Lee *et al.*, 2021; Moon *et al.*, 2021), fUSI signals have been shown so far to correlate well with local neural activity (Macé *et al.*, 2018; Boido *et al.*, 2019; Nunez-Elizalde *et al.*, 2022). Additionally, fUSI can be performed *in vivo* allowing for multiple experiments to be performed in the same animals, but it is currently largely limited to head-fixed behavior.

## 1.3.4 Calcium imaging

Calcium imaging is referred here as the monitoring of $Ca^{2+}$ concentrations using fluorescent $Ca^{2+}$ indicators. $Ca^{2+}$ is a ubiquitous intracellular messenger that regulates a great variety of functions, ranging from cell motility (Gasperini *et al.*, 2017) to genetic transcription (van Haasteren *et al.*, 1999), or cell death (Zhivotovsky and Orrenius, 2011). The first realization that it has a central role in controlling biological processes came from Sydney Ringer, who in 1883, described it as necessary for the maintenance of the heart's contraction in frogs (Ringer, 1883). However, it was not until the 1980s that Roger Tsien and colleagues synthetized the first organic $Ca^{2+}$ indicators (Tsien, 1980, 1981; Grynkiewicz, Poenie and Tsien, 1985), which would make monitoring of $Ca^{2+}$ possible. $Ca^{2+}$ indicators are dyes or proteins that, when they interact with $Ca^{2+}$, go through conformational changes that affect their fluorescence intensities and/or lifetimes or shift their emission or excitation spectra. In neurons, intracellular changes in free calcium concentrations have been shown to be elicited by action potentials. Thus, by using fluorescence microscopes and $Ca^{2+}$ sensors one could, for the first time, observe the spiking activity of groups of neurons rather than the activity of isolated cells (Yuste and Katz, 1991). However, during the first years after the development of $Ca^{2+}$ indicators, imaging of neural processes was largely limited to *in vitro* preparations. This was because light is strongly scattered by neural tissue and therefore imaging was only possible on thin slices.

A major breakthrough in 1990 was the invention of two-photon laser scanning fluorescence microscopy (Denk, Strickler and Webb, 1990; Denk *et al.*, 1994). Two-photon microscopy is a laser-scanning technique, in which a laser beam is focused through a microscope objective down to a micrometer-sized light spot to excite fluorescent molecules. There are two key features on this method that allowed *in vivo* imaging. First, in this system, two photons are absorbed virtually simultaneously to promote the excitation of the fluorescent protein or dye. In traditional fluorescence microscopy a single photon is used. Therefore, in two-photon imaging, since two

photons are combined, their individual energies can be relatively low, and the wavelength can be longer (two-photon: 700-1000 nm; one photon: 390-700 nm). With longer wavelengths, less light is scattered by tissue and photons can reach greater depths. On the other hand, because in two-photon imaging each photon does not carry enough energy to excite the fluorescent proteins or dyes, the fluorescence is only generated locally on the point of focus. As a consequence, by scanning the region of interest it is possible to generate 2D images of the fluorescence occurring at a particular time and depth. Carrying this out at various focal planes enables the formation of 3D models of the scanned tissue at a resolution good enough to resolve synaptic structures such as dendritic spines and axonal boutons. However, even with the most recent three-photon microscopes, the depth at which such imaging is possible is still contained within 1mm, which makes most of the brain only accessible through invasive procedures that remove entire brain structures located on top of the region of interest. Additionally, there is a practical trade-off between the spatial resolution and the field of view. Although conventional two-photon imaging systems are limited in their field of view to ~1 mm$^2$ (Miller *et al.*, 2014; Kondo *et al.*, 2017; de Malmazet, Kühn and Farrow, 2018), with current technologies it is possible to image single cell responses of multiple regions across the cortex (>9.5 mm$^2$) (Stirman *et al.*, 2016), and record from thousands of cells. Yet this still constitutes only a quarter of the mouse's total cortical surface. Alternatively, wide field cortical imaging of calcium signals using customizable set ups with different light emitting diodes (LED), filters and cameras (Storace *et al.*, 2015; Vanni *et al.*, 2017; Xiao *et al.*, 2017; Clancy, Orsolic and Mrsic-Flogel, 2019; Couto *et al.*, 2021), allow for imaging of the entire cortex, but without cellular resolution and still limited to cortical surface.

One of the reasons Ca$^{2+}$ imaging has been gaining momentum in the last decade is due to the development of genetically encoded calcium indicators (GECIs), which are fluorescent proteins that are used to report Ca$^{2+}$ in genetically defined cell-types (Miyawaki *et al.*, 1997; Chen *et al.*, 2013). Although the first GECIs had slow kinetics (seconds of time rise and fall) compared to fluorescent dyes (<40-150 msec rise time & <200-300 ms fall time;(Lock, Parker and Smith, 2015)) and low signal-to-noise ratios (Miyawaki *et al.*, 1997), since its invention, there has been great improvements with the constant development of proteins such as the GCaMP family (Nakai, Ohkura and Imoto, 2001; Tian *et al.*, 2009). Current GCaMPs (Chen *et al.*, 2013; Dana *et al.*, 2019), XCaMPs (Inoue *et al.*, 2019), have high sensitivity, being able to resolve single spikes, but also decreases in activity (Ali and Kwan, 2020), and the latest versions have kinetics that allow resolution of up to 20Hz spiking activity (Zhang *et al.*, 2020). Additionally, although some side effects have been reported in GCaMP expressing neurons (Steinmetz et *al.*, 2017; Yang et *al.*, 2018) new version are already addressing those problems (Yang et al., 2018).

Overall, Calcium imaging offers the opportunity to monitor simultaneously thousands of individual cells the interactions between them with higher temporal resolution and sensitivity than fUSI. However, the limited depth at which neural responses can be imaged constraints its capacity to explain functions that are governed through cortical and subcortical brain wide networks. Although Ca$^{2+}$ imaging is easily combined with electrophysiology recordings (Xiao *et al.*, 2017; Wei *et al.*, 2020), the responses obtained by these means correspond to neurons in a small column surrounding the electrode shaft, and the size of the optical microscopes make them hardly compatible with other brain wide imaging tools such as fMRI or fUSI.

## 1.3.5 Large-scale probe recordings

Electrode recordings have provided insights about neural function with single cell resolution since the early 1940s (Renshaw, Forbes and Morison, 1940). In the initial experiments, single microelectrodes were used and isolating individual neurons was a challenge. This was because, on the one side, neurons of the same class tend to generate similar spike waveforms (Buzsáki, 2004), so to isolate them one needed to move the electrode tip closer to that neuron than to any other one nearby. Additionally, when multiple nearby neurons overlapped in time, the spikes recorded by the electrode would be the sum of the different waveforms, rendering the isolation of the different neurons impossible (Steenland and McNaughton, 2015). Some of these limitations were overcome with the advent of multielectrode recordings. On the one side, by recording from multiple microelectrodes one could simply increase the yield of isolated neurons (Krüger and Bach, 1981; Krüger, 1982; Hoogerwerf and Wise, 1994), but a greater number of insertions also increased tissue damage. The invention of the stereotrode (McNaughton, O'Keefe and Barnes, 1983), consisting of two microwires twisted together, and thus with the tips spaced a few microns from each other, allowed increased yields with a single insertion. Because the amplitude of waveforms decreases as the distance from the originating neuron increases, this allowed for the detection of signals from cells in overlapping distances. Since each spike would be detected by both wires but with different sizes due to the relative distance of the neuron to each wire, this made the pair of signals unique to the position of the neuron and allowed the isolation from other neurons (figure 1.9). This idea was later perfected with the tetrode (four microwires, (Wilson and McNaughton, 1993)), but even using triangulations, a single tetrode can only record and separate waveforms from 5-15 neurons in a typical experiment (Buzsáki *et al.*, 2015).
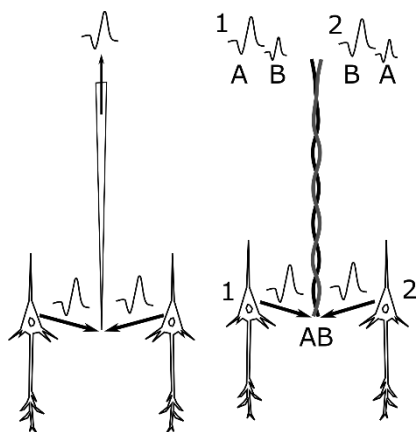
**Figure 1.9**. **Schematic comparison between single and multiple electrode recordings. Left**: scheme of a microelectrode recording spikes from two neurons located at similar distances from the electrode. If both neurons evoke similar waveforms, the two neurons cannot be separated. **Right**: scheme of stereotrode recoding spikes from two neurons located at similar distances from the electrode. Two wires, A & B, record the spikes of the same two neurons as the previous example (1 & 2). Because waveform amplitude decreases with distance, and the distance of neuron 1 to the wires A & B is different from the distance of neuron 2 to the same wires, these two neurons can now be differentiated.

An alternative to tetrodes was using probes with multiple recoding sites (Wise, Angell and Starr, 1970; Pickard, 1979). In this case, for a long time, the main limitation was the number of recording lines that could be implemented on the shank, which limited the number of sites that could be recorded simultaneously. However, through miniaturization, it was possible to gradually increase the density and number of recoding sites (up to ~100) (Kuperstein and Whittington, 1981; Kuperstein and Eichenbaum, 1985; Najafi and Wise, 1986; Drake *et al.*, 1988; Csicsvari *et al.*, 2003; Blanche *et al.*, 2005; Motta and Judy, 2005). In the last 10 years, new technological developments have allowed to accelerate and expand the number of recording sites up to a 1000 (Rios *et al.*, 2016; Scholvin *et al.*, 2016; Jun *et al.*, 2017; Raducanu *et al.*, 2017; Steinmetz *et al.*, 2021). For instance, using novel

nanofabrication processes such as electron-beam lithography, submicron wires were created to reduce space used by the wiring. The use of active probes (e.g. receive power), allowed functions such as multiplexing, where signals from multiple sources can travel through the same cable (Gingerich *et al.*, 2001; Seidl *et al.*, 2011; Steinmetz *et al.*, 2018). Finally, the use of complementary metal-oxide-semiconductor (CMOS) technology has been used to combine both thin wiring and active circuits (Jun *et al.*, 2017; Steinmetz *et al.*, 2021).

With the current technology it is possible to record simultaneously from multiple brain areas in small mammals (along ~4 – 7 mm), with recoding site densities that allow separation of dozens and up to hundreds of neurons from each recording (Steinmetz *et al.*, 2019; Böhm and Lee, 2020; Tasaka *et al.*, 2020; Feigin *et al.*, 2021; Zatka-Haas *et al.*, 2021). This allows researchers to record simultaneously from multiple interconnected areas and study the input and output functional relationships between them. Because of their compact and size, multiple probes can be inserted on a single animal, enabling the recording of more than 3000 channels (Steinmetz *et al.*, 2019). With these numbers, it is expected that it will be possible to better understand the computations performed by neural ensembles, direct interactions between pairs of neurons, and behavioral correlates at the single trial level (Steinmetz *et al.*, 2018).

Extracellular spike amplitudes get quickly attenuated while travelling away from the source neuron, meaning that these analyses can only be performed over cells within a narrow column around the probe, and that most of the brain will still act as a black box. Henze et al. (Henze *et al.*, 2000), doing simultaneous intra- and extracellular recordings, showed that neurons could be detected with a tetrode within a 140μm distance. However, beyond 50μm the reliability of the sorting decreased significantly. Additionally, from a cylinder of 50μm radius and 60μm height they calculated that 140 neurons could be potentially detected, but only 6-15 neurons were effectively recorded. A rough extrapolation onto the almost 4 mm of recording sites in a Neuropixels probes gives ~900 potential neurons to be recorded, but 50-300 cells have been reported (Steinmetz *et al.*, 2019; Feigin *et al.*, 2021). This discrepancy could be due to low spontaneous activity from many neurons, spikes with too small amplitudes to be properly sorted or detected, or due to neurons being damaged by the probe insertion. In practice, this means that there is a gap between the theoretically recordable neurons and the numbers that are actually recorded.

All in all, large-scale probe recordings provide a means to study large populations of neurons across multiple areas with single-cell and millisecond resolutions and thus will remain the gold standard for understanding how sensory information and behavior are represented and encoded in the activity of localized neural networks. However, these techniques only allow for the study of a few narrow columns of the brain at a time, and such recordings are generally performed in those areas where there is already evidence for the function under study to take place there, leaving out potentially important areas that fall outside of known regions of interest. fUSI, does not have the temporal and spatial resolutions of electrophysiology probes. However, it can provide a complementary unbiased means to observe interactions between hundreds of areas across the entire brain, which can reveal novel targets for manipulations and recordings.

# 1.4 Causality assessment using circuit-specific manipulations.

Whether it is hemodynamic, molecular or electrophysiological changes that are found to coincide with the appearance of a particular brain function, in order to assign causal relationships, it is

necessary to directly manipulate the circuits under study (Silvanto and Pascual-Leone, 2012). In the last decade, optogenetics and chemogenetics have revolutionized neuroscience by providing the means to transiently manipulate neural circuits in a cell-type specific manner (Jiang, Cui and Rahmouni, 2017; Atasoy and Sternson, 2018; Deubner, Coulon and Diester, 2019). In this project, both optogenetic and chemogenetic tools were used to test necessity and sufficiency of specific neurons to trigger collicular-dependent behaviors, to map collicular downstream pathways, and to observe visual properties and the transmission of visual information downstream of specific collicular cell-types. Thus, following, is a brief introduction to these techniques and the applications relevant to this project.

## 1.4.1 Optogenetics

Optogenetics rely on the use of light-sensitive proteins such as the algae derived channelrhodopsin-2 (ChR2) (Nagel et al., 2003), and the halorhodopsin from the archaea Natronomonas pharaonic (NpHR) (Zhang et al., 2007). In the presence of light, these opsins induce transient ion currents with millisecond precision (Boyden et al., 2005; Zhang et al., 2007). For instance, ChR2 is highly sensitive to blue light (470 nm) and when illuminated, it increases conductance to cations such as $Na^+$, $K^+$ or $H^+$, depolarizing, and thus activating, the expressing cells. On the other side, NpHR is a Chloride pump optimized for yellow light (590 nm) that when illuminated hyperpolarizes, and thus inhibits, the expressing cells. Since the discovery of their potential for neural manipulations, a non-stop development has provided a range of optogenetic tools with a broad variety of activation spectra, off-kinetics, and modulation of intracellular signaling (Fenno, Yizhar and Deisseroth, 2011; Yizhar et al., 2011; Rein and Deussing, 2012).

Optogenetics can be used in a variety of context. For instance, it can be used to assess the causal role of a genetically defined neural population. Typically, opsin expressing neurons are activated or inhibited via an optic fiber implanted over the target area and connected to a laser, or an LED, while mice explore an arena, or perform a task. This allows the experimenters to directly observe the behavioral effect of activating or inhibiting a particular set of neurons. This method has allowed in the last decade to uncover the role of a plethora of neural circuits mediating movement regulation, hunger, thirst, sleep, fear, reward and processing of olfactory, visual, auditory, or somatosensory information (Deisseroth, 2015). In combination with whole-brain imaging techniques such as PET or fMRI, optogenetics has been also used as a means to map functional multi-synaptic, brain-wide networks (Desai *et al.*, 2011; Thanos *et al.*, 2013; Liang *et al.*, 2015; Lee *et al.*, 2016; Bernal-Casas *et al.*, 2017; Lohani *et al.*, 2017). Finally, when combined with electrophysiology recordings, optogenetics allows for the post-hoc identification of a genetically defined population to monitor their natural responses (Lima et al., 2009). To do this, ChR2 is expressed in a subset of neurons, and at the end of an electrophysiology recording, those neurons are optogenetically activated while their activity is still being recorded. This will later allow researchers to identify ChR2-expressing neurons and analyze their activity during the previous task. This method has been used to study reward and punishment signals in dopaminergic and GABAergic neurons of the ventral tegmental area (Cohen et al., 2012), study visual responses of different collicular cell-types (Hoy, Bishop and Niell, 2019), or the mechanisms of cortical inhibition through NTSR neurons in layer 6 of the visual cortex (Bortone, Olsen and Scanziani, 2014), among others (Pfeffer *et al.*, 2013; Lee *et al.*, 2020).

Light delivery for optogenetic activation in subcortical brain areas requires the implantation of optical fibers into the brain. Thus, in such experiments, damage is produced on the tissue through which the fiber has to go through to reach the target area. Light delivery by itself can generate

temperature changes that could alter local activity in an unspecific manner (Owen, Liu and Kreitzer, 2019). Also, if the experiment requires manipulation of multiple areas, it renders the experiments increasingly complex, especially on freely moving paradigms. For instance, multiple fibers have to be implanted, increasing invasiveness. Additionally, either multiple light sources and patchcords have to be connected to the animal, increasing burden for movement and complexity for synchronization of devices, or light splitters have to be implemented, but these reduce dramatically power output and thus limit the stimulation protocols that can be used, for example, with LED sources. Thus, for those studies where optogenetics limitations outweigh the benefits, chemogenetics offer an alternative.

## 1.4.2 Chemogenetics

Ion channels control the electrical activity of neurons. Two important mechanisms to control their activity are, 1) directly through small molecules or peptides that bind to them (ligand-gated channels), or; 2) indirectly via G protein-coupled receptor (GPCR) signaling (Keramidas et al., 2004; Venkatakrishnan et al., 2013). The delivery of antagonist and agonist of ligand-gated channels has long been used as a means to study neural function (Booth, 1968; Kelly, Rothstein and Grossman, 1979; Olgiati et al., 1980). However, since both ligand-gated channels and GPCRs are generally expressed in multiple cell-types, pharmacological strategies are limited by the lack of specificity in their effects. To address this issue, a set of tools have been developed, such as modified muscarinic receptors that are no longer sensitive to their native endogenous ligand (Ach). Instead, they are activated by synthetic ligands that are otherwise inert and can be administered systemically (Armbruster *et al.*, 2007; Rogan and Roth, 2011). The so-called Designer Receptors Exclusively Activated by Designer Drugs (DREADDs), include mutated excitatory (hM3q) and inhibitory (hM4i) G-coupled receptors that, in vitro, are activated by clozapine-n-oxide (CNO). CNO is an inactive metabolite of the antipsychotic drug clozapine. It is important to note though, that more recent studies have suggested that the in vivo effect of DREADDs is due to converted clozapine from the systemically injected CNO (Gomez *et al.*, 2017). Gomez et al., showed that CNO did not enter the brain after systemic injections, and behavioral effects where due to converted clozapine that preferentially targeted DREADDs due to its high affinity for the modified receptors. Although other studies have found CNO can enter the brain (Jendryka *et al.*, 2019), it has become clear that CNO can have off-target interactions and thus controls for unspecific CNO effects are a must when designing such studies. Alternative synthetic drugs have also been developed in the last few years with higher affinity and potency (Bonaventura *et al.*, 2019; Goutaudier *et al.*, 2020), but none have proved exclusive binding to DREADDs and so still require control experiments for unspecific effects.

## 1.4.3 How do we get opsins or DREADDs into the brain?

There are two methods commonly used to express optogenetic and chemogenetic tools in the brain: (1) performing stereotactic injections of viral vectors carrying the genes of the opsin, DREADD, or Cre recombinase for conditional expression; (2) by using animals that have been genetically modified (transgenic animals) to carry the gene of the opsin or DREADD in their genomes.

Viral vectors are modified viruses in which their genomes have been removed and replaced with designed constructs carrying the genes of the proteins of interest. Thus, these viruses cannot replicate, and their sole purpose is to enter cells, neurons in this case, and allow the expression of the desired protein using the cells machinery. A variety of viruses have been used as viral vectors to take advantage of their anterograde, retrograde or transsynaptic properties, their different tropism,

diffusion, or the size of the genes they can carry. The most used ones include adeno-associated viruses (AAV), lentiviruses, herpes simplex virus (HSV), and the rabies virus.

(1) AAV viruses are often the preferred option for gene delivery due to the low immune reaction they induce, and the variety of serotypes that can be combined into chimeric AAVs to generate different degrees of cell-type specificity (tropism), and diffusion (Taymans *et al.*, 2007; Cearley *et al.*, 2008). AAVs deliver single-stranded DNA and mediate long-lasting expression in neurons and glia, mostly episomally (without incorporating into their chromosomes) (Penaud-Budloo *et al.*, 2008; Smith, 2008; Li *et al.*, 2011).

Viral injections provide localized expression of the proteins of interest with an efficiency that will depend on the specific serotype or type of virus. However, in certain experimental conditions viral vectors might not be enough. For example, if one wants to express the gene across an entire brain area that would require many injections and increased variability. Also, if one needs to label a percentage of the local populations beyond the efficiency of viral vectors. In such cases, transgenic mouse lines offer an alternative.

(2) Transgenic mouse lines are mouse lineages that have been genetically modified to carry certain mutations in their genomes. These include point mutations in specific genes (can result in loss or gain of function), and introduction or removal of entire genes. Two widely used methods for introducing exogenous genes are via gene-targeted knock-in and using bacterial artificial chromosomes (BAC) (Van Keuren *et al.*, 2009; Ukai, Kiyonari and Ueda, 2017). Through these techniques, genes such as the gene of the opsin ChR2 or reporter genes such as the yellow fluorescent protein (YFP), are introduced in the genome and made present in every cell (Madisen, *et al.*, 2012; Li *et al.*, 2018). To allow cell-type or region-specific expression, they are typically introduced with either stop-codons or inverted sequences flanked by loxp sites (floxed) that impede the expression of the protein. However, these loxp sites can be recognized by the cre recombinase, which is not expressed in mammal cells and has to be exogenously introduced (Yu and Bradley, 2001). If, for instance, a viral vector carrying the gene of the cre recombinase is injected in a particular brain area, the cre will either remove the stop-codon or revert the inverted sequence to allow for the expression of the protein of interest (ChR2 or YFP in this case). Alternatively, different transgenic mouse lines (knock in and BAC) have been developed to express the cre recombinase in cells that express particular genes (cell-types), constitutively (Cre lines). Thus, by crossing Cre lines with mouse lines with floxed genes, one can obtain expression of e.g. ChR2 in every cell expressing a particular gene across the entire brain.

# 1.5 Objectives

Based on the technical and scientific overview presented above, this project will focus on resolving two main questions.

On the one side, current imaging and recording techniques have advanced greatly in recent years and provided the means to study neural circuits in large scales. However, it is generally with either great detail (cellular and millisecond resolutions), but within a relatively small area, or broadly (millimeter and seconds resolutions), but across the entire brain. fUSI has been recently developed to bring these extremes closer, by providing both brain-wide monitoring and relatively high spatiotemporal resolutions (sub-millimeter and sub-second). Yet thus far the capabilities of fUSI in providing insights about the brain-wide networks that govern behavior have been hardly put to test. Thus, our first goal was to develop a new approach specifically designed to study brain-wide functional networks downstream of specific cell-types and test, concretely:

(1) Is the combination of optogenetics and fUSI a suitable alternative to study brain-wide networks and bridge the resolution gap between low resolution global monitoring (fMRI, molecular maps), and high resolution, local recording techniques (electrophysiology, $Ca^{2+}$ imaging)?

On the other side, although the superior colliculus is one of the most extensively studied structures in the brain, beyond its mono-synaptic targets, little is known about the downstream pathways that participate in mediating collicular-driven behaviors. Thus, taking advantage of the well-known local structure, functions, and available transgenic lines to target specific neural subpopulations, our second goal was to uncover the brain-wide networks downstream of specific collicular cell-types and their relationship with behavior. Concretely:

(2) How extensive are the networks downstream of individual collicular cell-types, and to what degree these functional networks constitute independent parallel streams of information or overlapping systems?

# CHAPTER 2

# Optogenetic fUSI for brain-wide mapping of neural activity mediating collicular-dependent behaviors

# 2.1 Abstract

Neuronal cell-types are arranged in brain-wide circuits that guide behavior. In mice, the superior colliculus innervates a set of targets that direct orientating and defensive actions. We combined functional ultrasound imaging (fUSI) with optogenetics to reveal the network of brain regions functionally activated by four collicular cell-types. Stimulating each neuronal group triggered different behaviors and activated distinct sets of brain nuclei. This included regions not previously thought to mediate defensive behaviors, e.g., the posterior paralaminar nuclei of the thalamus (PPnT) that we show plays a role in suppressing habituation. Neuronal recordings with Neuropixels probes show that: (1) patterns of spiking activity and fUSI signals correlate well in space and, (2) neurons in downstream nuclei preferentially respond to innately threatening visual stimuli. This work provides insight into the functional organization of the networks governing innate behaviors and demonstrates an experimental approach to explore the whole-brain neuronal activity downstream of targeted cell-types.

# 2.2 Introduction

Different behavioral tasks rely on distinct networks of neurons distributed across the brain. Insights into how specific cell-types are linked to sensation and behavior have seen some great advances through the application of molecular technologies, providing a list of critical circuit elements (Zeng and Sanes, 2017). On the other hand, computational understanding have been gained by comparing large-scale measurements of brain-wide activity with sensory inputs and behavior (Ahrens *et al.*, 2012; Aimon *et al.*, 2019; Steinmetz *et al.*, 2019; Stringer *et al.*, 2019). However, in mammals the link between individual cell-types, large scale neuronal activity and behavior remains unclear. In the superior colliculus (SC), there is evidence for a strong relationship between individual cell-types and behavior (Shang *et al.*, 2015, 2018; Hoy, Bishop and Niell, 2019; Masullo *et al.*, 2019; Zhang, *et al.*, 2019). Here, we use this relationship to delineate the cell-type specific brain-wide functional networks that lie downstream of the SC.

In mice, the SC is a major hub of visual processing, where the superficial layers of the SC receive direct sensory inputs from >85% of the retinal output neurons (Ellis *et al.*, 2016). The retino-recipient neurons in the SC contain at least six sets of genetically identified cell-types with distinct anatomy and visual response properties (May, 2006; Gale and Murphy, 2014; Inayat *et al.*, 2015; Gale and Murphy, 2018; Whyland, Slusarczyk and Bickford, 2020). Different cell-types project to different sets of targets, including nuclei of the thalamus and midbrain, thereby forming a putative structural basis for the relationship between cell-types and distinct behavioral properties (Gale and Murphy, 2014; Shang *et al.*, 2015; Wei *et al.*, 2015; Shang *et al.*, 2018; Gale and Murphy, 2018; Masullo *et al.*, 2019; Zhang, *et al.*, 2019).

Optogenetic activation of cell-types in the retino-recipient layers of the colliculus has provided insight into the relationship between output circuits of the SC and behavior. For instance, activation of neurons that project to the pulvinar (LP) has been shown to induce arrest behavior in mice (Wei *et al.*, 2015; Shang *et al.*, 2018), while activation of neurons projecting to the parabigeminal nucleus (PBG) leads to flight behavior (Shang *et al.*, 2018). These optogenetically induced behaviors resemble the reactions of mice to visual stimuli that mimic avian predators (Yilmaz and Meister, 2013; De Franceschi *et al.*, 2016). These experiments suggest that activation of neurons early in the visuo-motor circuits of the SC leads to downstream activity and behaviors that are comparable to the network activity and behaviors triggered by natural visual stimuli. But our view of these circuits remains limited to the specific circuits that have been investigated to date.

In rodents, combinations of cell-type specific stimulation and whole brain recordings using functional magnetic resonance imaging (fMRI) have provided insights into the relationship between cell-types and brain-wide network activity (Lee *et al.*, 2016; Nakamura *et al.*, 2020). In relation to the SC, fMRI studies in humans have provided evidence that the pathway linking the SC to the amygdala (AMG) via LP is involved in the processing of visual threats (Liddell *et al.*, 2005; Almeida, Soares and Castelo-Branco, 2015; Terpou *et al.*, 2019). However, recording techniques such as fMRI suffer from limited resolution, which makes it difficult to clearly assign activity to small brain nuclei, in particular in small mammals (Lee *et al.*, 2016; Bernal-Casas *et al.*, 2017). Functional ultrasound imaging (fUSI) has been developed to study brain-wide activation patterns at a spatial and temporal resolution in awake mice that makes it practical to follow neural activity in most nuclei of the brain at a resolution of ~100 µm (Macé *et al.*, 2011; 2013; Urban *et al.*, 2014; Macé *et al.*, 2018; Rabut *et al.*, 2019; Brunner *et al.*, 2020). In addition, its compact size allows for parallel interventions such as

optogenetic activation or local neuronal recordings in awake behaving animals (Aydin *et al.*, 2020; Brunner *et al.*, 2020).

By combining fUSI with optogenetics (opto-fUSI), we reveal the neural networks through which information is routed after activation of different cell-types in the SC. We unravel the differences in the spatial and temporal organization of cell-type dependent network activation, which we find to be consistent with differences in evoked behaviors. Opto-fUSI allows us to identify new brain areas that link sensory inputs to behavioral output. Finally, chemogenetic manipulations reveal the potential function of one newly identified group of nuclei, the posterior paralaminar nuclei of the thalamus (PPnT), in visually triggered behaviors.

# 2.3 Results

## 2.3.1 Different collicular cell-types trigger different innate behaviors

To understand the contributions of different collicular cell classes to defensive behaviors, we optogenetically manipulated the activity of four genetically defined cell populations: 1) a population of excitatory neurons expressing CAMKII, referred to as CAMKII; 2) NTSR neurons that project to the LP, referred to as NTSR (Gale and Murphy, 2014); 3) Parvalbumin expressing neurons (PV) that consists of local interneurons and excitatory projections to LP, PBG and pontine gray (PG); 4) a set of inhibitory neurons (GAD2) that innervates the lateral geniculate nucleus (LGN) and PBG (Gale and Murphy, 2014). We restricted the expression of light-sensitive channelrhodopsin2 (ChR2) to the distinct cell classes in two ways. First, to express ChR2 in NTSR, PV and GAD2 neurons, we crossed Cre-expressing transgenic mouse lines (NTSR-GN209-Cre, PV-Cre and GAD2-Cre) with a ChR2-reporter mouse line, Ai32 (Madisen *et al.*, 2010; Taniguchi *et al.*, 2011; Madisen, *et al.*, 2012; Gerfen, Paletzki and Heintz, 2013). Second, CAMKII neurons were labeled with an adeno-associated virus (AAV) that carried ChR2 under the CAMKII promotor (Wei *et al.*, 2015) (see Methods). Control experiments were carried out with Cre-negative litter mates. Histological analysis confirmed the layer-specificity and partial overlap of different cell-types (Figure 2.1; Figure S2.1), which was consistent with previous reports (Gale and Murphy, 2014; Shang *et al.*, 2015; Wei *et al.*, 2015; Shang *et al.*, 2018; Gale and Murphy, 2018; Hoy, Bishop and Niell, 2019). CAMKII and NTSR neurons had the highest overlap (NTSR-CAMKII = 64.97%, IQR = [60.92, 69.01), in contrast to PV and GAD2 neurons that had little overlap with other populations (PV-GAD2 = 12.67% IQR = [9.45, 15.9]).

We tested the behavioral effect of optogenetically stimulating each cell type in freely moving animals (Figure 2.1). The stimulus consisted of blue light pulses of either a high-frequency (1 s, 20 Hz or 50 Hz), or low-frequency (4 s, 5 Hz) optical stimulation. Activation of each neural population led to distinct behavioral responses, that ranged from stopping (CAMKII and NTSR neurons) to directed movement (PV and GAD2 neurons; Figure 2.1). To capture differences in the triggered behavior, we first looked at the speed dynamics (Figure 2.1C-D and Figure 2.1F). All experimental groups responded with a drop in speed during the first 333 ms following the start of the stimulation (Figure 2.1F; Mann-Whitney U-test compared with control, CAMKII: p=0.0003; NTSR1: p=0.0003; PV: p=0.026; GAD2: p=0.004), whereas control mice did not show any identifiable change in behavior. Activation of CAMKII neurons resulted in particularly long stopping events that lasted for up to 19.8 s (Figure S2.1G; median stopping duration: 9.21 s, IQR=[8.02, 12.65]), whereas stimulation of NTSR neurons resulted in mice stopping during the 1 s stimulus and resuming locomotion shortly after stimulus offset (median stopping duration 1.69 s, IQR=[1.42, 1.95]; Figure S2.1G). Activation of PV cells caused mice to slow down, but rarely led to a full stop (Figure S2.1H). Instead, their behavior

was characterized by active movement towards one of the corners (Figure 2.1H; median latency: 2.96 s, IQR=[2.7, 4.16]; Mann-Whitney U-test compared with control, p=0.01). Animals with ChR2 expression in GAD2 neurons showed a tendency to increase their speed during the stimulation (Figure 2.1F; Mann-Whitney U-test compared with control, GAD2: p=0.10). Interestingly, this was accompanied by movement contralateral to the stimulated hemisphere (Figure 2.1F-G) that manifested itself as turning ( Figure 2.1G Bottom, median Δ angle: -39°, IQR=[-70.01, -9.36]; Mann-Whitney U-test compared with control, GAD2: p=0.00002), or a whole-body drift contralateral to the stimulated hemisphere (Figure 2.1G Top; median perpendicular distance: -5.66 cm, IQR=[-12.36,-0.72]; Mann-Whitney U-test compared with control, GAD2: p=0.00002). Taken together, these findings suggest that each collicular cell-type makes a different contribution to behavior that can broadly be characterized as defensive or orienting.

To analyze the behavior in a less biased manner the positions of five body landmarks (nose, each ear, proximal and distal ends of the tail) were tracked to measure and cluster animal movements (Storchi et al., 2020) (see Methods). CAMKII had the highest proportion of long stopping (cluster 4), NTSR had the highest proportion of short stopping (cluster 1), GAD2 had a strong preference for contralateral movements (cluster 2), while PV showed a larger diversity of responses (Figure 2.1I-K). Taken together, these findings suggest that each collicular cell-type contributes differentially to behavior.

## 2.3.2 Brain-wide functional ultrasound imaging during optogenetic stimulation in mice

In order to assess the brain-wide neural activity that drives the different behaviors observed above, we developed a chronic preparation that allowed us to combine functional ultrasound brain imaging (fUSI) and optogenetics, in awake head fixed animals (Figure 2.2A-C). fUSI reports neuronal activity indirectly by measuring changes in blood volume of the microvasculature (Rubin *et al.*, 1994, 1995; Macé *et al.*, 2011). To accommodate the optogenetic fiber and image as much of the brain as possible, a large cranial window that spanned a single hemisphere was implanted (AP +2 to -6.5; L +1.25 to -4.5). An optic fiber was pointed at the surface of the ipsilateral SC near the midline at an angle of 56°, approached from the contralateral side (Figure 2.2B; Methods). All animals included in the fUSI experiments were tested for behavior before each imaging session.

Neural activity was monitored with a fUSI probe positioned over the craniotomy parallel to the long axis of the animal. Sagittal planes were imaged sequentially, each spanning the entire depth of the brain, where the probe was stepped (250 um) along the medial-lateral axis (Figure 2.2A-C). While imaging each plane, the colliculus was optically stimulated. In each experiment, each plane was imaged for two 20 s periods, when either a 1 s (20 Hz or 50 Hz), or 4 s (5 Hz) light stimulation was delivered via the implanted optic fiber 10 s after the imaging started. The parameters of the light stimulation were the same as those used during the behavioral experiments. Each mouse was imaged in 3-5 sessions that were separated by 48-72 hours.  Each voxel was assigned to an individual brain region by performing a 3D rigid registration of the series of sagittal images, obtained in the absence of visual stimulation (125 μm steps), to the Allen Mouse Brain Common Coordinate Framework version 3 (CCF v3) (Lein *et al.*, 2007) (Figure 2.2D). We used a modified version that is comprised of 264 brain areas in one hemisphere of the brain (Table S2.1).

To build a spatial map of brain activity, we compared, voxel by voxel, the hemodynamic signals (DI/I, referred to as "activity") obtained during and after the optogenetic stimulus to a 10 s period before the light stimulus (Figure 2.2D-F). The hemodynamic activity of all voxels within each area were

averaged to estimate the response for that region (Figure 2.1E and 2.1G). Temporal traces were obtained for each mouse and compared (t-test corrected for false discovery rate) to identify the
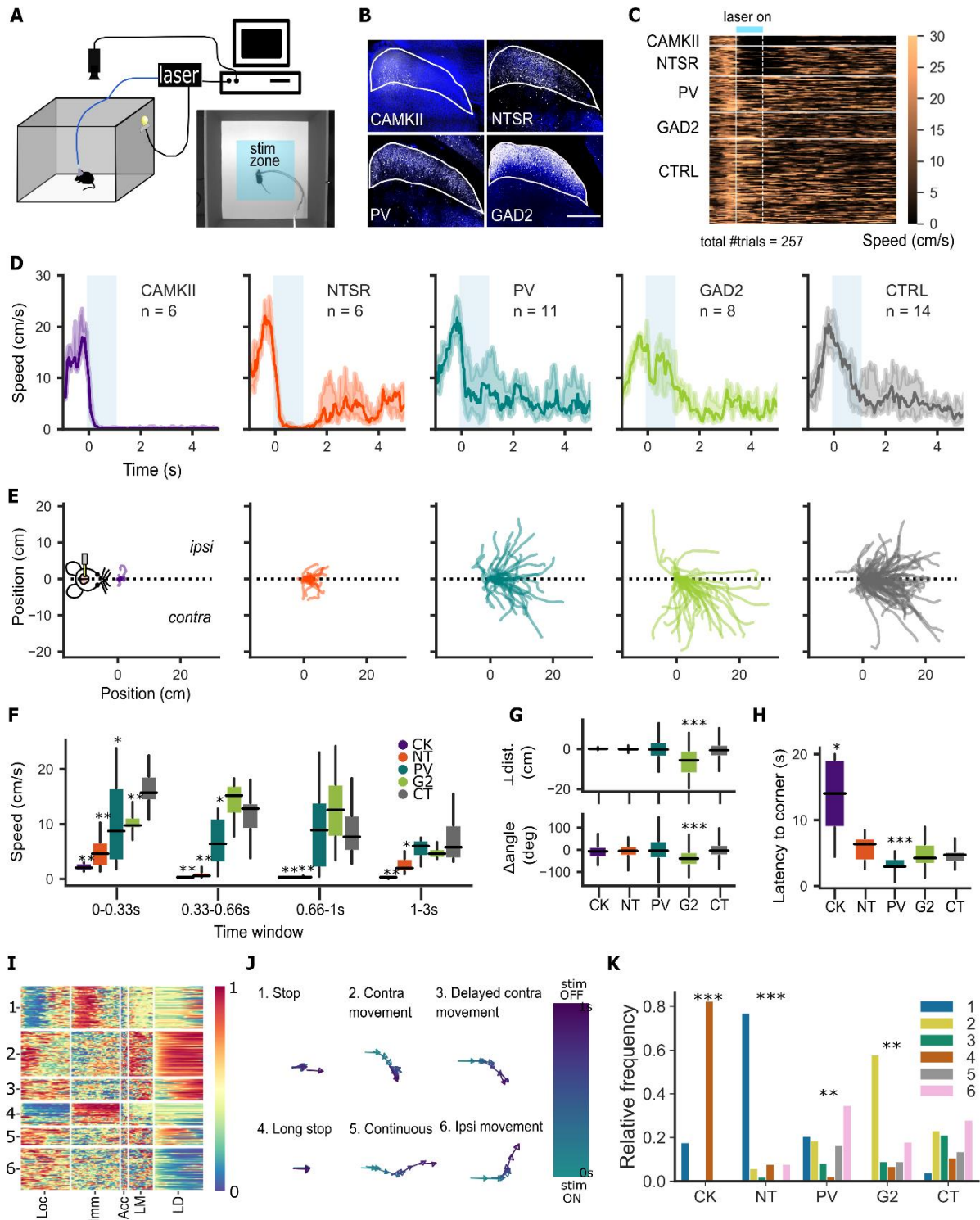


areas that displayed a response (Figure 2.1G-I). Average responses for each segmented area in each mouse line are shown in Figure 2.1J. The same analysis was applied to low-frequency stimulation data (Figure S2.3).

**Figure 2.1. Different SC cell-types trigger different defensive behaviors. A.** Schematic of the open field setup for optogenetics and a video frame of a mouse entering the stimulation zone (blue rectangular shading). **B.** Coronal section showing expression of ChR2 in distinct cell lines. Scale bar, 500 μm. **C.** Heatmap of mice speeds during optogenetic stimulation obtained from the first experimental sessions. Horizontal white lines separate different mouse lines. Vertical solid and dashed white lines mark stimulus onset and offset, respectively. Light blue bar marks the stimulus duration. **D.** Speed profiles. Each trace represents the median speed for each mouse line. Shaded area represents the interquartile range. **E.** Mice trajectories during the 1 s stimulus. Traces were aligned and rotated by the initial body position angle. CAMKII: n=6, 14 trials, NTSR: n=6, 41 trials, PV: n=11, 50 trials; GAD2: n=8, 43 trials; CTRL n=14, 109 trials. **F.** Speed quantification during chosen time windows. (0-0.33s: CAMKII p=0.0003, NTSR p=0.0003, PV p=0.026, GAD2 p=0.004; 0.33-0.66s: CAMKII p=0.0003, NTSR p=0.0004, PV p=0.03, GAD2 p=0.10; 0.66-1s: CAMKII p=0.003, NTSR p=0.0004, PV p=0.34, GAD2 p=0.10; 1-3s: CAMKII p=0.0003, NTSR p=0.007, PV p=0.38, GAD2 p=0.18) **G.** Quantification of body position at the stimulation offset, represented as a change of angle (bottom; CAMKII p=0.26; NTSR p=0.31; PV p=0.45; GAD2 p=0.00002) and perpendicular distance (top; CAMKII p=0.27; NTSR p=0.29; PV p=0.38; GAD2 p=0.00002), both in reference to X axis (dashed line in E). **H.** Latency of movement to a corner (CAMKII p=0.003; NTSR p=0.15; PV p=0.013; GAD2 p=0.49). All data points are averaged over mice, except in G (averaged over trials). Significance between control and each mouse line was tested using Mann-Whitney U-test. Box-and-whisker plots in F-H show median, interquartile range and range. **I.** Heatmap of the behavioral responses to stimulation. Each row shows a trial with different measures: locomotion (Loc), immobility (Imm), acceleration (Acc), lateral motility (LM) and lateral distance (LD), separated by vertical white lines. Clusters are separated by horizontal white lines. For LM and LD, 0 and 1 indicate leftwards and rightwards locomotion, respectively. **J.** Single-trial examples of clusters. Color shading indicates time. **K.** Cluster assignment distributions for each mouse line. Significance between control and each mouse line distribution was tested using Fisher's exact test (CAMKII p=6.9e-11, NTSR p=2.2e-16, PV p=0.0045, GAD2 p=0.0041). Alpha = 0.05, * p <0.05, ** p <0.01, *** p <0.001.

To assess whether head-fixed animals display comparable behaviors to freely moving animals, we performed similar experiments with NTSR and GAD2 mice that were head-fixed on a spherical treadmill (Figure S2.3A and S2.3B). From the behavioral side, we made three key observations that are consistent with the behaviors observed in freely moving animals. First, activation of NTSR neurons caused mice to stop (Figure S2.3C: top row; S2.3D: left; Mann-Whitney U-test compared with control, 1-2 s: p = 0.0058, 2-3 s: p = 0.0055). Second, activation of either GAD2 and NTSR neurons elicited pupil diameter changes (Figure S2.3C: middle row; S2.3D: center) in both animals that were running or still during the 1 s preceding stimulation (Mann-Whitney U-test compared with control, 0-1 s: NTr p = 0.0089, NTs p = 0.0058, G2r p > 0.5, G2s p = 0.0014; 1-2 s: NTr p = 0.0133, NTs p = 0.0058, G2r p = 0.0014, G2s p = 0.0014). Third, stimulation of GAD2 neurons evoked directional eye movements that tended to be downwards and nasal (Figure S2.3C: bottom row; S2.3D: right) in both running and still conditions (Mann- Whitney U-test compared with control, total: G2r p = 0.002, G2s p = 0.0014; x: G2r p = 0.0344, G2s p = 0.0014; y: G2r p = 0.0079, G2s p>0.1). On the other side, brain activity analysis suggested that the optogenetically evoked behaviors and corresponding brain-wide activity patterns are triggered independently of locomotion (see details in Figure S2.3). Here we compared animals that were stimulated during locomotion or during stillness. Analysis of the brain-wide activity of these mice (Figure S2.3E and S2.3F), highlighted the similarity in the active areas of mice that were running or still during the 1 s preceding stimulation (correlation of responses: NTSR running (NTr) vs NTSR still (NTs), r = 0.73; G2r vs G2s, r = 0.73). A few specific differences in areas such as the motor cortex (MO) were observed, where MO was more active in NTSR running mice compared to NTSR still mice (Figure S2.3E). The overall similarities held true when we compared these results to our previous experiments in head-fixed restrained animals on a platform (NTSR immobilized (Nti); correlation of NTi responses and the 99 imaged areas on treadmill: NTi vs NTs = 0.39; G2i vs G2s = 0.47). Thus, for the next part of the study, we decided to focus on our restrained preparation (Figure 2) using more extensive craniotomies suitable for imaging a larger portion of the brain with minimal movement artifacts.
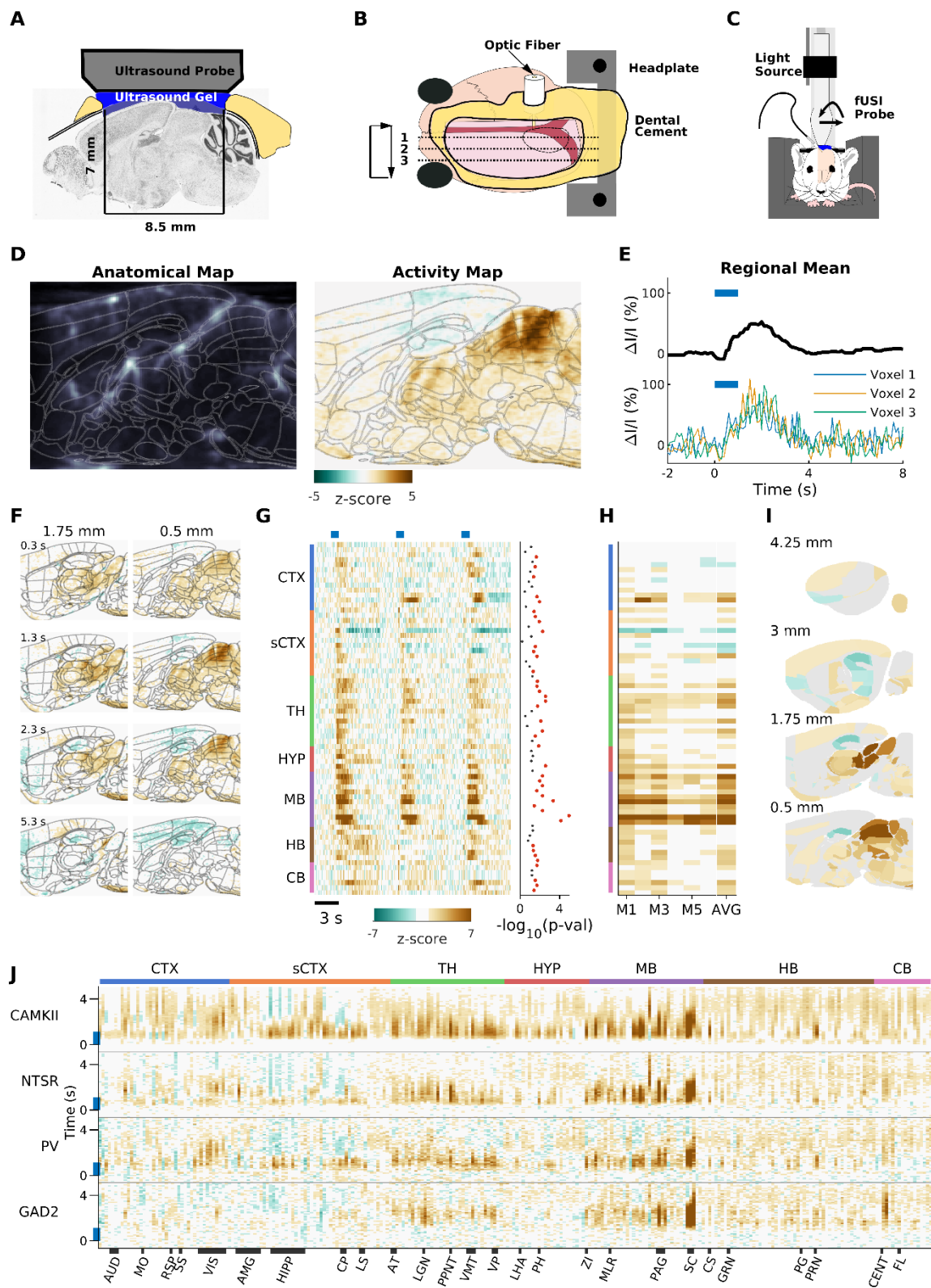
**Figure 2.2. Functional ultrasound imaging of awake mice during optogenetic stimulation. A.** Scheme of a sagittal cross-section of the chronic preparation. **B.** Top-view scheme of a chronic cranial window with implanted optic-fiber cannula inserted at 56 º. **C.** Schematic of experimental set-up for awake imaging. **D.** Left. Example sagittal section of a blood volume map registered to the Allen Mouse brain reference atlas (thin gray lines). Right. Voxel to voxel normalized response to optogenetic stimulation of plane shown in left panel, registered to the Allen Mouse brain reference atlas (thin gray lines). **E.** Bottom: relative hemodynamic response curves to the optogenetic stimulation of three example voxels in the intermediate superior colliculus. Top: mean response of

the intermediate superior colliculus. Blue lines indicate duration of optogenetic stimulation. **F.** Two example sagittal planes from the activity maps of a single animal. **G.** Left: Standardized responses of a selection of 72/264 segmented areas. Mean responses are shown for 3 different mice. Response for each mouse is an average of 6 trials. Blue lines indicate duration of optogenetic stimulation. black thick line indicates optogenetic stimulation. Right: Inactive (gray) and active (red) areas colored based on significance threshold corrected for multiple comparisons (p<0.05). **H.** Mean response of each segmented area shown in G during the 2 s after the start of the stimulus for 6 different NTSR mice and the average across all mice. Areas considered not significant (p>0.05) are set to zero in the average. **I.** Projection of the average activity vector from H onto a map of the mouse brain. **J.** Average time course of each of the 264 segmented areas for each stimulated cell population. Black bars along the bottom indicate span of the labeled brain regions.

CTX: cortex, sCTX: cortical subplate, TH: thalamus, HYP: hypothalamus, MB: midbrain, HB: hindbrain, CB: cerebellum, AUD: Auditory cortex, MO: Motor cortex, RSP: Retrosplenial cortex, SS: Somatosensory cortex, VIS: Visual cortex, AMG: Amygdala complex, HIPP: Hippocampus, CP: Caudatoputamen, LS: Lateral septum, AT: Anterior thalamus, LGN: Lateral geniculate nucleus, VMT: Ventromedial thalamus, VP: Ventral posterior thalamus, LHA: Lateral hypothalamic area, PH: Posterior hypothalamic area, ZI: Zona incerta, MLR: Mesencephalic locomotor region, CS: Superior central nucleus raphe, GRN: Gigantocellular reticular nucleus, PG: Pontine gray, PRN: Pontine reticular nuclei, CENT: Cerebellar lobuli, FL: Flocculus

## 2.3.3 Distribution of hemodynamic response properties

We began our analysis of how distinct cell-types of the SC distribute information across the brain by looking at the temporal structure of the hemodynamic changes induced by the optical stimulation (Figure 2.3). We found that our 1 s optical stimulus caused a reliable set of temporal responses that could be grouped into 4 broad categories (see Methods). These four response types could be broadly described as: Fast, Delayed, Slow and Inhibitory (Figure 2.3A and 2.3B). The Fast responses were characterized by a relatively fast rise time (1.27 +/- 0.42 s), resulting in a transient response. The Delayed responses showed a clear delay with time to peak of 3.3 +/- 0.79 s. The Slow responding areas started their responses early but took longer to reach their peak (2.1 s +/- 0.70 s) and showed a more sustained response (1.78 +/- 1.30 s). Finally, a set of responses that we will refer to as Inhibitory, showed a negative response. Inhibitory responses were commonly preceded by a very transient early positive response (time-to-peak = 0.91 +/- 0.65 s: decay time = 0.52 +/- 0.18 s) in each cell-class except the GAD2 (Figure 2.3A and 2.3B). The number of responsive areas and the distribution of the different response types varied among the mouse lines (Active areas: CK = 246, NT = 157, PV = 170, G2 = 82). We found that the Fast responses were more common in CAMKII and NTSR mice (CK 47%; NT 42%; PV 35%; G2 5%). PV mice had a similar proportion of fast (35%) and delayed (34%) responses, while GAD2 mice had predominantly delayed (45%) and slow (44%) responses. In addition, inhibitory response types were more common in NTSR and PV mice, as compared to CAMKII and GAD2 (CK 3%; NT 11%; PV 13%; G2 5%). The almost complete absence of Fast responses in the GAD2 mice is evident in the distribution of the response latencies, estimated as the time-to-peak (Figure 2.3C-D). The distribution of latencies formed two broad groups, those responding within the first 2 s, and those responding after 2 s (Figure 2.3C). While the distribution of latencies is similar for CAMKII, NTSR and PV cell populations, and spanned the entire range of times, activation of inhibitory GAD2 neurons did not cause any early responses (Figure 2.3A and 2.3D).

Stimulating the SC neurons at a lower frequency (5 Hz for 4 s), generated similar temporal dynamics triggered by each neuronal population (fast, delayed, slow, inhibitory), but exacerbated the differences between them (Figure S2.4). Additionally, the change in frequency corresponded with changes in the sign of the response in some areas such as the primary visual cortex, that had Fast responses at high frequency, but delayed strong inhibitory responses at low Frequency (see Figure 2.3 compared to Figure S2.4 where areas have not been rearranged).
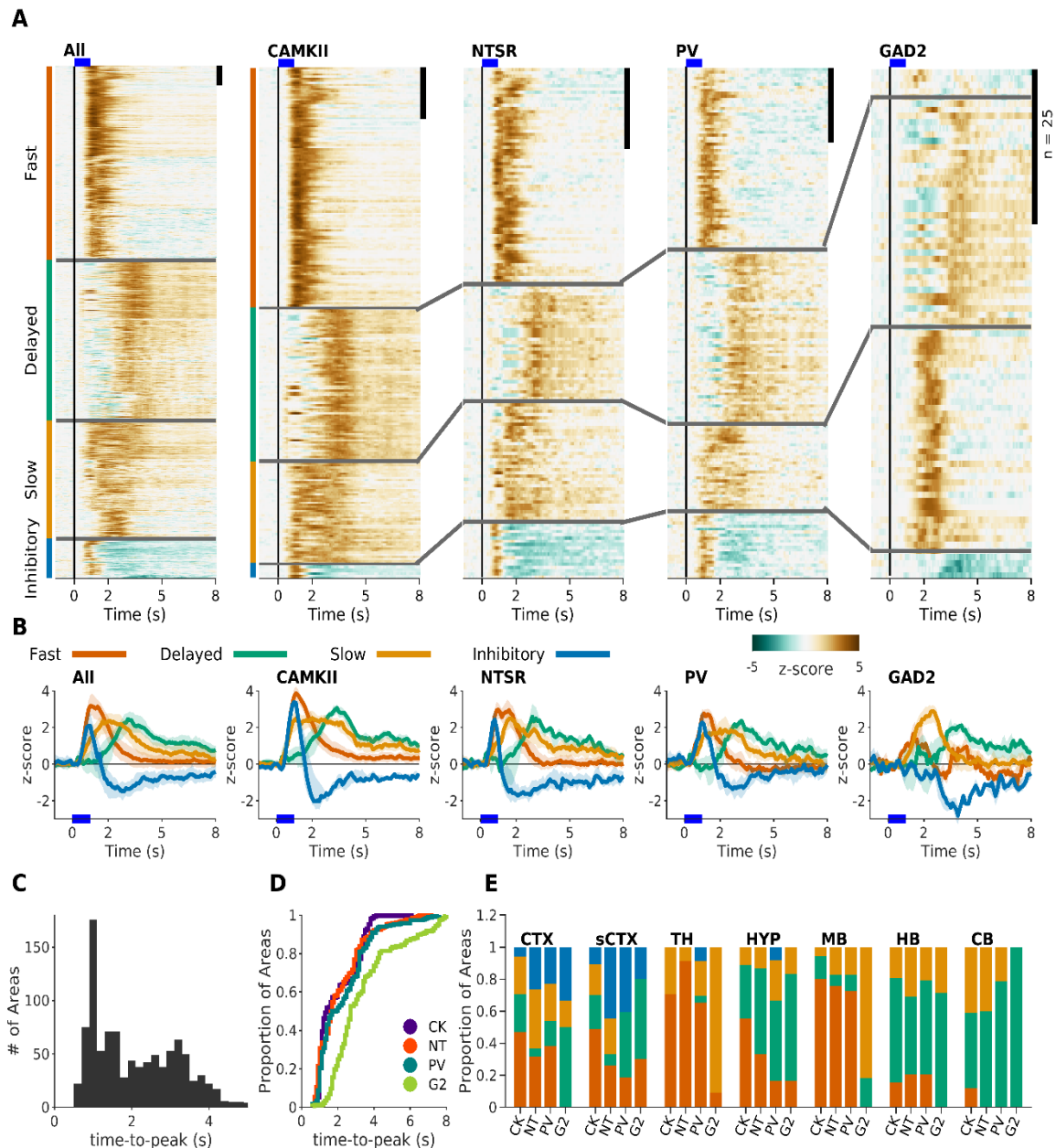


**Figure 2.3. Distribution of temporal responses dynamics. A.** Normalized responses to optic stimulation. Responses are organized into their respective clusters: Fast (orange), Delayed (green), Slow (yellow) and Inhibitory (blue). Black scale bar at top right of each panel represents 25 areas. Blue line represents the 1 s optical stimulus. Left Panel. Responses of all areas that had a statistically significant response across all cell populations (n = 659). Other panels are the active areas in each mouse line (CK = 246, NT = 157, PV = 170, G2 = 82). **B.** Average response of each of clustered responses. **C.** Histogram of the time-to-peak of each active area in all mouse lines. **D.** Cumulative histogram of time-to-peak in each mouse line. **E.** Proportion of each response type sorted by brain area and mouse line.

The distribution of the different response types across the major brain structures was relatively consistent between the different cell populations, except for slow responses (Figure 2.3E). Fast responses occurred mainly in the midbrain and thalamus, delayed activations took place in hypothalamus, hindbrain and cerebellum, and inhibitory responses in the cortex and cortical subplate. Slow responses were more homogeneously distributed. For example, CAMKII and NTSR had the largest proportion of slow responding areas in the cerebellum (23 and 24%, respectively), while GAD2 had none in that structure.

## 2.3.4 Each collicular cell-type modulates a distinct brain-wide network.

To understand how the activation of each neuronal population triggers distinct brain-wide networks, we compared the distribution of brain areas that had increased or decreased hemodynamic responses for each cell-type. Based on the temporal dynamics of the responses observed (Figure 2.3C), we performed this comparison in two distinct time windows, an early (0-2 s) and a late (3-8 s) phase (Figure 2.4A). Complete lists of the responsive areas to high- and low-frequency stimuli are provided in the supplementary materials (Table S2.2). 3D movies of the activated brain areas can be found in online version of the supplementary material of the published article (Sans-Dublanc et al., 2021), for the early and late phases.

The distribution of responsive areas across the brain in the early and late phases followed different patterns for each of the cell classes (Figure 2.4A and 2.4C). Broadly, stimulating CAMKII, NTSR and PV cell-types at high-frequency, resulted in more responses during the early phase (CK=193; NT=138; PV=129), as compared to the late phase (CK=142; NT=82; PV=97). In contrast, stimulating GAD2 cells resulted in 41 areas responding during the first two seconds, followed by an additional 68 areas responding during the late phase. When we compared the distributions of the active areas (Figure 2.4C), we found that stimulation of CAMKII evoked responses in large portions of the CTX (80%, 33/41 areas), sCTX (80%, 41/51 areas), TH (80%, 31/36 areas) and MB (89%, 33/37 areas) in the early phase, but was dominated by HB (72%, 39/54 areas) and CB (79%, 15/19 areas) in the late phase. Stimulating the NTSR population activated large portions of the MB (78%), and TH (78%), during the early phase (other structures ranged from 34%-58%) and had less but more distributed activity during the late phase (CTX: 24%, sCTX: 27%, TH: 28%, HY: 38%, MB: 41%, HB: 28%, CB: 42%). PV neurons preferentially modulated the MB (MB: 70; others: 31-59%) in the early phase, and the HB (HB: 74%; others: 22-43%) in the late phase. In GAD2 mice, most areas were activated in the MB in the early phase (MB: 38%; others: 2-19%). During the late phase, GAD2 activated more areas across the whole brain, particularly in the MB (early/late; 38% / 54%), the HB (early/late; 19% / 33%) and CB (early/late; 16% / 32%). Low-frequency stimulation did not change the overall distribution of responsive areas in early and late phases of the different cell-types (Figure S2.5A and S2.5B). However, compared to high-frequency, PV and GAD2 mice had a noticeable decrease of activated areas in both the early (high-frequency/low-frequency; PV: 129/72; GAD2: 41/14) and late (high-frequency/low-frequency; PV: 97/73; GAD2: 68/9) phases. Differently, NTSR mice had more responsive areas in both early and late phases, most noticeable in the HB during the late phase (high-frequency/low-frequency; HB: 28% / 93%). Of note, the early phase of NTSR mice had a large increase of negatively modulated areas of the cortex by low-frequency stimulation, which had positive responses upon high-frequency stimulation.

To gain insight into the different downstream networks, we next looked at the overlap between the areas modulated by the different cell classes (Figure 2.4D-2.4E). We found that in the early phase up to 93 areas had shared activity between at least three of the neuronal populations, 71 where shared

by only two, and 54 areas were unique. Consistent with the fact that the CAMKII population likely includes the other two excitatory cell-types, when two areas were shared, in most cases it was between CAMKII and either PV (29) or NTSR (34) mice. During the late phase, the specificity increased and only 47 areas where shared by three or more cell-types, compared to the ones shared by two (70) or uniquely modulated (84). To measure how similar the activated networks were from each other, we calculated the similarity between cell-lines of the maximum activity during early and late phases (Figure 2.4E). We found that during the early phase, the greatest similarity was between PV and NTSR with CAMKII (Figure 2.4E). GAD2 showed the least similarity with the other cell lines. During the late phase, GAD2 and NTSR mice showed the highest similarity towards each other (Figure 2.4E Bottom), and all other pairings showed very low similarity. Low-frequency stimulation was characterized by a large increase in the number of areas solely activated by NTSR neurons (Figure S2.5C). Similarity analysis showed that, in the early phase, CAMKII and PV networks were the most similar (Figure S2.5D Top). In the late phase, the similarity pattern was conserved, with GAD2 and NTSR networks being the most similar (Figure S2.5D Bottom).

Finally, in order to compare the activated networks from a holistic point of view, we generated functional connectivity maps of the relationship between areas across the whole brain (Figure 2.4F). To do this, we first quantified the pairwise correlation across all active areas of each neuronal population. Then, we compared the resulting matrices to each other (Figure 2.4G). Broadly, correlations across the brain upon high-frequency stimulation followed similar patterns in CAMKII, NTSR and PV, and were clearly different from GAD2. More concretely, CAMKII, NTSR and PV mice all had a marked high level of correlation between areas of the MB and TH. In GAD2 the highest correlations where between the MB, the HB and the CB. Low-frequency stimulation in CAMKII and NTSR mice resulted in strong positive correlations among subcortical structures (TH, HYP, MB, HB, and CB), while the correlation between subcortical and cortical (CTX and sCTX) structures tended to switch polarity (Figure S2.5E). The change in frequency did not affect the brain-wide correlations of PV mice, while the correlations for GAD2 became sparser and more localized within the different structures, making it the most differentiated cell-type (Figure S2.5F). Taken together, these results indicate that each collicular cell-type modulates distinct, partially overlapping brain-wide networks.
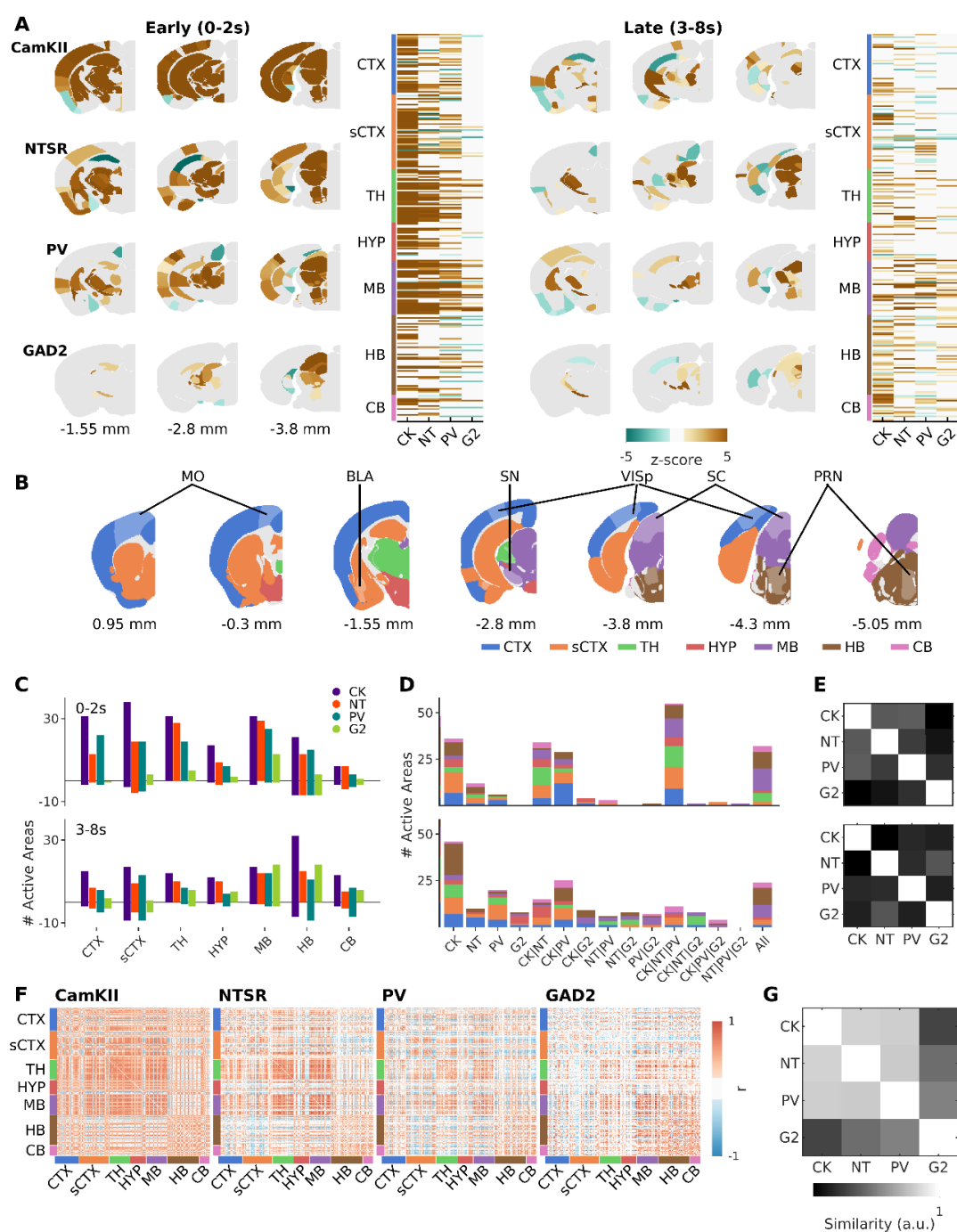
**Figure 2.4. Cell-type specific activation of downstream pathways of the superior colliculus. A.** Activation maps during early (Left, 0-2 sec) and late (Right, 3-8 sec) time windows. Three example coronal slices are shown for each mouse line. Active areas are shown in each plane with the mean z-score across mice (CK=6; NT=6; PV=13; G2=6). Next to the activation maps, is the peak response of all areas active in at least one mouse line. **B.** Summary of the extent of the imaging locations and corresponding names. Imaging was done in 264 brain regions. Here we delineate the major brain areas and highlight a few single regions for orientation. A complete list of the segmented brain regions and abbreviations are presented in Table S2. **C.** Distribution of active areas during early and late phases. **D.** Quantification of shared areas across mouse lines during early (Top) and late (Bottom) phases. Areas included in one group are excluded from the others. **E.** Similarity matrix (between cell populations) of maximum activity during early (Top) and late (Bottom) phases. **F.** Pairwise Pearson correlation coefficients between the mean response traces of the 264 segmented areas during the 8 s after stimulus onset. **G.** Similarity between the correlated hemodynamic responses in F.

## 2.3.5 Defensive and fear related networks are differentially modulated by each cell class.

To understand how the activation of each neuronal population triggers distinct aversive behaviors, we compared the activity patterns of each cell-type within a list of 30 areas that have been previously shown to mediate or modulate defensive behaviors (Figure 2.5A). This comparison showed that each neuronal population activated a different subset of areas or modulated the same areas in a different manner. For example, the central amygdala (CEA), the posterior medial and paraventricular hypothalamic areas (PMH, PVH), and the ventral tegmental area (VTA) were shared uniquely by cell classes that elicited freezing-like behaviors (CK, NT). On the contrary, the cuneiform (CUN), or the superior central nucleus (CS) were activated by all mouse lines but exhibited different temporal dynamics. The CUN had fast transient responses in CAMKII and NTSR and slower sustained responses in PV and GAD2 mice, whereas the CS had sustained responses in CAMKII and GAD2 but transient in NTSR and PV. Interestingly, there were also cases where different cell-types activated the same areas but in opposite directions. For example, areas of the ventral midline thalamus (RE and Xi), cingulate cortex (ACAd), and subthalamic nucleus (STN), had positive responses to CAMKII and NTSR types, but were dominated by negative responses in PV mice. Finally, a few areas were similarly activated by all mouse lines, namely the motor layers of the colliculus (SCi), the dorsal periaqueductal gray (PAGd) and the zona incerta (ZI), all with similar fast positive responses. When we compared the correlated activity across this group of areas (Figure 2.5B), and the similarity of the traces (Figure 2.5C) across the different mouse lines, it confirmed that CAMKII and NTSR evoked the most similar responses compared to PV, and GAD2. Principal component analysis of the trajectories followed by the responses (Figure 2.5D), showed that CAMKII and NTSR evoked almost identical responses during the first 2 seconds after the stimulus onset, but then diverged into different paths. This was likely due to the more sustained activity evoked by the excitation of CAMKII neurons (Figure 2.5E). These results are consistent with the different collicular cell-types activating distinct behaviors through parallel functional networks.

## 2.3.6 Activation of the medial part of the superior colliculus results asymmetric activity.

Orienting behaviors, including eye, head and body movements can be controlled via contralateral projections of the SC to the medial pontomedullary reticular formation (MPRF) (Isa and Sasaki, 2002; Sparks, 2002). In mice the MPRF is comprised of a set of nuclei that includes the pontine gray and pontine reticular nuclei (PRN) that we were able monitor on both sides of the brain as they lie close to the midline. On the contrary, defensive behaviors are thought to be mediated mainly by ipsilateral pathways originating in the medial part of the SC (Dean, Redgrave and Westby, 1989). Consistent with our stimulations targeting the medial part of the colliculus, we found that all cell-lines evoked asymmetric activations that where preferentially ipsilateral (Figure 2.5F-G). Also, activating GAD2 neurons generated the greatest number of asymmetries, including pontine areas such as the rostral part of the PRN, which is in line with that cell line being the only one triggering a change in orientation (Figure 2.1).
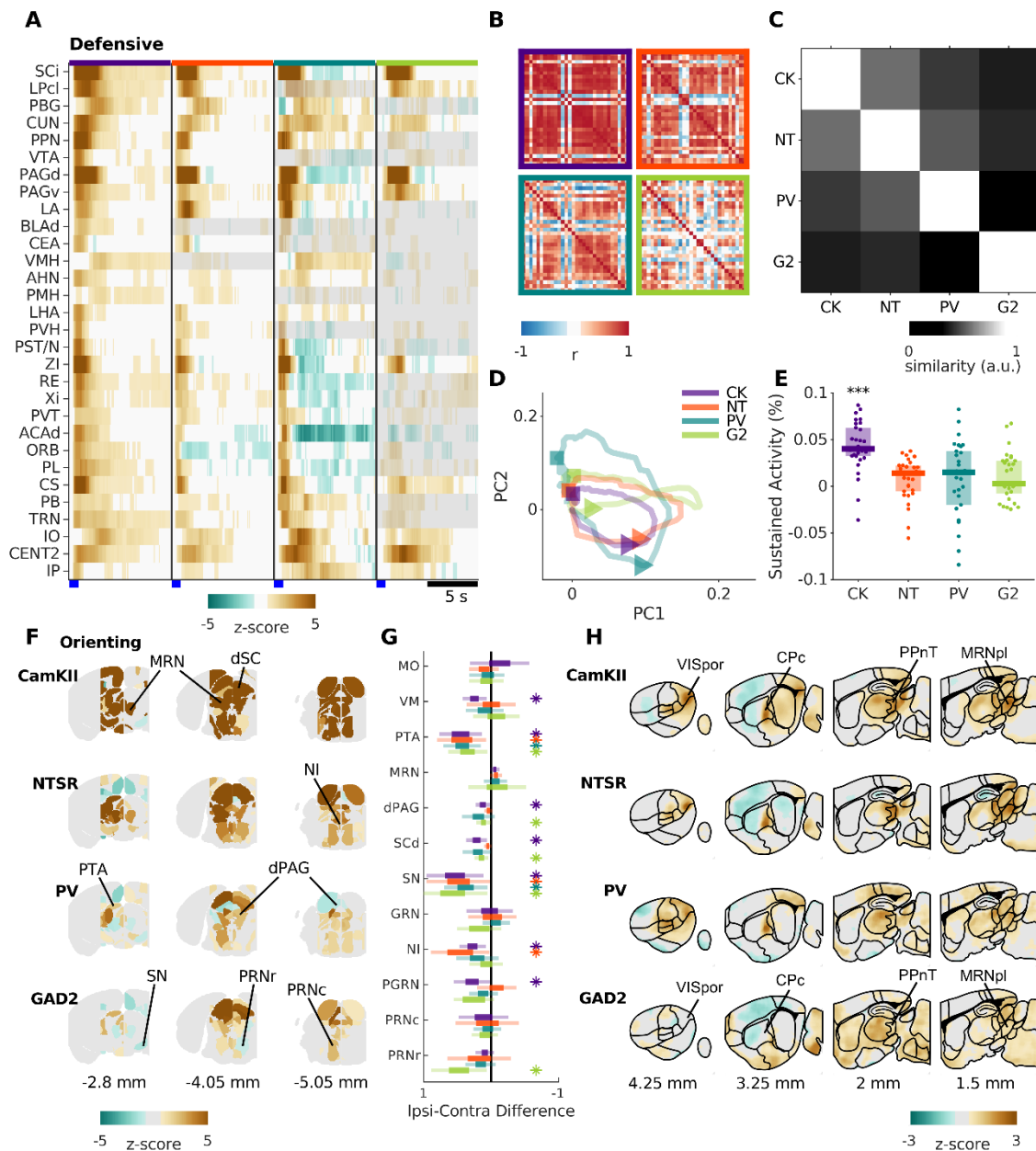
**Figure 2.5. Activity in behaviorally defined networks. A.** Heatmap of the average responses of 30 nuclei commonly associated with defensive behaviors triggered the different cell populations. **B.** Correlation matrix of the responses in each cell populations. **C.** Similarity of the response properties of these 30 areas across cell populations. **D.** 2D Trajectories of the neuronal activity in these 30 brain areas. Triangle and square are the points on the trajectories 1.5 s and 5 s after the stimulus, respectively. **E.** The average sustained activity for each of the 30 areas after high-frequency stimulus of each cell population. Each dot represents a brain area. **F.** Comparison of the activity in the nuclei that lie within 2 mm of the midline, both ipsi- and contralateral to the optogenetic fiber stimulus. Each ipsi-contra pair is shown when the difference is the highest within a 4 s window after stimulus onset **G.** The percent difference in the fUSI signal between the ipsi- and contralateral brain areas. * represent differences that were statistically significant (p < 0.05 permutation test, after correction for multiple comparisons). Light color lines represent the estimated 95% confidence intervals. Dark portions represent the interquartile range. **H.** Average pixel-pixel maps of four sagittal sections from each neuronal population that highlight brain areas not commonly reported to mediate visually guided defensive behaviors.

## 2.3.7 Novel areas involved in collicular-driven aversive behaviors

Visual inspection of brain-wide activity maps (Figure 2.5H), revealed a few highly responsive nodes in areas that have not been previously studied in the context of collicular-driven defensive behaviors. The four areas that were most salient were the the caudoputamen, especially its caudal part (CPc); the postrhinal visual area (VISpor); the posterior lateral part of the midbrain reticular formation (MRNpl) and a group of thalamic areas surrounding the medial geniculate complex referred to here as the posterior paralaminar nuclei of the thalamus (PPnT) (Herkenham, 1986). The VISpor and CPc are known di-synaptic targets of the colliculus, via the pulvinar, but have not been implicated in guiding defensive behaviors (Takahashi, 1985; Harting, Updyke and Van Lieshout, 2001; Beltramo and Scanziani, 2019; Bennett *et al.*, 2019). The MRNpl and PPnT have not been previously described to receive mono- or di-synaptic inputs from retino-recipient neurons of the SC.

## 2.3.8 Correspondence between hemodynamic response and neuronal activity

We found a strong resemblance between the spatial distribution and temporal profile of the hemodynamic response and underlying spiking activity. We used Neuropixels probes to record spiking activity in head-fixed mice evoked by optogenetic stimulation of NTSR neurons in the SC from a variety of cortical and subcortical brain regions (Figure 2.6A). A fluorescent dye (DiI) was used to visualize the recording sites and align the probe tracts to the Allen Brain Atlas and fUSI signal (Figure 2.6B). While some electrodes showed spiking activity that was triggered by each of the 20 light pulses, others only showed strong spiking responses to the first light pulse (Figure 2.6C). A raster plot of all 384 recording electrodes for one trial are shown for the penetration from Figure 2.6B that passed through the cortex, SC and periaqueductal gray (PAG) (Figure 2.6D). We averaged and normalized fUSI data pooled from 6 previous experiments along the Neuropixels probe tracks and compared it to the spiking activity. In the example recording, we found a high level of correlation between the fUSI and spiking signal (r = 0.83, Figure 2.6E). Across all Neuropixels recordings (4 probe locations, 12 animals, 26 recordings) we found that the spatial activity correlated well with the fUSI signal, with a higher correlation across brain regions where the hemodynamic responses were strong (Figure 2.6F).

Next, we compared the hemodynamic patterns observed in the fUSI and the local spiking activity in 6 subcortical areas: 1) superficial SC (SCs), 2) deep SC (SCd), 3) PAG, 4) pulvinar (LP), 5) CPc, and 6) PPnT (Figure 2.5H). In all six areas, we found neurons that responded to the optogenetic stimulation of NTSR cells in the SC (Figure 2.6G). Each area contained neurons that responded to all pulses of the 1 s stimulations, cells that responded to only the first stimulation, and others that were inhibited by further pulses. In addition, when accounting for the slow hemodynamic response, we found that the amplitude and the temporal changes in the spiking activity corresponded well to the fUSI signal recorded in the same brain areas (Figure 2.6G last column and Figure S2.6).

To quantify the neural responses during the 20 optogenetic pulses, we calculated the mean, background-subtracted response of each responding neuron to the 40 ms after each pulse, normalized these 20 measurements to its maximal response and calculated the area under the curve (AUC). An AUC of 1 indicates a cell that responds equally well to all 20 pulses, whereas negative AUC values indicate more inhibition than excitation. The resulting activity maps sorted by AUC indicate a different distribution of optogenetic responses in the different areas (Figure 2.6H). We found a higher proportion of sustained responses (high AUC) in the SCs, more transient responses in the

PPnT, CPc and PAG, and a higher percentage of inhibited neurons in the LP (Figure 2.6I). Subsequently, we classified the responses to optogenetic stimulation measured with Neuropixels probes into the 4 fUSI clusters (fast, delayed, slow, inhibition; Figure 2.6J). Neurons from the superficial and deep SC were mostly found in the early onset clusters (fast and slow), while delayed responses were more common in the PAG and CPc. The PPnT was dominated by the transient responses found in the fast cluster and inhibition was most pronounced in the LP. Taken together, these results show that optogenetic stimulation could be traced from the SC across several synapses. Different response patterns were observed at different stages downstream of NTSR neurons, which correspond well with the differences in the fUSI signal.

## 2.3.9 Visual responses downstream of NTSR neurons reveal preference for threat stimuli

Activation of pulvinar-projecting neurons has been shown to induce arrest behavior (Wei *et al.*, 2015; Shang *et al.*, 2018) and we found arrest-like behavior when activating NTSR neurons (Figure 2.1). In addition, NTSR neurons respond well to visual stimuli mimicking attacking and over-head flying predators (Gale and Murphy, 2016) that induce aversive behaviors (Yilmaz and Meister, 2013; De Franceschi *et al.*, 2016). We thus tested whether neurons at different stages in the NTSR output circuitry that respond to optogenetic activation of NTSR neurons would also respond to behaviorally relevant visual stimuli. We found responses to a looming stimulus mimicking an attacking predator in optogenetically activated neurons in all tested brain areas (Figure S2.7A; SCs: 31 out of 57 optogenetically activated neurons, SCd: 76/139, PAG: 58/60, LP: 25/44, CPc: 59/109, PPnT: 14/50). Neurons showed different response properties including early and late onset responses as well as transient and continuous activity, and inhibition to a looming visual stimulus. These activation patterns were distributed differently in the six tested brain areas (Figure 2.6K). It is known that stimuli with similar properties as looming, but without ecological relevance, e.g. a dimming stimulus, do not elicit aversive behaviors (Yilmaz and Meister, 2013). In accordance with these behavioral findings, we could not detect responses to the dimming stimulus in optogenetically activated neurons of the SCs (Figure 2.6L). Neurons in further downstream areas sometimes responded to dimming stimuli at similar strength as for looming (Figure 2.6L and 2.6M). However, in all areas, fewer neurons responded to dimming stimuli as compared to looming stimuli (SCs: 0 out of 6 optogenetically responding cells, SCd: 8/44, PAG: 3/59, LP: 12/44, CPc: 2/7, PPnT: 4/50). We found no dimming responses in the SCs even when including units that did not respond to optogenetic stimulation and similar higher percentages of dimming responses in the LP, CPc, and PPnT (Figure S2.7). These data show that ecologically relevant visual information is present throughout the multi-synaptic downstream networks of the colliculus that is revealed during opto-fUSI imaging.
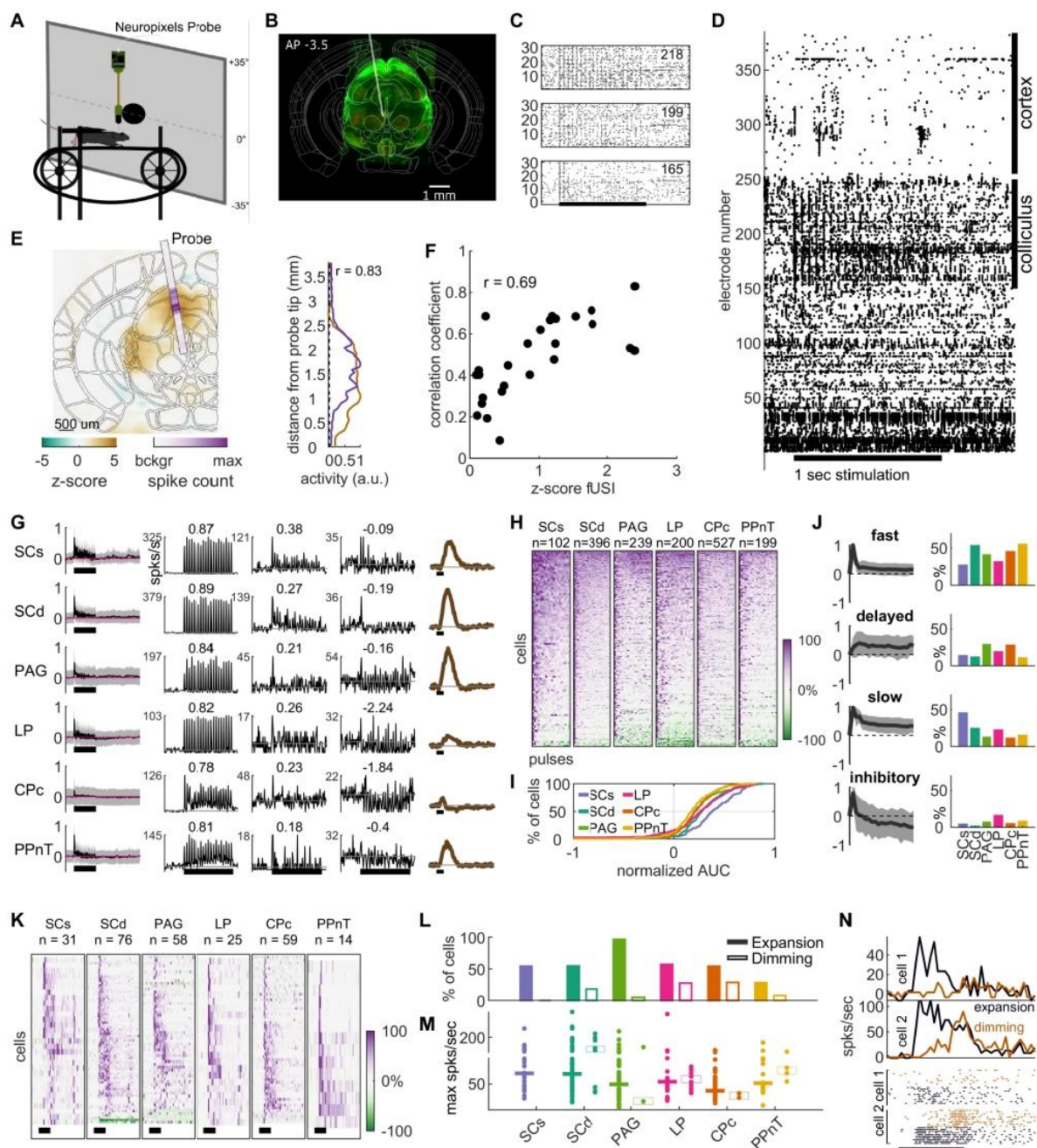
**Figure 2.6. Correspondence of fUSI and spiking activity. A.** Setup for Neuropixels recordings in awake, head-fixed mice. **B.** Example histological section with NTSR-ChR2 positive neurons (green) and the probe location indicated with a gray line. **C.** Raster of spikes for 30 repetitions of the optogenetic stimulus for three example electrodes. Black bar = Stimulus time (1 s, 20 pulses). **D.** Raw spiking data of the probe shown in B during a 1 s stimulation of NTSR neurons. **E.** Overlay of fUSI and spiking activity for a colliculus recording. r = correlation coefficient of the average activity on the probe and the corresponding pixels of the fUSI data. **F.** Dependence of correlation between fUSI and probe recordings on overall fUSI response strength. Each data point corresponds to one probe recording in the colliculus, thalamus or striatum. The z-score comes from the averaged fUSI z-score NTSR brain map. **G.** Average response (averaged across all optogenetic stimuli, background-subtracted and normalized) of sorted units in six selected areas (Left; mean ± std). Responses to optogenetic stimulation of 3 example cells for each area. The cell with the highest area under the curve (AUC) (second column), the medium AUC (third column) and the lowest AUC (fourth column) as well as the temporal fUSI response (last column). Numbers indicate AUC. **H.** Response strength to each optogenetic pulse sorted by AUC. 0% is background

activity. N indicates the number of single units. **I.** Cumulative distribution of AUCs for each area. **J.** Responses to the stimulation were classified into the 4 fUSI classes. Average and STD of the normalized response strength for each class as well as average response strength for each class (average AUC for fast: 0.22, delayed: 0.29, slow: 0.42, inhibitory: -0.16). % of cells for each response type and area (right). **K.** Normalized responses to a black looming disk of all optogenetically activated cells with looming responses in each area. N indicates the number of responding cells. **L.** Percentage of optogenetically activated cells with looming or dimming responses. 100% for looming/dimming for SCs n=57/6, SCd n=139/44, PAG n=60/59, LP n=44/44, CPc n=109/7, PPnT n=50/50. **M.** Maximal response strength to expansion and dimming stimuli for each responding cell and their median per area. **N.** Example of a cell with looming, but without dimming response (cell 1), and a cell responding to both (cell 2).

sSC: superficial superior colliculus, dSC: deep superior colliculus, PAG: periaqueductal gray, LP: lateral posterior nucleus of the thalamus (pulvinar), CPc: caudate putamen, PPnT: posterior paralaminar nuclei of the thalamus.

## 2.3.10 Inhibition of PPnT facilitates habituation to repeated stimulation of NTSR neurons.

The PPnT has not been previously shown to participate in collicular driven behaviors. Our fUSI data showed that it is consistently activated in response to the stimulation of CAMKII, NTSR and PV neurons of the colliculus (Figure 2.5). We corroborated that neurons in the PPnT respond to both optogenetic stimulation of NTSR neurons and visual stimuli (Figure 2.6 and 2.7). To investigate its role in defensive behaviors, we chemogenetically suppressed activity of its neurons while optogenetically stimulating NTSR neurons in the SC. We injected an AAV coding for the inhibitory DREADDs hM4D(qi) into the PPnT of NTSRxChR2 mice (Figure 2.7A and 2.7B). The same optogenetic stimulation protocol as in previous experiments was used to activate ChR2 in NTSR neurons. We tested mice in the open field arena (Figure 1A) and optogenetically stimulated (20 Hz for 1 s) as the mouse crossed the center of the arena. We conducted five experimental sessions, separated by at least 2 days (Figure 2.7A). To inhibit the PPnT, clozapine N-oxide (CNO) was injected intra-peritoneally 30-40 minutes before the beginning of the second session. In the subsequent session no CNO was administered.

We found that inhibition of PPnT increased the variability in the responsiveness of mice to the optical stimulation (Figure 2.7C-2.7E). This variability manifested as an increased speed (Figure 2.7G, session 2, Mann-Whitney U test; p = 0.013) and a decrease in the probability that arrest would be triggered (Figure 2.7H, session 2, Mann-Whitney U test; p = 0.008). An examination of the evolution of behavior over trials within Session 2 (CNO) revealed that hM4D mice habituated more rapidly to the stimulus (Figure 2.7F). During subsequent sessions mice did not regain the lost behavioral response (Figure 2.7G) and tended to maintain a higher speed than controls during the stimulation periods (Figure 2.7H).
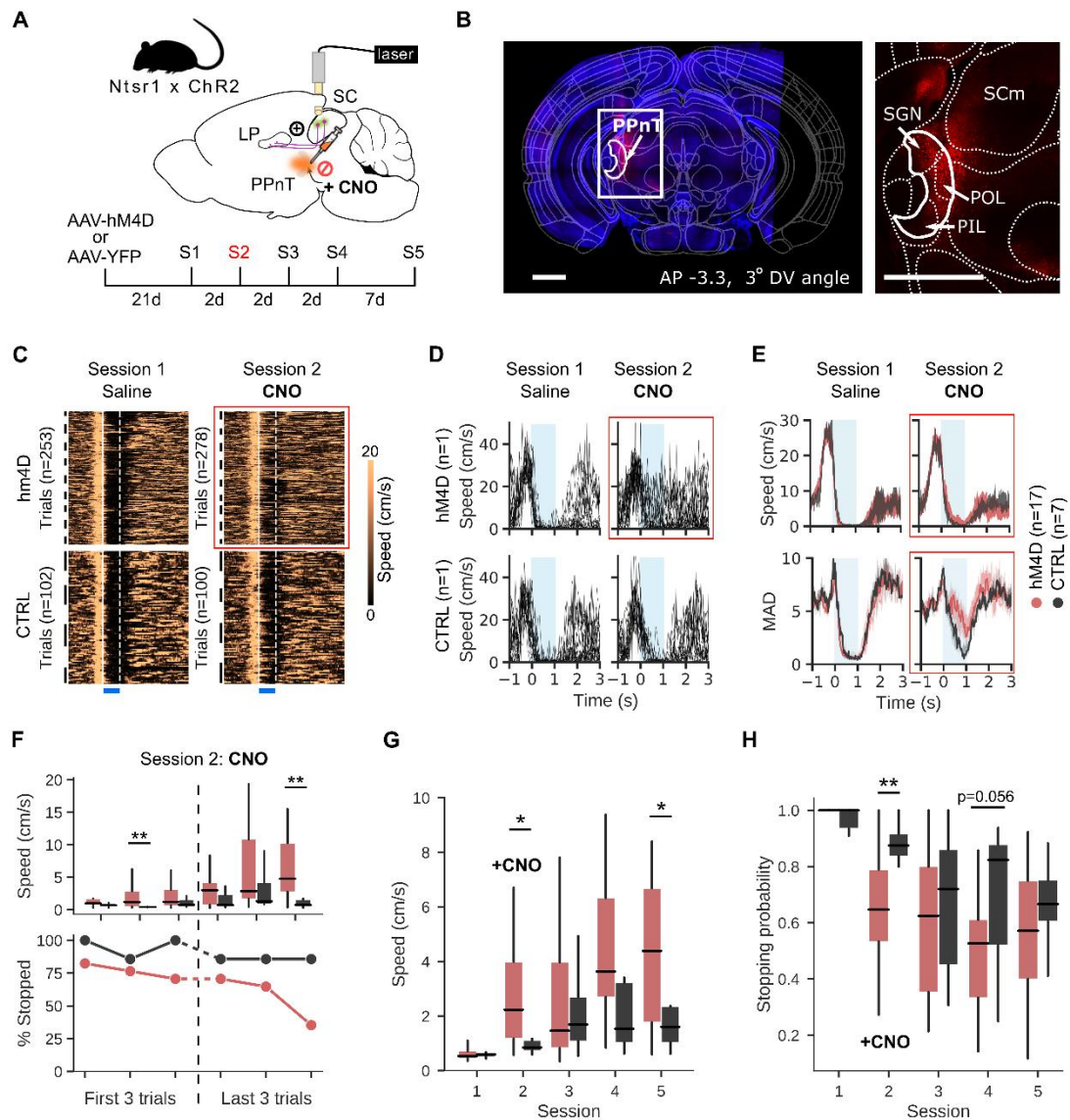
**Figure 2.7. PPnT inhibition facilitates habituation to repeated optogenetic stimulation. A.** Experimental paradigm **B.** Expression of AAV2-hSyn-hM4D(Gi)-mCherry (red) in the PPnT of a NTSR x Chr2 mouse. Left, coronal brain section aligned to Allen Mouse brain atlas. White rectangle indicates injection site and corresponds to right, zoomed in area. Scale bar 1 mm. **C.** Speed traces of NTSR x Chr2 mice injected with AAV-hM4D (Top row, n=17) and controls (n=7, Bottom row), injected with AAV-YFP for session 1 (saline) and session 2 (CNO). Black lines delineate trials belonging to single animals. White lines delineate onset and offset of optogenetic stimulus. **D.** Speed traces from all trials in session 1 (Left) and 2 (Right) from one example animal from each group. **E.** Top row: median speed traces from all hM4D (red) and CTRL (gray) mice during sessions 1 and 2. Bottom row: mean absolute deviation of the speed for hM4D (red) and CTRL (gray) mice. **F.** Median speed (Top row) and stopping probability (Bottom row) during the one second stimulation of hM4D (red) and CTRL (gray) mice, within the session where CNO was administered. **G.** Median speed of hM4D (red) and CTRL (gray) mice, during the 1 s stimulations across sessions **H.** Stopping probability of hM4D (red) and CTRL (gray) mice, during the 1 s stimulations across sessions. Box plots indicate median, interquartile range, and 5th to 95th percentiles of the distribution. *p < 0.05; **p < 0.01.

To investigate the relationship between stopping behavior and the specific location of hM4D expression in the PPnT, we examined the correlation between stopping probability in Session 2 (when CNO was first administered) and the coordinates of the center of expression (Figure S2.8A-S2.8C), or the antero-posterior spread of the expression (Figure S2.8D). Linear regression revealed

weak correlations with the AP, ML, DV planes and extent of expression (Pearson coefficient r=0.112, 0.245, -0.293 and -0.297 respectively). Additionally, we compared the stopping probability of animals with and without DREADD expression in the different areas included in the PPnT (Figure S2.8E). All the examined mice had expression in the POL. The PoT was present in most animals (n=13/17), but the presence or absence of expression in this area did not change the effect on stopping probability (Mann-Whitney U-test; p=0.198). Interestingly, expression in the PIL and SGN was observed in approximately 50% of the animals (PIL: n=9/17; SGN: n=8/17) and rather than causing the behavioral attenuation, expression in these areas seemed to interfere with the effect, increasing stopping probability (Mann-Whitney U-test; PIL: p=0.037; SGN: p=0.042). We also observed viral expression in the most caudal part of the LP in several animals (n=8/17), but its presence did not correlate with a reduced stopping probability (Mann-Whitney U-test; p=0.168, Figure S2.8F). Overall, these results suggest that the inhibition of the PPnT, most likely through the POL, facilitates habituation to the repeated activation of collicular NTSR neurons.

# 2.4 Discussion

In this study, we combined fUSI with optogenetics to reveal the whole-brain neuronal networks that link individual cell-types of the SC with a triggered behavior. We show here that the mouse colliculus distributes information encoded in specific cell-types through distinct networks that share a set of common nodes. Three main conclusions can be extracted from this work. First, the spatial and temporal activity patterns evoked by each cell-type are distinct from each other. Second, the observed differences (or similarities) in behavior could not be explained by the activity in any single brain region but appear to be the consequence of distributed activity across many, predominately, subcortical brain areas. Third, while fUSI imaging revealed activation of known downstream targets of each cell-type, it also revealed activity in a set of areas previously not considered as part of these behavioral networks. This allowed us to uncover a putative role of one of these novel targets, the PPnT, in habituation. Direct measurements of neural activity using silicon probes demonstrate a strong correspondence in both space and time between the fUSI signal and mean firing rate in each brain region. Using probe recordings, we also found responses to ecologically relevant visual stimuli in brain regions identified as part of the functional network. Taken together, these results support the notion that in the SC individual cell-types trigger distinct behaviors, not via single dedicated pathways, but instead via distinct brain-wide networks that share a common set of nodes.

## 2.4.1 Collicular cell-types activate different, partially overlapping downstream networks.

A variety of previous lines of evidence are consistent with our finding that activation of different cell-types of the SC and their output pathways leads to the broad yet restricted propagation of information across the brain. We found that each collicular cell-type relayed information through a different downstream network, that converge in a few key nodes (Figure 2.4 and 2.5). Our fUSI experiments show that activation of each cell-type modulated the neural activity of at least 82 and up to 246 brain areas. Among the pathways activated were a set of areas that are consistent with known output pathways of the SC and that have been identified to trigger freezing and escape behaviors (May, 2006; Gale and Murphy, 2014; Shang *et al.*, 2015, 2018; Evans *et al.*, 2018; Gale and Murphy, 2018; Zhang, W. Y. Liu, *et al.*, 2019). Here we demonstrate that activation of the same neural populations results in neural activity in a much larger than expected set of downstream areas. This extensive dissemination of information is likely due in part to recurrent connectivity within the

SC (Gale and Murphy, 2018; Whyland, Slusarczyk and Bickford, 2020), as well as recurrent feedback loops with, for example, deeper layers of the SC, PAG, thalamus and PBG (May, 2006). While we do observe the previously reported activity in specific nuclei, brain-wide fUSI allowed us to observe functional networks downstream of cell-types in the SC across most of the brain.
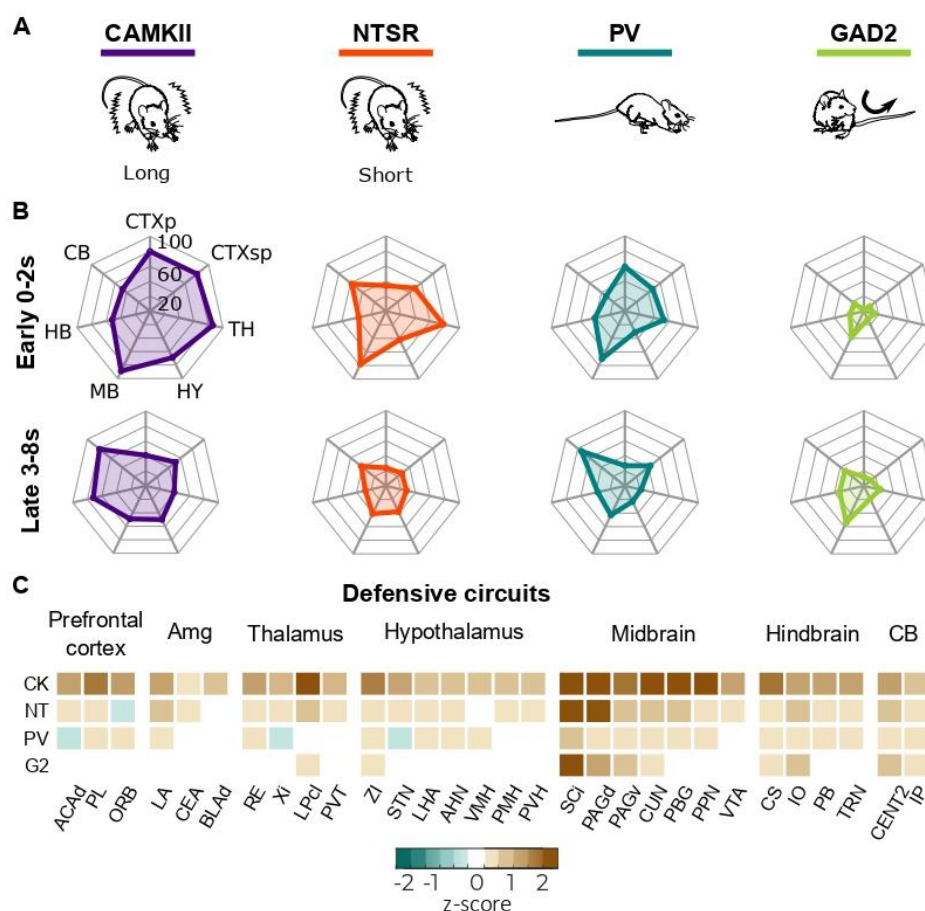


**Figure 2.8. Summary.** Optogenetic activation of different collicular cell-types evokes distinct behaviors (**A**) and activates different brain-wide networks. (**B**) Percentage of activated areas across major brain structures. The effects are shown for early (0-2 s from stimulus onset, top row), and late (3-8 s from stimulus onset, bottom row) time windows. **C.** Heatmap depicting the effect of activating different collicular cell types in a selected set of areas previously shown to be involved in defensive behaviors. The color indicates the mean normalised response (z-score) during the 8 s after stimulus onset. White spaces indicate areas that did not have statistically significant changes.

Conversely, the brain-wide activity we observed shows a higher degree of specificity than we would predict from meso-scale maps of area-to-area connectivity (Oh *et al.*, 2014). If, for example, we assume each brain area, like the retinal recipient layers of the SC, projects to at least 6 downstream structures we only need 3 synapses to modulate 216 brain areas. In many cases this underestimates the number of projections a brain area makes. The retina sends projections to approximately 40 targets (Martersteck *et al.*, 2017), while the primary visual cortex innervates at least 18 cortical and subcortical areas (Han *et al.*, 2018). We saw our maximal spread of activity when stimulating CAMKII neurons, which modulated 246 areas across the early and late phases, while NTSR neurons modulated 157 areas. This restriction in the extent of dissemination is likely due to the cell-type specific connection made in the SC and other brain regions. In the SC, distinct output pathways are known to selectively sample retinal inputs and project to selected downstream areas (Gale and Murphy, 2014; Reinhard *et al.*, 2019). In addition, outputs of the SC to the LP have been shown to be

relayed to a narrow set of downstream targets in the visual cortex and amygdala (Wei *et al.*, 2015; Beltramo and Scanziani, 2019). This cell-type and pathway specific relay of information is a common feature of several brain structures investigated, including the visual cortex, amygdala and VTA (Fadok *et al.*, 2017; Han *et al.*, 2018; Beier *et al.*, 2019).

## 2.4.2 Optogenetically triggered behavior is consistent with the network activity

How the SC routes the cell-type specific information to evoke different behaviors corresponded well with the observed similarities and differences in the network activity. We observed that activation of CAMKII and NTSR neurons each resulted in an interruption of locomotor activity, which was likely the result of the high overlap between these two populations (Figure S2.1A) and was reflected in the similarity in the brain-wide activity evoked by each cell population (Figure 2.4). While activating CAMKII and NTSR neurons each interrupted locomotor activity, activating CAMKII neurons resulted in prolonged periods of immobility as compared to NTSR neurons (Figure 2.1), which corresponded well with the observed differences in the temporal response profiles (Figure 2.5). For example, in comparison to NTSR, stimulation of CAMKII neurons evoked prolonged activity in areas including the premammillary nucleus of the hypothalamus (PMH) and the superior central nucleus raphe (CS). In addition, we showed that PV and GAD2 neurons had minimal overlap with the other studied populations (Figure S2.1B-S2.1D). Their activation facilitated different behaviors, orienting movements, which was consistent with the increases in the activity observed in motor areas of the cerebellum and hindbrain. To further discuss how different behaviors are mediated, we focus below on three brain areas: the subthalamic nucleus (STN), the cuneiform nucleus (CUN) and midline thalamus nuclei.

First, activating either CAMKII or NTSR neurons resulted in increase in the activity of the subthalamic nucleus (STN) – a region involved in the interruption of ongoing behaviors (Aron and Poldrack, 2006; Fife *et al.*, 2017). In contrast, the activity of STN was suppressed or not detectable after stimulation of PV and GAD2 cell-types, where locomotion was not interrupted. This suggests that the STN is either activated to pause ongoing behaviors or silenced to promote escape strategies. Second, we found distinct temporal responses in the CUN across mouse lines. The CUN has been shown to trigger freezing and escape (Dean, Redgrave and G. W. M. Westby, 1989), participate in the initiation and control of locomotion (Mori *et al.*, 1989; Capelli *et al.*, 2017) and modulate cardiovascular response (Korte *et al.*, 1992). We observed fast, transient responses in animals with freezing-like behaviors (CAMKII, NTSR) and slow, more sustained responses, in animals with continuous locomotion (PV, GAD2). It is therefore plausible that different neuronal subpopulations of the CUN are functionally connected with different collicular cell-types to play various roles in defensive behaviors. Third, we demonstrated that the nuclei of ventral midline thalamus (RE and Xi), which play a role in decision making when exposed to threat (Salay, Ishiko and Huberman, 2018), are modulated by both PV and CAMKII neurons but in opposite direction, with sustained activation and inhibition, respectively (Figure 2.5). Taken together our results suggest that opto-fUSI is a reliable method for studying how the cell-type specific information is disseminated from the SC across the brain to trigger behavior.

## 2.4.3 Opto-fUSI reveals new players in aversive behavior driven by the SC

In our experiments, we observed areas consistently activated that have not previously been reported to be involved in mediating visually guided aversive behaviors. Precise circuit dissections have highlighted three major pathways that pass information about visual threat from the SC to downstream areas. These cell-type specific pathways include projections to the amygdala through the LP or the PBG (Shang *et al.*, 2015, 2018; Wei *et al.*, 2015); and projections to the dPAG (Evans *et al.*, 2018). These dissections have led to an atomistic understanding of how the SC mediates aversive behaviors. Here we observed activity in many areas across the brain and four of them captured our attention, namely: the caudal part of caudoputamen (CPc), postrhinal visual area (VISpor), posterior lateral part of the midbrain reticular formation (MRNpl) and PPnT (Figure 2.5). Some of these areas have been implicated in modulation of visual behavior (Wilson, Hull and Buchwald, 1983; Nagy *et al.*, 2003; Schulz *et al.*, 2009; Reig and Silberberg, 2014). The PPnT stood out during visual inspection of activity maps of the brain, as it was both reliably activated upon optogenetic stimulation of NTSR neurons of the SC and during the presentation of visual stimuli. The PPnT is known for its role in associative learning during auditory fear conditioning and in mediating fear discrimination and extinction (Gross and Canteras, 2012; Grosso *et al.*, 2018). Our experiments revealed that this group of areas play a similar role in behaviors triggered by the SC by acting to suppress habituation. Our results are consistent with the proposed role of PPnT in fear extinction and suggest that PPnT is part of the pathway downstream of the SC and is involved in mediating behaviors triggered from the SC. These results highlight the power of combining optogenetic manipulations with brain-wide observation of neuronal activity, which provides a method to identify the brain-wide networks involved and thus the design experiments that allow us to build a more complete picture of how defensive behaviors are controlled.

## 2.4.4 Optogenetics and the relationship between fUSI and neural activity

One of the key questions for fUSI imaging is the degree to which it faithfully represents the underlying neural activity. In the context of fMRI, while it is generally accepted that the measured blood oxygen-level dependent (BOLD) signal changes are associated with neuronal activity (Logothetis and Wandell, 2004); how and where the BOLD signal reliably represents the spiking activity of individual neurons still remains an open question (Ekstrom, 2010). Like fMRI, fUSI also relies on the indirect measurement of neural activity through hemodynamic changes, in this case, in cerebral blood volume. Recently, it has been shown that fUS signals, can reliably represent both increases and decreases in local neuronal activity (Macé *et al.*, 2018; Aydin *et al.*, 2020). We provide additional evidence that the changes in blood volume detected by the fUSI are consistent with the local changes in neuronal activity in a number of different brain regions including parts of the cortex, striatum, hippocampus, thalamus and midbrain (Figure 6 and Figure S6).

Light delivery into the brain, similar to our optogenetic activation, has been reported to cause local temperature changes and arterial vasodilation in naïve mice and rats that can cause artefactual signals both in optogenetic fMRI and opto-fUSI (Christie *et al.*, 2013; Rungta *et al.*, 2017). To minimize such potential effects, in our experiments, we used shorter and lower light intensity stimuli (0.3-0.4 mW, 2 ms pulses, 20-50 Hz, 1 s) than the energy threshold calculated (<1 mW, 20 ms pulses, 20 Hz, 2 s) by Rungta et al. 2017. We did not observe any hemodynamic signal in control experiments using naïve mice in these conditions, indicating that the results reported in this study are driven by the activation of collicular cell-types. In addition, we found that the magnitude, sign,

and time course of the fUSI signal corresponded well with the local spiking activity measured in the same area of the brain and in response to the same stimuli.

Of note, optogenetic stimulation has been shown to be able to evoke frequency-dependent behavioral outcomes (Barbano et al., 2016; Viskaitis et al., 2017; Weitz et al., 2015), and it is therefore likely that the spread of the neural activity is subject to the patterns that drive them. However, in our experiments we tested high (20-50 Hz) and low (5 Hz) frequency stimulations and found both the behavioral and neural circuits activated to be largely conserved. Even so, it is important to note that optogenetic stimulations alone, which generate synchronous activation, cannot tell us how natural stimuli would drive the activity of a specific cell-type and its downstream pathways to generate a particular behavior. For example, visual stimuli are routed through different cortical and subcortical pathways, and we cannot predict how the interactions between them would affect the overall outcome. Our results only capture one behavioral effect of the causal influence of the cell-types tested and will miss the interactions between the different streams of information. Nonetheless, our results provide insights into how individual streams disseminate information across the brain; by selecting a single cell-type of the colliculus we capture the brain-wide functional connectivity and the behavioral consequence of its activation. This allows us to observe one of the behaviors to which each of these cell-types contributes to and through which putative pathways this is mediated and regulated.

## 2.4.5 Brain-wide mapping of function using Opto-fUSI

Understanding the neural basis of defensive behaviors is relevant not only because these behaviors are important for survival, but also because their dysregulation may contribute to anxiety and post-traumatic disorders. To accomplish this, it is necessary to have a holistic understanding of how the nervous system integrates information to guide appropriate behaviors, as well as to know how molecularly defined components of the nervous system contribute to this neuronal activity. Here, we have presented a set of experiments that highlight how combining optogenetics with fUSI can bridge this divide, enabling both the manipulation of targeted components of the nervous system and the simultaneous monitoring of brain-wide activity.

Various methods enable us to look at activity across large parts of the brain, including fMRI, wide-field calcium imaging, large-scale electrophysiology, and genetic markers of neural activity. However, fMRI suffers from low temporal and spatial resolution (Lewis *et al.*, 2016; Jung, Shim and Kim, 2019). Cortical wide calcium imaging and large-scale probe recordings have excellent temporal and spatial resolution but only allow for measurements that are limited to cortex, in the case of calcium imaging, or in thin columns near the electrode tract for silicon probe recordings (Allen *et al.*, 2017; Omlor *et al.*, 2019; Steinmetz *et al.*, 2019). Finally, genetic markers that putatively report elevated levels of neural activity (e.g. cfos or CaMPARI) provide single cell resolution across the whole brain but have poor temporal resolution and their activation is difficult to interpret (Morgan and Curran, 1991; Moeyaert *et al.*, 2018).

fUSI enables access to the whole brain at a spatial and temporal resolution (~100 $\mu m^3$, 0.1 s) that allowed us to map the neural network activated by defined cell populations of the SC across a larger portion of the brain. To our knowledge, this is the first time a comprehensive brain-wide mapping has been done at this spatiotemporal resolution of the circuits involved in innate defensive behaviors of mice. Previous experiments in humans and primates have provided evidence of the involvement of structures such as the LC, the PAG, the SC, the visual thalamus, the amygdala, the insular cortex and PFC (Morris, DeBonis and Dolan, 2002; Liddell *et al.*, 2005; Almeida, Soares and

Castelo-Branco, 2015; Shiba *et al.*, 2017; Koizumi *et al.*, 2019; Terpou *et al.*, 2019). In rodents, molecular (cfos) functional brain maps have implicated a few additional thalamic, hypothalamic and cerebellar areas in various fearful conditions (Mongeau *et al.*, 2003; Vianna *et al.*, 2003; Cho, Rendall and Gray, 2017; Chou *et al.*, 2018; Salay, Ishiko and Huberman, 2018; Mendes-Gomes *et al.*, 2020). We analyzed the activity of 264 areas across the mouse brain. Our results indicate that the neural pathways involved in mediating and modulating the behavioral responses to activation of the SC stimuli is far more complex that previously reported. We believe combining fUSI with targeted cell-type manipulations and natural stimuli will allow us to understand how different brain regions act in concert to guide defensive behaviors under a variety of conditions.

---

**My contributions:** First, I took part on the conceptualization of the project. I developed the opto-fUSI chronic preparation. I designed and performed all fUSI experiments, open field behavioral experiments for cell-type specific behavioral characterization and electrophysiology experiments and subsequent histochemical analysis. I designed the PPnT experiments that were performed by Dani Lemmon. I took part in the analysis of opto-fUSI experiments.

# SUPPLEMENTAL MATERIALS OF CHAPTER 2

## Figure S2.1. Histology and 5Hz optogenetic Behavior
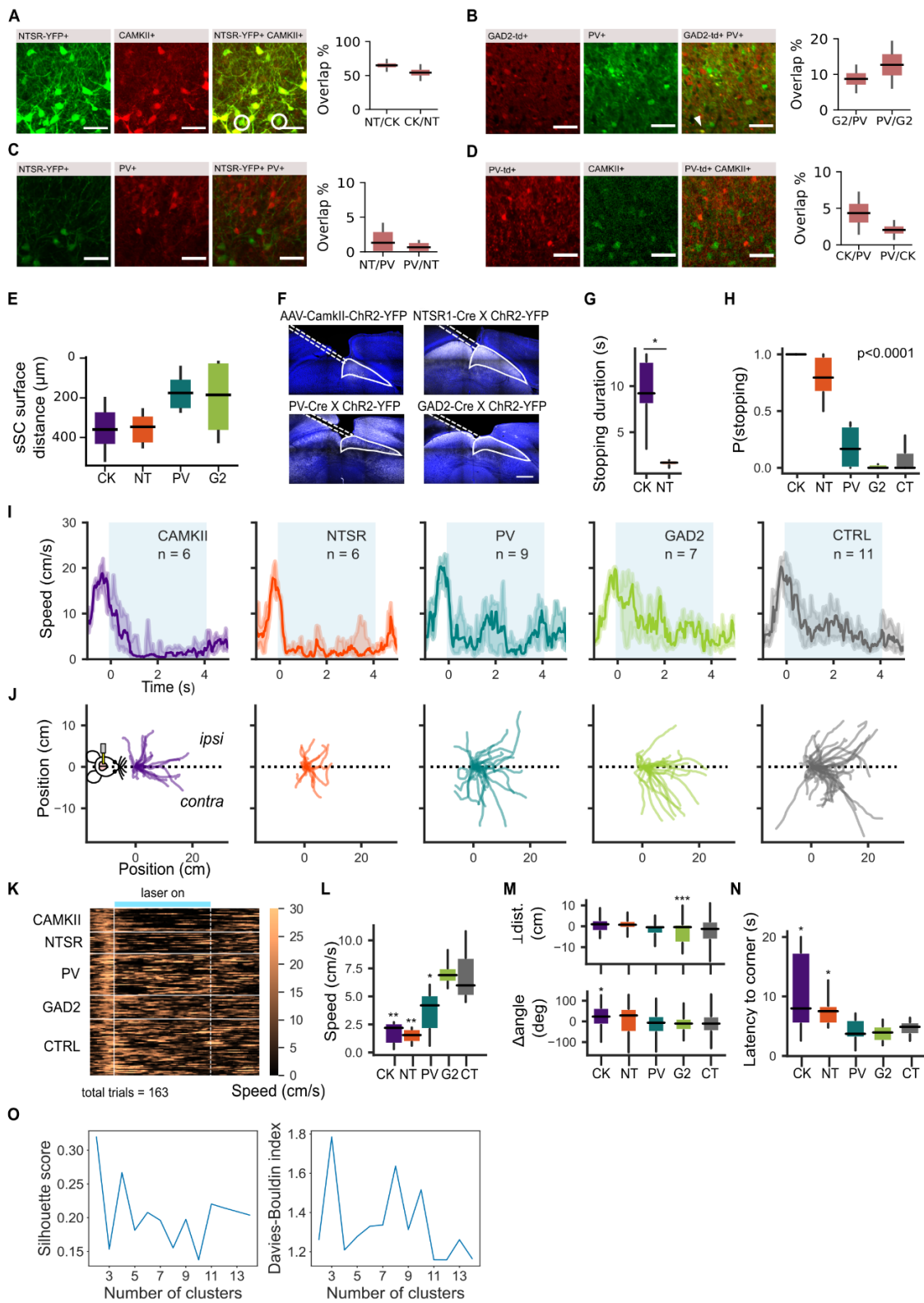
**Figure S2.1. Behavior, related to Figure 2.1. Cell-types overlap (A-E)** Example images (right) and quantifications (left) showing overlap between different cell-types in the SCs (A-D). **A.** Example image from NTSR-Cre mouse injected with an AAV carrying YFP and stained with antibodies against GFP and CAMKII. White circles on the merged image indicate NTSR-YFP+ neurons not labeled with CAMKII antibody. Quantification of overlap: 64.97% NTSR+ = CAMKII+, IQR = [60.92, 69.01], 54.18% CAMKII+ = NTSR+, IQR = [48.64, 59.71], n = 2. **B.** Example image from a mouse expressing tdTomato in GAD2 neurons, stained with antibodies against RFP and PV. White arrows indicate double-labeled cell. Quantification of overlap: 8.7% GAD2+ = PV+, IQR = [6.83, 10.57], 12.67% PV+ = GAD2+, IQR = [9.45, 15.9], n = 2. **C.** Example image from NTSR-Cre mouse injected with an AAV carrying YFP and stained with antibodies against GFP and PV. Quantification of overlap: 1.32% NTSR+ = PV+, IQR = [0, 2.99], 0.68% PV+ = NTSR+, IQR = [0, 1.41], n = 4. **D.** Example image from a mouse expressing tdTomato in PV neurons, stained with antibodies against RFP and CAMKII. Quantification of overlap: 4.34% CAMKII+ = PV+, IQR = [2.94, 5.75], 2.04% PV+ = CAKMII+, IQR = [1.43, 2.64], n = 2. **E.** Depth distributions of cell-types in the SCs, relative to the dorsal surface of the SC (CAMKII: 359.43 μm, IQR = [267.41, 438.27], n = 4; NTSR: 346.41 μm, IQR = [288.28, 430.92], n = 4; PV: 175.47 μm, IQR = [102.73, 258.20], n = 8; GAD2: 185.3 μm, IQR = [20.68, 367.66], n = 2. **F.** Coronal section showing expression of ChR2-YFP in distinct cell lines and optic fiber placement. **High frequency (20 or 50 Hz) stimulation (G-H) G**. Stopping duration, p = 0.02. **H.** Probability of stopping (CAMKII p = 0.0003; NTSR p = 0.0003; PV p = 0.00001; GAD2 p = 0.00008). **Low frequency (5 Hz) stimulation (I-N) I.** Speed profiles. Each trace represents the median speed obtained from each mouse line. Shaded area represents the interquartile range. **J**. Mice trajectories during the first second of 5 Hz stimulus duration. Traces were aligned and rotated by the initial body position angle. CAMKII: n = 6, 23 trials, NTSR: n = 6, 21 trials, PV: n = 9, 41 trials; GAD2: n = 7, 32 trials; CTRL n = 11, 46 trials. **K.** Heatmap of mice speeds during optogenetic stimulation trials. Values were obtained from the first experimental session for each animal. Horizontal white lines separate different mouse groups. Vertical solid and dashed white lines mark stimulus onset and offset, respectively. Light blue bar on the top marks the stimulus duration (4 s). **L**. Speed quantification during the stimulus duration (CAMKII p = 0.009, NTSR p = 0.002, PV p = 0.02, GAD2 p = 0.39). **M**. Quantification of preferred body position at the of the first stimulation second, represented as a change of angle (bottom; CAMKII p = 0.02; NTSR p = 0.06; PV p = 0.49; GAD2 p = 0.45) and perpendicular distance (top; CAMKII p = 0.27; NTSR1 p = 0.29; PV p = 0.38; GAD2 p = 0.00002), both in reference to X axis (dashed line in J). **N.** Quantification of latency to a corner (CAMKII p = 0.03; NTSR p = 0.02; PV p = 0.5; GAD2 p = 0.23). **O.** Silhouette score and Davies-Bouldin index for clustering solutions with different numbers of clusters. Clustering was performed using Gaussian Mixture Models. Scores presented are the best scoring solutions for each number of clusters across 30000 clustering initializations. Scale bar in A-D: 50 μm, scale bar in F: 500 μm. All data points are averaged over mice, except in M where the data points are averaged over trials. In G-H and L-N significance between control and each mouse line was tested using Mann-Whitney U test (alpha=0.05). Box-and-whisker plots show median, interquartile range and range. * P < 0.05, ** P < 0.01, *** P < 0.001.

# Figure S2.2. 5Hz opto-fUSI methods
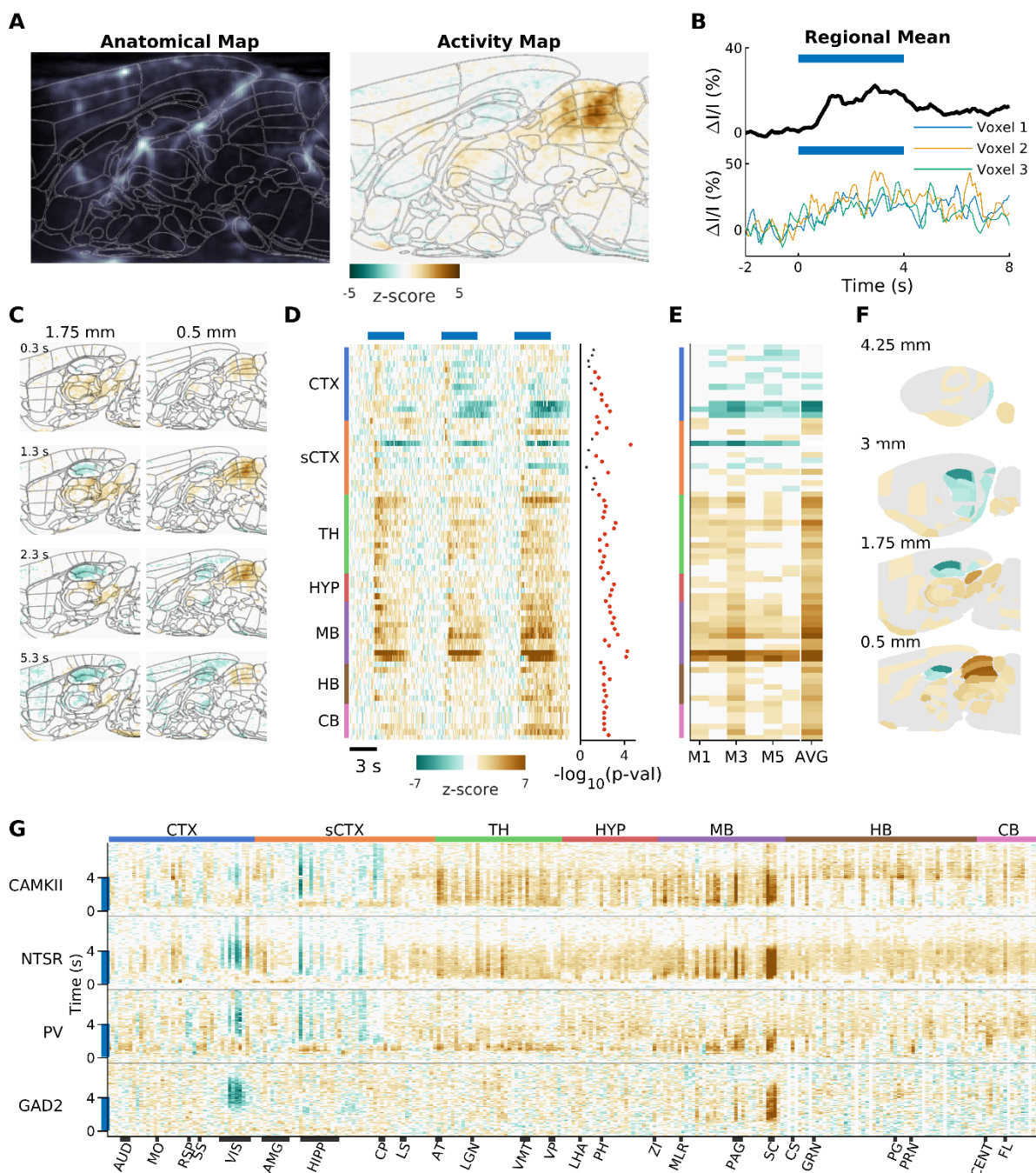


**Figure S2.2. Functional ultrasound imaging of awake mice during optogenetic stimulation at 5 Hz. Related to Figure 2.2. A.** Left. Example sagittal section of a blood volume map registered to the Allen Mouse brain reference atlas (thin gray lines). Right. Voxel to voxel normalized response to optogenetic stimulation of plane shown in left panel, registered to the Allen Mouse brain reference atlas (thin gray lines). **B.** Bottom: relative hemodynamic response curves to the optogenetic stimulation of three example voxels in the intermediate superior colliculus. Top: mean response of the intermediate superior colliculus. Blue lines indicate duration of optogenetic stimulation. **C.** Two example sagittal planes from the activity maps of a single animal. **D.** Left: Standardized responses of a selection of 72/264 segmented areas. Mean responses are shown for 3 different mice. Response for each mouse is an average of 6 trials. Blue lines indicate duration of optogenetic stimulation. black thick line indicates optogenetic stimulation. Right: Inactive (gray) and active (red) areas colored based on significance threshold corrected for multiple comparisons (p < .05). **E.** Mean response of each segmented area shown in D during the 2 s after the start of the stimulus for 6 different NTSR mice and the average across all mice. Areas considered not significant (p > .05) are set to zero in the average. **F.** Projection of the average activity

vector from H onto a map of the mouse brain. **G.** Average time course of each of the 264 segmented areas for each stimulated cell population. Black bars along the bottom indicate span of the labeled brain regions.

CTX: cortex, sCTX: cortical subplate, TH: thalamus, HYP: hypothalamus, MB: midbrain, HB: hindbrain, CB: cerebellum

AUD: Auditory cortex, MO: Motor cortex, RSP: Retrosplenial cortex, SS: Somatosensory cortex, VIS: Visual cortex, AMG: Amygdalar complex, HIPP: Hippocampus, CP: Caudatoputamen, LS: Lateral septum, AT: Anterior thalamus, LGN: Lateral geniculate nucleus, VMT: Ventromedial thalamus, VP: Ventral posterior thalamus, LHA: Lateral hypothalamic area, PH: Posterior hypothalamic area, ZI: Zona incerta, MLR: Mesencephalic locomotor region, CS: Superior central nucleus raphe, GRN: Gigantocellular reticular nucleus, PG: Pontine gray, PRN: Pontine reticular nuclei, CENT: Cerebellar lobuli, FL: Flocculus

# Figure S2.3. Opto-fUSI and head-fixed behavior
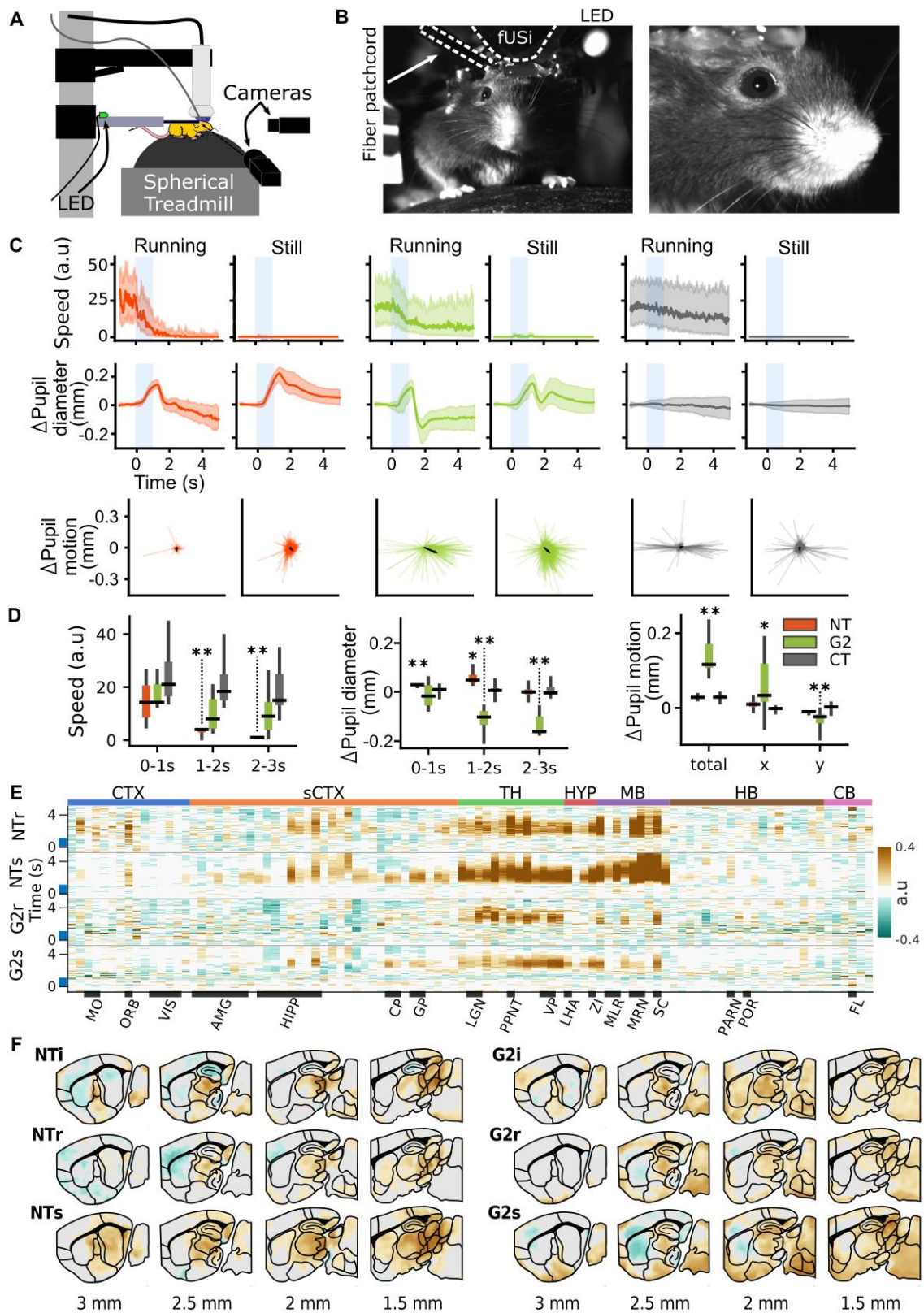
**Figure 2.3. Opto-fUSI and head-fixed behavior**. **Related to Figure 2.2.** A smaller craniotomy (1.5 L to 3.25 L) was performed in these mice, to reduce movement artifacts, and we only used one second, high frequency (NT: 20Hz, G2: 50Hz) stimulations. **A.** Scheme of opto-fUSI on spherical treadmill set up. **B.** Example images from frontal (left) and lateral (right) cameras used for behavioral tracking. **C.** Ball speed, pupil diameter and motion for the NTSR, GAD2 mouse groups in 2 conditions: running and rest. The control group consists of the behavior 7 seconds before stimulation onset of all mice (NTSR and GAD2). Running speed is the pitch of the floating ball. Trials were divided into running and rest categories based on whether the mouse's mean running speed one second before stimulation exceeded predefined thresholds. Pupil diameter is baseline subtracted where the baseline is the mean response 1 second before stimulation. Pupil motion is baseline subtracted where the baseline is the pupil position at stimulation onset. **D.** Quantifications for the behavioral responses in C. All data points are the median responses of mice. Significance between control and each mouse group was tested using Man-Whitney U-test. Box-and-whisker plots show median, interquartile range and range. * $p < 0.05$, ** $p < 0.01$, *** $p < 0.001$. **E.** Average time course of each of the 99 segmented areas for each stimulated cell population (NTSR rows 1 and 2; GAD2 rows 3 and 4) and condition (NTr: running before stimulus onset; NTs: still before stimulus onset; G2r: running before stimulus onset; G2s: still before stimulus onset). Black bars along the bottom indicate span of the labeled brain regions. **F.** Comparison of median pixel-pixel maps of four sagittal sections from NTSR (left) and GAD2 (right) mice, and the different analyzed conditions: immobilized on a platform (NTi, G2i), running on spherical treadmill (NTr, G2r) and still on spherical treadmill (NTs, G2s).

# Figure S2.4. 5Hz opto-fUSI temporal responses
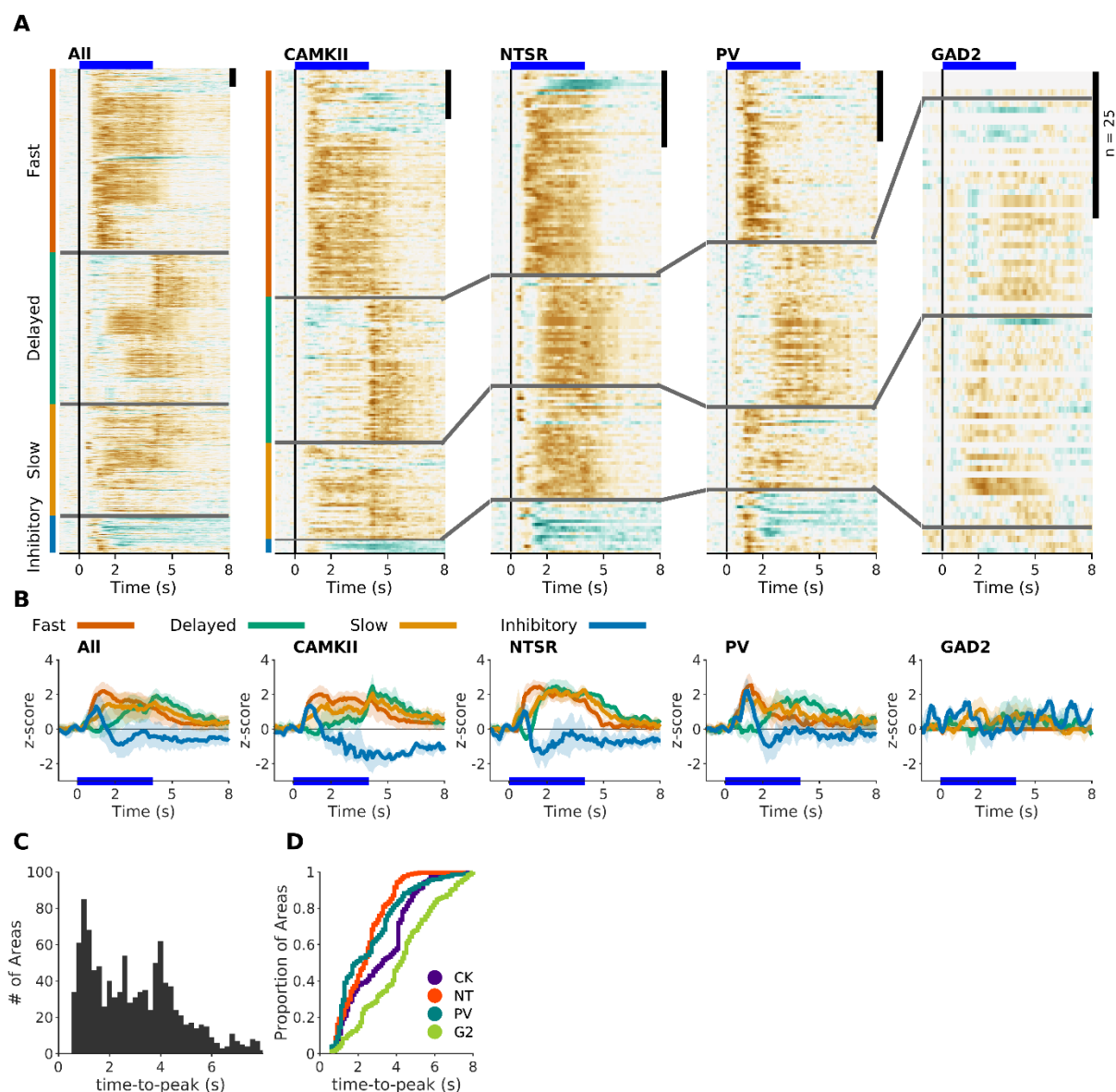


**Figure S2.4. Distribution of temporal responses dynamics (5 Hz). Related to Figure 2.3. A.** Normalized responses to optic stimulation. Responses are organized into their respective clusters: Fast (orange), Delayed (green), Slow (yellow) and Inhibitory (blue). Black scale bar at top right of each panel represents 25 areas. Blue line represents the 1 s optical stimulus. Left Panel. Responses of all areas that had a statistically significant response across all cell populations (n = 659). Other panels are the active areas in each mouse line (CK = 246, NT = 157, PV = 170, G2 = 82). **B.** Average response of each of clustered responses. **C.** Histogram of the time to peak of each active area in all mouse lines. **D.** Cumulative histogram of type to peak in each mouse line.

# Figure S2.5. 5Hz opto-fUSI holistic activity
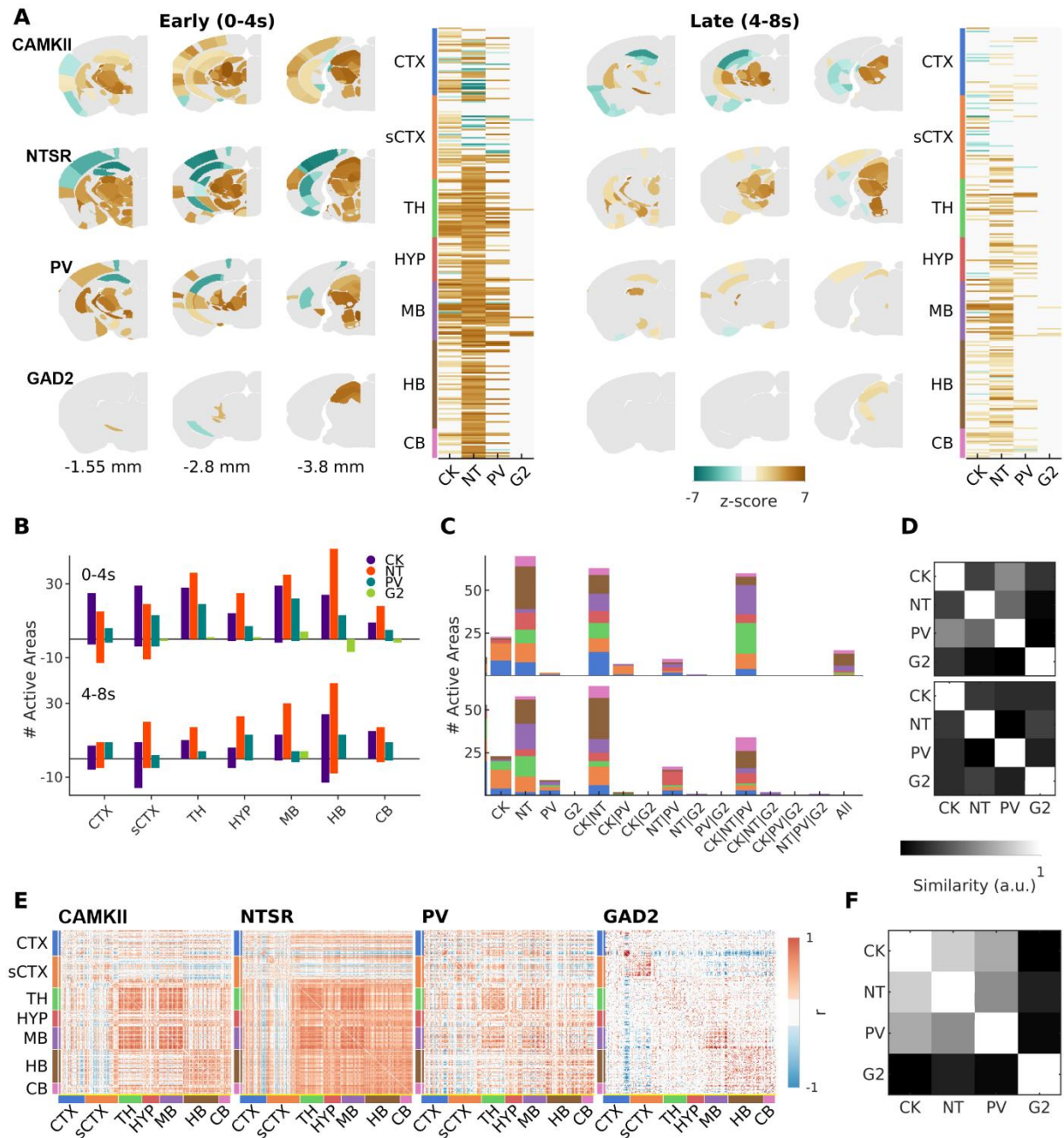


**Figure S2.5. Cell-type specific activation of downstream pathways of the superior colliculus (5 Hz). Related to Figure 2.4. A.** Activation maps during early (left, 0-2 sec) and late (right, 4-8 sec) time windows. Three example coronal slices are shown for each mouse line. Active areas are shown in each plane with the mean z-score across mice (CK = 2; NT = 6; PV = 13; G2 = 6). Next to the activation maps, is the peak response of all areas active in at least one mouse line. **B.** Distribution of active areas during early and late phases. **C.** Quantification of shared areas across mouse lines during early (top) and late (bottom) phases. Areas included in one group are excluded from the others. **D.** Similarity matrix (between cell population) of maximum activity during early (top) and late (bottom) phases. **E.** Pairwise Pearson correlation coefficients between the mean response traces of the 264 segmented areas during the 8 s after stimulus onset. **F.** Similarity between the correlated hemodynamic responses in E.

# Figure S2.6. Neuropixels recordings

**A**

Midbrain



Thalamus



Striatum



**B**



**C**
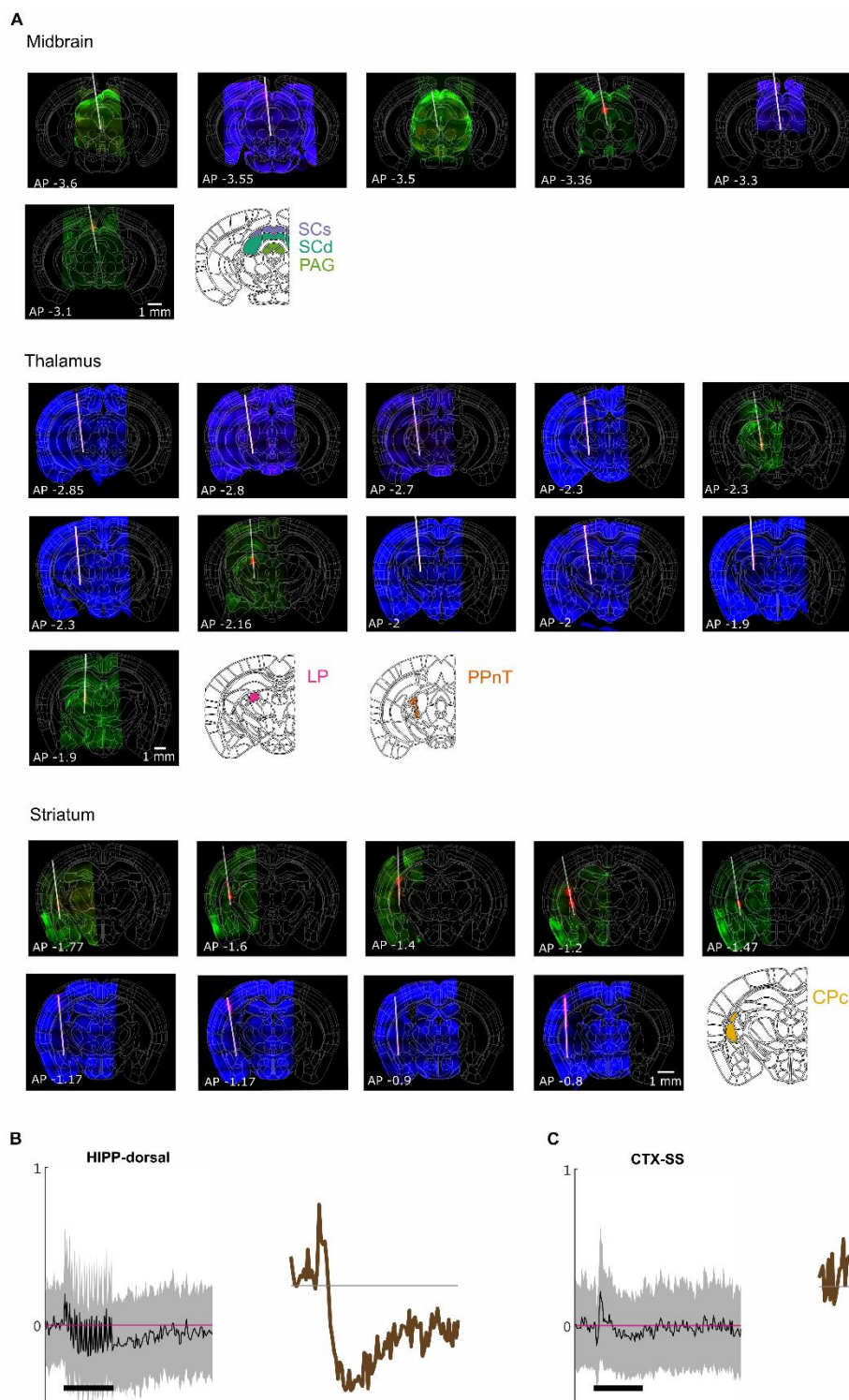


**Figure S2.6. Probe tracts and temporal response profile of Neuropixels recordings in NTSR+ mice, related to Figure 2.6**. **A.** One histological slice per recording is shown. The slices were stained for cell nuclei (DAPI, blue) or Chr2-YFP (green). The probe was coated in DiD before recordings (magenta). Probe tracts are represented with gray lines. For each location, an Allen Brain Atlas coronal slice is shown and the analyzed brain areas are highlighted. **B.** Mean ± std of all sorted units (spiking activity) in the dorsal hippocampus recorded

during Neuropixels probe recordings (left). Corresponding fUSI signal of the same area (right). **C.** Average spiking activity and corresponding fUSI signal for the somatosensory cortex.

SCs: superficial superior colliculus, SCd:   deep superior colliculus, PAG: periaqueductal gray, LP - lateral posterior nucleus of the thalamus (pulvinar); CPc - caudate putamen, caudal part; PPnT - posterior paralaminar nuclei of the thalamus; HIPP-dorsal – dorsal hippocampus; SSp – somatosensory cortex.

# Figure S2.7. Visual responses downstream of Ntsr collicular neurons.
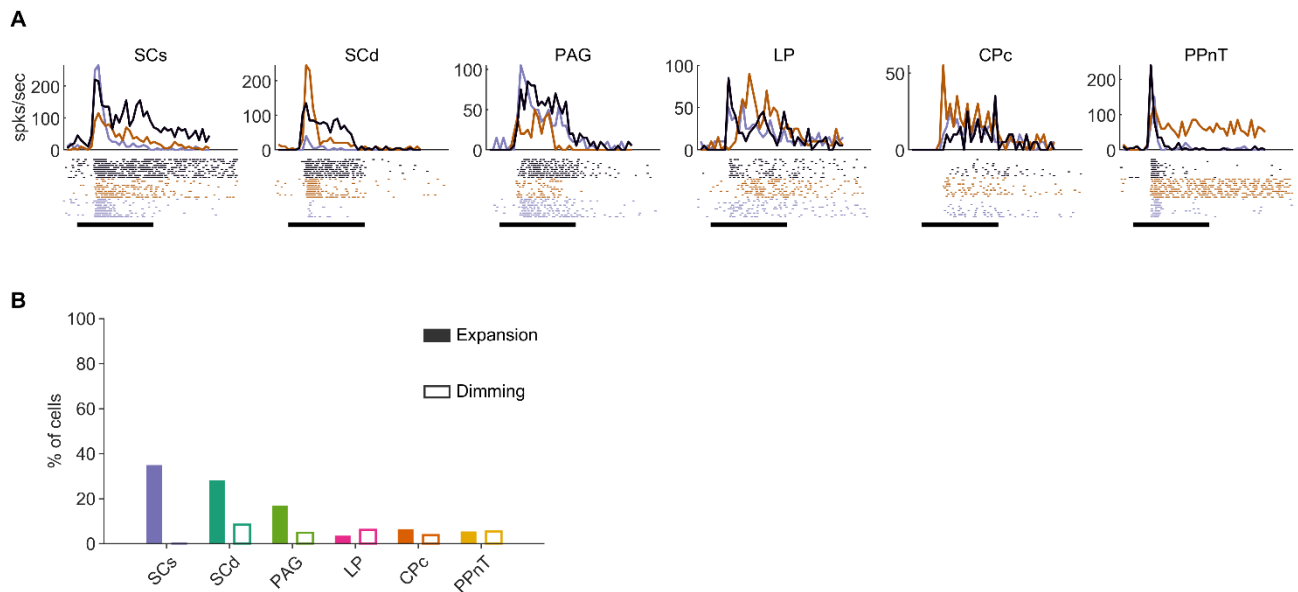


**Figure S2.7: Responses to expansion and dimming of sorted neurons, relates to Figure 2.6K-O**. **A.** Example responses (raster and spikes/s) to a black looming stimulus for 3 cells with median response strength for each area. Black bar indicates time of looming (0.315 s). **B.** Instead of only considering optogenetically activated neurons, visual responses of all recorded and sorted units in six brain areas are included. SCs 51/146 (expansion) | 0/21 (dimming), SCd 160/569 | 11/130, PAG 82/483 | 8/163, LP 12/338 | 16/263, CPc 136/2098 | 47/1255, PPnT 16/294, 16/294.

## Figure S2.8. PPnT chemogenetic inhibition
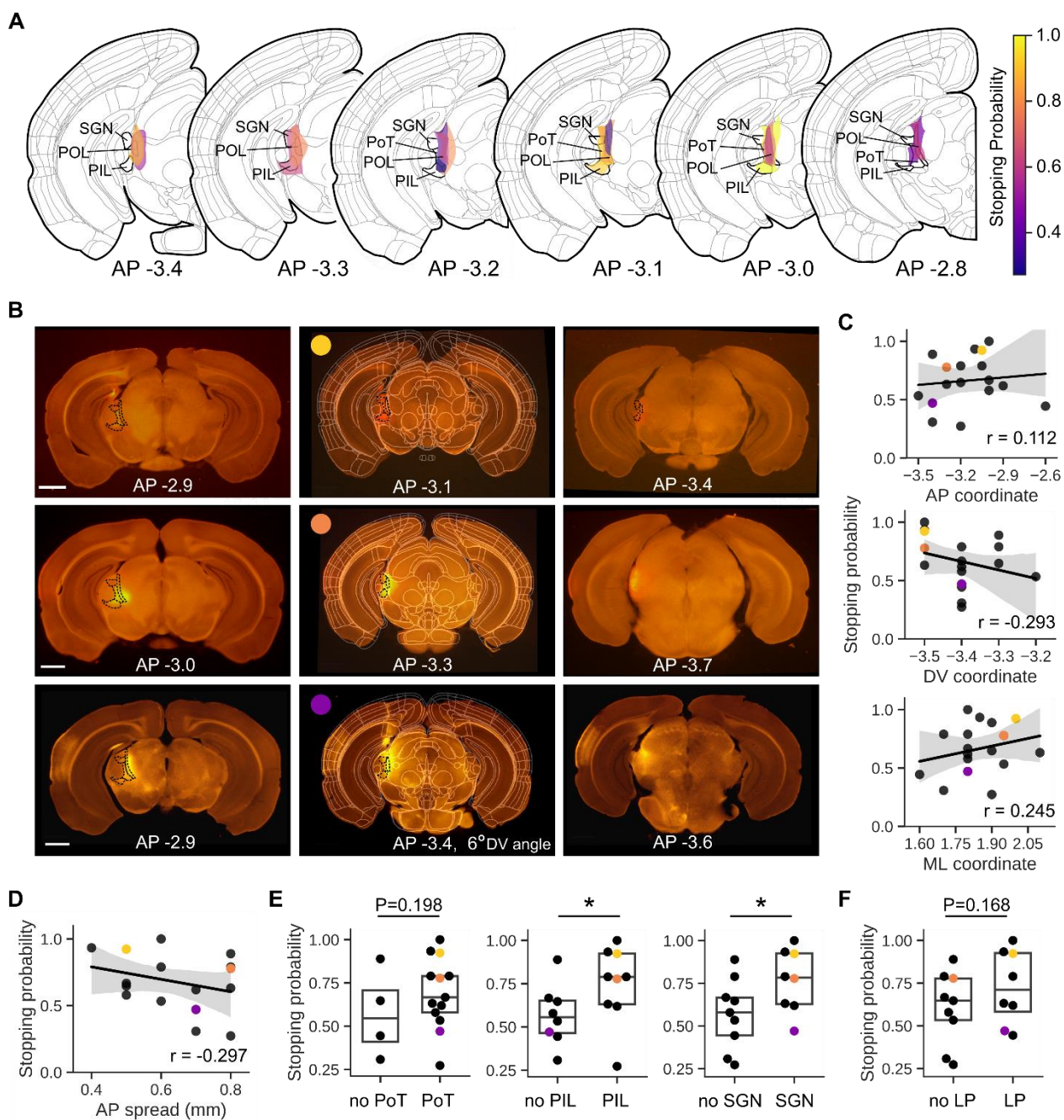


**Figure S2.8: Histological analysis of the AAV-hM4D expression in the PPnT, related to Figure 2.7.**
**A.** Schematic representation of the centers of AAV-hM4D expression for all animals (n=17) grouped on the AP plane. Color represents stopping probability in the CNO-administered. PPnT areas are outlined and labeled in black. **B.** Coronal slices of three example injections aligned to the reference atlas (CCFv3). Each row contains images from a single animal, and in each column is an image of the anterior limit of hM4D expression (left), center of expression (center), and posterior limit of expression (right). The PPnT areas are outlined by dashed black lines. Colored circle in the center column indicates stopping probability of the associated animal based on the colormap in Panel A. Scale = 1mm. **C.** Relationship of Session 2 (CNO) stopping probability of AAV-hM4D mice to injection center coordinates on the AP (top), DV (center), and ML (bottom) planes (n=17). Black line is line of best-fit from linear regression, and shaded area represents the 95% confidence interval. **D.** Relationship of Session 2 (CNO) stopping probability of AAV-hM4D mice to anteroposterior DREADD expression spread **E.** Stopping probability of AAV-hM4D mice with and without expression in the PoT (left, present in n=13/17, Mann-Whitney U-test; p=0.198), PIL (center, present in n=9/17, Mann-Whitney U-test; p=0.037), and SGN (right, present in n=8/17, Mann-Whitney U-test; p=0.042). **F.** Stopping probability of AAV-hM4D mice with and without

expression in the LP (present in n=8/17, Mann-Whitney U-test; p=0.168). Box plots indicate median and IQR. * = P < 0.05. **C-F.** Colored points correspond to histology examples in Panel B.

PoT: Posterior triangular nucleus of the thalamus; PIL: Posterior intralaminar nucleus; SGN: suprageniculate nucleus; LP: Lateral posterior nucleus of the thalamus.

# MATERIALS AND METHODS

## Animals

All experimental procedures were approved by the Ethical Committee for Animal Experimentation (ECD) of the KU Leuven and followed the European Communities Guidelines on the Care and Use of Laboratory Animals (004–2014/EEC, 240–2013/EEC, 252–2015/EEC). Male and female adult (2-4 months old) transgenic mice were used in our experiments including, *Ntsr1-GN209Cre, Ai9, Thy1-STOP-YFP, Ai32 x Ntsr1-GN209Cre, Ai32 x PvalbCre* and *Ai32 x Gad2Cre. Ntsr1-GN209Cre* mice (Genset: 030780-UCD) express Cre recombinase in *Ntsr1-GN209* expressing neurons. *Ai9* (JAX: 007909) and *Thy1-STOP-YFP* (JAX: 005630) are reporter lines that express tdTomato and YFP fluorescent proteins, respectively, when in presence of the Cre recombinase. *Ai32* (JAX: 012569) is a reporter line that expresses Channelrhodopsin2 in presence of Cre recombinase. *PvalbCre* mice express Cre recombinase in parvalbumin-expressing neurons. *Gad2Cre* mice express Cre recombinase in *Gad2*-expressing neurons. Mice were kept on a 12:12 h light:dark cycle and sterilized food pellets and water were provided *ad libitum.* Experiments were performed during the light phase.

## General surgical procedures

Anesthesia was induced at the beginning with an intraperitoneal injection of Ketamine (100 mg/kg) and Medetomidine (1 mg/kg). Before starting any surgical procedure, the paw of the animal was pinched to check for the absence of pedal reflex. After deep anesthesia was achieved, mice were placed in a stereotaxic workstation (Narishige, SR-5N), on a homeothermic blanket to keep a stable body temperature. Eye ointment was applied to protect the eyes from drying and from light (Dura tear, NOVARTIS, 288/28062–7) and Lidocaine (0.5%, 0.007 mg/g body weight) was injected under the skin above the skull. The surgical areas were shaved, and the skin was disinfected using iso-betadine. Then, the skin was cut following the midline and retracted to the sides to expose the skull. Anterior-posterior coordinates are measured from Bregma.

## Viral injections

Once the skull was exposed, a hole was performed at the right coordinates by gently rotating a needle against the skull. We used micropipettes (Wiretrol II capillary micropipettes, Drumond Scientific, 5-000-2005) with an open tip of around 30 µm, prepared with a Laser-Based Micropipette Puller (Sutter Instrument, P-2000), and an oil-based hydraulic micromanipulator MO-10 (Narishige) for all stereotactic injections. To trace back the injection sites, we coated the glass pipette tip with DiD (Thermo, D7757).

For optogenetic experiments, we restricted the expression of channelrhodopsin2 (ChR2) to different cell classes by employing two strategies that have previously been used to study these same populations. First, to express ChR2 in NTSR, PV and GAD2 neurons, we crossed Cre-expressing transgenic mouse lines (NTSR-GN209-Cre, PV-Cre and GAD2-Cre) with a ChR2-reporter mouse line, Ai32 (Gale and Murphy, 2014; Gerfen et al., 2013; Madisen et al., 2010, 2012; Taniguchi et al., 2011). Second, we labeled CAMKII neurons of the retinorecipient layers of the colliculus by injecting wild type mice with an adeno-associated virus (AAV2-CamkII-hChR2(E123T/T159C)-p2A-EYFP-WPRE; UNC vector core, AV5456B) that expresses ChR2 (Wei et al., 2015). We used *Ai9* and *Thy1-STOP-YFP* mice as wild type mice. We injected 200–300 nl of AAV in 100 nl doses with a waiting time

of 5–10 min after each injection. Coordinates for the superficial colliculus were AP: -3.6 to 3.8, ML: -0.2 to -0.3, DV: -1.1 to -1.4. For chemogenetic experiments, we injected 300 nl of AAV2-hSyn-hM4D(Gi)-mCherry (Addgene, 50475), or AAV2-hSyn-EYFP (UNC vector core, AV4376E) as control, into the PPnT. PPnT coordinates: AP -3 to -3.4, ML -1.8 to 2, DV: -3.5 to -3.3.

Following injection, the skin was glued with Vetbond tissue adhesive (3M,1469) to close the wound. Next, mice were injected with painkillers (Buprenorphine 0.2 mg/kg I.P.) and antibiotics (Cefazolin 15 mg/kg I.P.) and were allowed to recover on top of a heating pad. After recovery from anesthesia, animals were provided with soft food and water containing antibiotics (emdtrim, ecuphar, BE-V23552) and were monitored for 3 days and administrated Buprenorphine and Cefazolin depending on the condition of the animal. Any following surgery was performed 21 days after injection to allow for proper gene expression.

## Cranial Windows and optic-fiber Implantations

### opto-fUSI

Once the mouse was anesthetized and the skull was exposed, the lateral and posterior muscles were retracted. Vetbond was applied to open skin and exposed muscle, and a titanium head plate was attached to the skull using dental cement (Superbond C&B, Prestige-dental). Then a cranial window extending over almost the whole extent of the left hemisphere and part of the right hemisphere (AP: +2 to -6.5mm, ML 1.5 to -4.5) was made with a drill. Then, an optic-fiber cannula (Doric Lenses, MF1.25, 200/245-0.37, FLT) was implanted. The entry point of the fiber into the brain was AP: -3.6 to -3.8, ML +1.5 at a 56° angle. The fiber was slowly inserted 1.8 mm into the brain so that the tip would be placed at ML: 0 and DV: -1.1 to -1.2. Next, a ring of dental cement was formed around the craniotomy and the optic-fiber to stabilize the whole preparation. Finally, the cranial window was covered with silicone elastomer for protection and the mouse was allowed to recover on a heating pad. Mice were treated with painkillers (Buprenorphine 0.2 mg/kg I.P.), antibiotics (Cefazolin 15 mg/kg I.P.) and anti-inflammatory (Dexamethasone 0.1 mg/kg) drugs for 5 days.

For experiments where opto-fUSI and behavioral measurements were combined, the same protocol was followed but craniotomies expanded from ML -1.5 to -3.25.

### In vivo electrophysiology

Once the mouse was anesthetized and the skull was exposed, Vetbond was applied to open skin and exposed muscle, and a titanium head plate was attached to the skull using dental cement (Superbond C&B, Prestige-dental). Then, cranial windows (~0.5 to 1 mm$^2$) were performed over the coordinates of the target regions. The following coordinates were used as the center of craniotomies: SC: AP: -3.7, ML: -0.5; PPnT: AP: -3.3, ML: -1.9; lateral posterior nucleus of the thalamus: AP: -2.1, ML: -1.8; tail of caudate putamen: AP: -1.4, ML: -3.1. An additional hole was made for the implantation of an optic-fiber cannula. The entry point of the fiber into the brain was AP: -3.6 to -3.8, ML: +1.5 at a 56° angle. The fiber was slowly inserted 1.8 mm into the brain so that the tip would be placed at ML: 0 and DV: -1.1 to -1.2.

## Behavioral tests

### Opto-open field test

All behavioral experiments were performed in a custom made square wooden box (W: 50 cm x L: 50 cm x H: 36 cm). Dim ambient light (~50 lux) was provided by a lamp (Paulmann Licht GmbH,

PDG09/14) positioned above the arena and oriented away from it, towards a wall. Behavior was recorded at 30 fps using a camera (Point Grey Research, FMVU-03MTM-CS) positioned 53 cm above the center of the arena. For optogenetic activation we used a 473 nm DPSS laser system (Laserglow Technologies, R471003GX) connected to a patchcord with a rotatory joint (Thorlabs, RJPFL2). Optogenetic stimulation was controlled with custom software written in MATLAB. Before every experiment, the output of the laser was measured at 20 Hz or 50 Hz (2 ms pulse width) and set at 0.3-0.4 mW (9.5 − 12.5 mW/mm$^2$). For any given mouse line, a high-frequency stimulus was chosen based on preliminary behavioral data and the documented firing rates recorded in response to natural visual stimuli (Gale and Murphy, 2014, 2016; Hoy et al., 2019; Shang et al., 2015, 2018; Wei et al., 2015). In those mouse lines where 20 Hz stimulation did not evoke any visible response, the following experiments were done at 50 Hz. In the data shown here, CAMKII and NTSR mice were stimulated at 20 Hz whereas PV and GAD2 were stimulated at 50 Hz. We obtained similar results using either a 20 or 50 Hz (Figure 2.1) or 5 Hz (Figure S2.1I-S2.1N) stimulus. Control experiments were carried out with Cre-negative litter mates.

5 days after implantation of the optic fiber, mice were habituated to the handler, patchcord and experimental room for at least 3 days. The day of the test, mice were placed in the center of the arena and were allowed to freely explore for 2 min. After the acclimatization time, when the mice moved away (~10 cm) from the perimeter of the box, towards the center, light stimulation was manually triggered. During any given test, mice were stimulated at high (20 Hz or 50 Hz, 20 or 50 pulses) and low (5 Hz, 20 pulses) frequencies in a pseudo-random manner. Time between stimuli was set to be of at least 30 seconds. A typical experiment lasted 20-40 min.

Repeated tests were always separated by at least 48h.

In tests that combined optogenetics with DREADDs, the experiments were performed as explained above, except that mice were injected with either CNO (2 mg/kg) or saline 30-40 min prior to the test and were only stimulated at 20Hz. To examine the role of the PPnT, all animals underwent five sessions separated by 48 hours except for Session 5, which took place 7 days after Session 4. Each animal was stimulated approximately 15 times in each 20 minutes session (16 ± 2 for hM4D animals, 15 ± 2 for controls).

### Head-fixed tests

To assess the behavioral responses in head-fixed animals, mice were head-fixed on a custom 3d printed air-cushioned spherical treadmill (polystyrene white ball Ø 20cm). We recorded the movement of the ball using two motion sensors (Tindie, PMW3360). Eye and body movements of the mice were recorded using 2 cameras (frontal camera: Allied vision, mako G-030B + Lens: NAVITAR, HR F1.4/25MM; lateral camera: Allied vision, mako G-030B + Lens: Kowa, LMZ45T3) positioned at 25 cm (frontal) and 40 cm (lateral) from the mice head. Recording of the ball sensors and the cameras were triggered at the start of each trial and stopped and saved at the end of each trial. Stimulation time was confirmed using an LED that was triggered together with the laser and was placed behind the mouse (15cm) and recorded with the frontal camera. For the current work, only data from the lateral camera was used in the analysis.

## Protocol of Functional Ultrasound Imaging

5 days after surgery, mice were habituated to the handler, experimental room and to head-fixation on a platform for 7 days. All animals included in the fUSI experiments were tested for behavior (open field test) before each imaging session. Then, the awake mouse was head-fixed on the platform and

the body movement was partially restrained by a foam shelter. The silicone cap was removed, and the cranial window was covered with a 2-3 % agarose layer to reduce brain movement. A 473 nm DPSS laser system was then connected to the optic fiber cannula using a ferrule patch cable (Thorlabs, M83L01). Before every experiment, the output of the laser was measured at 20 Hz or 50 Hz and set to 0.3-0.4 mW (9.5 − 12.5 mW/mm2). Next, acoustic gel (~1 mL, Unigel, Asept) was applied on the agarose for ultrasound coupling and the ultrasound transducer (L22-14v, Verasonics) was lowered down to a distance of ~3 mm from the brain. The probe was moved along the lateral axis by a linear microprecision motor (Zaber, X-LRM-DE). At the beginning of each session, a reference anatomical scan was acquired for registration (53 sagittal planes from lateral +1.5 mm to -5 mm, 125 µm steps). Following, we acquired the functional scan (23 sagittal planes, from lateral +1.5 mm to -4.5 mm, 250 µm steps). Two optogenetic stimuli were applied at each plane (high and low frequencies) before moving to the next one. The parameters of the light stimulation were the same as those used during the behavioral experiments. For each stimulus, functional images were acquired for 20 s (10 Hz), and the stimulus was applied after a 10 s baseline. The functional imaging and optogenetic stimulation were controlled and synchronized using custom software written in MATLAB. Optogenetic stimuli consisted of a high (20 Hz, 20 pulses, 2 ms pulse width or 50 Hz, 50 pulses, 2 ms pulse width) and a low (5 Hz, 20 pulses, 2 ms pulse width, ~2 mW/mm$^2$) frequency stimulus. The acquisition of the 23 sagittal planes was acquired sequentially starting at lateral -4.5, and the whole craniotomy was imaged 7-12 times per session. Total acquisition time was ~3.5 h. Each mouse was imaged in 3 to 5 sessions separated by 48 to 72 hours.

## opto-fUSI behavior protocol

A similar protocol as described above was used when imaging animals on a spherical treadmill. In this condition, we scanned 11 planes for registration (1 to 3.5 lateral, 125 µm steps) and used 7 sagittal planes (1.5 to 3.25 lateral, 250 µm steps) for the functional scan. A single stimulation (high frequency: NTSR = 20Hz, G2= 50Hz; 1s) was applied at each plane before moving to the next one. For each stimulus, functional images were acquired for 20 s (10 Hz), and the stimulus was applied after a 10 s baseline. The acquisition of the 7 sagittal planes was acquired sequentially starting at -1.5L, and the whole craniotomy was imaged 35 times in a single session. Total acquisition time was ~2.5 h.

## Generation of a Functional Ultrasound Image

This procedure was adapted from the sequence for fast, whole-brain functional ultrasound imaging described in Macé et al., 2018. An ultrasound probe containing a linear array of 128 ultrasound emitters/receivers, emitted plane waves (15 MHz, 2 cycles) in five different angles (-6◦, -3◦, 0◦, 3◦, 6◦). The echoes from each plane wave were acquired with the receivers and adjusted with a time-gain compensation to account for the attenuation of ultrasound signals with depth (exponential amplification of 1 dB/mm). This process generated a single emit-receive image ('B-mode image') for each angle and was applied three times for averaging. The 15 individual B-mode images were then combined (~2 ms, 500 Hz), resulting in a higher quality image ('compound B-mode image').

50 compound B-mode images were acquired every 100 ms (10 Hz) to generate a functional ultrasound image. Blood cells flowing inside the vessels scatter back and shift the frequency of the emitted waves (Doppler effect). Such shifts were measured and extracted in real-time by a high-performance computing workstation equipped with 4 GPUs (AUTC, Estonia), using singular-value-decomposition-based spatiotemporal filtering, and high-pass temporal filtering (cut-off frequency:

20 Hz). From the filtered data, we calculated the mean intensity of the Doppler signal (Power Doppler) in each voxel. Power Doppler integrates all the Doppler signals in a voxel to obtain an intensity value that is proportional to the amount of blood cells moving in that voxel at a given time. Unlike Color Doppler, it lacks information about velocity or direction of the blood flow but reliably reports hemodynamic changes in blood volume (Babcock et al., 1996; Mace et al., 2013; Rubin et al., 1994). The intensity value of a voxel at a given time was calculated as: $I(x, y) = A(x, y, t)^2$ where $I$ is Power Doppler Intensity, $x$, $y$ are the coordinates of a given voxel in a given plane, $A$ is the amplitude of the compound B-mode images after filtering, and $t$ was time. The resulting functional ultrasound image was 143 x 128 voxels in which each voxel had a size of 52.5 µm x 100 µm x 300 µm (Macé et al., 2018).

## Electrophysiological recordings

12 *NTSR1-GN209-Cre x ChR2 (Ai32)* mice of either sex at the age of 2.5-3 months were used to record optogenetic and light driven responses in the superior colliculus and PAG (7 recordings), pulvinar (9 recordings), caudateputamen (9 recordings) andposterior paralaminar nuclei of the thalamus (3 recordings).

Two days after performing cranial windows, animals were habituated to the recording set up for 3–4 days. The day of the recording, head-posted animals were fixed on a treadmill or floating ball in front of a screen. Then, a Neuropixels probe phase 3A (Imec, Belgium) (Jun et al., 2017) coated with a fluorescent dye (DiD, Thermofisher) was inserted into the brain with the tip reaching down to 1-1.5 mm below the target area. Once the right depth was reached, it was left to rest for 20-30 min, before starting the recording. Artificial cerebrospinal fluid (150 mM NaCl, 5 mM K, 10 mM D-glucose, 2 mM NaH2PO4, 2.5 mM CaCl2, 1 mM MgCl2, 10 mM HEPES adjusted to pH 7.4 with NaOH) was used to cover the exposed brain and skull.

Neuropixel probes contain 960 recording sites on a single shaft distributed in two rows of 480 electrodes along 9600 µm (16 µm lateral spacing, 20 µm vertical spacing), of which 384 can be recorded simultaneously. In all our experiments, we recorded from the 384 electrodes closest to the tip, spanning 3840 µm. Signals were recorded at 30 kHz using the Neuropixels headstage (Imec), base station (Imec) and a Kintex-7 KC705 FPGA (Xilinx). High-frequencies (>300 Hz) and low-frequencies (<300 Hz) were acquired separately. To select the recording electrodes, adjust gain corrections, observe online recordings, and save data, we used SpikeGLX software. Timings of visual and optogenetic stimulation were recorded simultaneously using digital ports of the base station.

While recording from any given location, first, the superior colliculus of these mice received 30 repetitions of blue light trains (20 Hz, 20 pulses, 1 ms pulse width, 0.2 mW) spaced by 20 seconds intervals. Then, visual stimuli were presented.

## Visual stimuli

Visual stimuli were presented on a 32-inch LCD monitor (Samsung S32E590C, 1920x1080 pixel resolution, 60 Hz refresh rate, average luminance of 2.6 cd/m²) positioned perpendicular to the mouse head, at 35 cm from the right eye, so that the screen was covering 90° of azimuth and 70° of altitude of the right visual field. Visual stimuli were presented on a gray background (50% luminance), controlled by Octave (GNU Octave) and Psychtoolbox (Brainard, 1997; Pelli, 1997). The visual stimuli consisted of a small black disc that linearly expanded from 2° to 50° of diameter within

300 ms at the center of the screen and a disk of 50° diameter dimming from background to black within 300 ms. The stimuli were repeated 10 times.

## Immunohistochemistry

Animals were perfused and post-fixed overnight using 4% paraformaldehyde (HistoFix, Roche). Vibratome sections (100-200 µm) were collected in 1x phosphate-buffered saline (PBS) and were incubated in blocking buffer (1x PBS, 0.3% Triton X-100, 10% Donkey serum) at room temperature for 1 hour. Then slices were incubated with primary antibodies in blocking buffer overnight at 4°C. The next day, slices were washed 3 times for 10 min each in 1x PBS with 0.3% TritonX-100 and incubated in secondary antibody solution diluted in blocking buffer overnight at 4°C. We used rabbit anti-GFP (Thermo Fisher, A-11122, 1:500) as a primary antibody to label ChR2-positive cells, anti-mCherry (Novus, NBP2-25158, 1:500) to label hM4D-postive cells. Alexa488 donkey anti-rabbit (Thermo Fisher, A21206, 1:500-1000) and Cy3 donkey anti-chicken (ImmunoJackson, 703-166-155, 1:1000) were used as secondary antibodies. Nuclei were stained with DAPI (Roche, 10236276001, 1:500) together with the secondary antibody solution. Sections were then again washed 3 times for 10 min in 1x PBS with 0.3% TritonX-100 and 1 time in 1x PBS, covered with mounting medium (Dako, C0563) and a glass coverslip. Confocal microscopy was performed on a Zeiss LSM 710 microscope. Images of areas with ChR2- and hMD4-expressing cells, the fiber location and the Neuropixels track labelled with DiD were obtained using a 10x (plan-APOCHROMAT 0.45 NA, Zeiss) objective.

## Immunohistochemistry of overlapping markers

Selected tissue sections of 60 µm were obtained from 6 mice. We combined immunohistochemistry with crossed mouse lines and viral injections to check overlapping cell-types, namely: 1) for NTSR overlap with CAMKII or PV we used 1 *Ai9 x Ntsr1-GN209Cre* mouse and 3 *Ntsr1-GN209Cre* mice that were injected with an AAV expressing EYFP (AAV2-EF1a- DIO-hChR2(E123T/T159C)- p2A-EYFP-WPRE); 2) for overlap between GAD2 and PV we used 2 *Ai9 x Gad2Cre* mice; 3) and for PV overlapping with CAMKII we used 2 *Ai9 x PvalbCre* mice. We used the following primary antibodies to label different markers: rabbit anti-parvalbumin (abcam, ab11427, 1:1000-2000) to label parvalbumin positive cells, chicken anti-mCherry (Novus, NBP2-25158, 1:1000) and rabbit anti-mCherry (Rockland, 600-401-379, 1:1000) to label tdTomato positive cells, rabbit anti-CamkII (abcam, ab5683, 1:300-500) to label CAMKII positive cells. Alexa488 donkey anti-rabbit (Thermo Fisher, A21206, 1:500-1000), Alexa555 goat anti-rabbit (Thermo Fisher, A-21428, 1:1000) and Cy3 donkey anti-chicken (ImmunoJackson, 703-166-155, 1:1000), were used as secondary antibodies. The histochemistry procedure was the same as described in the previous Method section. Stacks of optical images were obtained from 1-3 sections containing the superior colliculus using confocal microscope with 10x or 63x objective, for counting and example high-magnification images, respectively. Labeled cells were counted using the *Cell Counter* plugin of ImageJ software (ImageJ 1.53c, https://imagej.nih.gov/ij/). Cell bodies were determined by overlaying DAPI-stained nuclei with secondary antibody signal. The depth of each cell-type specific layer was analyzed in ImageJ by sampling distances in 4 places across the SCs from its surface to a visually assessed upper and lower margin of labelled cells.

# QUANTIFICATION AND STATISTICAL ANALYSIS

All the statistical details of experiments can be found in the figure legends and results, including the statistical tests used, exact sample size and definition of significance. All values were calculated with Python or MATLAB. All the details concerning specific analysis are described below.

## Analysis of behavioral data

### Freely moving

Animal tracking was performed using DeeLabCut software (Mathis et al., 2018). Stimulus onsets and offsets were extracted with a custom-made Bonsai workflow (Lopes et al., 2015). Tracking data were sorted into peri-stimulus trials using custom made Python scripts. Trials where stimulation happened while the animal was at the very edge of the setup were not included in the analysis, unless explicitly stated. Behavioral parameters were calculated by pooling all trials per mouse and calculating the average, followed by averaging over mice. Speed was extracted based on positional data of the base of the tail obtained from DeepLabCut. Frames with probability lower than 0.9 were filtered out and linearly interpolated. Position data were smoothed with a median filter of window size = 5. The preferred body angle (Figure 2.1G) was obtained by first aligning the trajectories to the same initial position and by rotating them to cardinal X axis by an angel of their body position at the stimulus onset frame. The body position angle is the angle between the line connecting the tail base with the nose and the Cartesian X axis. Next, the preferred angle was calculated between then line of stimulus onset nose position and stimulus offset nose position. The whole-body drift was quantified as the perpendicular to the distance traveled in the first second relative to the axis of motion before the stimulus. Latency to the corner was analyzed as time needed to reach a corner (corner is defined as a square of 10 x 10 cm) after the stimulation onset.

### Clustering analysis

The clustering of behavioral responses to the optogenetic stimulation is based on the approach used in Storchi et al. (Storchi et al., 2020). This approach enables an analysis of the distribution of behavioral responses for each mouse line in an unsupervised manner. DeepLabCut was used to track predefined body parts (nose, ears, proximal and distal ends of the tail). The following measures were calculated based on these body parts: locomotion (Loc), immobility (Imm), acceleration (Acc), lateral motility (LM) and lateral distance (LD) traveled. Locomotion measures the movement of the body center, while immobility measures the immobility of all tracked body parts. Lateral motion measures lateral displacement relative to the body orientation in the previous frame and to the orientation at the start of the stimulus. Lateral distance measures lateral movement of the animal relative to its orientation at the start of the optogenetic stimulation.

    i.    $M(t) = T(t) - T(t - dt)$

    ii.    $R(t) = X_{nose} - X_{tail\_base}$

    iii.    $Loc(t) = \|M(t)\|_2$

    iv.    $Imm(t) = -\|X(t) - X(t - dt)\|_F$

    v.    $Acc(t) = Loc(t) - Loc(t - dt)$

    vi.    $LM(t) = O(t)\|M(t) - proj_{R(t-1)}(M(t))\|_2$

    vii.    $LD(t) = O(t)\|M(t) - proj_{R(0)}(M(t))\|_2$

Where T the body position (average coordinate of all body parts excluding the tail end), X the coordinates of all body parts, $O \in \{-1, 1\}$ with O = 1 for rightwards lateral movement and O=-1 for leftwards lateral movement, and $proj_u(v)$ the orthogonal projection of v onto u. Lateral motility (LM) measures the lateral movement at timestep (M(t)) relative to the mouse orientation at the previous timestep $(R(t-1))$. Lateral distance (LD) measures the lateral movement relative to the mouse orientation at the start of the stimulation $(R(t-0))$. Each measure was normalized to maximally spread all values over the [0,1] interval. All the values from a measure were first ordered from low to high and replaced by their rank in this ordering. These ranks were subsequently normalized between 0 and 1. The responses for each measure were then concatenated for each trial and reduced to a 5-dimensional vector using sparse PCA. We then clustered the low-dimensional trial vectors using a Gaussian Mixture Model with K-Means initialization. Based on the Silhouette score and Davies-Bouldin criteria (Figure S2.1O), we chose 11 clusters. As some clusters had only a few trials, we subsequently performed a merging step which resulted in 6 final clusters. To merge clusters, we assigned each trial clusters that had less than 10 trials to the clusters with the next-highest posterior probability for each trial. This process continued until all clusters had 10 or more trials.

## Head-Fixed behavior

Pupil diameter and motion were extracted from the video recorded by the lateral camera shown in Figure S3B (right). The DeepLabCut toolbox was used to track 4 parts of the pupil: the upper, lower, left and right edges. As in the open-field behavior analysis, tracked part positions with a likelihood lower than 0.9 in a frame were linearly interpolated. The traces were smoothed with a Median filter of size 3. The pupil diameter was measured as the mean of the height and width of the pupil. The pupil motion was defined as the difference in position of the pupil, calculated as the mean position of the 4 tracked points. Both pupil diameter and motion were baseline subtracted. The baseline for the pupil diameter was set as the mean response 1 second before stimulation. Distance units in the video were estimated by recording an object of known size to find the scaling factor. The baseline for pupil motion was set as the pupil position at stimulation onset. The speed was measured as the pitching motion of the ball, where large positive values indicate a forward movement by the animal, 0 indicates no movement, and large negative values indicate backward movement. Trials were divided into running and still categories based on whether the mouse's mean running speed one second before stimulation exceeded predefined thresholds. If the mean pitch motion during the 1 second before stimulation exceeded the predefined upper threshold (9 a.u.), the trial was labeled a running trial. If the mean pitch motion was less than the predefined lower threshold (3 a.u.), the trial was labeled a still trial. Thresholds were set by the experimenter through visual inspection of the videos.

# Analysis of fUSI data

## Registration

At the beginning of each session, we acquired a reference anatomical map. These anatomical maps were then registered to the Allen Mouse Brain Common Coordinate Framework version 3 (CCFv3) (Allen Brain API; brain-map.org/api/index.html) (Figure 2.2D). Registration was done semi-automatically based on anatomical landmarks that could be recognized on both the anatomical map and CCFv3 (external outline of the brain, dorsal hippocampus, 3rd and 4th ventricles, cerebellar outline, middle cerebral sinus, colliculus, and corpus callosum). These landmarks were used to readjust the 3D volume of the reference map to the CCFv3 by applying scaling in either of the x, y, z axis and rotations and translations in the coronal, sagittal or axial planes when necessary. Then, we

calculated the rotations and translations of the coronal, sagittal and axial planes to create a 3D transformation matrix (from anatomical map to CCFv3).

## Segmentation

fUSI from each session were automatically registered to the CCFv3 using the 3D transformation matrices obtained in the previous steps. Assignment of voxels to brain areas was based on the CCFv3 segmentation. For our analysis, we excluded fiber tracts, ventricles, unsegmented parts of main brain structures (CTX, CTXsp, TH, HY, MB, HB, CB), merged layers of brain areas, and excluded or merged neighboring areas with volumes < 300 $\mu m^3$. Our final version of the atlas was comprised of 264 brain areas in one hemisphere of the brain (see Table S2.2).

## Response Time Traces

The relative hemodynamic changes ($\Delta I/I$) were calculated for each voxel, where I was the baseline (mean of 10 s before stimulus onset) and $\Delta I$ was the subtraction of the baseline to the signal at each time point. The traces of the individual areas were obtained from each trial by summing all the voxels assigned to each area (Figure 2.2E).

## Data filtering and normalization

In order to analyze the response traces of each segmented area, first, we created a dataset with the temporal signals, $T_i$ i=1..Ntime, of each region, trial and session of each animal;

$T_{animal\ repetition}(region, time)$. In this dataset, all the trials of the different sessions were added. Therefore, the repetitions were $N_{sessions}* N_{trials}$. The intensity signal obtained from the Power doppler is susceptible to brain tissue motions caused by the awake animal's movements. However, motion artifacts can typically be distinguished from hemodynamic changes based on the shape (noise/real; quick spiky/slow curved), and amplitude (noise/real $\Delta I/I$; >100%/1-15%) of the signal. In this study, in order to remove trials affected by motion artifacts we computed the mean temporal signal of each region (Tm) and standard deviation (SD), and then eliminated outlier values where $T_i$-Tm were 2.5 times higher than the SD. The eliminated values were replaced by the previous non-eliminated value. To eliminate the global variations in the brain (baseline perturbations) we selected the 20% of the regions with lowest response during a 2 second time window after the stimulus onset, then averaged these regions to create a baseline signal. This baseline signal was then subtracted from all segmented areas. The resulting normalized temporal traces were used for statistical analysis (Figure 2.2G).

## Active Brain Regions

To determine if a brain region was activated by a stimulus, first, we used the normalized temporal traces of every trial to calculate a T-score for each animal, using a general linear model, as commonly used in fMRI (Friston et al., 1995). To take into account the different temporal dynamics present in the responses, the GLM was applied using both 1 and 2 second windows stepped (0.5 seconds steps) from the beginning of the stimulus until 7.5 seconds after stimulus onset. Next, a one-sample two-tailed t test was performed on the n T-scores obtained for the n animals. The region was considered active if the resulting p-value, adjusted for a false discovery rate (Benjamini and Hochberg FDR procedure), was <0.05 (Figure S4D) (Benjamini and Hochberg, 1995). For display (such as in Figure 2J), we quantified the median response time courses across animals, we standardized the responses with regard to the values before stimulus onset (z-score) and we corrected for the relative differences between the stimulation levels of each animal. To do this we calculated a correction factor from normalizing the peak response (A = average of the signal 0.5 s around the maximal value within a time window after stimulus onset), across all brain areas

where: $A_{norm(region)} = \frac{A(region)}{\sqrt{sum(A(region)^2)}}$, , then divided each time point by the correction. The Average of all the corrected response traces, for each mouse line, are shown in Figure 2.2J and S2.2G and are used in the subsequent figures.

## Pixel-to-pixel Activity Maps

To visualize pixel-to-pixel activity maps, for each voxel, we quantified the median of the response time courses across trials. We then standardized the responses computing the z-score, using the 10 seconds before stimulus onset and a 2 second time window after stimulus onset. Next, we averaged activity maps of animals belonging to the same mouse line applied a median filtering of 4 x 4 pixels on the resulting z-score map. The filtered z-score maps were used for visual inspection of the brain activity and for data visualization (Figure 5H).

## Clustering of fUSI time courses

Time course of all active brain regions in the four neuronal groups were clustered using hierarchical classification and the e-linkage algorithm, an extensions of Ward's minimum variance method (Szekely and Rizzo, 2005). The optimal number of clusters was determined by inspection of the mean silhouette value (Rousseeuw, 1987) and Davies-Bouldin Index (Davies and Bouldin, 1979). Clustering was only preformed on the 1056 active areas for the 1 s optogenetic stimulus. Four clusters were finally included, namely: Fast, Delayed, Slow and Inhibitory, and can be described as follows. The Fast responses were characterized by a relatively fast rise time (1.27 +/- 0.42 s), resulting in a transient response. The Delayed responses showed a clear delay with time to peak of 3.3 +/- 0.79 s. The Slow responding areas started their responses early but took longer to reach their peak (2.1 s +/- 0.70 s) and showed a more sustained response (1.78 +/- 1.30 s). Finally, Inhibitory responses, showed a negative response. Inhibitory responses were preceded by a very transient early positive response (time-to-peak = 0.91 +/- 0.65 s: decay time = 0.52 +/- 0.18 s) in each cell-class except the GAD2 (Figure 3A and 3B).

## Comparative network analysis

To assess the correlation between the functional responses either across the whole brain or within a predetermined group of areas, we calculated the Pairwise Pearson correlation coefficients between the mean response traces of the segmented areas during the 8 s after stimulus onset using the 'corrcoef' function in MATLAB.

Principal component analysis of the trajectories of the neuronal activity in 30 "defensive" brain areas was performed using the 'svd' MATLAB function.

Similarity matrices of the response properties of the different mouse lines or the similarity between correlation matrices was calculated measuring the Pairwise distance between each mouse line's mean responses (One minus the sample correlation between points), or between correlation matrices (One minus the sample Spearman's rank correlation between observations) using the 'pdist' function in MATLAB. To determine whether the differences in active brain regions were statistically significant, we performed a bootstrap analysis of whether the distance between evoked activity of different mouse lines was different from 0. To accomplish this, distributions were estimated using 1000 repetitions of random sampling of the evoked activity in individual mice. After correction for multiple comparisons (Yekutieli and Benjamini, 2001), p values were considered significant at alpha = 0.05.

# Analysis of Neuropixels recordings

## Raw spiking activity

To extract spikes from raw Neuropixels data, the average voltage on each electrode in the 0.5 s before onset of the optogenetic stimulation was subtracted from the signal during stimulation. Spikes were identified using the 'findpeaks' function in MATLAB with a threshold of 4 standard deviations of the signal before the stimulation. Spikes during the 1 ms of each light pulse were excluded as they could cause artifacts, especially on the electrodes in the superior colliculus.

## Activity maps

Confocal images of brain slices containing the probe tracks were aligned with the Allen Brain Atlas using the allen CCF tool (Shamash et al., 2018). This allowed us to identify the same slice of the fUSI data set. To compare the activity on the probe with the fUSI signal, we averaged the z-scored fUSI signal (averaged across all stimulation repetitions and tested NTSR animals) of x-2 to x+2 pixels for each x location of the probe. The raw spiking data on the whole probe during the 4 seconds after each optogenetic stimulation was averaged across stimulations and resampled to match the spatial resolution of the fUSI data. We normalized each data set separately to its maximal value, resulting in the plot shown in Figure 6G and analyzed in Figure 6F. Correlation coefficients were calculated using the 'corrcoef' function in MATLAB.

## Spike sorting

The high-pass filtered in-vivo data was automatically sorted into individual units using SpyKING CIRCUS (Yger et al., 2018) with the following parameters: cc_merge = 0.95 (merging if cross-correlation similarity > 0.95), spike_thresh = 6.5 (threshold for spike detection), cut_off = 500 (cut-off frequency for the butterworth filter in Hz). Automated clustering was followed by manual inspection, merging of units if necessary and discarding of noise and multi-units using phy2 (https://github.com/cortex-lab/phy). Units were evaluated based on the average waveform shape and auto-correlogram. Only cells with < 1% of inter-spike intervals of ≤ 1 ms were considered and cross correlograms with nearby neurons were inspected to find spikes from the same neurons (Segev et al., 2004).

## Detection of responding units

Peri-stimulus histograms (PSTH) were calculated using a bin size of 20 ms. For detection of responding cells and for plotting, the mean spikes/s during 0.3 (looming, dimming) or 0.5 seconds (optogenetic stimulus) before stimulus onset were subtracted from the cell's activity. We calculated a quality index to capture the reliability of a cell's response to the 10-30 stimulus repetitions. The quality index was defined as $QI = \frac{Var[\bar{C_r}]_t}{\overline{Var[C_t]}_r}$ with C being the TxR response matrix, t = time dimension and r = repetition dimension (Baden et al., 2016). Cells were labelled as 'responding' if the maximal z-score during the stimulus exceeded 3 and if the quality index was at least 0.15.

## Transiency measurements

For response transiency when stimulated with 20 light pulses (optogenetics), the mean response during the 40 ms after onset of each pulse was normalized to the absolute maximum of these 20 responses (positive or negative). The transiency of the response was defined as the area under the curve (AUC), i.e. the sum of these 20 values divided by 20. An AUC of 1 means that the cell responded equally well to all 20 pulses, an AUC of -1 means that the cell's activity was equally suppressed by each pulse.

## Clustering optogenetically induced responses

We classified the responses to optogenetic stimulation measured with Neuropixels probes into the 4 fUSI clusters (fast, delayed, slow, inhibition). To achieve this, we extracted the peak firing rate for each of the 20 optogenetic stimuli, normalized these 20 measurements to the maximum response, and classified the normalized peak responses following a step-wise process:

Fast: Peak response needs to happen for the first stimulus, and the normalized response needs to drop below 0.52 after the third stimulus, and the response cannot drop below -0.1 (no strong inhibition).

Delayed: Peak happens later than the first stimulus, and the response for the second stimulus is <0.72, and the response cannot drop below -0.1 (no strong inhibition).

Slow: Peak happens before the fourth stimulus, and the response cannot drop below -0.1 (no strong inhibition).

Inhibition: The average response after the eighth stimulus is <0.

# CHAPTER 3

# Functional Mapping Combining volumetric fUSI and Optogenetic Stimulation

# 3.1 Abstract

Imaging large-scale circuit dynamics is crucial to understanding brain function, but most techniques are limited by a trade-off between the spatiotemporal resolution and field of view. To bridge this gap, volumetric functional ultrasound imaging (vfUSI), a platform for brain-wide imaging of hemodynamic activity at sub-millimmeter and sub-second resolutions, has been recently developed. To demonstrate the potential and high sensitivity of vfUSI for studying brain-wide networks, we imaged the brain of awake head-fixed mice during optogenetic activation of 3 different collicular cell-types. We were able to detect multiple areas across the entire brain modulated by each cell-type. The activated areas were consistent with the known downstream pathways of the colliculus. Additionally, compared to 2D fUSI, this approach reduced the acquisition time 6-8 fold, while increasing the number of brain volumes that could be obtained in each session 4-6 fold and reducing the number of stimulations needed by a factor of ~20. This allowed us to reveal that collicular narrow field neurons are highly sensitive to repeated stimulations.

# 3.2 Introduction

Functional ultrasound imaging has provided new opportunities to image simultaneously large portions of the brain of small mammals at high temporal (0.1s) and spatial resolutions (52.5 x 100 x 300 μm$^3$) (Macé *et al.*, 2018). Although other techniques offer either larger fields of view (fMRI), or better spatial resolution (Ca imaging), fUSI filled a gap between such techniques allowing imaging of multiple deep-brain areas at high spatio-temporal resolutions. However, until recently, fUSI was limited to a single cross-sectional imaging plane. To visualize activity of the entire brain, experimenters had to sequentially image multiple planes repeating stimulus presentations at each location making acquisitions long (3-4h) (Macé *et al.*, 2018; Sans-Dublanc *et al.*, 2021), and susceptible to habituation (Thompson and Spencer, 1966; Miller, Miller and Yuste, 2018; Tafreshiha *et al.*, 2021).

Similar to habituation triggered by repeated sensory stimulation (Simons-Weidenmaier *et al.*, 2006; Glanzman, 2009), optogenetic stimulation has been shown to modulate synaptic plasticity both *in vitro* (Morozov, Sukato and Ito, 2011; Pascoli, Turiault and Lüscher, 2012; Xiong and Jin, 2012), and *in vivo* (Adamantidis *et al.*, 2011; Huff *et al.*, 2013; Ramirez *et al.*, 2013; Tye *et al.*, 2013)*.* This poses the question of to what degree the maps of brain activity obtained in our previous opto-fUSI experiments are susceptible to adaptation. In such experiments, hundreds of stimulations are used to obtain a whole brain map of activated areas downstream of individual cell-types (Sans-Dublanc *et al.*, 2021). Therefore, if connectivity patterns were to change due to repeated stimulation, this would complicate the interpretability of the results obtained. For instance, some of the responding areas might have been recruited as a result of habituation. Others, that where not found to respond, might have responded initially, but decreased their excitability over time.

To overcome the long acquisitions and potential adaptation confounds, different groups have recently developed 2D-array transducers to acquire images simultaneously from multiple planes, and thus image activity from large volumes of the brain of small mammals (Rabut *et al.*, 2019; Brunner *et al.*, 2020). Specifically, volumetric functional ultrasound imaging (vfUSI) being developed at the Neuro-electronics research flanders institute (NERF), provides 3D imaging of a large part of the mouse brain (~600 mm$^3$) with a high spatial (220 x 280 x 175 μm$^3$) and temporal resolution (up to 6 Hz). vfUSI has a slightly slower temporal resolution when compared to the standard fUSI (vfUSI: up to 6Hz vs fUSI: up to 10 Hz) and slightly lower spatial resolution (vfUSI: 220 x 175 x 280 μm$^3$ vs fUSI: 52.5 x 100 x 300 μm$^3$). However, it could offer the perfect means to study brain-wide networks activated by specific cell-types reducing dramatically the acquisition times and the needed stimulus repetitions. Thus, to validate the potential of vfUSI in mapping neural networks downstream of specific cell-types, here we combined vfUSI with optogenetic activation of different genetically defined neural populations. Three distinct cell-types in the superior colliculus (SC), two of which had been studied with opto-fUSI (NTSR and Gad2), and an additional cell-type that was imaged for the first time (GRP). Finally, as a control, the downstream networks of thy1 expressing neurons of an adjacent area of the colliculus, the retrosplenial cortex, were also analyzed.

These experiments showed that vfUSI can be effectively combined with optogenetics. We showed that stimulation of NTSR, Gad2 and Thy1 neurons reliably evoked activity in multiple areas across the brain. Interestinlgy, stimulation of GRP expressing neurons of the SC led to a prolonged reduction in evoked hemodynamic responses along the activated circuit (↓50% in 15 trials). Thus, opto-vfUSI allows brain-wide mapping of multi-synaptic functional networks downstream of single cell-types

and provide the means to detect even those networks that are susceptible to connectivity changes induced by repeated stimulation.

This work was included in a series of proof-of-concept experiments to show the potential of vfUSI as a new tool for studying neural functions from a brain-wide perspective in awake and behaving animals (Brunner *et al.*, 2020).

# 3.3 Results

## 3.3.1 Opto-vfUSI detects brain-wide networks downstream of specific cell-types.

Similar to our opto-fUSI study (Sans-Dublanc *et al.*, 2021), we combined optogenetic stimulation with vfUSI (termed opto-vfUSI) to identify both target and circuit dynamic activation of specific cell types. In our previous study, in order to obtain maps of the neural networks activated by individual cell-types we averaged the activity evoked by 35-40 repetitions of the optogenetic stimulation on each of the 23 imaged planes (total of 800-900 stimulations). It took 3 to 5 sessions of 3-4h to obtain the data from each mouse. vfUSI simultaneously images the entire brain, reducing the number of stimulations and duration of session but has lower temporal and spatial resolution than 2D fUSI (Supplemental Figure 3.1). Thus, to assess whether opto-vfUSI also has the capability to detect brain-wide networks downstream of individual cell-types we performed the same craniotomies and chronic preparations as described in chapter 2. Briefly, we performed a large cranial window (AP +2 to −6.5; L +1.25 to −4.5) and implanted an optic fiber at the surface of the ipsilateral SC, near the midline, at an angle of 54°. We used a Cre-dependent ChR2-EYFP reporter line (Ai32) crossed with several transgenic lines expressing Cre in either excitatory narrow-field cells (Grp-Cre, n = 3), wide-field neurons (Ntsr-Cre, n = 2) or inhibitory horizontal cells (Gad2-Cre, n = 2). These cell-types have different projection patterns (Gale and Murphy, 2018; Hoy, Bishop and Niell, 2019) and in our previous study we showed that activating Ntsr and Gad2 neurons activate different but partially overlapping neural networks. Additionally, to assess the specificity of our approach, we used a Thy1-ChR2-YFP mouse line (n = 2) to activate Thy1 neurons of an adjacent area to the SC, the retrosplenial cortex. Thy1 is known to be expressed broadly in pyramidal neurons of the cortex and across the colliculus (Chen *et al.*, 2012).

To activate the different cell-types we used a low-intensity stimulation (40 pulses, 2 ms pulse width, 20 Hz, 0.3 mW mean power) that was repeated 50 times. During each stimulation the ipsilateral hemisphere to the stimulation was imaged for 35 seconds (14 s baseline, 2 s stimulus, and 19 s recovery). Each imaging session lasted 30 minutes and was repeated 2 to 3 times per mouse.

Activation of each cell-type elicited robust and reliable hemodynamic responses in the ipsilateral hemisphere in the activated region and in downstream areas distributed across the brain (Figure 3.1A). The hemodynamic responses to optogenetic stimulation measured both in cortical and subcortical regions fit well to the canonical hemodynamic response function observed during evoked responses to short stimuli, as previously observed in rats (Figure 3.1B; (Urban *et al.*, 2014)). Moreover, we noticed that onset time, peak amplitude, and post-stimulus decay obtained with opto-vfUSI (data not shown) are in the range of those measured with optogenetic fMRI (Desai *et al.*, 2011).
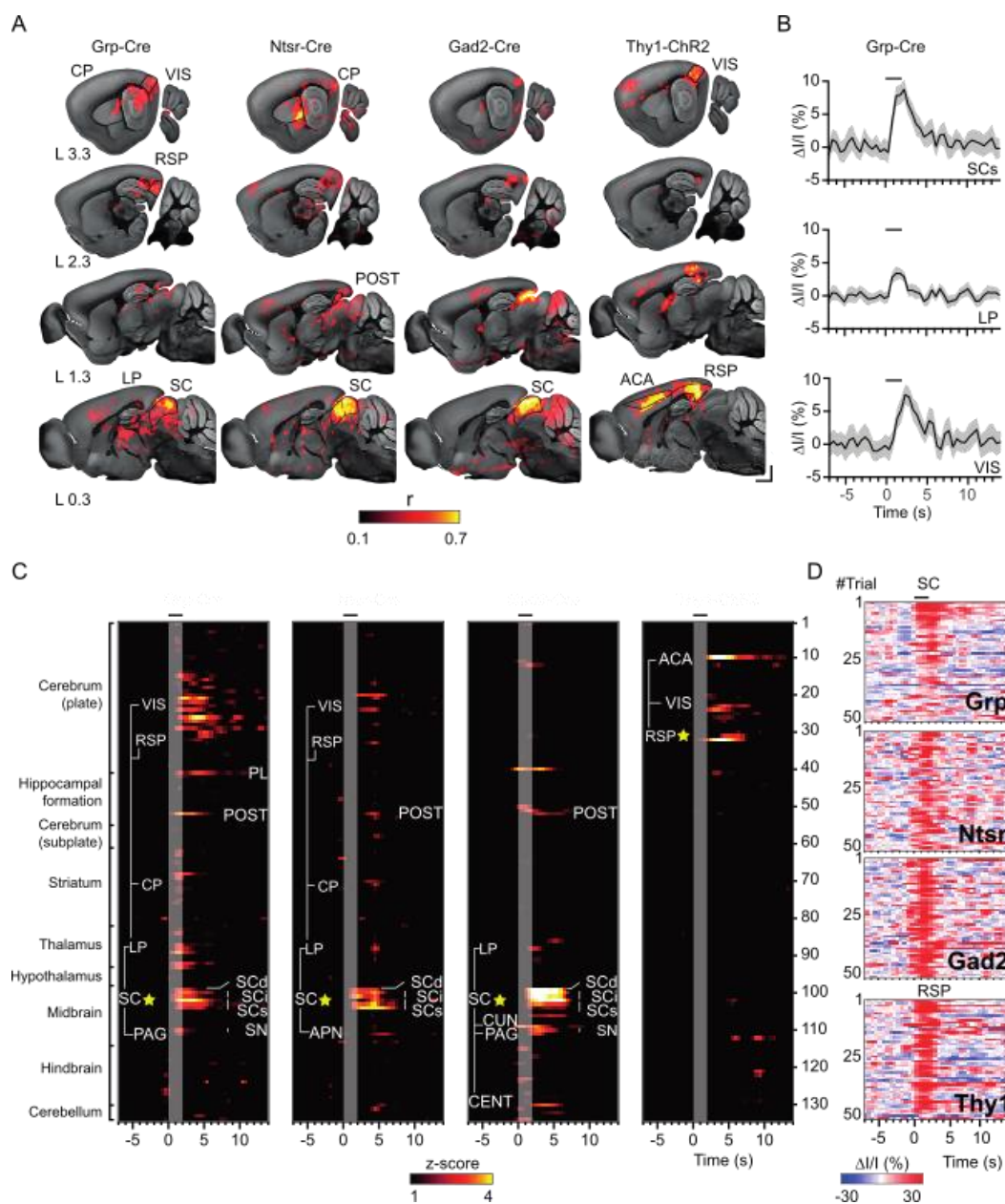
**Figure 3.1. Functional Mapping Combining vfUSI and Optogenetic Stimulation. A.** Example slices from the 3D correlation map presented in the sagittal view showing activated voxels during optogenetic stimulation in the Grp (n=3), Ntsr (n=2), Gad2 (n=2), and Thy1-ChR2 (n=2) lines (average of 50 trials for Ntsr, Gad, and Thy1-ChR2 and 15 trials for Grp). Brain regions significantly activated are outlined in black in the sagittal sections. Significant activation corresponds to r values >0.2. Scale bars, 1 mm. **B.** Average hemodynamic response curves of superior colliculus, LP, and VIS brain regions presented in (D). Black thick line represents the stimulus. Gray highlighted traces show the standard error of the mean. **C.** Average hemodynamic responses (Z score) of the 134 regions in the left hemisphere in response to optogenetic stimulation. Regions were ordered by major anatomical structures (Appendix 2; Table S1). A selected set of brain regions showing a statistically significant increase in hemodynamic activity are presented in white. White lines between areas indicate known anatomical projections. Black thick line shows the stimulus. Yellow stars indicate the location of the fiber-optic cannula. **D.** Trial-to-trial evolution of the hemodynamic response during optogenetic stimulation in each mouse line. Black thick line shows the stimulus.

A, anterior; P, posterior; D, dorsal; V, ventral; L, left; R, right. All color-coded correlation maps are superimposed on Allen Mouse Common Coordinate Framework histological slices and white-outlined segmented brain regions.

Consistent with our previous study, collicular cell-types activated overlapping networks (Figure 3.1C). For instance, stimulation of GRP, NTSR and Gad2 collicular neurons evoked responses in both

CHAPTER 3

intermediate (SCi) and deep layers (SCd) of the colliculus, the lateral posterior nucleus of the thalamus (LP) and postsubiculum (POST). Additionally, several differences were observed between the different cell-lines. For instance, the caudateputamen (CP), retrosplenial cortex (RSP) and visual cortex (VIS) were activated by both NTSR and GRP neurons, but not Gad2 collicular neurons. GRP and Gad2 neurons, but not NTSR neurons, activated the substantia nigra (SN), and NTSR, but not GRP or Gad2 neurons, activated the anterior pretectal areas (APN). Finally, Gad2 neurons where the cell-type that activated the greatest number of motor areas in the hindbrain and cerebellum and was the only cell-type to activate the primary motor cortex (MOp). Consistent with the known anatomical connectivity of RSP, activation of thy1 neurons in this area triggered hemodynamic responses in a subset of its downstream targets, such as the VIS and anterior cingulate cortex area (ACA; Mitchell et al., 2018).

Additionally, opto-vfUSI revealed that repeated optogenetic stimulation of the superior colliculus in the GRP mice led to a prolonged reduction in evoked hemodynamic response in the SC (50% in 15 trials; Figure 3.1D), which was not observed in any other lines. Similarly, across the brain, multiple regions of GRP mice exhibited a pronounced and rapid decay of the responses over repeated stimulations that was not present in the other mouse lines (Figure 3.2).



91
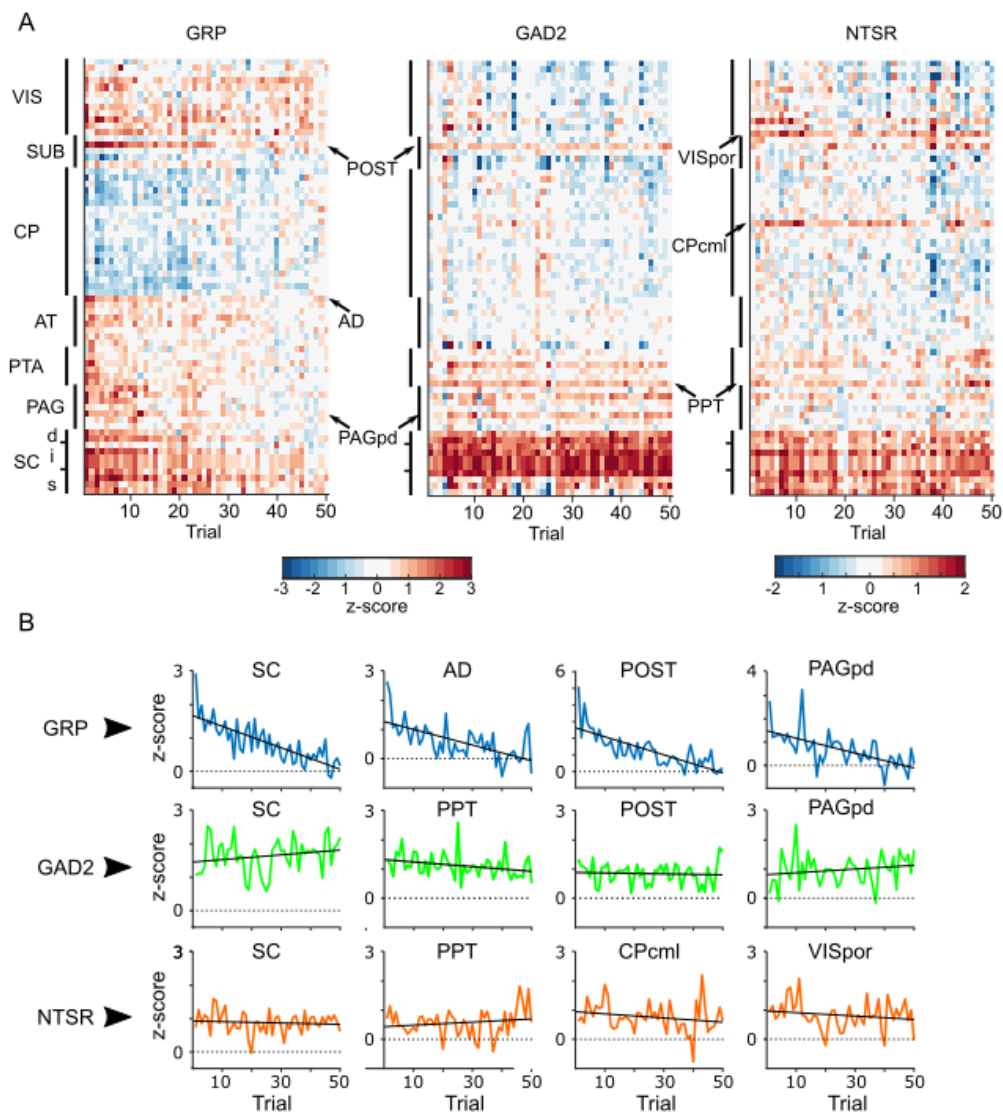
**Figure 3.2. Trial-by-trial responses to optogenetic stimulation across the brain. A.** Trial-by-trial responses of a selection of areas modulated by optogenetic activation of Grp+ collicular neurons, and the corresponding responses after optogenetic activation of Gad2+ and Ntsr+ neurons. Each row represents a segmented region or subregion. Vertical dark lines group related anatomical structures. Trial responses correspond to mean z-score during the 4 seconds that followed optogenetic stimulation. Grp (n=3), Ntsr (n=2), Gad2 (n=2). **B.** Example trial-by-trial responses of 4 different segmented areas for each mouse line. Black line corresponds to linear fit (y = α + βx).

VIS: Visual cortical areas; VISpor: Postrhinal visual area; SUB: Subicular region; POST: Postsubiculum. CP: Caudateputamen; CPcml: Caudateputamen, caudal medial lateral. AT: Anterior thalamic areas; AD: Anterodorsal thalamic nucleus. PTA: Pretectal areas; PPT: Posterior pretectal nucleus. PAG: Periaqueductal gray; PAGpd: Periaqueductal gray, posterior dorsal. SC: Superior colliculus (including subregions of the s: superficial layers, i: intermediate layers, and d: deep layers);

# 3.4 Discussion

In this study we combined optogenetics and volumetric fUSI to show that this technique has great potential for studying neural networks downstream of specific cell-types. Our results are consistent with our previous study (chapter 2), and the idea of different collicular cell-types activating different but partially overlapping neural pathways across the brain. This approach reduced the acquisition time 6-8 fold, while increasing the number of brain volumes that could be obtained in each session 4-6 fold and reducing the number of stimulations needed by a factor of ~20.

We were able to detect multiple areas downstream of each cell-type and these were consistent with the known anatomy. For instance, activation of NTSR+ neurons of the colliculus evoked activity in areas such as the lateral posterior nucleus of the thalamus (LP), visual cortical areas (VIS), caudateputamen (CP), postsubiculum and restrosplenial cortex (Figure 3.1C). in the SC, wide-field neurons (NTSR +) are a conserved cell-type that has been studied in multiple species (May, 2006; Basso, Bickford and Cang, 2021). These neurons have been shown to have a single projection to the thalamus, concretely, LP (May, 2006; Gale and Murphy, 2014). The LP in turn has ascending and descending projections to multiple areas such as primary and secondary visual cortical areas (VIS), the CP and lateral amygdala (Kamishina *et al.*, 2009; Wei *et al.*, 2015; Zhou *et al.*, 2018; Juavinett *et al.*, 2020). The visual cortex is reciprocally connected with the retrosplenial cortex, which in turn, provides input to subicular areas such as the postsubiculum (Mitchell *et al.*, 2018). Thus, the activity evoked by stimulating NTSR neurons of the colliculus can be readily explained with the known anatomical connections of the areas present within 3 synapses of the colliculus.

Interestingly, activation of GRP neurons activated a highly overlapping set of areas compared to the NTSR downstream pathways. GRP+ neurons are thought to correspond to the cell-type known as narrow-field cells (Gale and Murphy, 2014, 2018). GRP neurons have two main output targets, the intermediate layers of the colliculus (SCi), and the parabigeminal nucleus. Little is known about their function, but recent studies have shown that their activity, in conjunction with that of wide-field neurons, is necessary to provide critical visual aspects for hunting (Hoy, Bishop and Niell, 2019). GRP and NTSR neurons respond to different features of the visual space (Gale and Murphy, 2014), but in complex behaviors such as hunting, different types of information need to be used and coordinated before reaching the target. Consistent with this idea, SCi neurons project to the LP (Benavidez *et al.*, 2021), which might explain the high overlap between NTSR and GRP activated pathways, that could be used to coordinate the different visual aspects necessary to guide behaviors such as hunting. However, activation of GRP neurons also evoked activity in one of the major outputs of the SCi, the dorsal part of the periaqueductal gray (PAG), that has been shown to be important to trigger escape responses from threatening stimuli (Evans *et al.*, 2018). Thus, GRP neurons could be involved in

multiple complex behaviors and trigger different downstream pathways depending on the incoming visual information and its behavioral relevance using synaptic thresholds (Evans *et al.*, 2018).

It is of note that, as a proof-of-concept experiment, the number of animals used in this study was limited and thus it is to be expected that the overall sensitivity to identify areas activated by the different cell-types was reduced. Thus, if more animals were added, the total number and the specific areas activated by each cell-type could vary.

Importantly, repeated stimulation of GRP neurons induced a rapid decline in the evoked hemodynamic responses both in the SC, where the ChR2+ neurons were located, and its downstream targets, which was not observed in the other cell-lines (Figure 3.2). It has long been known that some neurons in the superior colliculus show signs of adaptation and habituation to repeated presentation of visual stimuli and others do not (Oyster and Takahashi, 1975; Boehnke *et al.*, 2007; Netser, Zahar and Gutfreund, 2011). Recent studies in mice have shown that a subpopulation of neurons in the superficial layers has fast adaptive properties that could be used to signal novel stimuli (Franceschi and Solomon, 2020). It is thus possible that GRP neurons are part of such adaptive populations and subject to local inhibitory suppression that would impede neural transmission upon successive stimulations. However, the relationship between neural activity and the corresponding vascular response is still poorly understood. Our knowledge is mostly limited to cortical cell-types, but we know it can vary depending on the cell-types involved (Uhlirova *et al.*, 2016; Iadecola, 2017). Additionally, a study by Anenberg and colleagues showed that optogenetic activation of GABAergic interneurons in the cortex could modulate blood flow even when neurotransmission was pharmacologically blocked (Anenberg *et al.*, 2015). This suggest that regulation of vascular flow can be performed independently of the local neural activity. Therefore, when measuring neural activity through hemodynamic changes, that can lead to misinterpretations if it is not accompanied with subsequent direct measures of local neural activity. As shown in previous experiments with standard fUSI (Urban *et al.*, 2014; Macé *et al.*, 2018), vfUSI can be combined with acute or chronic electrophysiological recordings to address this limitation and offering multimodal capabilities across various spatiotemporal scales.

All in all, these results show that vfUSI is sensitive enough to detect trial-by-trial hemodynamic variations and provides the means to identify neural networks sensitive to repeated stimulation. Also, by reducing the number of stimuli needed, it can mitigate the impact of adaptation and improve animal welfare by shortening experimental sessions. Even if the spatial resolution of vfUSI is lower ($\sim$250 $\mu m^3$) than 2D fUSI ($\sim$100 $\mu m^3$, see Figure S6 for comparison), the dramatic increase in efficiency, the ease of use, reliability, and affordability of vfUSI make it an excellent candidate for driving future brain-wide neuroimaging research.

**My contributions:** I conceptualized, designed, and performed opto-vfUSI experiments and some of the analysis (response decay). Gabriel Montaldo did major contributions to the analysis and wrote the section of the manuscript that include the results presented here.

# SUPPLEMENTAL MATERIALS OF CHAPTER 3

## Figure S3.1. Comparison between volumetric-fUSI and 2D-fUSI.



**2D-array transducer**
Coronal sections extracted from the 3D volume (300-μm step)

Number of elements: 1024
Pitch: 300x300 μm
Frequency: 15 MHz
Electronic focusing (no lens)
Voxel size: 220x280x175 μm³
Field of view: 9.6x9.6x10 mm³
Frame rate: 1.4-6 Hz
Acquistion time: 0.5s/full volume
3D image

**Linear transducer**
Motorized scan with a 300-μm step size

Number of elements: 128
Pitch: 100 μm
Frequency: 15 MHz
Focal distance: 8 mm (acoustic lens)
Voxel size: 100x300x100 μm³
Field of view: 12.8x0.3x10 mm³
Frame rate: 2-10 Hz
Step size: Motorized
Acquistion time: 30s/full scan
2D image

**Figure S3.1. Comparison between volumetric-fUSI and 2D-fUSI**. Comparison of ultrasound transducer specifications between the 2D array (vfUSI) used in this study and the linear transducer (2D-fUSI) used in previous studies (Macé et al., 2018; Urban et al., 2014) for the same mouse. A 3D Doppler image was acquired using the 2D-array transducer (middle), here presented in a coronal view with a 300-µm step size from anterior to posterior (top to bottom and left to right). A mechanical scan of the brain was performed using a 300-µm step size with the linear transducer array (bottom). Scale bars, 1 mm.

# MATERIALS AND METHODS

## Animals

All experimental procedures were approved by the Ethical Committee for Animal Experimentation (ECD) of the KU Leuven and followed the European Communities Guidelines on the Care and Use of Laboratory Animals (004–2014/EEC, 240–2013/EEC, 252–2015/EEC). Male and female adult (2-4 months old) transgenic mice were used in our experiments including, *Ai32 x Ntsr1-GN209Cre, Ai32 x Gad2Cre, Ai32 x GRP-KH288Cre and Thy1-ChR2-YFP. Ai32* (JAX: 012569) is a reporter line that expresses Channelrhodopsin2 in presence of Cre recombinase. *Ntsr1-GN209Cre* mice (GENSAT: 030780-UCD) express Cre recombinase in *Ntsr1-GN209* expressing neurons. *Gad2Cre* mice express Cre recombinase in *Gad2*-expressing neurons. *GRP-KH288Cre* mice (GENSAT: 037585-UCD) express Cre recombinase in *GRP*-expressing neurons. *Thy1-ChR2-YFP* mice (Thy1) (JAX: 007612) express Cre recombinase in *Thy1*-expressing neurons. Mice were kept on a 12:12 h light:dark cycle and sterilized food pellets and water were provided *ad libitum.* Experiments were performed during the light phase.

## Craniotomy and fiber implantation

Craniotomies and fiber implantation were performed as in the previous Chapter 2.

## Optogenetic stimulation

Optogenetic stimulation consisted of 40 pulses of 2 ms at 20 Hz using a 473-nm DPSS laser (R471003GX, Laserglow Technologies, USA). The average power at the tip of the fiber-optic was 0.3 mW (~1.5 mW/mm$^2$). For the non-implanted Thy1 mice, a cannula was acutely positioned with a micromanipulator on the retrosplenial cortex's surface at coordinates AP = 3.6-3.8 L = 0 V = -0.5 mm. Each trial consisted of 14 s baseline, 2 s stimulus, and 19 s recovery for a total of 50 images.

## 2D-array transducer

The transducer geometry is a 2D-array of 32 × 32 (1024) piezoelectric elements organized in 4 rectangular sectors of 8 × 32 (256) elements. Each element has a size of 0.3 × 0.3 mm$^2$, and the total size of the matrix is 9.8 × 9.8 mm$^2$. The transducer's central frequency is 14.5 MHz with a 70% bandwidth at 6 dB (ranging from 9.2 to 18.9 MHz). The piezoelectric elements can be excited with 20-Vpp bipolar impulsion at a pulse repetition rate of 20-kHz without risk of thermal damages. The transducer is wired directly to a multiplexer adaptor (UTA 1024-MUX Adaptor, Verasonics, USA). Such an adaptor allows the direct connection of the 2D-matrix transducer to the ultrasound electronics (Vantage 256, Verasonics, USA).

## Ultrasound sequence

Ultrasound sequences are characterized by five parameters as follow:

- *Sectors* Number of sectors used to image. Each sector covers a surface of 2.7 × 9.6 mm$^2$.

- *Averaging* Number of averaging used for a plane-wave acquisition.

- *Angles* Set of angles used for producing a compound image.

- *Ncompound* Number of compound images for producing a single Doppler image.

- *Frate* Final framerate of the vfUSI acquisition.

A plane-wave image is acquired by sequential emission in all the *Sectors* and averaged several times (*Averaging*). A set of tilted plane waves with n *Angles* are emitted to create a compound image. Finally, a single Doppler image is computed using a set of *Ncompound* images. Opto-vfUSI experiments used: *Sectors*: 2; *Averaging*: 3; *Angles*: −6, −4, −2, 0, 2, 4, 6; *Ncompound*: 200; *Frate: 0.7s.*

## Computing of the 3D Doppler images

The data was digitalized in 14 bits at a 60 MHz sampling rate, but the transducer used only half-band (8 to 25 MHz). Only two values over four were kept for all samples to reduce the bandwidth by a factor 2 (from 4.4 to 2.2 GB/s). The original data sampled at 60 MHz was recovered with an interpolation filter implemented directly at the GPU level. A double buffer was implemented inside the processing electronics allowing simultaneous recording of the vfUSI data in one buffer while the second is transferred to the workstation. Such architecture allows continuous data transfer at an average rate of 2.2 GB/s. The processing of compound images composed of up to 1400 plane-wave images is distributed in 4 GPUs and performed as followed:

## RF Data Interpolation

The subsampled data was interpolated to 60 MHz using a bandpass FIR filter of 41 coefficients between 25% and 75% of the band. A second low pass FIR filter of 25 coefficients at 25% of the band interpolated the sample to 240 MHz. This filter enabled a higher phase resolution during the beamforming procedure.

## Beamforming

The raw ultrasound data is composed of the 1400 plane-wave emissions that were beamformed using a classical delay-and-sum algorithm adapted to 3D plane-wave imaging. The seven plane-wave images of each compound image were added to obtain 200 compounded images. The beamforming voxel was $220 \times 280 \times 175$ µm$^3$ which was approximately the resolution of the image.

## Filtering

The beamforming output is a set of 200 3D compound images annotated: $s(x, y, z, t), \ t = 1 \dots 200$

These images are a superposition of signal coming from both the blood flow and the tissue:

$$s(x, y, z, t) = s_{Blood}(x, y, z, t) + s_{Tissue}(x, y, z, t).$$

As used in the opto-fUSI experiments, the blood component was separated from the tissue component by removing the first singular values of this data and applying a 20-Hz high-pass filter.

## Doppler Image

The Doppler image is obtained as the intensity of the blood signal: $I(x, y, z, t) = \sum_{t=1}^{n} s_{Blood}^2(x, y, z, t)$.

The 4 GPUs are parallelized with a delay of 1/4 of the computing period. Using this parallelization of acquisition, data transfer, and computing, an average bandwidth of 2.2 GB/s was obtained corresponding to a vfUSI period of 0.7 s for acquiring each image (0.5 s acquisition, 0.2 s dead time, 71% duty cycle).

# QUANTIFICATION AND STATISTICAL ANALYSIS

## Registration and segmentation

### Allen Mouse Common Coordinate Framework

The registration and segmentation are based on the Allen Mouse Common Coordinate Framework (CCFv3, Allen Brain API; brain-map.org/api/index.html). The digital atlas is segmented in 622 regions with a 25-µm$^3$ voxel resolution. Data size and processing time were reduced by subsampling the atlas to a 50-µm$^3$ resolution. It was then adapted to vfUSI by eliminating non-vascular regions (ventricles and white matter). Small areas (< 0.5 mm$^3$) below the technology resolution (220 × 280 × 175-µm$^3$) were pooled with neighboring anatomical regions. Olfactory bulbs and posterior cerebellum areas were excluded from the list because not imaged in this paper. The laminar organization of the cortex, hippocampus, and superior colliculus were removed, and layers were pooled. Regions larger than 15 mm$^3$ (e.g., caudoputamen) were anatomically subdivided. The list contains a set of 134 selected regions/hemisphere (including 220 individual regions in total; Appendix 2; Table S2).

### Registration

For each imaging session, a single Doppler volume was used for registration to the Allen Mouse Common Coordinate Framework. The imaged volume was interpolated to 50-µm$^3$ voxel size and semi-automatically registered using affine transforms performed through a graphical user interface. The transformation was saved and systematically applied to the dataset associated with the full experimental session. Following this procedure, all output data we used was registered to our custom Allen Mouse Common Coordinate Framework.

### Resolution

vfUSI resolution was measured by imaging a 150-µm bead (phantom) placed inside a block of 1.5% agarose. The bead was imaged with a 50 µm3 beamformed voxel. The Doppler image resolution was measured at 220 × 280 × 175 µm3, in the x, y, z dimensions, respectively.

## General processing of the segmented data

In visual and optogenetic experiments, several trials were repeated. The segmented data is represented as a 3D matrix $P(r, t, T)$ where r is the region, t the time and T the trial. 3D matrix data were computed as the mean value in each region $\bar{p}(r) = \langle P(r, t, T) \rangle_{t,T}$ and outliers eliminated if $P(r, t, T) > 1.4\bar{p}(r)$. Then, the 3D matrix was converted into a z-score as follow: $z(r, t) = p(r, t)/\sigma(r)$, with $\sigma(r) = \langle (p(r, t) - \bar{p}(r))^2 \rangle_t$.

Brain-wide variations in the vfUSI signal were filtered and removed from z(r,t) by subtracting the average intensity across the brain (s(t)) to the signal in each voxel (called "Filter Average").

## Correlation map

The median value was calculated in all trials of a session. The median value was preferred as compared to the mean value to remove outliers linked to animal movements. The correlation map was computed as the Pearson's correlation coefficient of the image signal in each voxel with a stimulus pattern defined as a binary function (1 if the stimulus is presented and 0 elsewhere) convoluted by a model of the hemodynamic response function (Friston, 1994) with the following parameters: delay of response 3 s, delay of undershoot 16 s, dispersion of response 1, dispersion of undershoot 1, ratio of response to undershoot 20, onset 0 s, length of kernel 16 s.(https://github.com/neurodebian/spm12/blob/master/spm_hrf.m).

$$r(x,y,z) = \frac{\sum_{i=1}^{N}(I(x,y,z,t_i) - \bar{I}(x,y,z))(A(t_i) - \bar{A})}{\sqrt{\sum_{i=1}^{N}(I(x,y,z,t_i) - \bar{I}(x,y,z))^2} \sqrt{\sum_{i=1}^{N}(A(t_i) - \bar{A})^2}}$$

where $\bar{I}(x,y,z) = \frac{1}{N}\sum_{i=1}^{N}I(x,y,z,t_i)$ and $\overline{A} = \frac{1}{N}\sum_{i=1}^{N}A(t_i)$. A median spatial filter of 3 x 3 pixels was applied to the final correlation map. The z-score value was then calculated using a Fisher's transform, $z = \frac{1}{2}\sqrt{N-3}.\ln\frac{1+r}{1-r}$. Only pixels with a z-score > 1.6 were considered significantly activated (p < 0.05 for a one-tailed test). Moreover, for removing the false-positive, we used a connectivity filter that kept only the activated regions with a minimal size of 9 connected voxels.

# CHAPTER 4

# Conclusions

# 4.1 Combining optogenetics and functional ultrasound imaging for studying brain-wide networks.

In this project, we have shown that both 2D and 3D vfUSI are excellent tools to study brain wide functional networks in awake, and even behaving animals. To understand how the activity of neurons across the entire brain interact to guide behavior, one needs both, local, single neuron, and global, brain-wide monitoring of neural activity. Despite the technological improvements of the last few decades, neural recordings are still relatively limited to both ends of the spectrum. Individual neurons, although in greater numbers every day, can still only be monitored in either a narrow column around an array of electrodes, or across wide fields but within 1 mm of the cortical surface. On the other side, global imaging using non-invasive imaging such as fMRI or PET are limited in spatial (typically millimeter) and temporal (seconds) resolutions and, in small mammals, are largely limited to anesthetized conditions. In recent years, fUSI has been developed to bring global and local monitoring closer together by providing whole brain imaging at both sub-millimeter and sub-second resolutions in fully awake and behaving animals. However, due to its recent development, there was little evidence to what degree fUSI can provide insights about the brain-wide networks that govern behavior. Thus here, we combined fUSI and vfUSI with optogenetic activation of genetically defined cell-types and identified dozens of areas across the brain that were modulated by the activation of specific collicular subpopulations.

Similar strategies have been used in the past. For instance, combining optogenetics with functional magnetic resonance imaging (ofMRI). ofMRI has shown that it can detect the impact of activating individual cell-types on the activity of global networks. For instance, it has shown that dopaminergic neurons in the midbrain modulate the activity of the striatum associated with reward-seeking behaviors (Ferenczi *et al.*, 2016; Lohani *et al.*, 2017). Other studies have shown that although the dorsal and ventral hippocampus have bidirectional connections between them, information flow goes mostly from dorsal to ventral hippocampus (Takata *et al.*, 2015), and despite their strong interconnectivity, each hippocampal subregion activates a different set of areas across the brain in a frequency dependent manner (Takata *et al.*, 2015; Weitz *et al.*, 2015). Additionally, ofMRI was used to show that PKCδ+ and SST+ neurons of the central amygdala mediate nociception through different functional subnetworks (Wank *et al.*, 2021).

Genetic manipulations are still limited in primates; thus cell-type specific studies are typically performed in rodents. Because of the small size of their brains, the low resolution of fMRI becomes a major limiting factor, since multiple small areas can be found inside each voxel. Additionally, the relatively low sensitivity of ofMRI requires that the optogenetic stimulations that are required in these experiments last tens of seconds (Lee *et al.*, 2010; Bernal-Casas *et al.*, 2017; Leong *et al.*, 2018, 2019). Long stimulations can add confounding effects such as temperature increases, that can activate neurons unspecifically (Christie *et al.*, 2013; Schmid *et al.*, 2017), or the effect of feedback inhibition on the stimulated circuits (Isaacson and Scanziani, 2011; Large *et al.*, 2016). By combining optogenetics with fUSI (both 2D and volumetric), we bring the study of global networks a step further by providing a platform that allows imaging of awake and behaving animals, detection of activity evoked by short (< 2 sec), low power stimulations (1-10 mW/mm$^2$), at a spatial resolution that allows the identification of >100 (3D vfUSI) to >200 (2D fUSI) individual areas across the entire mouse brain.

A critical aspect in the study of neural networks is understanding not only the areas involved but also the direction of the information flow. Both fMRI and fUSI rely on indirect measures of neural activity derived from the neurovascular coupling. The temporal scale in which hemodynamic changes follow neural activity is thought to be too slow to interpret the direction of information flow. However, a recent study showed that by analyzing the temporal dynamics of the hemodynamic responses one can also follow the information over multiple synapses (Jung *et al.*, 2021). In that study Jung and colleagues compared the networks activated by somatosensory forepaw stimulation and optogenetic activation of primary motor cortex. To do this, they used an fMRI machine with an ultrahigh magnetic field (15.2 Tesla) and imaged 3 planes of anesthetized mouse brains to obtain a high spatiotemporal resolution (Temporal: 250 ms. Spatial: $156 \times 156 \times 500$ μm$^3$). When analyzing both the activated areas and the temporal sequence of the activation, they found that both somatosensory and optogenetic stimulations evoked activity consistent with the known anatomy, and the temporal dynamics followed the canonical understanding of somatosensory information flow. Since both the described spatial and temporal resolutions are well within the capabilities of fUSI and vfUSI, this suggest that opto-fUSI could go beyond the description of global networks and provide information about the order of events. In our studies, we did not explore this line of analysis, but we did find that optogenetic activation of different collicular cell-types evoked different types of hemodynamic responses such as fast, slow, or delayed responses. If further explored, these results could still provide new insights about the relationships between the identified areas downstream of the different collicular cell-types.

It is important to note that combining optogenetics with fUSI or vfUSI has also inherent limitations. For instance, the temporal resolution of fUSI cannot differentiate between neural activity evoked by the optogenetic stimulation and the activity evoked by the resulting behavior itself. That implies that the networks identified with the opto-fUSI are likely to be an overestimation. In our studies when comparing immobilized and behaving animals we did not find large differences in the activated networks suggesting that the behavior itself was not a large contributor to the identified networks. On the other hand, current cell-types are likely to include multiple subpopulations that participate in different functions through specific subnetworks. Opto-fUSI was able to trigger one of such functions but activated all circuits downstream of that particular cell-type. Thus, it is unlikely that all the identified areas are necessary or relevant for that particular function. Future refinement of cell-type classifications through different genetic markers and stimulation of circuit-specific projections will provide more accurate descriptions of brain-wide networks governing specific behaviors.

All in all, the combination of optogenetics with fUSI/vfUSI fills a gap in the set of available tools to study neural networks in their full complexity and has all the necessary capabilities to become an indispensable tool for neuroscience in the coming years. Yet, in order to reach widespread use more work is needed to understand how well it represents the underlying neural activity or to what degree it correlates with other imaging techniques. A few studies, including this one, have shown a good correlation between local neural activity and the fUSI signal (Macé *et al.*, 2018; Boido *et al.*, 2019; Aydin *et al.*, 2020; Nunez-Elizalde *et al.*, 2021). However, neurovascular coupling is likely to vary depending on the recorded area and thus further electrophysiology studies should test how consistent across regions and experimental conditions is the relationship between the fUSI signal and local neural activity. For instance, CBV measurements during resting state periods can have spontaneous hemodynamic fluctuations in the absence of local neural activity (Winder *et al.*, 2017). In V1 there is evidence of a good relationship between spontaneous activity and hemodynamic fluctuations measured with fUSI (Nunez-Elizalde *et al.*, 2021). However, in this study they did not track the behavior of the mouse, which could be the main contributor to recorded neural activity and fUSI signal instead of being true spontaneous activity (Winder *et al.*, 2017). Finally, it would be interesting for future studies to combine fUSI with other modalities such as IEG analysis to assess the

mutual correspondence. This is only now possible due to the development of vfUSI that allows for short experiments that can be combined with the relevant time scales of IEG expression. Combining vfUSI and IEGs could bring insights into 1) the minimal cell populations necessary to observe a fUSI signal, 2) the cell-type origin and identity of the fUSI signals, 3) the regional specificity of IEG expression and 4) the temporal specificity and dynamics of IEG functional maps.

## 4.2 The superior colliculus, the old puppet master behind the cortical curtain?

The superior colliculus is an ancient brain structure and one of the most studied areas in the brain. Manipulation of collicular activity using electrical stimulation or pharmacological approaches, initially showed that the colliculus could trigger behaviors such as orienting, gnawing, escaping, freezing, or jumping (Redgrave *et al.*, 1981; McHaffie and Stein, 1982; Hikosaka and Wurtz, 1985; Sahibzada, Dean and Redgrave, 1986; Dean, Mitchell and Redgrave, 1988; Cowie and Robinson, 1994; DesJardin *et al.*, 2013). With the rise of optogenetics as a tool for dissecting the functions of genetically defined populations, a new battery of studies have provided evidence that individual cell-types of the colliculus mediate specific behaviors. Namely, PV+ neurons projecting to the parabigeminal nucleus have been associated with escape behavior (Shang *et al.*, 2015, 2018), projections to the pulvinar, presumably NTSR+, but also PV+, have been shown to trigger freezing (Wei *et al.*, 2015; Shang *et al.*, 2018), and both NTSR+ and GRP+ neurons have been shown to be necessary for hunting in mice (Hoy, Bishop and Niell, 2019). Consistent with these results, our results indicate that different cell-types in the superior colliculus promote different behaviors, including freezing-like behaviors (CamkII, NTSR), avoidance (PV), and orienting (Gad2).

Importantly, although a lot is known about collicular activity, function and even local connectivity, the downstream areas through which these cell-types mediate the different functions was largely unknown. In our studies, we have probed the extent of the functional networks downstream to specific cell-types of the colliculus, including CamKII+, NTSR+, PV+, Gad2+ and GRP+ neurons. We showed that each of these cell-types is functionally connected to extensive partially overlapping networks, across the entire brain. These networks were made up of dozens of brain regions, as many as 243 of the 264 regions we analyzed. Models of subcortical networks downstream of the colliculus had been previously hypothesized and shown to be anatomically possible, but rarely tested. These models, that have been proposed to mediate i.e. motor commands, or responses to visual threats, typically include less than twenty areas (McHaffie *et al.*, 2005; Redgrave *et al.*, 2010; Coe and Munoz, 2017; White *et al.*, 2017; Branco and Redgrave, 2020), and are based on both anatomical connections and the particular roles that have been previously ascribed to those areas. However, only the direct outputs of the superficial layers of the colliculus, and single mono-synaptic targets, such as the intermediate layers of the colliculus, already include more than 20 output areas (Benavidez *et al.*, 2021). This suggests that the areas potentially involved in any behavior is much higher than generally assumed.

Our results show that even the simplest behaviors could involve the coordination of several dozen areas across the entire brain. On the other hand, there are more functions ascribed to the colliculus than cell-types that have been described. For instance, beyond innate behaviors, which already outnumber cell-types (i.e., grawing, jumping, escape, freezing, orienting of eye, head, and body, and different aspects of hunting), the colliculus has been shown to be an active player in higher cognitive functions such as attention, computation of evidence, and choice (Bergeron, Matsuo and Guitton,

2003; Krauzlis and Carello, 2003; Lovejoy and Krauzlis, 2010; Duan, Erlich and Brody, 2015; L. Wang *et al.*, 2020; Duan *et al.*, 2021; Jun *et al.*, 2021). Therefore, it is also likely that: 1) the colliculus is populated by more cell-types that currently known and future refinement will further subdivide the current cell-lines and their projections; and 2) each cell-type might participate in multiple functions and activate different pathways depending on the context. This could be performed with the use of, for instance, synaptic thresholds already known to exist in the colliculus (Evans *et al.*, 2018). Since we observed overlap between the different networks, it is also possible that multiple cell-types act in coordination to guide behavior. Different combinations of activated cell-types could result in different evoked behaviors. Thus, in more natural conditions, it is possible that although each cell-type is functionally connected to dozens of areas, only subsets of neurons within those cell-types might be activated to mediate particular behaviors, and only a subset of the downstream pathways might be needed in each case.

Finally, in this project we have shown that the downstream pathways of the colliculus are far more extensive than previously thought. The colliculus was viewed for many years as to be mostly dedicated to drive gaze shifts using eye, head or body orienting movements towards or away from objects of interest (Dean, Redgrave and G. W. Westby, 1989; May, 2006; Gandhi and Katnani, 2011). Also, it was assumed that the decision centers were in the cortex, and so the colliculus was an executive area of cortically driven cognitive functions (Wurtz and Optican, 1994; Sparks, 1999; Hikosaka, Takikawa and Kawagoe, 2000; Schiller and Tehovnik, 2005). However, it has been recently recognized that the colliculus plays an active role in functions such as attention and decision making (Basso and May, 2017; Crapse, Lau and Basso, 2018). In our study, we have shown that the colliculus has the potential to influence the activity of neurons across virtually the entire brain, including the cortex. The increasing refinement of manipulation tools, together with the increasing evidence that mice can perform complex behaviors (Wang and Krauzlis, 2018), and even have neural signatures of conscious states (Gutierrez-Barragan *et al.*, 2022), opens the door to put the list of collicular functions to test. It is possible that soon, functions that are currently viewed as being governed by the cortex and its prefrontal areas, and thus under the control of our awareness, will have to be reimagined. In contrast, an increasing number of functions assigned as being inadvertently guided by the colliculus might challenge the core of our understanding of human behavior and free will.

# 4.3 Future perspectives

As it is often in life, answering a question is not the end of doubt, but the realization of new unknowns. In this project we have shown that combining optogenetics with functional ultrasound imaging can provide novel insights into the downstream networks of individual cell-types. However, our results also raised new questions. For instance, what are the functions of the plethora of areas activated by the different collicular cell-types? We found that the frequency used for stimulation had an effect in the resulting activity pattern of regions such as the visual cortex. So, what is the functional effect of such frequency changes? Could testing further frequencies and stimulation patterns provide insights about how individual cell-types can differently modulate global networks depending on their activity patterns? Which of the optogenetically identified pathways are activated by which visual stimuli? Does it depend on the behavioral relevance of the stimuli? What are the contributions of different cell-types to those visually driven neural networks? Current research in the lab has started to probe at some of those questions.

## 4.3.1 Visually evoked neural activity downstream of individual cell-types.

In this project, opto-fUSI allowed us to (1) demonstrate and detail the complexity of the functional outputs of the colliculus; (2) determine the degree to which component cell-types activate distinct downstream circuits and independently contribute to this complexity and (3) provide a first view of how the functional circuits link cell-types of the superior colliculus with the triggering of distinct behaviors. However, from this work it is unclear whether the optogenetic stimuli used are a reliable recapitulation of the neuronal activity evoked during natural visual stimuli. This is because, on the one hand, visual stimuli directly activate many, > 30, retino-recipient regions in mice, not just the superior colliculus (Morin and Studholme, 2014; Emily M. Martersteck *et al.*, 2017), and visual stimuli tend to activate more than one cell-type simultaneously within the retina and superior colliculus. This means activity measured across the brain during visual stimuli would be hard to trace back to specific cell-types within the superior colliculus. On the other side, optogenetics, powerful as it is as a tool for functional dissection of neural circuits, has a set of caveats (Guru *et al.*, 2015). For instance, optogenetic stimulation synchronizes the activity of all targeted cells. If there is information in the firing pattern of individual neurons, this might be lost in optogenetic stimulations. Also, optogenetic stimulations might induce firing that is outside the physiological range for that population, which could have effects on the spread of the signal across multiple synapses and provide incomplete or supernumerary results. Finally, current genetic tools are likely to target multiple subpopulations of neurons that do not necessarily act in coordination in physiological conditions.

To understand how natural visually evoked brain-wide neural activity relates to the artificially driven activity, we have started performing experiments explicitly designed to determine how individual pathways contribute to the brain-wide activity observed during the presentation of different visual stimuli. This project is set with two main goals; (1) use vfUSI to characterize the brain-wide networks activated by visual stimuli with different behavioral relevance (e.g., Figure 4.1); (2) combine vfUSI and chemogenetic silencing of individual cell-types to assess what is their contribution to the visually driven brain-wide activity.

These experiments will provide a better understanding of how the brain governs behavior, and will likely raise new unknowns that we cannot yet fathom.
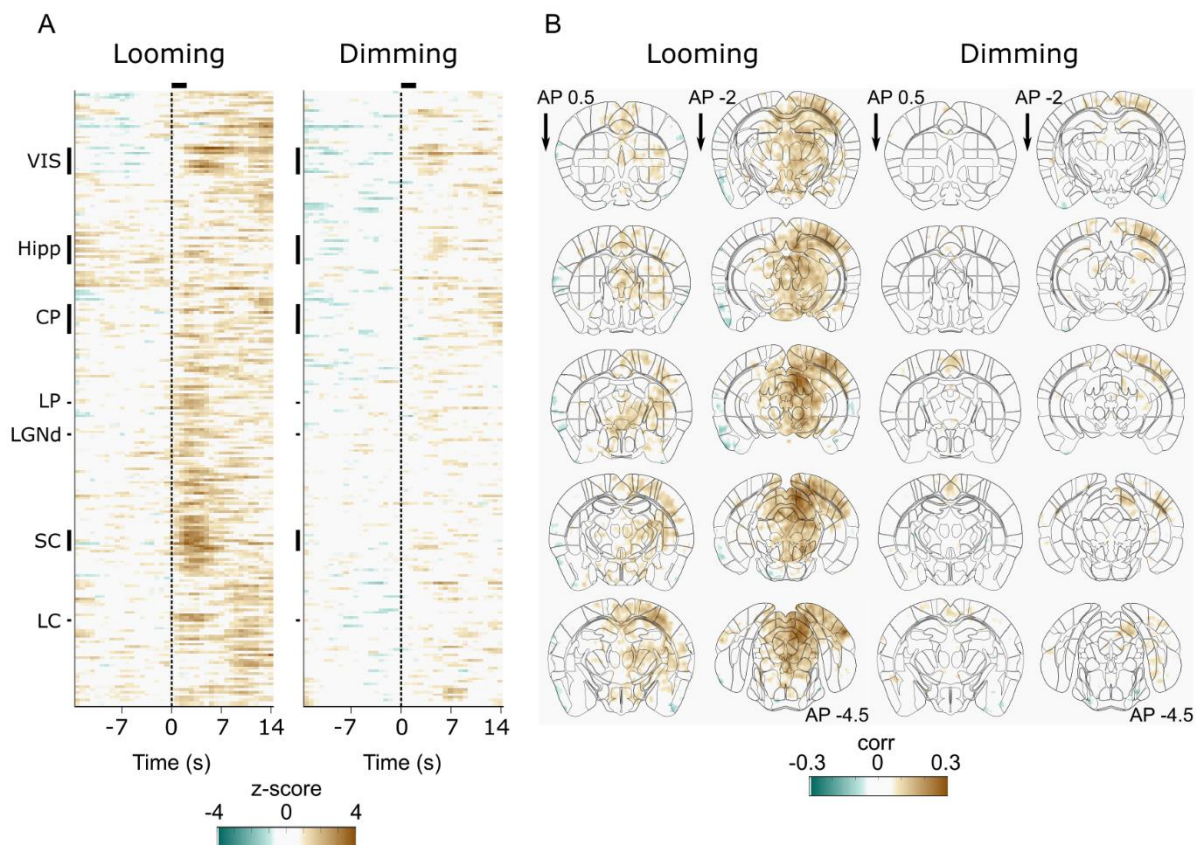
**4.1. Brain-wide responses to two different visual stimuli. A.** Evoked responses from 232 segmented areas to two visual stimuli with similar properties (e.g. contrast change, shape, duration). First, a looming stimulus (expanding black disc on gray background, 2-50 degrees in 300 ms), Left; and second, a Dimming stimulus (50 degrees disc that goes from gray to black in 300 ms on a gray background), Right. Stimuli were presented unilaterally and centered at 45° azimuth and 45° altitude. **B.** Pixel-pixel correlation maps of the brain wide responses to looming and dimming visual stimuli, shown in 10 example coronal slices spaced by 500 μm.

# Appendix 1: Chapter 2

## Table S2.1 | Brain regions

| | ABBREVIATION | FULL NAME |
|---|---|---|
| **CORTEX (CTX)** | ACAd | Anterior cingulate area, dorsal part |
| | ACAv | Anterior ci ... al part |
| | AIa | Agranular insular area |
| | AUDd | Dorsal auditory area |
| | AUDp | Primary auditory area |
| | AUDpo | Posterior auditory area |
| | AUDv | Ventral auditory area |
| | AON | Anterior olfactory nucleus |
| | APr | Area prostriata |
| | DP | Dorsal peduncular area |
| | ECT | Ectorhinal area |
| | GU | Gustatory areas |
| | ILA | Infralimbic area |
| | MOp | Primary motor area |
| | MOs | Secondary motor area |
| | NLOT | Nucleus of the lateral olfactory tract |
| | OLF | Olfactory areas |
| | ORB | Orbital area |
| | OT | Olfactory tubercle |
| | PERI | Perirhinal area |
| | PIR | Piriform area |
| | PL | Prelimbic area |
| | RSPagl | Restrosplenial area, lateral agranular part |
| | RSPd | Retrosplenial area, dorsal part |
| | RSPv | Retrosplenial area, ventral part |
| | SSp | Primary somatosensory area |
| | SSs | Supplemental somatosensory area |
| | TEa | Temporal association areas |
| | TR | Postpiriform transition area |
| | TT | Taenia tecta |
| | VISC | Visceral area |
| | VISa | Anterior visual area |
| | VISal | Anterolateral visual area |
| | VISam | Anteromedial visual area |
| | VISl | Lateral visual area |
| | VISli | Laterointermediate visual area |
| | VISp | Primary visual cortex |
| | VISpl | Posterolateral visual area |
| | VISpm | Posteromedial visual area |
| | VISpor | Postrhinal area |
| | VISrl | Rostrolateral visual area |
| | PA | Posterior amygdalar nucleus |
| | PAA | Piriform-amygdalar area |

**CORTEX SUBPLATE (sCTX)**

| | |
|---|---|
| MEA | Medial amygdalar nucleus |
| LA | Lateral amygdalar nucleus |
| IA | Intercalated amygdalar nucleus |
| COA | Cortical amygdalar area |
| AAA | Anterior amygdalar area |
| BLAd | Basolateral amygdalar nucleus, dorsal part |
| BLAv | Basolateral amygdalar nucleus, ventral part |
| BMA | Basomedial amygdalar nucleus |
| CEA | Central amygdalar nucleus |
| EP | Endopiriform nucleus |
| HATA | Hippocampo-amygdalar transition area |
| CA1d | CA1 subfield, dorsal part |
| CA1i | CA1 subfield, intermediate |
| CA1v | CA1 subfield, ventral |
| CA2d | CA2 subfield, dorsal part |
| CA2i | CA2 subfield, intermediate |
| CA2v | CA2 subfield, ventral |
| CA3d | CA3 subfield, dorsal part |
| CA3i | CA3 subfield, intermediate |
| CA3v | CA3 subfield, ventral |
| DGd | Dentate gyrus, dorsal part |
| DGi | Dentate gyrus, intermediate |
| DGv | Dentate gyrus, ventral |
| ENTl | Entorhinal area, lateral part |
| ENTm | Entorhinal area, medial part |
| PAR | Parasubiculum |
| POST | Postsubiculum |
| PRE | Presubiculum |
| ProS | Prosubiculum |
| SUB | Subiculum |
| ACB | Nucleus accumbens |
| BST | Bed nuclei of the stria terminalis |
| CLA | Claustrum |
| CPa | Caudoputamen, anterior ventral lateral |
| CPm | Caudoputamen, medial ventral medial |
| CPc | Caudoputamen, caudal ventral |
| FS | Fundus of striatum |
| GPe | Globus pallidus, external segment |
| GPi | Globus pallidus, internal segment |
| LSd | Lateral septal nucleus, dorsal |
| LSv | Lateral septal nucleus, ventral part |
| MS | Medial septal nucleus |
| MA | Magnocellular nucleus |
| NDB | Diagonal band nucleus |
| PAL | Pallidum |
| SF | Septofimbrial nucleus |
| SI | Substantia innominata |

| | | |
|---|---|---|
| STR | Striatum unassigned |
| TRS | Triangular nucleus of septum |

| | | |
|---|---|---|
| AD | Anterodorsal nucleus |
| AM | Anteromedial nucleus |
| AV | Anteroventral nucleus of thalamus |
| CL | Central lateral nucleus of the thalamus |
| CM | Central medial nucleus of the thalamus |
| Eth | Ethmoid nucleus of the thalamus |
| IAt | Interanteromedial nucleus of the thalamus |
| IGL | Intergeniculate leaflet of the lateral geniculate complex |
| IMD | Intermediodorsal nucleus of the thalamus |
| LD | Lateral dorsal nucleus of thalamus |
| LGd | Dorsal part of the lateral geniculate complex |
| LGv | Ventral part of the lateral geniculate complex |
| LPcl | Lateral posterior nucleus of the thalamus, caudal lateral |
| LPam | Lateral posterior nucleus of the thalamus, anterior medial |
| MD | Mediodorsal nucleus of thalamus |
| MG | Medial geniculate complex |
| PCN | Paracentral nucleus |
| PF | Parafascicular nucleus |
| PO | Posterior complex of the thalamus |
| PPnT | Posterior Paralaminar nuclei of the thalamus |
| PP | Peripeduncular nucleus |
| PR | Perireunensis nucleus |
| PT | Parataenial nucleus |
| PVT | Paraventricular nucleus of the thalamus |
| RE | Nucleus of reuniens |
| RH | Rhomboid nucleus |
| RT | Reticular nucleus of the thalamus |
| SMT | Submedial nucleus of the thalamus |
| SPA | Subparafascicular area |
| SPFm | Subparafascicular nucleus, magnocellular part |
| VAL | Ventral anterior-lateral complex of the thalamus |
| VM | Ventral medial nucleus of the thalamus |
| VPL | Ventral posterolateral nucleus of the thalamus |
| VPM | Ventral posteromedial nucleus of the thalamus |
| VPMpc | Ventral posteromedial nucleus of the thalamus, parvicellular part |
| Xi | Xiphoid thalamic nucleus |

THALAMUS (TH)

| | | |
|---|---|---|
| AHN | Anterior hypothalamic nucleus |
| AVP | Anteroventral preoptic nucleus |
| AVPV | Anteroventral periventricular nucleus |
| DMH | Dorsomedial nucleus of the hypothalamus |
| FF | Fields of Forel |
| LHA | Lateral hypothalamic area |
| LM | Lateral mammillary nucleus |
| LPO | Lateral preoptic area |
| ME | Median eminence |

| | | |
|---|---|---|
| **HYPOTHALAMUS (HYP)** | PON | Median preoptic nucleus |
| | Mmm | Medial mammillary nuclei |
| | PH | Posterior hypothalamic nucleus |
| | PMH | Ventral premammillary nucleus |
| | PS | Parastrial nucleus |
| | STN | Subthalamic nucleus |
| | PVH | Paraventricular hypothalamic nucleus |
| | PVHd | Paraventricular hypothalamic nucleus, descending division |
| | PeVH | Arcuate hypothalamic nucleus |
| | PeF | Perifornical nucleus |
| | RCH | Retrochiasmatic area |
| | SO | Supraoptic nucleus |
| | SUM | Supramammillary nucleus |
| | TM | Tuberomammillary nucleus |
| | TU | Tuberal nucleus |
| | VL/VMPO | Ventrolateral and ventromedial preoptic nucleus |
| | VMH | Ventromedial hypothalamic nucleus |
| | ZI | Zona incerta |
| **MIDBRAIN (MB)** | HBn | Medial habenula |
| | RPF | Retroparafascicular nucleus |
| | APN | Anterior pretectal nucleus |
| | PTA | Posterior pretectal areas |
| | NPC | Nucleus of the posterior commissure |
| | PRC/SCO | Pre- and Sub-commissural organ |
| | PPN | Pedunculopontine nucleus |
| | CUN | Cuneiform nucleus |
| | AT/VTN | Anterior and Ventral tegmental nucleus |
| | CLI | Central linear nucleus raphe |
| | DR | Dorsal nucleus raphe |
| | IC | Inferior colliculus |
| | IF | Interfascicular nucleus raphe |
| | IPN | Interpeduncular nucleus |
| | MRNal | Midbrain reticular nucleus, anterior lateral |
| | MRNam | Midbrain reticular nucleus, anterior medial |
| | MRNpl | Midbrain reticular nucleus, posterior lateral |
| | MRNpm | Midbrain reticular nucleus, posterior medial |
| | Tn | Lateral terminal nucleus of the accessory optic tract |
| | NB | Nucleus of the brachium of the inferior colliculus |
| | EW/MA3/ND | accesory oculomotor nuclei |
| | PAGa | Periaqueductal gray, anterior part |
| | PAGd | Periaqueductal gray, posterior dorsal |
| | PAGv | Periaqueductal gray, posterior ventral |
| | PAGl | Periaqueductal gray, medial lateral |
| | PBG | Parabigeminal nucleus |
| | Pa4/IV | Trochlear nucleus and Paratrochlear |
| | RL | Rostral linear nucleus raphe |
| | RN | Red nucleus |

| | | |
|---|---|---|
| | RR | Midbrain reticular nucleus, retrorubral area |
| | SAG | Nucleus sagulum |
| | SCd | Superior colliculus, deep layers, |
| | Sci | Superior colliculus, intermediate layers |
| | SCs | Superior colliculus, superficial layers |
| | SN | Substantia nigra |
| | VTA | Ventral tegmental area |
| **HINDBRAIN (HB)** | AMB | Nucleus ambiguus |
| | AP | Area postrema |
| | CS | Superior central nucleus raphe |
| | CU/GR | Cuneate and Gracile nucleus |
| | DCO | Dorsal cochlear nucleus |
| | DMX | Dorsal motor nucleus of the vagus nerve |
| | DTN/PDTg | Dorsal and Posterodorsal tegmental nucleus |
| | ECU | External cuneate nucleus |
| | GRN | Gigantocellular reticular nucleus |
| | I5/PC5 | Intertrigeminal and Parvicellular motor 5 nucleus |
| | V | Motor nucleus of trigeminal |
| | IO | Inferior olivary complex |
| | IRN | Intermediate reticular nucleus |
| | KF | Koelliker-Fuse subnucleus |
| | LAC | Lateral vestibular nucleus |
| | LC/B | Barrington's nucleus, Sublaterodorsal nucleus, subceruleus and Locus ceruleus |
| | LDT | Laterodorsal tegmental nucleus |
| | LIN | Linear nucleus of the medulla |
| | LRN | Lateral reticular nucleus |
| | MARN | Magnocellular reticular nucleus |
| | MDRN | Medullary reticular nucleus |
| | MV | Medial vestibular nucleus |
| | NI | Nucleus incertus |
| | NLL | Nucleus of the lateral lemniscus |
| | NR/XII | Nucleus of Roller and Hypoglossal nucleus |
| | NTB | Nucleus of the trapezoid body |
| | NTS/PAS | Nucleus of the solitary tract and Parasolitary nucleus |
| | P5/Acs5 | Peritrigeminal zone and Accessory trigeminal nucleus |
| | PARN | Parvicellular reticular nucleus |
| | PB | Parabrachial nucleus |
| | PCG/SG | Pontine central gray and Supragenual nucleus |
| | PG | Pontine gray |
| | PGRN | Paragigantocellular reticular nucleus |
| | POR | Superior olivary complex, periolivary region |
| | PPY | Parapyramidal nucleus |
| | PRNc | Pontine reticular nucleus, caudal |
| | PRNr | Pontine reticular nucleus, rostral |
| | PRP | Nucleus prepositus |
| | PSV | Principal sensory nucleus of the trigeminal |
| | Pa5 | Paratrigeminal nucleus |

| | | |
|---|---|---|
| | RM/RO | Nucleus raphe magnus and obscurus |
| | RPA | Nucleus raphe pallidus |
| | RPO | Nucleus raphe pontis |
| | SOC | Superior olivary complex, medial part |
| | SPIV | Spinal vestibular nucleus |
| | SPVC | Spinal nucleus of the trigeminal, caudal part |
| | SPVI | Spinal nucleus of the trigeminal, interpolar part |
| | SPVO | Spinal nucleus of the trigeminal, oral part |
| | SUT | Supratrigeminal nucleus |
| | SUV | Superior vestibular nucleus |
| | TRN | Tegmental reticular nucleus |
| | VCO | Ventral cochlear nucleus |
| | VII | Facial motor nucleus |
| | x | Nucleus x |
| **CEREBELLUM (CB)** | CB | Cerebellum unassigned |
| | ANcr1 | Crus 1 |
| | ANcr2 | Crus 2 |
| | CENT2 | Lobule II |
| | CENT3 | Lobule III |
| | COPY | Copula pyramidis |
| | DEC | Declive (VI) |
| | DN | Dentate nucleus |
| | FL | Flocculus |
| | FOTU | Folium-tuber vermis (VII) |
| | IP | Interposed nucleus |
| | LING | Lingula (I) |
| | NOD | Nodulus (X) |
| | PFL | Paraflocculus |
| | PRM | Paramedian lobule |
| | PYR | Pyramus (VIII) |
| | SIM | Simple lobule |
| | UVU | Uvula (IX) |
| | VeCB/ICB | Vestibulocerebellar and Infracerebellar nucleus |

## Table S2.2 | Responsive areas - high-frequency stimulation

| Brain Areas | Early (0 – 2 s) | | | | Late (3 – 8 s) | | | |
|---|---|---|---|---|---|---|---|---|
| | CAMKII | NTSR | PV | GAD2 | CAMKII | NTSR | PV | GAD2 |
| ACAd | 1 | 1 | 1 | 0 | 1 | 0 | -1 | 0 |
| ACAv | 1 | 0 | 0 | -1 | 1 | 0 | 0 | 0 |
| Ala | 1 | 1 | 1 | 0 | 1 | -1 | -1 | 0 |
| AUDd | 1 | 0 | 1 | 0 | 1 | 0 | 0 | 0 |
| AUDp | 1 | 0 | 1 | 0 | 1 | 0 | 0 | 0 |
| AUDpo | 1 | 0 | 1 | 0 | 1 | -1 | 0 | 0 |
| AUDv | 1 | 0 | 1 | 0 | 1 | 0 | -1 | 0 |
| AON | 1 | 0 | 0 | 0 | 1 | 0 | 0 | 0 |
| APr | 1 | 0 | 0 | 0 | 1 | 0 | 0 | 0 |
| DP | 0 | 0 | 0 | 0 | 0 | 1 | 1 | 1 |
| ECT | 1 | 0 | 1 | 0 | 1 | -1 | 0 | 0 |
| GU | 1 | -1 | 1 | 0 | 1 | 0 | -1 | 0 |
| ILA | 1 | 0 | 1 | 0 | 1 | 0 | 0 | 0 |
| MOp | 1 | 1 | 0 | 0 | 1 | 0 | -1 | -1 |
| MOs | 1 | 0 | 1 | 0 | 1 | -1 | -1 | 0 |
| NLOT | 0 | 0 | 0 | 0 | 0 | 0 | 1 | 0 |
| OLF | 0 | 0 | 0 | 0 | 0 | 0 | 1 | 0 |
| ORB | 1 | 1 | 1 | 0 | 1 | -1 | -1 | 0 |
| OT | -1 | 0 | 1 | 0 | -1 | 1 | 1 | 0 |
| PERI | 1 | 0 | 1 | 0 | 1 | 0 | 0 | 0 |
| PIR | -1 | 0 | 0 | 0 | -1 | 0 | 1 | 0 |
| PL | 1 | 1 | 1 | 0 | 1 | -1 | 0 | 0 |
| RSPagl | 1 | 0 | 0 | 0 | 1 | 0 | 0 | 0 |
| RSPd | 0 | 0 | 0 | 0 | 0 | 0 | 0 | 0 |
| RSPv | 0 | 0 | -1 | 0 | 0 | -1 | 0 | 0 |
| SSp | 1 | 1 | 0 | 0 | 1 | 0 | -1 | 0 |
| SSs | 1 | 0 | 0 | 0 | 1 | 0 | 0 | 0 |
| TEa | 1 | 0 | 1 | 0 | 1 | -1 | 0 | 0 |
| TR | 0 | 0 | -1 | 0 | 0 | 0 | 0 | 0 |
| TT | -1 | 0 | 0 | 0 | -1 | 0 | 1 | 0 |
| VISC | 1 | 0 | 1 | 0 | 1 | 0 | 0 | 0 |
| VISa | 0 | 0 | 0 | 0 | 0 | 0 | 0 | 0 |
| VISal | 1 | 0 | 1 | 0 | 1 | 0 | 0 | 0 |
| VISam | 1 | 0 | 0 | 0 | 1 | 0 | 0 | 0 |
| VISl | 1 | 1 | 1 | 0 | 1 | 0 | 0 | 0 |
| VISli | 1 | 1 | 1 | 0 | 1 | 0 | -1 | 0 |
| VISp | 1 | 1 | 0 | 0 | 1 | -1 | 0 | 0 |
| VISpl | 1 | 1 | 1 | 0 | 1 | -1 | 0 | -1 |
| VISpm | 1 | 0 | 0 | 0 | 1 | 0 | 0 | 0 |
| VISpor | 1 | 1 | 1 | 0 | 1 | -1 | 1 | 0 |
| VISrl | 0 | 0 | 1 | 0 | 0 | 0 | 0 | 0 |
| PA | 0 | 1 | 0 | 0 | 0 | 0 | 0 | 0 |
| PAA | -1 | 1 | 0 | 0 | -1 | 0 | 1 | 0 |
| MEA | 0 | -1 | -1 | 0 | 0 | 0 | 1 | 0 |
| LA | 1 | 1 | 1 | 0 | 1 | 0 | 0 | 0 |
| IA | 0 | 0 | 0 | 0 | 0 | 0 | 0 | 0 |
| COA | 0 | 1 | 0 | 0 | 0 | 1 | 1 | 0 |
| AAA | 0 | 0 | 0 | 0 | 0 | 0 | 1 | 0 |
| BLAd | 1 | 0 | 0 | 0 | 1 | 0 | 0 | 0 |

| | | | | | | | | |
|------|----|----|----|----|----|----|----|----|
| BLAv | 0 | 0 | 0 | 0 | 0 | 0 | 0 | 0 |
| BMA | 0 | 1 | 0 | 0 | 0 | 0 | 0 | 0 |
| CEA | 1 | 1 | 0 | 0 | 1 | -1 | 0 | 0 |
| EP | 1 | 1 | 0 | 0 | 1 | -1 | -1 | 0 |
| HATA | 1 | 0 | 0 | 0 | 1 | 0 | 0 | 0 |
| CA1d | 1 | 0 | 0 | 0 | 1 | -1 | -1 | -1 |
| CA1i | 1 | 1 | 1 | 0 | 1 | 0 | 0 | 0 |
| CA1v | 1 | 0 | 1 | 0 | 1 | -1 | 0 | 0 |
| CA2d | 1 | -1 | 1 | 0 | 1 | -1 | -1 | 0 |
| CA2i | 1 | 1 | 1 | 0 | 1 | 0 | 0 | 0 |
| CA2v | 1 | 0 | 0 | 0 | 1 | 0 | 0 | 0 |
| CA3d | 1 | 0 | 0 | 0 | 1 | -1 | 0 | 0 |
| CA3i | 1 | 1 | 1 | 0 | 1 | -1 | 0 | 0 |
| CA3v | 1 | 0 | 0 | 0 | 1 | 0 | 0 | 0 |
| DGd | 1 | 0 | 1 | 1 | 1 | 0 | 0 | 0 |
| DGi | 1 | 0 | 0 | 0 | 1 | 0 | 0 | 0 |
| DGv | -1 | -1 | -1 | -1 | -1 | 0 | 1 | 0 |
| ENTl | 1 | 1 | 1 | 0 | 1 | 0 | 0 | 0 |
| ENTm | 1 | 1 | 0 | 0 | 1 | 0 | 0 | 0 |
| PAR | 0 | 0 | 0 | 0 | 0 | 0 | 1 | 0 |
| POST | 1 | 0 | 0 | 0 | 1 | 1 | 0 | 1 |
| PRE | 1 | 0 | -1 | -1 | 1 | 1 | 1 | 1 |
| ProS | 1 | 1 | 1 | 0 | 1 | -1 | -1 | -1 |
| SUB | 1 | 1 | 0 | 0 | 1 | -1 | 0 | 0 |
| ACB | 1 | 0 | 1 | 0 | 1 | 0 | 0 | -1 |
| BST | 1 | 0 | 1 | 0 | 1 | 0 | -1 | 0 |
| CLA | 1 | -1 | 1 | 0 | 1 | -1 | -1 | 0 |
| CPa | 1 | 1 | 1 | 0 | 1 | 0 | -1 | 0 |
| CPm | 1 | 0 | 1 | 0 | 1 | -1 | -1 | 0 |
| CPc | 1 | 1 | 1 | 0 | 1 | 0 | -1 | 0 |
| FS | -1 | -1 | -1 | 0 | -1 | 0 | 1 | 0 |
| GPe | 1 | 1 | 1 | 0 | 1 | -1 | -1 | 0 |
| GPi | 1 | 1 | 1 | 1 | 1 | 0 | 0 | 0 |
| LSd | 1 | 0 | 1 | 0 | 1 | 0 | -1 | 0 |
| LSv | 1 | 0 | 0 | 1 | 1 | 0 | 0 | 0 |
| MS | 1 | 0 | 1 | 0 | 1 | 0 | -1 | 0 |
| MA | 0 | 0 | 0 | 0 | 0 | 0 | 1 | 0 |
| NDB | 1 | 0 | 0 | 0 | 1 | 0 | 1 | 0 |
| PAL | 1 | 0 | 0 | 0 | 1 | 0 | 1 | 0 |
| SF | 1 | 0 | 0 | 0 | 1 | 1 | 0 | 0 |
| SI | 1 | 0 | 0 | 0 | 1 | 0 | 1 | 0 |
| STR | 1 | 1 | 0 | 0 | 1 | 0 | 1 | 0 |
| TRS | 0 | 0 | 0 | 0 | 0 | 0 | 0 | 0 |
| AD | 1 | 0 | 0 | 0 | 1 | 0 | 0 | 0 |
| AM | 1 | 1 | 1 | 0 | 1 | -1 | -1 | 0 |
| AV | 1 | 1 | 1 | 0 | 1 | 0 | -1 | 0 |
| CL | 0 | 1 | 0 | 0 | 0 | 0 | -1 | 0 |
| CM | 1 | 0 | 0 | 0 | 1 | 0 | 0 | 0 |
| Eth | 0 | 1 | 0 | 0 | 0 | 0 | 0 | 0 |
| IAt | 1 | 0 | 1 | 0 | 1 | 1 | -1 | 0 |
| IGL | 1 | 1 | 1 | 1 | 1 | -1 | 1 | 1 |
| IMD | 0 | 0 | 0 | 0 | 0 | 0 | 0 | 0 |
| LD | 1 | 1 | 0 | 0 | 1 | 0 | 0 | 0 |
| LGd | 1 | 1 | 1 | 1 | 1 | -1 | 0 | 1 |

| | | | | | | | | |
|---|---|---|---|---|---|---|---|---|
| LGv | 1 | 1 | 1 | 1 | 1 | -1 | 0 | 1 |
| LPcl | 1 | 1 | 0 | 0 | 1 | -1 | 0 | 0 |
| LPam | 1 | 1 | 0 | 0 | 1 | 0 | 1 | 0 |
| MD | 0 | 0 | 1 | 0 | 0 | 0 | 0 | 0 |
| MG | 1 | 1 | 1 | 1 | 1 | -1 | 0 | 0 |
| PCN | 1 | 0 | 0 | 0 | 1 | 0 | 0 | 0 |
| PF | 1 | 1 | 0 | 0 | 1 | 0 | -1 | 0 |
| PO | 1 | 1 | 0 | 0 | 1 | 0 | 0 | 0 |
| PPnT | 1 | 1 | 1 | 1 | 1 | -1 | 0 | 0 |
| PP | 1 | 1 | 1 | 0 | 1 | 0 | 0 | 0 |
| PR | 1 | 1 | 0 | 0 | 1 | 0 | 0 | 0 |
| PT | 1 | 0 | 1 | 0 | 1 | 0 | 0 | 0 |
| PVT | 1 | 1 | 0 | 0 | 1 | 0 | 0 | 0 |
| RE | 1 | 1 | 1 | 0 | 1 | 0 | 0 | 0 |
| RH | 0 | 0 | 0 | 0 | 0 | 0 | 0 | 0 |
| RT | 1 | 1 | 1 | 0 | 1 | -1 | 0 | -1 |
| SMT | 1 | 1 | 1 | 0 | 1 | 0 | 0 | 0 |
| SPA | 1 | 1 | 0 | 0 | 1 | 0 | 0 | 0 |
| SPFm | 1 | 1 | 0 | 0 | 1 | 0 | 0 | 0 |
| VAL | 1 | 1 | 1 | 0 | 1 | 0 | 0 | 0 |
| VM | 1 | 1 | 1 | 0 | 1 | -1 | 0 | 0 |
| VPL | 1 | 1 | 1 | 0 | 1 | -1 | 0 | -1 |
| VPM | 1 | 1 | 1 | 0 | 1 | -1 | -1 | 0 |
| VPMpc | 1 | 1 | 0 | 0 | 1 | -1 | 0 | 1 |
| Xi | 1 | 1 | 0 | 0 | 1 | 0 | -1 | 0 |
| AHN | 1 | 0 | 1 | 0 | 1 | 1 | 0 | 0 |
| AVP | 1 | 0 | 0 | 0 | 1 | 0 | 0 | 0 |
| AVPV | 0 | -1 | 0 | 0 | 0 | 1 | 0 | 0 |
| DMH | 0 | 0 | 0 | 0 | 0 | 1 | 0 | 0 |
| FF | 1 | 1 | 1 | 0 | 1 | 0 | -1 | 0 |
| LHA | 1 | 1 | 1 | 0 | 1 | 0 | 0 | 0 |
| LM | 1 | 0 | 0 | 0 | 1 | 0 | 0 | 0 |
| LPO | 1 | 0 | 0 | 1 | 1 | 0 | 0 | 1 |
| ME | 0 | 0 | 0 | 0 | 0 | 1 | 0 | 0 |
| PON | 1 | 0 | 1 | 0 | 1 | 0 | 0 | 1 |
| Mmm | 1 | 0 | 0 | 0 | 1 | 0 | 0 | 1 |
| PH | 1 | 1 | 0 | 0 | 1 | 0 | 0 | 0 |
| PMH | 0 | 0 | 0 | 0 | 0 | 1 | 0 | 0 |
| PS | 1 | 1 | 0 | 0 | 1 | 0 | 0 | 0 |
| STN | 1 | 1 | 1 | 0 | 1 | 0 | -1 | 0 |
| PVH | 1 | 1 | 0 | 0 | 1 | 0 | 0 | 0 |
| PVHd | 1 | 1 | 0 | 0 | 1 | 0 | 0 | 0 |
| PeVH | 1 | 0 | 0 | 0 | 1 | 1 | 0 | 0 |
| PeF | 1 | 1 | 1 | 0 | 1 | 0 | 0 | 0 |
| RCH | 0 | 0 | 0 | 0 | 0 | 1 | 1 | 0 |
| SO | 0 | 0 | 0 | 0 | 0 | 1 | 1 | 0 |
| SUM | 1 | 0 | 0 | 0 | 1 | 0 | 0 | 1 |
| TM | -1 | -1 | -1 | 0 | -1 | 1 | 1 | 0 |
| TU | 0 | 0 | 0 | 0 | 0 | 0 | 0 | 0 |
| VL/VMPO | 0 | 0 | 0 | 0 | 0 | 1 | 1 | 0 |
| VMH | 0 | 0 | 0 | 0 | 0 | 0 | 1 | 0 |
| ZI | 1 | 1 | 1 | 1 | 1 | -1 | -1 | -1 |
| HBn | 1 | 1 | 0 | 0 | 1 | 0 | 0 | 0 |
| RPF | 1 | 1 | 1 | 0 | 1 | 0 | -1 | 0 |

| | | | | | | | | |
|---|---|---|---|---|---|---|---|---|
| APN | 1 | 1 | 1 | 1 | 1 | -1 | 0 | -1 |
| PTA | 1 | 1 | 1 | 1 | 1 | -1 | 0 | 1 |
| NPC | 1 | 1 | 1 | 0 | 1 | 0 | 0 | 0 |
| PRC/SCO | -1 | 1 | 0 | 0 | -1 | 1 | 1 | 0 |
| PPN | 1 | 1 | 1 | 0 | 1 | -1 | 0 | 0 |
| CUN | 1 | 0 | 1 | 0 | 1 | 0 | 1 | 1 |
| AT/VTN | 1 | 1 | 1 | 0 | 1 | 0 | 0 | 1 |
| CLI | 1 | 0 | 1 | 0 | 1 | 1 | -1 | 0 |
| DR | 1 | 0 | 1 | 0 | 1 | 0 | 0 | 0 |
| IC | 0 | 1 | 1 | 1 | 0 | 0 | -1 | 0 |
| IF | 0 | 0 | 0 | 0 | 0 | 0 | 1 | 1 |
| IPN | -1 | 1 | -1 | -1 | -1 | 0 | 1 | 0 |
| MRNal | 1 | 1 | 1 | 0 | 1 | -1 | -1 | -1 |
| MRNam | 1 | 1 | 1 | 1 | 1 | -1 | -1 | 0 |
| MRNpl | 1 | 1 | 1 | 1 | 1 | -1 | -1 | 0 |
| MRNpm | 1 | 1 | 1 | 1 | 1 | -1 | -1 | 0 |
| Tn | 1 | 1 | 0 | 1 | 1 | 0 | 0 | 0 |
| NB | -1 | 0 | 0 | 0 | -1 | 1 | 0 | 1 |
| EW/MA3/ND | 1 | 1 | 1 | 0 | 1 | 0 | 0 | 0 |
| PAGa | 1 | 1 | 1 | 0 | 1 | 0 | -1 | 0 |
| PAGd | 1 | 1 | 1 | 1 | 1 | -1 | -1 | -1 |
| PAGv | 1 | 1 | 1 | 0 | 1 | 1 | 0 | 1 |
| PAGl | 1 | 1 | 1 | 1 | 1 | -1 | -1 | -1 |
| PBG | 0 | 0 | 0 | 0 | 0 | 1 | 1 | 0 |
| Pa4/IV | 1 | 0 | 1 | 0 | 1 | 0 | 0 | 0 |
| RL | 1 | 0 | 0 | 0 | 1 | 0 | 0 | 0 |
| RN | 1 | 1 | 1 | 1 | 1 | -1 | -1 | 0 |
| RR | 1 | 1 | 1 | 0 | 1 | 0 | 0 | 0 |
| SAG | 1 | 1 | 0 | 0 | 1 | 0 | 0 | 0 |
| SCd | 1 | 1 | 1 | 1 | 1 | -1 | -1 | -1 |
| Sci | 1 | 1 | 1 | 1 | 1 | -1 | 0 | -1 |
| SCs | 1 | 1 | 1 | 1 | 1 | -1 | 1 | 1 |
| SN | 1 | 1 | 0 | 0 | 1 | 0 | 0 | 0 |
| VTA | 1 | 1 | 0 | 0 | 1 | 0 | 0 | 0 |
| AMB | 0 | 0 | 0 | 0 | 0 | 0 | 0 | 0 |
| AP | -1 | 0 | -1 | -1 | -1 | 1 | 1 | 1 |
| CS | 1 | 1 | 1 | 0 | 1 | 0 | -1 | 0 |
| CU/GR | -1 | 0 | -1 | -1 | -1 | 1 | 1 | 1 |
| DCO | 0 | 1 | 0 | 0 | 0 | 0 | 1 | 0 |
| DMX | 0 | 0 | 0 | 0 | 0 | 0 | 1 | 0 |
| DTN/PDTg | 1 | 1 | 1 | 0 | 1 | 1 | 0 | 1 |
| ECU | -1 | 0 | -1 | -1 | -1 | 1 | 1 | 1 |
| GRN | 1 | 0 | 1 | 0 | 1 | 0 | 1 | 1 |
| I5/PC5 | 0 | 0 | 0 | 0 | 0 | 0 | 0 | 0 |
| V | 1 | 0 | 0 | 0 | 1 | 0 | 0 | 0 |
| IO | 0 | 0 | 0 | 0 | 0 | 1 | 1 | 0 |
| IRN | 0 | 0 | 0 | 0 | 0 | 0 | 0 | 0 |
| KF | 1 | 0 | 0 | 0 | 1 | 0 | 0 | 0 |
| LAC | 1 | 0 | 0 | 0 | 1 | 0 | 0 | 0 |
| LC/B | 1 | 0 | 0 | 0 | 1 | 1 | 0 | 0 |
| LDT | 1 | 0 | 1 | 0 | 1 | 1 | 0 | 0 |
| LIN | 0 | 0 | 0 | 0 | 0 | 0 | 0 | 0 |

| | | | | | | | | |
|------|----|----|----|----|----|----|----|----|
| LRN | 0 | 0 | 0 | 0 | 0 | 0 | 1 | 0 |
| MARN | 1 | 0 | 0 | 0 | 1 | 0 | 1 | 0 |
| MDRN | -1 | 0 | -1 | -1 | -1 | 1 | 1 | 1 |
| MV | 0 | 0 | 0 | 0 | 0 | 1 | 1 | 0 |
| NI | 1 | 1 | 1 | 0 | 1 | 1 | 0 | 1 |
| NLL | 0 | 0 | 0 | 0 | 0 | 0 | 0 | 0 |
| NR/XII | -1 | 0 | -1 | -1 | -1 | 1 | 1 | 1 |
| NTB | 0 | 0 | 0 | 0 | 0 | 0 | 0 | 0 |
| NTS/PAS | 0 | 0 | 0 | 0 | 0 | 0 | 0 | 0 |
| P5/Acs5 | 1 | 0 | 1 | 0 | 1 | 0 | 0 | 0 |
| PARN | 0 | 0 | 0 | 0 | 0 | 0 | 0 | 1 |
| PB | 1 | 1 | 1 | 0 | 1 | 0 | 0 | 0 |
| PCG/SG | 1 | 1 | 1 | 0 | 1 | 1 | 0 | 1 |
| PG | 0 | 0 | 0 | 0 | 0 | 0 | 0 | 0 |
| PGRN | 0 | 0 | 1 | 1 | 0 | 0 | 1 | 0 |
| POR | 0 | 0 | 0 | 0 | 0 | 0 | 0 | 0 |
| PPY | 0 | 0 | 0 | 0 | 0 | 1 | 0 | 0 |
| PRNc | 1 | 1 | 1 | 1 | 1 | 0 | 0 | 0 |
| PRNr | 1 | 1 | 1 | 1 | 1 | -1 | -1 | 0 |
| PRP | 0 | 0 | 0 | 0 | 0 | 0 | 1 | 1 |
| PSV | 1 | 0 | 1 | 0 | 1 | 0 | 0 | 0 |
| Pa5 | -1 | 0 | -1 | -1 | -1 | 1 | 1 | 1 |
| RM/RO | 0 | 0 | 1 | 0 | 0 | 0 | 0 | 0 |
| RPA | 0 | 0 | 0 | 0 | 0 | 0 | 0 | 1 |
| RPO | 1 | 1 | 1 | 0 | 1 | 0 | 0 | 0 |
| SOC | 0 | 1 | 0 | 0 | 0 | 0 | 0 | 0 |
| SPIV | 0 | 0 | 0 | 0 | 0 | 0 | 0 | 0 |
| SPVC | -1 | 0 | -1 | -1 | -1 | 1 | 1 | 1 |
| SPVI | 0 | 0 | 0 | 0 | 0 | 0 | 1 | 0 |
| SPVO | 0 | 0 | 0 | 0 | 0 | 0 | 1 | 0 |
| SUT | 1 | 0 | 0 | 0 | 1 | 0 | 0 | 0 |
| SUV | 1 | 0 | 0 | 0 | 1 | 0 | 0 | 0 |
| TRN | 1 | 1 | 1 | 0 | 1 | 0 | 0 | 0 |
| VCO | 1 | 1 | 0 | 0 | 1 | 0 | 1 | 0 |
| VII | 0 | 1 | 0 | 0 | 0 | 0 | 1 | 0 |
| x | 0 | 0 | 0 | 0 | 0 | 1 | 1 | 0 |
| CB | 0 | -1 | 1 | 0 | 0 | 1 | 1 | 0 |
| ANcr1 | 0 | -1 | -1 | 0 | 0 | 1 | 1 | 0 |
| ANcr2 | 0 | 0 | 0 | 0 | 0 | 1 | 0 | 0 |
| CENT2 | 1 | 1 | 1 | 0 | 1 | 0 | 1 | 1 |
| CENT3 | 1 | 1 | 1 | 1 | 1 | 0 | 1 | 1 |
| COPY | 1 | 1 | 0 | 0 | 1 | 0 | 1 | 0 |
| DEC | 1 | 0 | 0 | 0 | 1 | 0 | 1 | 0 |
| DN | 1 | 0 | 0 | 0 | 1 | 0 | 0 | 0 |
| FL | 0 | 1 | 0 | 0 | 0 | 0 | 1 | 0 |
| FOTU | -1 | 0 | -1 | -1 | -1 | 1 | 1 | 1 |
| IP | 1 | 1 | 0 | 0 | 1 | 0 | 1 | 1 |
| LING | 0 | 0 | 0 | 0 | 0 | 1 | 1 | 1 |
| NOD | 0 | 0 | 0 | 0 | 0 | 1 | 1 | 0 |
| PFL | 0 | 1 | 0 | 0 | 0 | 1 | 1 | 0 |
| PRM | 1 | 0 | 0 | 0 | 1 | 0 | 1 | 0 |
| PYR | -1 | 0 | -1 | -1 | -1 | 1 | 1 | 1 |
| SIM | 0 | 0 | 0 | 0 | 0 | 0 | 0 | 0 |
| UVU | 0 | 0 | 0 | 0 | 0 | 0 | 0 | 0 |

| | | | | | | | |
|---|---|---|---|---|---|---|---|
| ■ VeCB/ICB | 0 | 0 | 0 | 0 ‖ 0 | 1 | 0 | 0 |

## Responsive areas - low-frequency stimulation

| Brain Areas | Early (0 – 2 s) | | | Late (3 – 8 s) | | |
|---|---|---|---|---|---|---|
| | NTSR | PV | GAD2 | NTSR | PV | GAD2 |
| ACAd | 0 | 0 | 0 | 0 | 0 | 0 |
| ACAv | 0 | 0 | 0 | 1 | 0 | 0 |
| AIa | 0 | 0 | 0 | 0 | 0 | 0 |
| AUDd | 0 | 0 | 0 | 0 | 0 | 0 |
| AUDp | 0 | 0 | 0 | 0 | 0 | 0 |
| AUDpo | 0 | 0 | 0 | 0 | 0 | 0 |
| AUDv | 0 | 1 | 0 | 0 | 1 | 0 |
| AON | 1 | 0 | 0 | 0 | 1 | 0 |
| APr | 0 | 0 | 0 | -1 | -1 | 0 |
| DP | -1 | 0 | 0 | 1 | 1 | 0 |
| ECT | 1 | 1 | 0 | 1 | 1 | 0 |
| GU | -1 | 0 | 0 | 1 | 0 | 0 |
| ILA | 0 | 1 | 0 | 0 | 1 | 0 |
| MOp | 0 | 0 | 0 | 0 | 0 | 0 |
| MOs | 0 | 0 | 0 | 0 | 0 | 0 |
| NLOT | -1 | -1 | 0 | 1 | 1 | 0 |
| OLF | 1 | 0 | 0 | 1 | 1 | 0 |
| ORB | 0 | 0 | 0 | -1 | 0 | 0 |
| OT | 0 | 0 | 0 | 1 | 0 | 0 |
| PERI | 0 | 0 | 0 | 1 | 0 | 0 |
| PIR | 0 | 0 | 0 | 1 | 0 | 0 |
| PL | 1 | 0 | 0 | 1 | 0 | 0 |
| RSPagl | 0 | 0 | 0 | -1 | -1 | 0 |
| RSPd | 0 | 0 | 0 | 0 | -1 | 0 |
| RSPv | 0 | 0 | 0 | 0 | 0 | 0 |
| SSp | 1 | 1 | 0 | 0 | 0 | 0 |
| SSs | -1 | 0 | 0 | 1 | 0 | 0 |
| TEa | 0 | 0 | 0 | 0 | 1 | 0 |
| TR | 0 | 0 | 0 | 1 | 0 | 0 |
| TT | 0 | 0 | 0 | 1 | 1 | 0 |
| VISC | 1 | 0 | 0 | 0 | 0 | 0 |
| VISa | 1 | 0 | 0 | 0 | 0 | 0 |
| VISal | 1 | 1 | 0 | -1 | 0 | 0 |
| VISam | 1 | 0 | 0 | 0 | 0 | 0 |
| VISl | 1 | 0 | 0 | -1 | -1 | 0 |
| VISli | 0 | 0 | 0 | -1 | 0 | 0 |
| VISp | 1 | 0 | 0 | -1 | -1 | -1 |
| VISpl | 0 | 1 | 0 | -1 | -1 | 0 |
| VISpm | 1 | 0 | 0 | 0 | 0 | 0 |
| VISpor | 0 | 0 | 0 | 1 | 0 | 0 |
| VISrl | 1 | 0 | 0 | -1 | 0 | 0 |
| PA | 0 | 0 | 0 | 1 | 0 | 0 |
| PAA | 0 | 0 | 0 | 1 | 0 | 0 |
| MEA | -1 | 0 | 0 | 1 | 1 | 0 |
| LA | 1 | 0 | 0 | 1 | 0 | 0 |
| IA | -1 | 0 | 0 | 1 | 0 | 0 |
| COA | 0 | 0 | 0 | 1 | 1 | 0 |
| AAA | -1 | 0 | 0 | 1 | 1 | 0 |

| | | | | | | |
|---|---|---|---|---|---|---|
| BLAd | 0 | 0 | 0 | 0 | 0 | 0 |
| BLAv | 0 | 0 | 0 | 0 | 0 | 0 |
| BMA | 0 | 0 | 0 | 1 | 0 | 0 |
| CEA | 0 | 0 | 0 | 0 | 0 | 0 |
| EP | 0 | 0 | 0 | 0 | 0 | 0 |
| HATA | 0 | 0 | 0 | 0 | 0 | 0 |
| CA1d | 1 | 0 | 0 | -1 | -1 | 0 |
| CA1i | 0 | 1 | 0 | 0 | 0 | 0 |
| CA1v | -1 | 1 | 0 | 0 | 0 | 1 |
| CA2d | 0 | 0 | 0 | -1 | -1 | 0 |
| CA2i | 0 | 1 | 0 | 0 | 0 | 0 |
| CA2v | -1 | 0 | 0 | 1 | 0 | 0 |
| CA3d | 0 | 0 | 0 | -1 | 0 | 0 |
| CA3i | 0 | 1 | 0 | 0 | 0 | 0 |
| CA3v | 0 | 0 | 0 | 1 | 0 | 0 |
| DGd | 0 | 0 | 0 | 0 | 0 | 0 |
| DGi | 0 | 0 | 0 | 0 | 1 | 0 |
| DGv | -1 | 0 | 0 | 0 | 1 | 0 |
| ENTl | 0 | 0 | 0 | 0 | 0 | 0 |
| ENTm | -1 | 0 | 0 | 0 | 0 | 0 |
| PAR | 0 | 0 | 0 | 0 | 1 | 0 |
| POST | 0 | 0 | 0 | 0 | 0 | 0 |
| PRE | 0 | 0 | 0 | 1 | 0 | 0 |
| ProS | -1 | 0 | 0 | -1 | -1 | 0 |
| SUB | 0 | 0 | 0 | -1 | -1 | 0 |
| ACB | 1 | 0 | 0 | 0 | 0 | 0 |
| BST | 1 | 0 | 0 | 0 | 0 | 0 |
| CLA | 0 | 0 | 0 | 0 | 0 | 0 |
| CPa | 0 | 1 | 0 | -1 | 0 | 0 |
| CPm | 0 | 1 | 0 | 0 | 0 | 0 |
| CPc | 1 | 1 | 0 | 1 | 0 | 0 |
| FS | 0 | 0 | 0 | 1 | 1 | 0 |
| GPe | 1 | 1 | 0 | 1 | 0 | 0 |
| GPi | 1 | 1 | 0 | 1 | 0 | 0 |
| LSd | 0 | 1 | 0 | 0 | 0 | 0 |
| LSv | 0 | 0 | 0 | 0 | 0 | 0 |
| MS | 0 | 0 | 0 | 0 | 0 | 0 |
| MA | 1 | 0 | 0 | 1 | 1 | 0 |
| NDB | 0 | 0 | 0 | 1 | 0 | 0 |
| PAL | 1 | 0 | 0 | 1 | 0 | 0 |
| SF | 0 | 0 | 0 | 1 | 1 | 0 |
| SI | 1 | 0 | 0 | 1 | 0 | 0 |
| STR | 1 | 0 | 0 | 1 | 0 | 0 |
| TRS | 1 | 0 | 0 | 1 | 0 | 0 |
| AD | 1 | 0 | 0 | 0 | 0 | 0 |
| AM | 1 | 1 | 0 | 1 | 0 | 0 |
| AV | 1 | 1 | 0 | 1 | 0 | 0 |
| CL | 1 | 0 | 0 | 1 | 0 | 0 |
| CM | 1 | 0 | 0 | 1 | 0 | 0 |
| Eth | 1 | 0 | 0 | 1 | 0 | 0 |
| IAt | 1 | 0 | 0 | 1 | 0 | 0 |
| IGL | 1 | 0 | 0 | 0 | 0 | 0 |
| IMD | 1 | 0 | 0 | -1 | 0 | 0 |
| LD | 1 | 1 | 0 | 0 | -1 | 0 |

| | | | | | | |
|---|---|---|---|---|---|---|
| LGd | 1 | 0 | 0 | -1 | -1 | 0 |
| LGv | 1 | 1 | 0 | 1 | -1 | 0 |
| LPcl | 1 | 1 | 0 | 1 | 0 | 0 |
| LPam | 1 | 0 | 0 | 1 | 0 | 0 |
| MD | 1 | 0 | 0 | -1 | 0 | 0 |
| MG | 1 | 1 | 0 | 1 | 0 | 0 |
| PCN | 1 | 0 | 0 | 1 | 0 | 0 |
| PF | 1 | 0 | 0 | 1 | 0 | 0 |
| PO | 1 | 1 | 0 | 1 | 0 | 0 |
| PPnT | 1 | 1 | 0 | 1 | 0 | 0 |
| PP | 1 | 0 | 0 | 1 | 1 | 0 |
| PR | 1 | 1 | 0 | 1 | 0 | 0 |
| PT | 1 | 1 | 0 | 1 | 0 | 0 |
| PVT | 1 | 0 | 0 | 1 | 1 | 0 |
| RE | 1 | 1 | 0 | -1 | 1 | 0 |
| RH | 0 | 0 | 0 | 1 | 0 | 0 |
| RT | 1 | 1 | 0 | -1 | 0 | 0 |
| SMT | 1 | 1 | 0 | 1 | 0 | 0 |
| SPA | 1 | 1 | 0 | 1 | 0 | 0 |
| SPFm | 1 | 1 | 0 | 1 | 0 | 0 |
| VAL | 1 | 1 | 0 | 0 | 0 | 0 |
| VM | 1 | 0 | 0 | 0 | 0 | 0 |
| VPL | 1 | 0 | 0 | 0 | 0 | 0 |
| VPM | 1 | 1 | 0 | 0 | 0 | 0 |
| VPMpc | 1 | 1 | 0 | 1 | 0 | 0 |
| Xi | 1 | 1 | 0 | -1 | 0 | 0 |
| AHN | 1 | 0 | 0 | 1 | 1 | 0 |
| AVP | 0 | 0 | 0 | 0 | 0 | 0 |
| AVPV | 0 | 0 | 0 | 1 | 0 | 0 |
| DMH | 0 | 0 | 0 | 1 | 0 | 0 |
| FF | 1 | 0 | 0 | 1 | 0 | 0 |
| LHA | 1 | 1 | 0 | 1 | 1 | 0 |
| LM | 1 | 0 | 0 | 1 | 1 | 0 |
| LPO | -1 | 0 | 0 | 1 | 1 | 0 |
| ME | 0 | 0 | 0 | 1 | 1 | 0 |
| PON | 0 | 0 | 0 | 1 | 1 | 0 |
| Mmm | 0 | 0 | 0 | 1 | 1 | 0 |
| PH | 1 | 0 | 0 | -1 | 1 | 0 |
| PMH | 0 | 0 | 0 | 1 | 1 | 0 |
| PS | 0 | 0 | 0 | 0 | 0 | 0 |
| STN | 1 | 1 | 0 | 1 | 0 | 0 |
| PVH | 1 | 1 | 0 | 1 | 0 | 0 |
| PVHd | 1 | 1 | 0 | 1 | 1 | 0 |
| PeVH | 0 | 0 | 0 | 1 | 1 | 0 |
| PeF | 1 | 0 | 0 | 1 | 0 | 0 |
| RCH | 0 | 0 | 0 | 1 | 1 | 0 |
| SO | -1 | 0 | 0 | 1 | 0 | 0 |
| SUM | 0 | 0 | 0 | 1 | 0 | 0 |
| TM | -1 | -1 | 0 | 1 | 1 | 0 |
| TU | 0 | 0 | 0 | 1 | 1 | 0 |
| VL/VMPO | 0 | 0 | 0 | 1 | 0 | 0 |
| VMH | -1 | 0 | 0 | 1 | 1 | 0 |
| ZI | 1 | 1 | 0 | 1 | 0 | 0 |
| HBn | 1 | 1 | 0 | 1 | 0 | 0 |

| | | | | | | |
|---|---|---|---|---|---|---|
| RPF | 1 | 1 | 0 | 1 | 0 | 0 |
| APN | 1 | 0 | 0 | -1 | 0 | 0 |
| PTA | 1 | 0 | 0 | 1 | 0 | 0 |
| NPC | 1 | 1 | 0 | 1 | 1 | 0 |
| PRC/SCO | 0 | 0 | 0 | 1 | 1 | 0 |
| PPN | 1 | 1 | 0 | 1 | 0 | 0 |
| CUN | 1 | 1 | 0 | 1 | 1 | 0 |
| AT/VTN | 1 | 1 | 0 | 1 | 0 | 0 |
| CLI | 1 | 0 | 0 | 0 | 1 | 0 |
| DR | 1 | 0 | 0 | 1 | 1 | 0 |
| IC | 1 | 1 | 0 | 1 | 0 | 0 |
| IF | 1 | 0 | 0 | 1 | 1 | 0 |
| IPN | 1 | -1 | 0 | 1 | 1 | 0 |
| MRNal | 1 | 1 | 0 | 1 | 0 | 0 |
| MRNam | 1 | 1 | 0 | 1 | 0 | 0 |
| MRNpl | 1 | 1 | 0 | 1 | 0 | 0 |
| MRNpm | 1 | 1 | 0 | 1 | 0 | 0 |
| Tn | 1 | 0 | 0 | 1 | 0 | 0 |
| NB | 0 | 0 | 0 | 1 | 1 | 0 |
| EW/MA3/ND | 1 | 1 | 0 | 1 | 0 | 0 |
| PAGa | 1 | 1 | 0 | 1 | 0 | 0 |
| PAGd | 1 | 1 | 1 | 1 | -1 | 0 |
| PAGv | 1 | 1 | 0 | 1 | 0 | 0 |
| PAGl | 1 | 0 | 0 | 1 | 0 | 0 |
| PBG | -1 | 0 | 0 | 1 | 1 | 0 |
| Pa4/IV | 1 | 1 | 0 | 1 | 0 | 0 |
| RL | 0 | 0 | 0 | 0 | 1 | 0 |
| RN | 1 | 0 | 0 | -1 | 0 | 0 |
| RR | 1 | 0 | 0 | 1 | 0 | 1 |
| SAG | 1 | 0 | 0 | 1 | 0 | 0 |
| SCd | 1 | 1 | 1 | 1 | -1 | 0 |
| Sci | 1 | 1 | 1 | 1 | -1 | 0 |
| SCs | 1 | 0 | 1 | 1 | 1 | 1 |
| SN | 1 | 0 | 0 | 1 | 0 | 0 |
| VTA | 1 | 0 | 0 | 1 | 0 | 0 |
| AMB | 0 | 0 | 0 | 1 | 0 | 0 |
| AP | -1 | 0 | 0 | 1 | 1 | 0 |
| CS | 1 | 1 | 0 | -1 | 0 | 0 |
| CU/GR | -1 | 0 | 0 | 1 | 1 | 0 |
| DCO | 1 | 0 | 0 | 1 | 0 | 0 |
| DMX | 0 | 0 | 0 | 0 | 0 | 0 |
| DTN/PDTg | 1 | 1 | 0 | 1 | 1 | 0 |
| ECU | -1 | 0 | 0 | 1 | 1 | 0 |
| GRN | 1 | 0 | 0 | 1 | 0 | 0 |
| I5/PC5 | 0 | 0 | 0 | 1 | 0 | 0 |
| V | 0 | 0 | 0 | 1 | 0 | 0 |
| IO | 0 | 0 | 0 | 1 | 0 | 0 |
| IRN | 0 | 0 | 0 | 1 | 0 | 0 |
| KF | 0 | 0 | 0 | 1 | 0 | 0 |
| LAC | 0 | 0 | 0 | 1 | 0 | 0 |
| LC/B | 1 | 0 | 0 | 1 | 0 | 0 |
| LDT | 1 | 1 | 0 | 1 | 0 | 0 |

| | | | | | | |
|---|---|---|---|---|---|---|
| LIN | 0 | 0 | 0 | 1 | 0 | |
| LRN | 0 | 0 | 0 | 1 | 0 | |
| MARN | 0 | 0 | 0 | 1 | 0 | 0 |
| MDRN | -1 | 0 | 0 | 1 | 1 | 0 |
| MV | 0 | 0 | 0 | 1 | 0 | 0 |
| NI | 1 | 0 | 0 | 1 | 0 | 0 |
| NLL | 0 | 0 | 0 | 1 | 1 | 0 |
| NR/XII | -1 | 0 | 0 | 1 | 1 | 0 |
| NTB | 0 | 0 | 0 | 1 | 0 | 0 |
| NTS/PAS | 0 | 0 | 0 | 1 | 0 | 0 |
| P5/Acs5 | 1 | 0 | 0 | 0 | 0 | 0 |
| PARN | 0 | 0 | 0 | 1 | 0 | 0 |
| PB | 1 | 0 | 0 | 1 | 0 | 0 |
| PCG/SG | 1 | 1 | 0 | 1 | 1 | 0 |
| PG | 0 | 0 | 0 | 1 | 0 | 0 |
| PGRN | 0 | 0 | 0 | 1 | 0 | 0 |
| POR | 0 | 0 | 0 | 1 | 0 | 0 |
| PPY | 0 | 0 | 0 | 1 | 0 | 0 |
| PRNc | 1 | 0 | 0 | 1 | 0 | 0 |
| PRNr | 1 | 1 | 0 | 1 | 0 | 0 |
| PRP | -1 | 1 | 0 | 1 | 1 | 0 |
| PSV | 1 | 0 | 0 | 0 | 1 | 0 |
| Pa5 | -1 | 0 | 0 | 1 | 1 | 0 |
| RM/RO | 0 | 0 | 0 | 1 | 1 | 0 |
| RPA | 0 | 0 | 0 | 1 | 1 | 0 |
| RPO | 1 | 0 | 0 | 1 | 1 | 0 |
| SOC | 0 | 0 | 0 | 1 | 0 | 0 |
| SPIV | 0 | 0 | 0 | 1 | 0 | 0 |
| SPVC | -1 | 0 | 0 | 1 | 1 | 0 |
| SPVI | 0 | 0 | 0 | 1 | 0 | 0 |
| SPVO | 0 | 0 | 0 | 1 | 0 | 0 |
| SUT | 1 | 0 | 0 | 1 | 0 | 0 |
| SUV | -1 | 0 | 0 | 1 | 0 | 0 |
| TRN | 1 | 1 | 0 | 1 | 0 | 0 |
| VCO | 0 | 0 | 0 | 1 | 1 | 0 |
| VII | 0 | 0 | 0 | 1 | 0 | 0 |
| x | 0 | 0 | 0 | 1 | 0 | 0 |
| CB | -1 | 0 | 0 | 1 | 1 | 0 |
| ANcr1 | -1 | 0 | 0 | 1 | 0 | 0 |
| ANcr2 | 0 | 0 | 0 | 1 | 1 | 0 |
| CENT2 | 1 | 1 | 0 | 1 | 0 | 0 |
| CENT3 | 1 | 1 | 0 | 1 | 0 | 0 |
| COPY | 1 | 0 | 0 | 1 | 0 | 0 |
| DEC | 1 | 0 | 0 | 1 | 0 | 0 |
| DN | 1 | 0 | 0 | 1 | 1 | 0 |
| FL | 1 | 0 | 0 | 1 | 1 | 0 |
| FOTU | -1 | 0 | 0 | 1 | 1 | 0 |
| IP | 0 | 0 | 0 | 1 | 0 | 0 |
| LING | 0 | 0 | 0 | 1 | 1 | 0 |
| NOD | 0 | 0 | 0 | 1 | 1 | 0 |
| PFL | 1 | -1 | 0 | 1 | 1 | 0 |
| PRM | 1 | 0 | 0 | 1 | 1 | 0 |
| PYR | -1 | 0 | 0 | 1 | 1 | 0 |
| SIM | 1 | 0 | 0 | 1 | 0 | 0 |

| | UVU | -1 | 1 | 0 | | 1 | 1 | 0 |
| | VeCB/ICB | 0 | 0 | 0 | | 1 | 0 | 0 |

# Appendix 2: Chapter 3

## Table S3.1. List of the 134 brain regions related to Figure 3.1.

| Region Number | Region Abbreviation | Brain region(s) | Name of the region | Volume of the region (mm3) |
|---|---|---|---|---|
| Cerebrum (CB) - Cortical Plate | | | | |
| 1 | GU | GU | Gustatory areas | 1.77 |
| 2 | SSp-bf | SSp-bf | Primary somatosensory area, barrel field | 6.29 |
| 3 | SSp-ll | SSp-ll | Primary somatosensory area, lower limb | 2.35 |
| 4 | SSp-tr | SSp-tr | Primary somatosensory area, trunk | 1.40 |
| 5 | SSp-m | SSp-m | Primary somatosensory area, mouth | 6.21 |
| 6 | SSp-n | SSp-n | Primary somatosensory area, nose | 3.02 |
| 7 | SSp-ul | SSp-ul | Primary somatosensory area, upper limb | 3.77 |
| 8 | SSp-un | SSp-un | Primary somatosensory area, unassigned | 1.26 |
| 9 | SSs | SSs | Supplemental somatosensory area | 9.03 |
| 10 | ACA | ACAd, ACAv | Anterior cingulate area | 5.51 |
| 11 | VISC | VISC | Visceral area | 2.35 |
| 12 | MOp | MOp | Primary motor area | 11.35 |
| 13 | MOs | MOs | Secondary motor area | 13.11 |
| 14 | AUDd | AUDd | Dorsal auditory area | 1.21 |
| 15 | AUDp | AUDp | Primary auditory area | 2.15 |
| 16 | AUDpo | AUDpo | Posterior auditory area | 0.61 |
| 17 | AUDv | AUDv | Ventral auditory area | 1.83 |
| 18 | VISa | VISa | Anterior visual area | 1.44 |
| 19 | VISrl | VISrl | Rostrolateral visual area | 1.02 |
| 20 | VISpor | VISpor | Postrhinal visual area | 1.25 |
| 21 | VISli | VISli | Laterointermediate visual area | 0.49 |
| 22 | VISal | VISal | Anterolateral visual area | 0.76 |
| 23 | VISam | VISam | Anteromedial visual area | 0.79 |
| 24 | VISpl | VISpl | Posterolateral visual area | 0.79 |
| 25 | VISpm | VISpm | Posteromedial visual area | 1.23 |
| 26 | VISl | VISl | Lateral visual area | 1.67 |
| 27 | VISp(pl) | VISp(pl) | Primary visual area, posterior lateral | 2.16 |
| 28 | VISp(pm) | VISp(pm) | Primary visual area, posterior medial | 1.04 |
| 29 | VISp(al) | VISp(al) | Primary visual area, anterior lateral | 1.34 |
| 30 | RSPagl | RSPagl | Restrosplenial area, lateral agranular part | 2.36 |
| 31 | RSPd | RSPd | Retrosplenial area, dorsal part | 3.80 |
| 32 | RSPv | RSPv | Retrosplenial area, ventral part | 4.33 |
| 33 | TEa | TEa | Temporal association areas | 3.11 |
| 34 | PERI | PERI | Perirhinal area | 0.79 |
| 35 | ECT | ECT | Ectorhinal area | 1.66 |

| 36 | PIR | PIR | Piriform area | 11.57 |
| 37 | TR | TR | Postpiriform transition area | 1.40 |
| 38 | COA | COAa, COApl, COApm | Cortical amygdalar area | 3.27 |
| 39 | PAA | PAA | Piriform-amygdalar area | 1.19 |
| 40 | AI | AId, AIv | Agranular insular area | 5.47 |
| 41 | PL | PL | Prelimbic area | 2.40 |
| | | | **Hippocampal Formation (HPF)** | |
| 42 | CA1d CA2d CA3d | CA1d, CA2d, CA3d | CA1 CA2 CA3 subfields, dorsal part | 9.27 |
| 43 | CA1i | CA1i | CA1 subfield, intermediate | 2.05 |
| 44 | CA1v | CA1v | CA1 subfield, ventral | 2.07 |
| 45 | CA2i | CA2i | CA2 subfield, intermediate | 0.11 |
| 46 | CA2v | CA2v | CA2 subfield, ventral | 0.09 |
| 47 | CA3i | CA3i | CA3 subfield, intermediate | 1.80 |
| 48 | CA3v | CA3v | CA3 subfield, ventral | 1.56 |
| 49 | ENTl | ENTl | Entorhinal area, lateral part | 6.38 |
| 50 | ENTm | ENTm | Entorhinal area, medial part | 5.03 |
| 51 | PRE | PRE | Presubiculum | 0.92 |
| 52 | POST | POST | Postsubiculum | 1.08 |
| 53 | PAR | PAR | Parasubiculum | 0.93 |
| 54 | SUB | SUB | Subiculum | 2.10 |
| 55 | ProS | ProS | Prosubiculum | 1.30 |
| | | | **Cerebrum (CB) - Cortical Subplate** | |
| 56 | CLA | CLA | Claustrum | 0.55 |
| 57 | EP | EPd, EPv | Endopiriform nucleus | 2.79 |
| 58 | LA | LA | Lateral amygdalar nucleus | 0.84 |
| 59 | BLA | BLAa, BLAp, BLAv | Basolateral amygdalar nucleus | 1.90 |
| 60 | BMA | BMAa, BMAp | Basomedial amygdalar nucleus | 1.48 |
| 61 | PA | PA | Posterior amygdalar nucleus | 0.97 |
| | | | **Striatum (STR)** | |
| 62 | LSX | LSc, LSr, LSv | Lateral septal complex | 3.05 |
| 63 | CPadl | CPadl | Caudoputamen, anterior dorsal lateral | 1.00 |
| 64 | CPadm | CPadm | Caudoputamen, anterior dorsal medial | 1.80 |
| 65 | CPaml | CPaml | Caudoputamen, anterior medial lateral | 1.94 |
| 66 | CPamm | CPamm | Caudoputamen, anterior medial medial | 2.53 |
| 67 | CPavm | CPavm | Caudoputamen, anterior ventral medial | 1.12 |
| 68 | CPcdl | CPcdl | Caudoputamen, caudal dorsal lateral | 0.55 |
| 69 | CPcdm | CPcdm | Caudoputamen, caudal dorsal medial | 0.89 |
| 70 | CPcml | CPcml | Caudoputamen, caudal medial lateral | 2.17 |
| 71 | CPcv | CPcv | Caudoputamen, caudal ventral | 0.75 |
| 72 | CPmdc | CPmdc | Caudoputamen, medial dorsal central | 2.25 |

| | | | | |
|---|---|---|---|---|
| 73 | CPmdl | CPmdl | Caudoputamen, medial dorsal lateral | 0.36 |
| 74 | CPmdm | CPmdm | Caudoputamen, medial dorsal medial | 1.29 |
| 75 | CPmmc | CPmmc | Caudoputamen, medial medial central | 2.16 |
| 76 | CPmml | CPmml | Caudoputamen, medial medial lateral | 1.43 |
| 77 | CPmvc | CPmvc | Caudoputamen, medial ventral central | 2.03 |
| 78 | CPmvl | CPmvl | Caudoputamen, medial ventral lateral | 0.99 |
| 79 | ACB | ACB | Nucleus accumbens | 4.40 |
| 80 | OT | OT | Olfactory tubercle | 3.82 |
| 81 | sAMY | AAA, CEAc, CEAl, CEAm, IA, MEA | Striatum-like amygdalar nuclei | 4.02 |
| 82 | PAL | PAL | Pallidum | 1.13 |
| **Thalamus (TH)** | | | | |
| 83 | VAL | VAL | Ventral anterior-lateral complex of the thalamus | 0.82 |
| 84 | VM | VM | Ventral medial nucleus of the thalamus | 0.93 |
| 85 | VP | VPL, VPLpc, VPM, VPMpc | Ventral posterior complex of the thalamus | 2.83 |
| 86 | PP | PP | Peripeduncular nucleus | 0.06 |
| 87 | LGd | LGd-co, LGd-ip, LGd-sh | Dorsal part of the lateral geniculate complex | 0.63 |
| 88 | LP Eth | LP, Eth | Lateral posterior nucleus of the thalamus | 1.20 |
| 89 | PO | PO | Posterior complex of the thalamus | 1.25 |
| 90 | MD | MD | Mediodorsal nucleus of thalamus | 1.38 |
| 91 | RT | RT | Reticular nucleus of the thalamus | 1.45 |
| 92 | AT | AD, Amd, Amv, AV, IAD, IAM, LD | Anterior group of the dorsal thalamus | 2.16 |
| 93 | MED | IMD, PR, SMT | Medial group of the dorsal thalamus | 0.63 |
| **Hypothalamus (HY)** | | | | |
| 94 | MEZ | AHN, PMd, LM, Mmd, Mml, Mmm, Mmme, Mmp, SUM, TMd, TMv, MPN, PVHd, PH, PMv, VMH | Hypothalamic medial zone | 3.84 |
| 95 | PVR | ADP, AVPV, AVP, DMH, MPO, MEPO, PS, PVp, PVpo, PD, SFO, SBPV, SCH, OV, VLPO, VMPO | Periventricular region | 2.05 |
| 96 | ME | ME | Median eminence | 0.08 |
| 97 | LZ | LHA, LPO, PSTN, PeF, PST, RCH, STN, TU, ZI | Hypothalamic lateral zone | 5.43 |
| 98 | PVZ | ASO, ARH, PVH, PVa, PVi, SO | Periventricular zone | 0.77 |
| **Midbrain (MB)** | | | | |
| 99 | SCd | SCd(a), SCd(p) | Superior colliculus, deep layers | 1.52 |
| 100 | SCi | SCi(al), SCi(am) | Superior colliculus, intermediate layers | 3.58 |
| 101 | SCi(pl) | SCi(pl) | Superior colliculus, intermediate layers, posterior lateral | |

| | | | | |
|---|---|---|---|---|
| 102 | SCs(a) | SCs(am), SCs(al) | Superior colliculus, superficial layers, anterior | 0.96 |
| 103 | SCs(pl) | SCs(pl) | Superior colliculus, superficial layers, posterior lateral | 0.59 |
| 104 | SCs(pm) | SCs(pm) | Superior colliculus, superficial layers, posterior medial | 0.61 |
| 105 | ICc | ICc | Inferior colliculus, central nucleus | 1.13 |
| 106 | ICd | ICd | Inferior colliculus, dorsal nucleus | 1.32 |
| 107 | ICe | ICe | Inferior colliculus, external nucleus | 2.00 |
| 108 | MRN | MRNal, MRNam, MRNpl, MRNpm | Midbrain reticular nucleus | 5.14 |
| 109 | CUN | CUN | Cuneiform nucleus | 0.55 |
| 110 | SN | SNr, SNc | Substantia nigra | 1.55 |
| 111 | PAG | PAGa, PAGmd, PAGml, PAGmv, PAGpd, PAGpl, PAGpv | Periaqueductal gray | 4.30 |
| 112 | PTA | PPT, MPT, NOT, OP, APN | pretectal areas | 1.28 |
| 113 | RN | RN | Red nucleus | 0.79 |
| 114 | PPN | PPN | Pedunculopontine nucleus | 0.89 |
| **Hindbrain (HB)** | | | | |
| 115 | NLL | NLL | Nucleus of the lateral lemniscus | 0.72 |
| 116 | PSV | PSV | Principal sensory nucleus of the trigeminal | 1.10 |
| 117 | PB | PB | Parabrachial nucleus | 0.95 |
| 118 | SOC | SOCl, SOCm | Superior olivary complex | 0.53 |
| 119 | PRNc | PRNc | Pontine reticular nucleus, caudal part | 2.35 |
| 120 | PCG | PCG | Pontine central gray | 0.54 |
| 121 | PG | PG | Pontine gray | 0.96 |
| 122 | TRN | TRN | Tegmental reticular nucleus | 0.69 |
| 123 | CS | CS | Superior central nucleus raphe | 0.59 |
| 124 | PRNr | PRNr | Pontine reticular nucleus | 2.36 |
| 125 | VII | VII | Facial motor nucleus | 0.92 |
| 126 | GRN | GRN | Gigantocellular reticular nucleus | 2.61 |
| 127 | IRN | IRN | Intermediate reticular nucleus | 2.78 |
| 128 | MARN | MARN | Magnocellular reticular nucleus | 0.53 |
| 129 | PARN | PARN | Parvicellular reticular nucleus | 2.25 |
| **Cerebellum (CBL)** | | | | |
| 130 | CENT | CENT2, CENT3 | Central lobule | 4.05 |
| 131 | SIM | SIM | Simple lobule | 5.69 |
| 132 | CUL | CUL4,5 | Lobules IV-V | 6.71 |
| 133 | PFL | PFL | Paraflocculus | 5.72 |
| 134 | FL | FL | Flocculus | 1.34 |

# References

Adamantidis, A.R. *et al.* (2011) 'Optogenetic Interrogation of Dopaminergic Modulation of the Multiple Phases of Reward-Seeking Behavior', *Journal of Neuroscience*, 31(30), pp. 10829–10835. doi:10.1523/JNEUROSCI.2246-11.2011.

Adelman, G. (1987) *Encyclopedia of neuroscience*. Boston: Birkhaeuser.

Ahmadi, H., Fatemizadeh, E. and Motie-Nasrabadi, A. (2020) 'Identifying brain functional connectivity alterations during different stages of Alzheimer's disease', *The International Journal of Neuroscience*, pp. 1–9. doi:10.1080/00207454.2020.1860037.

Ahrens, M.B. *et al.* (2012) 'Brain-wide neuronal dynamics during motor adaptation in zebrafish.', *Nature*, 485(7399), pp. 471–477. doi:10.1038/nature11057.

Aimon, S. *et al.* (2019) 'Fast near-whole–brain imaging in adult Drosophila during responses to stimuli and behavior', *PLOS Biology*, 17(2), p. e2006732.

Albin, R.L., Young, A.B. and Penney, J.B. (1989) 'The functional anatomy of basal ganglia disorders', *Trends in Neurosciences*, 12(10), pp. 366–375. doi:10.1016/0166-2236(89)90074-x.

Alexander, G.M. *et al.* (2009) 'Remote control of neuronal activity in transgenic mice expressing evolved G protein-coupled receptors', *Neuron*, 63(1), pp. 27–39. doi:10.1016/j.neuron.2009.06.014.

Ali, F. and Kwan, A.C. (2020) 'Interpreting in vivo calcium signals from neuronal cell bodies, axons, and dendrites: a review', *Neurophotonics*, 7(1), p. 011402. doi:10.1117/1.NPh.7.1.011402.

Allen, W.E. *et al.* (2017) 'Global Representations of Goal-Directed Behavior in Distinct Cell Types of Mouse Neocortex', *Neuron*, 94, pp. 891-907.e6. doi:10.1016/j.neuron.2017.04.017.

Almeida, I., Soares, S.C. and Castelo-Branco, M. (2015) 'The distinct role of the amygdala, superior colliculus and pulvinar in processing of central and peripheral snakes', *PLoS ONE*, 10(6). doi:10.1371/journal.pone.0129949.

Anenberg, E. *et al.* (2015) 'Optogenetic stimulation of GABA neurons can decrease local neuronal activity while increasing cortical blood flow', *Journal of Cerebral Blood Flow and Metabolism: Official Journal of the International Society of Cerebral Blood Flow and Metabolism*, 35(10), pp. 1579–1586. doi:10.1038/jcbfm.2015.140.

Angenstein, F., Kammerer, E. and Scheich, H. (2009) 'The BOLD response in the rat hippocampus depends rather on local processing of signals than on the input or output activity. A combined functional MRI and electrophysiological study', *The Journal of Neuroscience: The Official Journal of the Society for Neuroscience*, 29(8), pp. 2428–2439. doi:10.1523/JNEUROSCI.5015-08.2009.

Applegate, C.D., Pretel, S. and Piekut, D.T. (1995) 'The substantia nigra pars reticulata, seizures and Fos expression', *Epilepsy Research*, 20(1), pp. 31–39. doi:10.1016/0920-1211(94)00064-4.

Apter, J.T. (1946) 'Eye movements following strychninization of the superior colliculus of cats', *Journal of Neurophysiology*, 9(2), pp. 73–86. doi:10.1152/jn.1946.9.2.73.

Armbruster, B.N. *et al.* (2007) 'Evolving the lock to fit the key to create a family of G protein-coupled receptors potently activated by an inert ligand', *Proceedings of the National Academy of Sciences of the United States of America*, 104(12), pp. 5163–5168. doi:10.1073/pnas.0700293104.

Aron, A.R. and Poldrack, R.A. (2006) 'Cortical and subcortical contributions to stop signal response inhibition: Role of the subthalamic nucleus', *Journal of Neuroscience*, 26(9), pp. 2424–2433. doi:10.1523/JNEUROSCI.4682-05.2006.

Astic, L. *et al.* (1993) 'The CVS strain of rabies virus as transneuronal tracer in the olfactory system of mice', *Brain Research*, 619(1–2), pp. 146–156. doi:10.1016/0006-8993(93)91606-s.

Atasoy, D. and Sternson, S.M. (2018) 'Chemogenetic Tools for Causal Cellular and Neuronal Biology', *Physiological Reviews*, 98(1), pp. 391–418. doi:10.1152/physrev.00009.2017.

Aydin, A.-K. *et al.* (2020) 'Transfer functions linking neural calcium to single voxel functional ultrasound signal', *Nature Communications*, 11(1), p. 2954. doi:10.1038/s41467-020-16774-9.

Baker, J.T. *et al.* (2006) 'Distribution of activity across the monkey cerebral cortical surface, thalamus and midbrain during rapid, visually guided saccades', *Cerebral Cortex (New York, N.Y.: 1991)*, 16(4), pp. 447–459. doi:10.1093/cercor/bhi124.

Baleydier, C. and Magnin, M. (1979) 'Afferent and efferent connections of the parabigeminal nucleus in cat revealed by retrograde axonal transport of horseradish peroxidase', *Brain Research*, 161(2), pp. 187–198. doi:10.1016/0006-8993(79)90062-3.

Barker, F.G. (1995) 'Phineas among the phrenologists: the American crowbar case and nineteenth-century theories of cerebral localization', *Journal of Neurosurgery*, 82(4), pp. 672–682. doi:10.3171/jns.1995.82.4.0672.

Barlow, H.B. (1972) 'Single Units and Sensation: A Neuron Doctrine for Perceptual Psychology?', *Perception*, 1(4), pp. 371–394. doi:10.1068/p010371.

# References

Barlow, H.B., Hill, R.M. and Levick, W.R. (1964) 'Retinal ganglion cells responding selectively to direction and speed of image motion in the rabbit', *The Journal of Physiology*, 173(3), pp. 377–407.

Barry, D.N., Coogan, A.N. and Commins, S. (2016) 'The time course of systems consolidation of spatial memory from recent to remote retention: A comparison of the Immediate Early Genes Zif268, c-Fos and Arc', *Neurobiology of Learning and Memory*, 128, pp. 46–55. doi:10.1016/j.nlm.2015.12.010.

Barth, A.L., Gerkin, R.C. and Dean, K.L. (2004) 'Alteration of neuronal firing properties after in vivo experience in a FosGFP transgenic mouse', *The Journal of Neuroscience: The Official Journal of the Society for Neuroscience*, 24(29), pp. 6466–6475. doi:10.1523/JNEUROSCI.4737-03.2004.

Basso, M.A., Bickford, M.E. and Cang, J. (2021) 'Unraveling circuits of visual perception and cognition through the superior colliculus', *Neuron*, 109(6), pp. 918–937. doi:10.1016/j.neuron.2021.01.013.

Basso, M.A. and May, P.J. (2017) 'Circuits for Action and Cognition: A View from the Superior Colliculus', *Annual Review of Vision Science*, 3, pp. 197–226. doi:10.1146/annurev-vision-102016-061234.

Beier, K.T. *et al.* (2019) 'Topological Organization of Ventral Tegmental Area Connectivity Revealed by Viral-Genetic Dissection of Input-Output Relations.', *Cell reports*, 26(1), pp. 159-167.e6. doi:10.1016/j.celrep.2018.12.040.

Beltramo, R. and Scanziani, M. (2019) 'A collicular visual cortex: Neocortical space for an ancient midbrain visual structure', *Science*, 363(6422), pp. 64–69. doi:10.1126/science.aau7052.

Benavidez, N.L. *et al.* (2021) 'Organization of the inputs and outputs of the mouse superior colliculus', *Nature Communications*, 12(1), p. 4004. doi:10.1038/s41467-021-24241-2.

Bennett, C. *et al.* (2019) 'Higher-Order Thalamic Circuits Channel Parallel Streams of Visual Information in Mice', *Neuron*, 102(2), pp. 477-492.e5. doi:10.1016/j.neuron.2019.02.010.

Bergel, A. *et al.* (2018) 'Local hippocampal fast gamma rhythms precede brain-wide hyperemic patterns during spontaneous rodent REM sleep', *Nature Communications*, 9(1), p. 5364. doi:10.1038/s41467-018-07752-3.

Bergel, A. *et al.* (2020) 'Adaptive modulation of brain hemodynamics across stereotyped running episodes', *Nature Communications*, 11(1), p. 6193. doi:10.1038/s41467-020-19948-7.

Bergeron, A., Matsuo, S. and Guitton, D. (2003) 'Superior colliculus encodes distance to target, not saccade amplitude, in multi-step gaze shifts', *Nature Neuroscience*, 6(4), pp. 404–413. doi:10.1038/nn1027.

Bernal-Casas, D. *et al.* (2017) 'Studying brain circuit function with dynamic causal modeling for optogenetic fMRI', *Neuron*, 93(3), pp. 522-532.e5. doi:10.1016/j.neuron.2016.12.035.

Berwick, J. *et al.* (2008) 'Fine detail of neurovascular coupling revealed by spatiotemporal analysis of the hemodynamic response to single whisker stimulation in rat barrel cortex', *Journal of Neurophysiology*, 99(2), pp. 787–798. doi:10.1152/jn.00658.2007.

Beyeler, A. *et al.* (2016) 'Divergent Routing of Positive and Negative Information from the Amygdala during Memory Retrieval', *Neuron*, 90(2), pp. 348–361. doi:10.1016/j.neuron.2016.03.004.

Bhat, R.V. and Baraban, J.M. (1992) 'High basal expression of zif268 in cortex is dependent on intact noradrenergic system', *European Journal of Pharmacology*, 227(4), pp. 447–448. doi:10.1016/0922-4106(92)90165-r.

Bimbard, C. *et al.* (2018) 'Multi-scale mapping along the auditory hierarchy using high-resolution functional UltraSound in the awake ferret', *eLife*. Edited by A.J. King, 7, p. e35028. doi:10.7554/eLife.35028.

Blaize, K. *et al.* (2020) 'Functional ultrasound imaging of deep visual cortex in awake nonhuman primates', *Proceedings of the National Academy of Sciences*, 117(25), pp. 14453–14463. doi:10.1073/pnas.1916787117.

Blanche, T.J. *et al.* (2005) 'Polytrodes: high-density silicon electrode arrays for large-scale multiunit recording', *Journal of Neurophysiology*, 93(5), pp. 2987–3000. doi:10.1152/jn.01023.2004.

Boehnke, S. *et al.* (2007) 'Adaptation and habituation of visual responses in the superficial and intermediate layers of the superior colliculus (SC)', *Journal of Vision*, 7(9), p. 188. doi:10.1167/7.9.188.

Bognár, A. and Vogels, R. (2021) 'Moving a Shape behind a Slit: Partial Shape Representations in Inferior Temporal Cortex', *The Journal of Neuroscience: The Official Journal of the Society for Neuroscience*, 41(30), pp. 6484–6501. doi:10.1523/JNEUROSCI.0348-21.2021.

Bohlen, M.O., Warren, S. and May, P.J. (2016) 'A Central Mesencephalic Reticular Formation Projection to the Supraoculomotor Area in Macaque Monkeys', *Brain structure & function*, 221(4), pp. 2209–2229. doi:10.1007/s00429-015-1039-2.

Böhm, C. and Lee, A.K. (2020) 'Canonical goal-selective representations are absent from prefrontal cortex in a spatial working memory task requiring behavioral flexibility', *eLife*, 9, p. e63035. doi:10.7554/eLife.63035.

Boido, D. *et al.* (2019) 'Mesoscopic and microscopic imaging of sensory responses in the same animal', *Nature Communications*, 10(1), p. 1110. doi:10.1038/s41467-019-09082-4.

Bollmann, S. and Barth, M. (2021) 'New acquisition techniques and their prospects for the achievable resolution of fMRI', *Progress in Neurobiology*, 207, p. 101936. doi:10.1016/j.pneurobio.2020.101936.

Bonaventura, J. *et al.* (2019) 'High-potency ligands for DREADD imaging and activation in rodents and monkeys', *Nature Communications*, 10(1), p. 4627. doi:10.1038/s41467-019-12236-z.

Booth, D.A. (1968) 'Mechanism of Action of Norepinephrine in Eliciting an Eating Response on Injection into the Rat Hypothalamus', *Journal of Pharmacology and Experimental Therapeutics*, 160(2), pp. 336–348.

Bortone, D.S., Olsen, S.R. and Scanziani, M. (2014) 'Translaminar inhibitory cells recruited by layer 6 corticothalamic neurons suppress visual cortex', *Neuron*, 82(2), pp. 474–485. doi:10.1016/j.neuron.2014.02.021.

Boyden, E.S. *et al.* (2005) 'Millisecond-timescale, genetically targeted optical control of neural activity', *Nature Neuroscience*, 8(9), pp. 1263–1268. doi:10.1038/nn1525.

Branco, T. and Redgrave, P. (2020) 'The Neural Basis of Escape Behavior in Vertebrates', *Annual Review of Neuroscience*, 43, pp. 417–439. doi:10.1146/annurev-neuro-100219-122527.

Brunner, C. *et al.* (2020) 'A Platform for Brain-wide Volumetric Functional Ultrasound Imaging and Analysis of Circuit Dynamics in Awake Mice', *Neuron*, 108(5), pp. 861-875.e7. doi:10.1016/j.neuron.2020.09.020.

Burke, R.E. (2007) 'Sir Charles Sherrington's the integrative action of the nervous system: a centenary appreciation', *Brain: A Journal of Neurology*, 130(Pt 4), pp. 887–894. doi:10.1093/brain/awm022.

Büttner, U., Büttner-Ennever, J.A. and Henn, V. (1977) 'Vertical eye movement related unit activity in the rostral mesencephalic reticular formation of the alert monkey', *Brain Research*, 130(2), pp. 239–252. doi:10.1016/0006-8993(77)90273-6.

Buzsáki, G. (2004) 'Large-scale recording of neuronal ensembles', *Nature Neuroscience*, 7(5), pp. 446–451. doi:10.1038/nn1233.

Buzsáki, G. *et al.* (2015) 'Tools for probing local circuits: high-density silicon probes combined with optogenetics', *Neuron*, 86(1), pp. 92–105. doi:10.1016/j.neuron.2015.01.028.

Buzsáki, G. and Watson, B.O. (2012) 'Brain rhythms and neural syntax: implications for efficient coding of cognitive content and neuropsychiatric disease.', *Dialogues in Clinical Neuroscience*, 14(4), pp. 345–367.

Byun, H. *et al.* (2016) 'Molecular features distinguish ten neuronal types in the mouse superficial superior colliculus', *The Journal of Comparative Neurology*, 524(11), pp. 2300–2321. doi:10.1002/cne.23952.

Calabrò, R.S. *et al.* (2015) 'Neural correlates of consciousness: what we know and what we have to learn!', *Neurological Sciences: Official Journal of the Italian Neurological Society and of the Italian Society of Clinical Neurophysiology*, 36(4), pp. 505–513. doi:10.1007/s10072-015-2072-x.

Cameron, A.A. *et al.* (1995) 'The efferent projections of the periaqueductal gray in the rat: a Phaseolus vulgaris-leucoagglutinin study. II. Descending projections', *The Journal of Comparative Neurology*, 351(4), pp. 585–601. doi:10.1002/cne.903510408.

Capelli, P. *et al.* (2017) 'Locomotor speed control circuits in the caudal brainstem', *Nature*, 551(7680), pp. 373–377. doi:10.1038/nature24064.

Carello, C.D. and Krauzlis, R.J. (2004) 'Manipulating intent: evidence for a causal role of the superior colliculus in target selection', *Neuron*, 43(4), pp. 575–583. doi:10.1016/j.neuron.2004.07.026.

Carrillo-Reid, L. *et al.* (2019) 'Controlling Visually Guided Behavior by Holographic Recalling of Cortical Ensembles', *Cell*, 178(2), pp. 447-457.e5. doi:10.1016/j.cell.2019.05.045.

Casagrande, V.A. *et al.* (1972) 'Superior colliculus of the tree shrew: a structural and functional subdivision into superficial and deep layers', *Science (New York, N.Y.)*, 177(4047), pp. 444–447. doi:10.1126/science.177.4047.444.

Cavanaugh, J. *et al.* (2012) 'Optogenetic inactivation modifies monkey visuomotor behavior', *Neuron*, 76(5), pp. 901–907. doi:10.1016/j.neuron.2012.10.016.

Cearley, C.N. *et al.* (2008) 'Expanded repertoire of AAV vector serotypes mediate unique patterns of transduction in mouse brain', *Molecular Therapy: The Journal of the American Society of Gene Therapy*, 16(10), pp. 1710–1718. doi:10.1038/mt.2008.166.

Chamberlin, N.L. *et al.* (1998) 'Recombinant adeno-associated virus vector: use for transgene expression and anterograde tract tracing in the CNS', *Brain Research*, 793(1–2), pp. 169–175. doi:10.1016/s0006-8993(98)00169-3.

Chaudhuri, A. *et al.* (1997) 'Dual activity maps in primate visual cortex produced by different temporal patterns of zif268 mRNA and protein expression', *Proceedings of the National Academy of Sciences of the United States of America*, 94(6), pp. 2671–2675. doi:10.1073/pnas.94.6.2671.

Chaudhuri, A., Matsubara, J.A. and Cynader, M.S. (1995) 'Neuronal activity in primate visual cortex assessed by immunostaining for the transcription factor Zif268', *Visual Neuroscience*, 12(1), pp. 35–50. doi:10.1017/s095252380000729x.

Chaudhury, D. *et al.* (2013) 'Rapid regulation of depression-related behaviours by control of midbrain dopamine neurons', *Nature*, 493(7433), pp. 532–536. doi:10.1038/nature11713.

Chen, Q. *et al.* (2012) 'Imaging neural activity using Thy1-GCaMP transgenic mice', *Neuron*, 76(2), pp. 297–308. doi:10.1016/j.neuron.2012.07.011.

# References

Chen, T.-W. *et al.* (2013) 'Ultrasensitive fluorescent proteins for imaging neuronal activity', *Nature*, 499(7458), pp. 295–300. doi:10.1038/nature12354.

Chernov, M.M. *et al.* (2018) 'Functionally specific optogenetic modulation in primate visual cortex', *Proceedings of the National Academy of Sciences of the United States of America*, 115(41), pp. 10505–10510. doi:10.1073/pnas.1802018115.

Chevalier, G. *et al.* (1981) 'Evidence for a GABAergic inhibitory nigrotectal pathway in the rat', *Neuroscience Letters*, 21(1), pp. 67–70. doi:10.1016/0304-3940(81)90059-8.

Chevalier, G., Vacher, S. and Deniau, J.M. (1984) 'Inhibitory nigral influence on tectospinal neurons, a possible implication of basal ganglia in orienting behavior', *Experimental Brain Research*, 53(2), pp. 320–326. doi:10.1007/BF00238161.

Cho, J.H., Rendall, S.D. and Gray, J.M. (2017) 'Brain-wide maps of Fos expression during fear learning and recall', *Learning and Memory*, 24(4), pp. 169–181. doi:10.1101/lm.044446.116.

Chou, X.L. *et al.* (2018) 'Inhibitory gain modulation of defense behaviors by zona incerta', *Nature Communications*, 9(1). doi:10.1038/s41467-018-03581-6.

Christie, I.N. *et al.* (2013) 'FMRI response to blue light delivery in the naïve brain: Implications for combined optogenetic fMRI studies', *NeuroImage*, 66, pp. 634–641. doi:10.1016/j.neuroimage.2012.10.074.

Chung, K. *et al.* (2013) 'Structural and molecular interrogation of intact biological systems', *Nature*, 497(7449), pp. 332–337. doi:10.1038/nature12107.

Chvátal, A. (2015) 'Discovering the Structure of Nerve Tissue: Part 2: Gabriel Valentin, Robert Remak, and Jan Evangelista Purkyně', *Journal of the History of the Neurosciences*, 24(4), pp. 326–351. doi:10.1080/0964704X.2014.977677.

Clancy, K.B., Orsolic, I. and Mrsic-Flogel, T.D. (2019) 'Locomotion-dependent remapping of distributed cortical networks', *Nature Neuroscience*, 22(5), pp. 778–786. doi:10.1038/s41593-019-0357-8.

Coe, B.C. and Munoz, D.P. (2017) 'Mechanisms of saccade suppression revealed in the anti-saccade task', *Philosophical Transactions of the Royal Society B: Biological Sciences*, 372(1718), p. 20160192. doi:10.1098/rstb.2016.0192.

Cohen, B. and Henn, V. (1972) 'Unit activity in the pontine reticular formation associated with eye movements', *Brain Research*, 46, pp. 403–410. doi:10.1016/0006-8993(72)90030-3.

Cohen, J.Y. *et al.* (2012) 'Neuron-type-specific signals for reward and punishment in the ventral tegmental area', *Nature*, 482(7383), pp. 85–88. doi:10.1038/nature10754.

Coizet, V. *et al.* (2009) 'Short-latency visual input to the subthalamic nucleus is provided by the midbrain superior colliculus', *The Journal of Neuroscience: The Official Journal of the Society for Neuroscience*, 29(17), pp. 5701–5709. doi:10.1523/JNEUROSCI.0247-09.2009.

Coman, I.M. (2005) 'Christian Andreas Doppler--the man and his legacy', *European Journal of Echocardiography: The Journal of the Working Group on Echocardiography of the European Society of Cardiology*, 6(1), pp. 7–10. doi:10.1016/j.euje.2004.06.004.

Comoli, E. *et al.* (2003) 'A direct projection from superior colliculus to substantia nigra for detecting salient visual events', *Nature Neuroscience*, 6(9), pp. 974–980. doi:10.1038/nn1113.

Cook, S.J. *et al.* (2019) 'Whole-animal connectomes of both Caenorhabditis elegans sexes', *Nature*, 571(7763), pp. 63–71. doi:10.1038/s41586-019-1352-7.

Corbetta, M. and Shulman, G.L. (2002) 'Control of goal-directed and stimulus-driven attention in the brain', *Nature Reviews. Neuroscience*, 3(3), pp. 201–215. doi:10.1038/nrn755.

Corrigan, J.F. (1924) 'STEPHEN GRAY (1696—1736): An Early Electrical Experimenter', *Science Progress in the Twentieth Century (1919-1933)*, 19(73), pp. 102–114.

Couto, J. *et al.* (2021) 'Chronic, cortex-wide imaging of specific cell populations during behavior', *Nature Protocols*, 16(7), pp. 3241–3263. doi:10.1038/s41596-021-00527-z.

Cover, C.G. *et al.* (2021) 'Whole brain dynamics during optogenetic self-stimulation of the medial prefrontal cortex in mice', *Communications Biology*, 4(1), p. 66. doi:10.1038/s42003-020-01612-x.

Cowie, R.J. and Robinson, D.L. (1994) 'Subcortical contributions to head movements in macaques. I. Contrasting effects of electrical stimulation of a medial pontomedullary region and the superior colliculus', *Journal of Neurophysiology*, 72(6), pp. 2648–2664. doi:10.1152/jn.1994.72.6.2648.

Cowie, S.E. (2000) 'A place in history: Paul Broca and cerebral localization', *Journal of Investigative Surgery: The Official Journal of the Academy of Surgical Research*, 13(6), pp. 297–298. doi:10.1080/089419300750059334.

Crapse, T.B., Lau, H. and Basso, M.A. (2018) 'A Role for the Superior Colliculus in Decision Criteria', *Neuron*, 97(1), pp. 181-194.e6. doi:10.1016/j.neuron.2017.12.006.

Csicsvari, J. *et al.* (2003) 'Massively Parallel Recording of Unit and Local Field Potentials With Silicon-Based Electrodes', *Journal of Neurophysiology*, 90(2), pp. 1314–1323. doi:10.1152/jn.00116.2003.

Dana, H. *et al.* (2019) 'High-performance calcium sensors for imaging activity in neuronal populations and microcompartments', *Nature Methods*, 16(7), pp. 649–657. doi:10.1038/s41592-019-0435-6.

Dean, P., Mitchell, I.J. and Redgrave, P. (1988) 'Responses resembling defensive behaviour produced by microinjection of glutamate into superior colliculus of rats', *Neuroscience*, 24(2), pp. 501–510. doi:10.1016/0306-4522(88)90345-4.

Dean, P., Redgrave, P. and Westby, G.W. (1989) 'Event or emergency? Two response systems in the mammalian superior colliculus', *Trends in Neurosciences*, 12(4), pp. 137–147. doi:10.1016/0166-2236(89)90052-0.

Deisseroth, K. (2015) 'Optogenetics: 10 years of microbial opsins in neuroscience', *Nature Neuroscience*, 18(9), pp. 1213–1225. doi:10.1038/nn.4091.

Demené, C. *et al.* (2015) 'Spatiotemporal Clutter Filtering of Ultrafast Ultrasound Data Highly Increases Doppler and fUltrasound Sensitivity', *IEEE Transactions on Medical Imaging*, 34(11), pp. 2271–2285. doi:10.1109/TMI.2015.2428634.

Deng, H., Xiao, X. and Wang, Z. (2016) 'Periaqueductal Gray Neuronal Activities Underlie Different Aspects of Defensive Behaviors', *The Journal of Neuroscience: The Official Journal of the Society for Neuroscience*, 36(29), pp. 7580–7588. doi:10.1523/JNEUROSCI.4425-15.2016.

Deniau, J.M. *et al.* (2007) 'The pars reticulata of the substantia nigra: a window to basal ganglia output', *Progress in Brain Research*, 160, pp. 151–172. doi:10.1016/S0079-6123(06)60009-5.

Deniau, J.M., Menetrey, A. and Charpier, S. (1996) 'The lamellar organization of the rat substantia nigra pars reticulata: segregated patterns of striatal afferents and relationship to the topography of corticostriatal projections', *Neuroscience*, 73(3), pp. 761–781. doi:10.1016/0306-4522(96)00088-7.

Denk, W. *et al.* (1994) 'Anatomical and functional imaging of neurons using 2-photon laser scanning microscopy', *Journal of Neuroscience Methods*, 54(2), pp. 151–162. doi:10.1016/0165-0270(94)90189-9.

Denk, W., Strickler, J.H. and Webb, W.W. (1990) 'Two-photon laser scanning fluorescence microscopy', *Science (New York, N.Y.)*, 248(4951), pp. 73–76. doi:10.1126/science.2321027.

Denys, K. *et al.* (2004) 'The processing of visual shape in the cerebral cortex of human and nonhuman primates: a functional magnetic resonance imaging study', *The Journal of Neuroscience: The Official Journal of the Society for Neuroscience*, 24(10), pp. 2551–2565. doi:10.1523/JNEUROSCI.3569-03.2004.

Desai, M. *et al.* (2011) 'Mapping brain networks in awake mice using combined optical neural control and fMRI', *Journal of Neurophysiology*, 105(3), pp. 1393–1405. doi:10.1152/jn.00828.2010.

Desimone, R. *et al.* (1984) 'Stimulus-selective properties of inferior temporal neurons in the macaque', *Journal of Neuroscience*, 4(8), pp. 2051–2062. doi:10.1523/JNEUROSCI.04-08-02051.1984.

DesJardin, J.T. *et al.* (2013) 'Defense-Like Behaviors Evoked by Pharmacological Disinhibition of the Superior Colliculus in the Primate', *Journal of Neuroscience*, 33(1), pp. 150–155. doi:10.1523/JNEUROSCI.2924-12.2013.

Desjardins, M. *et al.* (2019) 'Awake Mouse Imaging: From Two-Photon Microscopy to Blood Oxygen Level-Dependent Functional Magnetic Resonance Imaging', *Biological Psychiatry. Cognitive Neuroscience and Neuroimaging*, 4(6), pp. 533–542. doi:10.1016/j.bpsc.2018.12.002.

Deubner, J., Coulon, P. and Diester, I. (2019) 'Optogenetic approaches to study the mammalian brain', *Current Opinion in Structural Biology*, 57, pp. 157–163. doi:10.1016/j.sbi.2019.04.003.

Dizeux, A. *et al.* (2019) 'Functional ultrasound imaging of the brain reveals propagation of task-related brain activity in behaving primates', *Nature Communications*, 10(1), p. 1400. doi:10.1038/s41467-019-09349-w.

Dommett, E. *et al.* (2005) 'How visual stimuli activate dopaminergic neurons at short latency', *Science (New York, N.Y.)*, 307(5714), pp. 1476–1479. doi:10.1126/science.1107026.

Dopfel, D. and Zhang, N. (2018) 'Mapping stress networks using functional magnetic resonance imaging in awake animals', *Neurobiology of Stress*, 9, pp. 251–263. doi:10.1016/j.ynstr.2018.06.002.

Dorris, M.C., Olivier, E. and Munoz, D.P. (2007) 'Competitive integration of visual and preparatory signals in the superior colliculus during saccadic programming', *The Journal of Neuroscience: The Official Journal of the Society for Neuroscience*, 27(19), pp. 5053–5062. doi:10.1523/JNEUROSCI.4212-06.2007.

Dräger, U.C. and Hubel, D.H. (1975) 'Responses to visual stimulation and relationship between visual, auditory, and somatosensory inputs in mouse superior colliculus', *Journal of Neurophysiology*, 38(3), pp. 690–713. doi:10.1152/jn.1975.38.3.690.

Dragunow, M. and Robertson, H.A. (1987) 'Kindling stimulation induces c-fos protein(s) in granule cells of the rat dentate gyrus', *Nature*, 329(6138), pp. 441–442. doi:10.1038/329441a0.

Drake, K.L. *et al.* (1988) 'Performance of planar multisite microprobes in recording extracellular single-unit intracortical activity', *IEEE transactions on bio-medical engineering*, 35(9), pp. 719–732. doi:10.1109/10.7273.

Drew, P.J. (2019) 'Vascular and neural basis of the BOLD signal', *Current Opinion in Neurobiology*, 58, pp. 61–69. doi:10.1016/j.conb.2019.06.004.

Duan, C.A. *et al.* (2021) 'Collicular circuits for flexible sensorimotor routing', *Nature Neuroscience*, 24(8), pp. 1110–1120. doi:10.1038/s41593-021-00865-x.

# References

Duan, C.A., Erlich, J.C. and Brody, C.D. (2015) 'Requirement of Prefrontal and Midbrain Regions for Rapid Executive Control of Behavior in the Rat', *Neuron*, 86(6), pp. 1491–1503. doi:10.1016/j.neuron.2015.05.042.

Dumoulin, S.O. *et al.* (2018) 'Ultra-high field MRI: Advancing systems neuroscience towards mesoscopic human brain function', *NeuroImage*, 168, pp. 345–357. doi:10.1016/j.neuroimage.2017.01.028.

Dupont, J.-C. (2018) 'Historical perspective on neuroembryology: Wilhelm His and his contemporaries', *Genesis (New York, N.Y.: 2000)*, 56(6–7), p. e23218. doi:10.1002/dvg.23218.

Ebina, T. *et al.* (2019) 'Arm movements induced by noninvasive optogenetic stimulation of the motor cortex in the common marmoset', *Proceedings of the National Academy of Sciences*, 116(45), pp. 22844–22850. doi:10.1073/pnas.1903445116.

Edelman, B.J. *et al.* (2021) 'High-sensitivity detection of optogenetically-induced neural activity with functional ultrasound imaging', *NeuroImage*, 242, p. 118434. doi:10.1016/j.neuroimage.2021.118434.

Edelman, B.J. and Macé, E. (2021) 'Functional ultrasound brain imaging: Bridging networks, neurons, and behavior', *Current Opinion in Biomedical Engineering*, 18, p. 100286. doi:10.1016/j.cobme.2021.100286.

Ekstrom, A. (2010) 'How and when the fMRI BOLD signal relates to underlying neural activity: The danger in dissociation', *Brain Research Reviews*, 62(2), pp. 233–244. doi:https://doi.org/10.1016/j.brainresrev.2009.12.004.

Ellis, E.M. *et al.* (2016) 'Shared and distinct retinal input to the mouse superior colliculus and dorsal lateral geniculate nucleus', *Journal of Neurophysiology*, 116(2), pp. 602–610. doi:10.1152/jn.00227.2016.

Endo, T. *et al.* (2003) 'Characteristics of GABAergic neurons in the superficial superior colliculus in mice', *Neuroscience Letters*, 346(1–2), pp. 81–84. doi:10.1016/s0304-3940(03)00570-6.

Errico, C. *et al.* (2016) 'Transcranial functional ultrasound imaging of the brain using microbubble-enhanced ultrasensitive Doppler', *NeuroImage*, 124, pp. 752–761. doi:10.1016/j.neuroimage.2015.09.037.

Ertürk, A. *et al.* (2012) 'Three-dimensional imaging of solvent-cleared organs using 3DISCO', *Nature Protocols*, 7(11), pp. 1983–1995. doi:10.1038/nprot.2012.119.

Evans, D.A. *et al.* (2018) 'A synaptic threshold mechanism for computing escape decisions', *Nature*, 558(7711), pp. 590–594. doi:10.1038/s41586-018-0244-6.

Ewing, S.G., Porr, B. and Pratt, J.A. (2013) 'Deep brain stimulation of the mediodorsal thalamic nucleus yields increases in the expression of zif-268 but not c-fos in the frontal cortex', *Journal of Chemical Neuroanatomy*, 52, pp. 20–24. doi:10.1016/j.jchemneu.2013.04.002.

Fadok, J.P. *et al.* (2017) 'A competitive inhibitory circuit for selection of active and passive fear responses', *Nature*, 542(7639), pp. 96–99. doi:10.1038/nature21047.

Fan, X. and Markram, H. (2019) 'A Brief History of Simulation Neuroscience', *Frontiers in Neuroinformatics*, 13, p. 32. doi:10.3389/fninf.2019.00032.

Féger, J., Bevan, M. and Crossman, A.R. (1994) 'The projections from the parafascicular thalamic nucleus to the subthalamic nucleus and the striatum arise from separate neuronal populations: a comparison with the corticostriatal and corticosubthalamic efferents in a retrograde fluorescent double-labelling study', *Neuroscience*, 60(1), pp. 125–132. doi:10.1016/0306-4522(94)90208-9.

Feigin, L. *et al.* (2021) 'Sparse Coding in Temporal Association Cortex Improves Complex Sound Discriminability', *Journal of Neuroscience*, 41(33), pp. 7048–7064. doi:10.1523/JNEUROSCI.3167-20.2021.

Feinberg, D.A. *et al.* (2010) 'Multiplexed echo planar imaging for sub-second whole brain FMRI and fast diffusion imaging', *PloS One*, 5(12), p. e15710. doi:10.1371/journal.pone.0015710.

Fenno, L., Yizhar, O. and Deisseroth, K. (2011) 'The development and application of optogenetics', *Annual Review of Neuroscience*, 34, pp. 389–412. doi:10.1146/annurev-neuro-061010-113817.

Ferenczi, E.A. *et al.* (2016) 'Prefrontal cortical regulation of brainwide circuit dynamics and reward-related behavior', *Science (New York, N.Y.)*, 351(6268), p. aac9698. doi:10.1126/science.aac9698.

Ferrier, J. *et al.* (2020) 'Functional imaging evidence for task-induced deactivation and disconnection of a major default mode network hub in the mouse brain', *Proceedings of the National Academy of Sciences*, 117(26), pp. 15270–15280. doi:10.1073/pnas.1920475117.

Fife, K.H. *et al.* (2017) 'Causal role for the subthalamic nucleus in interrupting behavior', *eLife*, 6, pp. 1–13. doi:10.7554/eLife.27689.

Filippi, M. *et al.* (2018) 'Functional MRI in Idiopathic Parkinson's Disease', *International Review of Neurobiology*, 141, pp. 439–467. doi:10.1016/bs.irn.2018.08.005.

Fisher, S.D. and Reynolds, J.N.J. (2014) 'The intralaminar thalamus-an expressway linking visual stimuli to circuits determining agency and action selection', *Frontiers in Behavioral Neuroscience*, 8, p. 115. doi:10.3389/fnbeh.2014.00115.

Fodstad, H. (2001) 'The Neuron Theory', *Stereotactic and Functional Neurosurgery*, 77(1–4), pp. 20–24. doi:10.1159/000064596.

Förster, D. *et al.* (2017) 'An optogenetic toolbox for unbiased discovery of functionally connected cells in neural circuits', *Nature Communications*, 8(1), p. 116. doi:10.1038/s41467-017-00160-z.

Förster, D. *et al.* (2020) 'Retinotectal circuitry of larval zebrafish is adapted to detection and pursuit of prey', *eLife*, 9, p. e58596. doi:10.7554/eLife.58596.

Foster, F.S. *et al.* (2000) 'Advances in ultrasound biomicroscopy', *Ultrasound in Medicine & Biology*, 26(1), pp. 1–27. doi:10.1016/s0301-5629(99)00096-4.

De Franceschi, G. *et al.* (2016) 'Vision Guides Selection of Freeze or Flight Defense Strategies in Mice', *Current Biology*, 26(16), pp. 2150–2154. doi:10.1016/j.cub.2016.06.006.

Franceschi, G.D. and Solomon, S.G. (2020) 'Dynamic Contextual Modulation in Superior Colliculus of Awake Mouse', *eNeuro*, 7(5). doi:10.1523/ENEURO.0131-20.2020.

Fratzl, A. *et al.* (2021) 'Flexible inhibitory control of visually evoked defensive behavior by the ventral lateral geniculate nucleus', *Neuron*, 109(23), pp. 3810-3822.e9. doi:10.1016/j.neuron.2021.09.003.

Fukuda, M., Poplawsky, A.J. and Kim, S.-G. (2016) 'Submillimeter-resolution fMRI: Toward understanding local neural processing', *Progress in Brain Research*, 225, pp. 123–152. doi:10.1016/bs.pbr.2016.03.003.

Fukuda, M., Poplawsky, A.J. and Kim, S.-G. (2021) 'Time-dependent spatial specificity of high-resolution fMRI: insights into mesoscopic neurovascular coupling', *Philosophical Transactions of the Royal Society of London. Series B, Biological Sciences*, 376(1815), p. 20190623. doi:10.1098/rstb.2019.0623.

Furigo, I.C. *et al.* (2010) 'The role of the superior colliculus in predatory hunting', *Neuroscience*, 165(1), pp. 1–15. doi:10.1016/j.neuroscience.2009.10.004.

Furlan, M., Smith, A.T. and Walker, R. (2015) 'Activity in the human superior colliculus relating to endogenous saccade preparation and execution', *Journal of Neurophysiology*, 114(2), pp. 1048–1058. doi:10.1152/jn.00825.2014.

Gale, S.D. and Murphy, G.J. (2014) 'Distinct representation and distribution of visual information by specific cell types in mouse superficial superior colliculus', *The Journal of neuroscience : the official journal of the Society for Neuroscience*, 34(40), pp. 13458–13471. doi:10.1523/JNEUROSCI.2768-14.2014.

Gale, S.D. and Murphy, G.J. (2016) 'Active Dendritic Properties and Local Inhibitory Input Enable Selectivity for Object Motion in Mouse Superior Colliculus Neurons.', *The Journal of neuroscience : the official journal of the Society for Neuroscience*, 36(35), pp. 9111–23. doi:10.1523/JNEUROSCI.0645-16.2016.

Gale, S.D. and Murphy, G.J. (2018) 'Distinct cell types in the superficial superior colliculus project to the dorsal lateral geniculate and lateral posterior thalamic nuclei', *Journal of Neurophysiology*, 120(3), pp. 1286–1292. doi:10.1152/jn.00248.2018.

Galliano, E., Mazzarello, P. and D'Angelo, E. (2010) 'Discovery and rediscoveries of Golgi cells', *The Journal of Physiology*, 588(Pt 19), pp. 3639–3655. doi:10.1113/jphysiol.2010.189605.

Gandhi, N.J. and Katnani, H.A. (2011) 'Motor functions of the superior colliculus', *Annual Review of Neuroscience*, 34, pp. 205–231. doi:10.1146/annurev-neuro-061010-113728.

Garson, J. (2015) 'The birth of information in the brain: Edgar Adrian and the vacuum tube', *Science in Context*, 28(1), pp. 31–52. doi:10.1017/S0269889714000313.

Gasperini, R.J. *et al.* (2017) 'How does calcium interact with the cytoskeleton to regulate growth cone motility during axon pathfinding?', *Molecular and Cellular Neurosciences*, 84, pp. 29–35. doi:10.1016/j.mcn.2017.07.006.

Gengyo-Ando, K. *et al.* (2017) 'A new platform for long-term tracking and recording of neural activity and simultaneous optogenetic control in freely behaving Caenorhabditis elegans', *Journal of Neuroscience Methods*, 286, pp. 56–68. doi:10.1016/j.jneumeth.2017.05.017.

Gerfen, C.R., Paletzki, R. and Heintz, N. (2013) 'GENSAT BAC cre-recombinase driver lines to study the functional organization of cerebral cortical and basal ganglia circuits.', *Neuron*, 80(6), pp. 1368–1383. doi:10.1016/j.neuron.2013.10.016.

Gerits, A. *et al.* (2012) 'Optogenetically-induced behavioral and functional network changes in primates', *Current biology : CB*, 22(18), pp. 1722–1726. doi:10.1016/j.cub.2012.07.023.

Gesnik, M. *et al.* (2017) '3D functional ultrasound imaging of the cerebral visual system in rodents', *NeuroImage*, 149, pp. 267–274. doi:10.1016/j.neuroimage.2017.01.071.

Gilbert, C.D., Sigman, M. and Crist, R.E. (2001) 'The neural basis of perceptual learning', *Neuron*, 31(5), pp. 681–697. doi:10.1016/s0896-6273(01)00424-x.

Gingerich, M.D. *et al.* (2001) 'A 256-Site 3D CMOS Microelectrode Array for Multipoint Stimulation and Recording in the Central Nervous System', in Obermeier, E. (ed.) *Transducers '01 Eurosensors XV*. Berlin, Heidelberg: Springer, pp. 416–419. doi:10.1007/978-3-642-59497-7_99.

Giorgi, A. *et al.* (2017) 'Brain-wide Mapping of Endogenous Serotonergic Transmission via Chemogenetic fMRI', *Cell Reports*, 21(4), pp. 910–918. doi:10.1016/j.celrep.2017.09.087.

# References

Gkagkanasiou, M. *et al.* (2016) 'USPIO-Enhanced MRI Neuroimaging: A Review', *Journal of Neuroimaging: Official Journal of the American Society of Neuroimaging*, 26(2), pp. 161–168. doi:10.1111/jon.12318.

Glanzman, D.L. (2009) 'Habituation in Aplysia: The Cheshire Cat of neurobiology', *Neurobiology of Learning and Memory*, 92(2), pp. 147–154. doi:10.1016/j.nlm.2009.03.005.

Godement, P., Salaün, J. and Imbert, M. (1984) 'Prenatal and postnatal development of retinogeniculate and retinocollicular projections in the mouse', *The Journal of Comparative Neurology*, 230(4), pp. 552–575. doi:10.1002/cne.902300406.

Goelman, G. *et al.* (2021) 'Altered sensorimotor fMRI directed connectivity in Parkinson's disease patients', *The European Journal of Neuroscience*, 53(6), pp. 1976–1987. doi:10.1111/ejn.15053.

Goldberg, M.E. and Wurtz, R.H. (1972) 'Activity of superior colliculus in behaving monkey. II. Effect of attention on neuronal responses.', *Journal of Neurophysiology*, 35(4), pp. 560–574. doi:10.1152/jn.1972.35.4.560.

Gomez, J.L. *et al.* (2017) 'Chemogenetics revealed: DREADD occupancy and activation via converted clozapine', *Science (New York, N.Y.)*, 357(6350), pp. 503–507. doi:10.1126/science.aan2475.

Gonzales, B.J. *et al.* (2020) 'Subregion-specific rules govern the distribution of neuronal immediate-early gene induction', *Proceedings of the National Academy of Sciences*, 117(38), pp. 23304–23310. doi:10.1073/pnas.1913658116.

Goutaudier, R. *et al.* (2020) 'Compound 21, a two-edged sword with both DREADD-selective and off-target outcomes in rats', *PloS One*, 15(9), p. e0238156. doi:10.1371/journal.pone.0238156.

Graham, J. and Casagrande, V.A. (1980) 'A light microscopic and electron microscopic study of the superficial layers of the superior colliculus of the tree shrew (Tupaia glis)', *The Journal of Comparative Neurology*, 191(1), pp. 133–151. doi:10.1002/cne.901910108.

Grandjean, J. *et al.* (2017) 'Structural Basis of Large-Scale Functional Connectivity in the Mouse', *The Journal of Neuroscience: The Official Journal of the Society for Neuroscience*, 37(34), pp. 8092–8101. doi:10.1523/JNEUROSCI.0438-17.2017.

Greenberg, M.E., Ziff, E.B. and Greene, L.A. (1986) 'Stimulation of neuronal acetylcholine receptors induces rapid gene transcription', *Science (New York, N.Y.)*, 234(4772), pp. 80–83. doi:10.1126/science.3749894.

Grillner, S. and Robertson, B. (2016) 'The Basal Ganglia Over 500 Million Years', *Current biology: CB*, 26(20), pp. R1088–R1100. doi:10.1016/j.cub.2016.06.041.

Grimm, R. and Tischmeyer, W. (1997) 'Complex patterns of immediate early gene induction in rat brain following brightness discrimination training and pseudotraining', *Behavioural Brain Research*, 84(1–2), pp. 109–116. doi:10.1016/s0166-4328(97)83330-x.

Grodzinsky, Y., Pieperhoff, P. and Thompson, C. (2021) 'Stable brain loci for the processing of complex syntax: A review of the current neuroimaging evidence', *Cortex; a Journal Devoted to the Study of the Nervous System and Behavior*, 142, pp. 252–271. doi:10.1016/j.cortex.2021.06.003.

Gross, C. (2013) 'Some Revolutions in Neuroscience', *Journal of Cognitive Neuroscience*, 25(1), pp. 4–13. doi:10.1162/jocn_a_00308.

Gross, C.T. and Canteras, N.S. (2012) 'The many paths to fear', *Nature Reviews Neuroscience*. Nat Rev Neurosci, pp. 651–658. doi:10.1038/nrn3301.

Grosso, A. *et al.* (2018) 'A neuronal basis for fear discrimination in the lateral amygdala', *Nature Communications*, 9(1). doi:10.1038/s41467-018-03682-2.

Grynkiewicz, G., Poenie, M. and Tsien, R.Y. (1985) 'A new generation of Ca2+ indicators with greatly improved fluorescence properties', *The Journal of Biological Chemistry*, 260(6), pp. 3440–3450.

Guenthner, C.J. *et al.* (2013) 'Permanent genetic access to transiently active neurons via TRAP: targeted recombination in active populations', *Neuron*, 78(5), pp. 773–784. doi:10.1016/j.neuron.2013.03.025.

Guru, A. *et al.* (2015) 'Making Sense of Optogenetics', *International Journal of Neuropsychopharmacology*, 18(11), p. pyv079. doi:10.1093/ijnp/pyv079.

Gutierrez-Barragan, D. *et al.* (2022) 'Unique spatiotemporal fMRI dynamics in the awake mouse brain', *Current Biology* [Preprint]. doi:10.1016/j.cub.2021.12.015.

Guzowski, J.F. *et al.* (1999) 'Environment-specific expression of the immediate-early gene Arc in hippocampal neuronal ensembles', *Nature Neuroscience*, 2(12), pp. 1120–1124. doi:10.1038/16046.

Guzowski, J.F. *et al.* (2001) 'Experience-dependent gene expression in the rat hippocampus after spatial learning: a comparison of the immediate-early genes Arc, c-fos, and zif268', *The Journal of Neuroscience: The Official Journal of the Society for Neuroscience*, 21(14), pp. 5089–5098.

Guzowski, J.F. and Worley, P.F. (2001) 'Cellular compartment analysis of temporal activity by fluorescence in situ hybridization (catFISH)', *Current Protocols in Neuroscience*, Chapter 1, p. Unit 1.8. doi:10.1002/0471142301.ns0108s15.

Haas, L.F. (2003) 'Fridtjof Nansen (1861-1930)', *Journal of Neurology, Neurosurgery, and Psychiatry*, 74(4), p. 515. doi:10.1136/jnnp.74.4.515.

van Haasteren, G. *et al.* (1999) 'Calcium signalling and gene expression', *Journal of Receptor and Signal Transduction Research*, 19(1–4), pp. 481–492. doi:10.3109/10799899909036666.

Hagner, M. (2012) 'The electrical excitability of the brain: toward the emergence of an experiment', *Journal of the History of the Neurosciences*, 21(3), pp. 237–249. doi:10.1080/0964704X.2011.595634.

Hampel, S. *et al.* (2015) 'A neural command circuit for grooming movement control', *eLife*. Edited by A. Borst, 4, p. e08758. doi:10.7554/eLife.08758.

Han, W. *et al.* (2017) 'Integrated Control of Predatory Hunting by the Central Nucleus of the Amygdala', *Cell*, 168(1–2), pp. 311-324.e18. doi:10.1016/j.cell.2016.12.027.

Han, Y. *et al.* (2018) 'The logic of single-cell projections from visual cortex', *Nature*, 556(7699), pp. 51–56. doi:10.1038/nature26159.

Harris, A.P. *et al.* (2015) 'Imaging learned fear circuitry in awake mice using fMRI', *The European Journal of Neuroscience*, 42(5), pp. 2125–2134. doi:10.1111/ejn.12939.

Harris, J.A. *et al.* (2019) 'Hierarchical organization of cortical and thalamic connectivity', *Nature*, 575(7781), pp. 195–202. doi:10.1038/s41586-019-1716-z.

Harting, J.K., Updyke, B. V. and Van Lieshout, D.P. (2001) 'Striatal projections from the cat visual thalamus', *European Journal of Neuroscience*, 14(5), pp. 893–896. doi:10.1046/j.0953-816X.2001.01712.x.

Haustead, D.J. *et al.* (2008) 'Functional topography and integration of the contralateral and ipsilateral retinocollicular projections of ephrin-A-/- mice', *The Journal of Neuroscience: The Official Journal of the Society for Neuroscience*, 28(29), pp. 7376–7386. doi:10.1523/JNEUROSCI.1135-08.2008.

Headley, D.B. *et al.* (2019) 'Embracing Complexity in Defensive Networks', *Neuron*, 103(2), pp. 189–201. doi:10.1016/j.neuron.2019.05.024.

Hebb, D.O. (1949) *The organization of behavior; a neuropsychological theory*. Oxford, England: Wiley (The organization of behavior; a neuropsychological theory), pp. xix, 335.

Helmchen, C. *et al.* (1998) 'Deficits in vertical and torsional eye movements after uni- and bilateral muscimol inactivation of the interstitial nucleus of Cajal of the alert monkey', *Experimental Brain Research*, 119(4), pp. 436–452. doi:10.1007/s002210050359.

Helmchen, C., Rambold, H. and Büttner, U. (1996) 'Saccade-related burst neurons with torsional and vertical on-directions in the interstitial nucleus of Cajal of the alert monkey', *Experimental Brain Research*, 112(1), pp. 63–78. doi:10.1007/BF00227179.

Hendriks, A.D. *et al.* (2020) 'Pushing functional MRI spatial and temporal resolution further: High-density receive arrays combined with shot-selective 2D CAIPIRINHA for 3D echo-planar imaging at 7 T', *Nmr in Biomedicine*, 33(5), p. e4281. doi:10.1002/nbm.4281.

Henze, D.A. *et al.* (2000) 'Intracellular Features Predicted by Extracellular Recordings in the Hippocampus In Vivo', *Journal of Neurophysiology*, 84(1), pp. 390–400. doi:10.1152/jn.2000.84.1.390.

Herkenham, M. (1986) 'New Perspectives on the Organization and Evolution of Nonspecific Thalamocortical Projections', in. Springer, Boston, MA, pp. 403–445. doi:10.1007/978-1-4613-2149-1_11.

Heroux, N.A. *et al.* (2018) 'Differential expression of the immediate early genes c-Fos, Arc, Egr-1, and Npas4 during long-term memory formation in the context preexposure facilitation effect (CPFE)', *Neurobiology of Learning and Memory*, 147, pp. 128–138. doi:10.1016/j.nlm.2017.11.016.

Herreras, O. (2016) 'Local Field Potentials: Myths and Misunderstandings', *Frontiers in Neural Circuits*, 10, p. 101. doi:10.3389/fncir.2016.00101.

Hesselmann, G. (2013) 'Dissecting visual awareness with FMRI', *The Neuroscientist: A Review Journal Bringing Neurobiology, Neurology and Psychiatry*, 19(5), pp. 495–508. doi:10.1177/1073858413485988.

van den Heuvel, M.P. and Hulshoff Pol, H.E. (2010) 'Exploring the brain network: a review on resting-state fMRI functional connectivity', *European Neuropsychopharmacology: The Journal of the European College of Neuropsychopharmacology*, 20(8), pp. 519–534. doi:10.1016/j.euroneuro.2010.03.008.

Hikosaka, O., Nakamura, K. and Nakahara, H. (2006) 'Basal ganglia orient eyes to reward', *Journal of Neurophysiology*, 95(2), pp. 567–584. doi:10.1152/jn.00458.2005.

Hikosaka, O., Sakamoto, M. and Usui, S. (1989) 'Functional properties of monkey caudate neurons. I. Activities related to saccadic eye movements', *Journal of Neurophysiology*, 61(4), pp. 780–798. doi:10.1152/jn.1989.61.4.780.

Hikosaka, O., Takikawa, Y. and Kawagoe, R. (2000) 'Role of the basal ganglia in the control of purposive saccadic eye movements', *Physiological Reviews*, 80(3), pp. 953–978. doi:10.1152/physrev.2000.80.3.953.

# References

Hikosaka, O. and Wurtz, R.H. (1983) 'Visual and oculomotor functions of monkey substantia nigra pars reticulata. I. Relation of visual and auditory responses to saccades', *Journal of Neurophysiology*, 49(5), pp. 1230–1253. doi:10.1152/jn.1983.49.5.1230.

Hikosaka, O. and Wurtz, R.H. (1985) 'Modification of saccadic eye movements by GABA-related substances. I. Effect of muscimol and bicuculline in monkey superior colliculus', *Journal of Neurophysiology*, 53(1), pp. 266–291. doi:10.1152/jn.1985.53.1.266.

Himmelbach, M., Linzenbold, W. and Ilg, U.J. (2013) 'Dissociation of reach-related and visual signals in the human superior colliculus', *NeuroImage*, 82, pp. 61–67. doi:10.1016/j.neuroimage.2013.05.101.

Hirano Y, Stefanovic B, Silva AC. 2011. Spatiotemporal evolution of the functional magnetic resonance imaging response to ultrashort stimuli. J. Neurosci. 31(4):1440–47

Hofbauer, A. and Dräger, U.C. (1985) 'Depth segregation of retinal ganglion cells projecting to mouse superior colliculus', *The Journal of Comparative Neurology*, 234(4), pp. 465–474. doi:10.1002/cne.902340405.

Hoffmann, K.-P. and Fischer, W.H. (2001) 'Directional effect of inactivation of the nucleus of the optic tract on optokinetic nystagmus in the cat', *Vision Research*, 41(25), pp. 3389–3398. doi:10.1016/S0042-6989(01)00184-5.

Hong, Y.K., Kim, I.-J. and Sanes, J.R. (2011) 'Stereotyped axonal arbors of retinal ganglion cell subsets in the mouse superior colliculus', *The Journal of Comparative Neurology*, 519(9), pp. 1691–1711. doi:10.1002/cne.22595.

Hoogerwerf, A.C. and Wise, K.D. (1994) 'A three-dimensional microelectrode array for chronic neural recording', *IEEE Transactions on Biomedical Engineering*, 41(12), pp. 1136–1146. doi:10.1109/10.335862.

Hoopfer, E.D. *et al.* (2015) 'P1 interneurons promote a persistent internal state that enhances inter-male aggression in Drosophila', *eLife*. Edited by M. Ramaswami, 4, p. e11346. doi:10.7554/eLife.11346.

Hoy, J.L, Bishop, H.I. and Niell, C.M. (2019) 'Defined Cell Types in Superior Colliculus Make Distinct Contributions to Prey Capture Behavior in the Mouse.', *Current biology : CB*, 29(23), pp. 4130-4138.e5. doi:10.1016/j.cub.2019.10.017.

Huang, L. *et al.* (2017) 'A retinoraphe projection regulates serotonergic activity and looming-evoked defensive behaviour', *Nature Communications*, 8, p. 14908. doi:10.1038/ncomms14908.

Huang, M. *et al.* (2021) 'The tectonigral pathway regulates appetitive locomotion in predatory hunting in mice', *Nature Communications*, 12(1), p. 4409. doi:10.1038/s41467-021-24696-3.

Hubel, D.H. (1957) 'Tungsten Microelectrode for Recording from Single Units', *Science (New York, N.Y.)*, 125(3247), pp. 549–550. doi:10.1126/science.125.3247.549.

Hubel, D.H. and Wiesel, T.N. (1959) 'Receptive fields of single neurones in the cat's striate cortex', *The Journal of Physiology*, 148(3), pp. 574–591.

Hubel, D.H., Wiesel, T.N. and Stryker, M.P. (1977) 'Orientation columns in macaque monkey visual cortex demonstrated by the 2-deoxyglucose autoradiographic technique', *Nature*, 269(5626), pp. 328–330. doi:10.1038/269328a0.

Huber, G.C. and Crosby, E.C. (1933) 'A Phylogenetic Consideration of the Optic Tectum', *Proceedings of the National Academy of Sciences of the United States of America*, 19(1), pp. 15–22. doi:10.1073/pnas.19.1.15.

Huff, M.L. *et al.* (2013) 'Posttraining optogenetic manipulations of basolateral amygdala activity modulate consolidation of inhibitory avoidance memory in rats', *Proceedings of the National Academy of Sciences*, 110(9), pp. 3597–3602. doi:10.1073/pnas.1219593110.

Huo, B.-X., Smith, J.B. and Drew, P.J. (2014) 'Neurovascular coupling and decoupling in the cortex during voluntary locomotion', *The Journal of Neuroscience: The Official Journal of the Society for Neuroscience*, 34(33), pp. 10975–10981. doi:10.1523/JNEUROSCI.1369-14.2014.

Huth, A.G. *et al.* (2016) 'Natural speech reveals the semantic maps that tile human cerebral cortex', *Nature*, 532(7600), pp. 453–458. doi:10.1038/nature17637.

Iadecola, C. (2017) 'The Neurovascular Unit Coming of Age: A Journey through Neurovascular Coupling in Health and Disease', *Neuron*, 96(1), pp. 17–42. doi:10.1016/j.neuron.2017.07.030.

Inayat, S. *et al.* (2015) 'Neurons in the Most Superficial Lamina of the Mouse Superior Colliculus Are Highly Selective for Stimulus Direction', *Journal of Neuroscience*, 35(20), pp. 7992–8003. doi:10.1523/JNEUROSCI.0173-15.2015.

Inoue, M. *et al.* (2019) 'Rational Engineering of XCaMPs, a Multicolor GECI Suite for In Vivo Imaging of Complex Brain Circuit Dynamics', *Cell*, 177(5), pp. 1346-1360.e24. doi:10.1016/j.cell.2019.04.007.

Isa, T. and Sasaki, S. (2002) 'Brainstem control of head movements during orienting; Organization of the premotor circuits', *Progress in Neurobiology*, 66(4), pp. 205–241. doi:10.1016/S0301-0082(02)00006-0.

Isaacson, J.S. and Scanziani, M. (2011) 'How inhibition shapes cortical activity', *Neuron*, 72(2), pp. 231–243. doi:10.1016/j.neuron.2011.09.027.

Ishida, Y. *et al.* (2000) 'Basal expression of c-Fos and Zif268 in the rat basal ganglia: immunohistochemical characterization of striatal Zif268-positive neurons', *The European Journal of Neuroscience*, 12(2), pp. 771–775. doi:10.1046/j.1460-9568.2000.00968.x.

Jefferies, E. *et al.* (2020) 'The neurocognitive basis of knowledge about object identity and events: dissociations reflect opposing effects of semantic coherence and control', *Philosophical Transactions of the Royal Society of London. Series B, Biological Sciences*, 375(1791), p. 20190300. doi:10.1098/rstb.2019.0300.

Jendryka, M. *et al.* (2019) 'Pharmacokinetic and pharmacodynamic actions of clozapine-N-oxide, clozapine, and compound 21 in DREADD-based chemogenetics in mice', *Scientific Reports*, 9(1), p. 4522. doi:10.1038/s41598-019-41088-2.

Jensen, K.H.R. and Berg, R.W. (2017) 'Advances and perspectives in tissue clearing using CLARITY', *Journal of Chemical Neuroanatomy*, 86, pp. 19–34. doi:10.1016/j.jchemneu.2017.07.005.

Jiang, J., Cui, H. and Rahmouni, K. (2017) 'Optogenetics and pharmacogenetics: principles and applications', *American Journal of Physiology - Regulatory, Integrative and Comparative Physiology*, 313(6), pp. R633–R645. doi:10.1152/ajpregu.00091.2017.

Johnson, Z.V. *et al.* (2010) 'A similar pattern of neuronal Fos activation in 10 brain regions following exposure to reward- or aversion-associated contextual cues in mice', *Physiology & Behavior*, 99(3), pp. 412–418. doi:10.1016/j.physbeh.2009.12.013.

Juavinett, A.L. *et al.* (2020) 'A systematic topographical relationship between mouse lateral posterior thalamic neurons and their visual cortical projection targets', *The Journal of Comparative Neurology*, 528(1), pp. 95–107. doi:10.1002/cne.24737.

Jun, E.J. *et al.* (2021) 'Causal role for the primate superior colliculus in the computation of evidence for perceptual decisions', *Nature Neuroscience*, 24(8), pp. 1121–1131. doi:10.1038/s41593-021-00878-6.

Jun, J.J. *et al.* (2017) 'Fully integrated silicon probes for high-density recording of neural activity', *Nature*, 551(7679), pp. 232–236. doi:10.1038/nature24636.

Jung, W.B. *et al.* (2021) 'Early fMRI responses to somatosensory and optogenetic stimulation reflect neural information flow', *Proceedings of the National Academy of Sciences of the United States of America*, 118(11), p. e2023265118. doi:10.1073/pnas.2023265118.

Jung, W.B., Shim, H.J. and Kim, S.G. (2019) 'Mouse BOLD fMRI at ultrahigh field detects somatosensory networks including thalamic nuclei', *NeuroImage*, 195(March), pp. 203–214. doi:10.1016/j.neuroimage.2019.03.063.

Jure, R. (2018) 'Autism Pathogenesis: The Superior Colliculus', *Frontiers in Neuroscience*, 12, p. 1029. doi:10.3389/fnins.2018.01029.

Kamishina, H. *et al.* (2009) 'Cortical connections of the rat lateral posterior thalamic nucleus', *Brain Research*, 1264, pp. 39–56. doi:10.1016/j.brainres.2009.01.024.

Kanwisher, N., McDermott, J. and Chun, M.M. (1997) 'The fusiform face area: a module in human extrastriate cortex specialized for face perception', *The Journal of Neuroscience: The Official Journal of the Society for Neuroscience*, 17(11), pp. 4302–4311.

Kay, J.N. *et al.* (2011) 'Retinal ganglion cells with distinct directional preferences differ in molecular identity, structure, and central projections', *The Journal of Neuroscience: The Official Journal of the Society for Neuroscience*, 31(21), pp. 7753–7762. doi:10.1523/JNEUROSCI.0907-11.2011.

Keating, M.J. and Gaze, R.M. (1970) 'The ipsilateral retinotectal pathway in the frog', *Quarterly Journal of Experimental Physiology and Cognate Medical Sciences*, 55(4), pp. 284–292. doi:10.1113/expphysiol.1970.sp002080.

Kebschull, J.M. *et al.* (2016) 'High-Throughput Mapping of Single-Neuron Projections by Sequencing of Barcoded RNA', *Neuron*, 91(5), pp. 975–987. doi:10.1016/j.neuron.2016.07.036.

Kelly, J., Rothstein, J. and Grossman, S.P. (1979) 'GABA and hypothalamic feeding systems. I. Topographic analysis of the effects of microinjections of muscimol', *Physiology & Behavior*, 23(6), pp. 1123–1134. doi:10.1016/0031-9384(79)90306-8.

Kennedy, C. *et al.* (1975) 'Mapping of functional neural pathways by autoradiographic survey of local metabolic rate with (14C)deoxyglucose', *Science (New York, N.Y.)*, 187(4179), pp. 850–853. doi:10.1126/science.1114332.

Kennedy, C. *et al.* (1976) 'Metabolic mapping of the primary visual system of the monkey by means of the autoradiographic [14C]deoxyglucose technique', *Proceedings of the National Academy of Sciences of the United States of America*, 73(11), pp. 4230–4234. doi:10.1073/pnas.73.11.4230.

Keramidas, A. *et al.* (2004) 'Ligand-gated ion channels: mechanisms underlying ion selectivity', *Progress in Biophysics and Molecular Biology*, 86(2), pp. 161–204. doi:10.1016/j.pbiomolbio.2003.09.002.

Kim, H. (2019) 'Neural correlates of explicit and implicit memory at encoding and retrieval: A unified framework and meta-analysis of functional neuroimaging studies', *Biological Psychology*, 145, pp. 96–111. doi:10.1016/j.biopsycho.2019.04.006.

Kim, I.-J. *et al.* (2010) 'Laminar restriction of retinal ganglion cell dendrites and axons: subtype-specific developmental patterns revealed with transgenic markers', *The Journal of Neuroscience: The Official Journal of the Society for Neuroscience*, 30(4), pp. 1452–1462. doi:10.1523/JNEUROSCI.4779-09.2010.

# References

Kim, S.-G. *et al.* (2013) 'Cerebral Blood Volume MRI with Intravascular Superparamagentic Iron Oxide Nanoparticles', *NMR in biomedicine*, 26(8), p. 949. doi:10.1002/nbm.2885.

Kim, T. *et al.* (2020) 'Dendritic and parallel processing of visual threats in the retina control defensive responses', *Science Advances*, 6(47), p. eabc9920. doi:10.1126/sciadv.abc9920.

Kim, Y. *et al.* (2015) 'Mapping Social Behavior-Induced Brain Activation at Cellular Resolution in the Mouse', *Cell Reports*, 10(2), pp. 292–305. doi:10.1016/j.celrep.2014.12.014.

King, W.M. and Fuchs, A.F. (1979) 'Reticular control of vertical saccadic eye movements by mesencephalic burst neurons', *Journal of Neurophysiology*, 42(3), pp. 861–876. doi:10.1152/jn.1979.42.3.861.

Kitama, T. *et al.* (1991) 'Stimulation of the caudate nucleus induces contraversive saccadic eye movements as well as head turning in the cat', *Neuroscience Research*, 12(1), pp. 287–292. doi:10.1016/0168-0102(91)90118-i.

Knights, E. *et al.* (2021) 'Hand-Selective Visual Regions Represent How to Grasp 3D Tools: Brain Decoding during Real Actions', *The Journal of Neuroscience: The Official Journal of the Society for Neuroscience*, 41(24), pp. 5263–5273. doi:10.1523/JNEUROSCI.0083-21.2021.

Knoll, M. and Ruska, E. (1932) 'Das Elektronenmikroskop', *Zeitschrift für Physik*, 78(5), pp. 318–339. doi:10.1007/BF01342199.

Kodama, T. and Lac, S. du (2016) 'Adaptive Acceleration of Visually Evoked Smooth Eye Movements in Mice', *Journal of Neuroscience*, 36(25), pp. 6836–6849. doi:10.1523/JNEUROSCI.0067-16.2016.

Koizumi, A. *et al.* (2019) 'Threat anticipation in pulvinar and in superficial layers of primary visual cortex (V1). Evidence from Layer-Specific Ultra-High Field 7T fMRI', *eNeuro*, 6(6). doi:10.1523/ENEURO.0429-19.2019.

Kondo, M. *et al.* (2017) 'Two-photon calcium imaging of the medial prefrontal cortex and hippocampus without cortical invasion', *eLife*, 6, p. e26839. doi:10.7554/eLife.26839.

Kornblith, S. *et al.* (2013) 'A network for scene processing in the macaque temporal lobe', *Neuron*, 79(4), pp. 766–781. doi:10.1016/j.neuron.2013.06.015.

Korte, S.M. *et al.* (1992) 'Mesencephalic cuneiform nucleus and its ascending and descending projections serve stress-related cardiovascular responses in the rat', *Journal of the Autonomic Nervous System*, 41(1–2), pp. 157–176. doi:10.1016/0165-1838(92)90137-6.

Kovács, K.J. (1998) 'c-Fos as a transcription factor: a stressful (re)view from a functional map', *Neurochemistry International*, 33(4), pp. 287–297. doi:10.1016/s0197-0186(98)00023-0.

Kragel, P.A. *et al.* (2021) 'A human colliculus-pulvinar-amygdala pathway encodes negative emotion', *Neuron*, 109(15), pp. 2404-2412.e5. doi:10.1016/j.neuron.2021.06.001.

Krashes, M.J. *et al.* (2014) 'An excitatory paraventricular nucleus to AgRP neuron circuit that drives hunger', *Nature*, 507(7491), pp. 238–242. doi:10.1038/nature12956.

Krauzlis, R.J. and Carello, C.D. (2003) 'Going for the goal', *Nature Neuroscience*, 6(4), pp. 332–333. doi:10.1038/nn0403-332.

Kristensson, K., Ghetti, B. and Wiśniewski, H.M. (1974) 'Study on the propagation of Herpes simplex virus (type 2) into the brain after intraocular injection', *Brain Research*, 69(2), pp. 189–201. doi:10.1016/0006-8993(74)90001-8.

Krüger, J. (1982) 'A 12-fold microelectrode for recording from vertically aligned cortical neurones', *Journal of Neuroscience Methods*, 6(4), pp. 347–350. doi:10.1016/0165-0270(82)90035-8.

Krüger, J. and Bach, M. (1981) 'Simultaneous recording with 30 microelectrodes in monkey visual cortex', *Experimental Brain Research*, 41(2), pp. 191–194. doi:10.1007/BF00236609.

Kuljis, R.O. and Karten, H.J. (1988) 'Neuroactive peptides as markers of retinal ganglion cell populations that differ in anatomical organization and function', *Visual Neuroscience*, 1(1), pp. 73–81. doi:10.1017/s0952523800001024.

Kuperstein, M. and Eichenbaum, H. (1985) 'Unit activity, evoked potentials and slow waves in the rat hippocampus and olfactory bulb recorded with a 24-channel microelectrode', *Neuroscience*, 15(3), pp. 703–712. doi:10.1016/0306-4522(85)90072-7.

Kuperstein, M. and Whittington, D.A. (1981) 'A Practical 24 Channel Microelectrode for Neural Recording in Vivo', *IEEE Transactions on Biomedical Engineering*, BME-28(3), pp. 288–293. doi:10.1109/TBME.1981.324702.

Kuwajima, T. *et al.* (2013) 'ClearT: a detergent- and solvent-free clearing method for neuronal and non-neuronal tissue', *Development (Cambridge, England)*, 140(6), pp. 1364–1368. doi:10.1242/dev.091844.

Labiner, D.M. *et al.* (1993) 'Induction of c-fos mRNA by kindled seizures: complex relationship with neuronal burst firing', *The Journal of Neuroscience: The Official Journal of the Society for Neuroscience*, 13(2), pp. 744–751.

Lacroix, A. *et al.* (2015) 'COX-2-Derived Prostaglandin E2 Produced by Pyramidal Neurons Contributes to Neurovascular Coupling in the Rodent Cerebral Cortex', *The Journal of Neuroscience: The Official Journal of the Society for Neuroscience*, 35(34), pp. 11791–11810. doi:10.1523/JNEUROSCI.0651-15.2015.

Laemle, L.K. (1983) 'A Golgi study of cell morphology in the deep layers of the human superior colliculus', *Journal Fur Hirnforschung*, 24(3), pp. 297–306.

Lammel, S. *et al.* (2012) 'Input-specific control of reward and aversion in the ventral tegmental area', *Nature*, 491(7423), pp. 212–217. doi:10.1038/nature11527.

Landemard, A. *et al.* (2021) 'Distinct higher-order representations of natural sounds in human and ferret auditory cortex', *eLife*, 10, p. e65566. doi:10.7554/eLife.65566.

Langer, T.P. and Kaneko, C.R. (1990) 'Brainstem afferents to the oculomotor omnipause neurons in monkey', *The Journal of Comparative Neurology*, 295(3), pp. 413–427. doi:10.1002/cne.902950306.

Langer, T.P. and Lund, R.D. (1974) 'The upper layers of the superior colliculus of the rat: a Golgi study', *The Journal of Comparative Neurology*, 158(4), pp. 418–435. doi:10.1002/cne.901580404.

Large, A.M. *et al.* (2016) 'Balanced feedforward inhibition and dominant recurrent inhibition in olfactory cortex', *Proceedings of the National Academy of Sciences*, 113(8), pp. 2276–2281. doi:10.1073/pnas.1519295113.

Laursen, A.M. (1962) 'Movements evoked from the region of the caudate nucleus in cats', *Acta Physiologica Scandinavica*, 54, pp. 175–184. doi:10.1111/j.1748-1716.1962.tb02342.x.

LaVail, J.H. and LaVail, M.M. (1972) 'Retrograde Axonal Transport in the Central Nervous System', *Science*, 176(4042), pp. 1416–1417. doi:10.1126/science.176.4042.1416.

Lee, C. *et al.* (2020) 'Light Up the Brain: The Application of Optogenetics in Cell-Type Specific Dissection of Mouse Brain Circuits', *Frontiers in Neural Circuits*, 14, p. 18. doi:10.3389/fncir.2020.00018.

Lee, E.-S. *et al.* (2016) 'Default Mode Network Functional Connectivity in Early and Late Mild Cognitive Impairment: Results From the Alzheimer's Disease Neuroimaging Initiative', *Alzheimer Disease and Associated Disorders*, 30(4), pp. 289–296. doi:10.1097/WAD.0000000000000143.

Lee, H.J. *et al.* (2016) 'Activation of Direct and Indirect Pathway Medium Spiny Neurons Drives Distinct Brain-wide Responses', *Neuron*, 91(2), pp. 412–424. doi:10.1016/j.neuron.2016.06.010.

Lee, J. *et al.* (2021) 'Opposed hemodynamic responses following increased excitation and parvalbumin-based inhibition', *Journal of Cerebral Blood Flow and Metabolism: Official Journal of the International Society of Cerebral Blood Flow and Metabolism*, 41(4), pp. 841–856. doi:10.1177/0271678X20930831.

Lee, J.H. *et al.* (2010) 'Global and local fMRI signals driven by neurons defined optogenetically by type and wiring', *Nature*, 465(7299), pp. 788–792. doi:10.1038/nature09108.

Lee, K.H. *et al.* (2020) 'The sifting of visual information in the superior colliculus', *eLife*, 9, p. e50678. doi:10.7554/eLife.50678.

Lein, E.S. *et al.* (2007) 'Genome-wide atlas of gene expression in the adult mouse brain.', *Nature*, 445(7124), pp. 168–176. doi:10.1038/nature05453.

Leitão, J. *et al.* (2015) 'Concurrent TMS-fMRI Reveals Interactions between Dorsal and Ventral Attentional Systems', *The Journal of Neuroscience: The Official Journal of the Society for Neuroscience*, 35(32), pp. 11445–11457. doi:10.1523/JNEUROSCI.0939-15.2015.

Leong, A.T.L. *et al.* (2018) 'Optogenetic auditory fMRI reveals the effects of visual cortical inputs on auditory midbrain response', *Scientific Reports*, 8(1), p. 8736. doi:10.1038/s41598-018-26568-1.

Leong, A.T.L. *et al.* (2019) 'Optogenetic fMRI interrogation of brain-wide central vestibular pathways', *Proceedings of the National Academy of Sciences*, 116(20), pp. 10122–10129. doi:10.1073/pnas.1812453116.

Lettvin, J.Y. *et al.* (1959) 'What the Frog's Eye Tells the Frog's Brain', *Proceedings of the IRE*, 47(11), pp. 1940–1951. doi:10.1109/JRPROC.1959.287207.

Lewis, L.D. *et al.* (2016) 'Fast fMRI can detect Oscillatory neural activity in humans', *Proceedings of the National Academy of Sciences of the United States of America*, 113(43), pp. E6679–E6685. doi:10.1073/pnas.1608117113.

Li, H. *et al.* (2011) 'Assessing the potential for AAV vector genotoxicity in a murine model', *Blood*, 117(12), pp. 3311–3319. doi:10.1182/blood-2010-08-302729.

Li, J.-N. and Sheets, P.L. (2018) 'The central amygdala to periaqueductal gray pathway comprises intrinsically distinct neurons differentially affected in a model of inflammatory pain', *The Journal of Physiology*, 596(24), pp. 6289–6305. doi:10.1113/JP276935.

Li, L. *et al.* (2018) 'Stress Accelerates Defensive Responses to Looming in Mice and Involves a Locus Coeruleus-Superior Colliculus Projection', *Current biology: CB*, 28(6), pp. 859-871.e5. doi:10.1016/j.cub.2018.02.005.

Li, S. *et al.* (2018) 'Overview of the reporter genes and reporter mouse models', *Animal Models and Experimental Medicine*, 1(1), pp. 29–35. doi:10.1002/ame2.12008.

Li, X.-Y. *et al.* (2019) 'AGRP Neurons Project to the Medial Preoptic Area and Modulate Maternal Nest-Building', *The Journal of Neuroscience: The Official Journal of the Society for Neuroscience*, 39(3), pp. 456–471. doi:10.1523/JNEUROSCI.0958-18.2018.

# References

Li, Y. *et al.* (2018) 'Hypothalamic Circuits for Predation and Evasion', *Neuron*, 97(4), pp. 911-924.e5. doi:10.1016/j.neuron.2018.01.005.

Liang, Z. *et al.* (2015) 'Mapping the functional network of medial prefrontal cortex by combining optogenetics and fMRI in awake rats', *NeuroImage*, 117, pp. 114–123. doi:10.1016/j.neuroimage.2015.05.036.

Lichtman, D. *et al.* (2021) 'Structural and functional brain-wide alterations in A350V Iqsec2 mutant mice displaying autistic-like behavior', *Translational Psychiatry*, 11(1), p. 181. doi:10.1038/s41398-021-01289-8.

Liddell, B.J. *et al.* (2005) 'A direct brainstem-amygdala-cortical "alarm" system for subliminal signals of fear', *NeuroImage*, 24(1), pp. 235–243. doi:10.1016/j.neuroimage.2004.08.016.

Lima, S.Q. *et al.* (2009) 'PINP: a new method of tagging neuronal populations for identification during in vivo electrophysiological recording', *PloS One*, 4(7), p. e6099. doi:10.1371/journal.pone.0006099.

Lin, D. *et al.* (2011) 'Functional identification of an aggression locus in the mouse hypothalamus', *Nature*, 470(7333), pp. 221–226. doi:10.1038/nature09736.

Linzenbold, W. and Himmelbach, M. (2012) 'Signals from the deep: reach-related activity in the human superior colliculus', *The Journal of Neuroscience: The Official Journal of the Society for Neuroscience*, 32(40), pp. 13881–13888. doi:10.1523/JNEUROSCI.0619-12.2012.

Liu, X. *et al.* (2012) 'Optogenetic stimulation of a hippocampal engram activates fear memory recall', *Nature*, 484(7394), pp. 381–385. doi:10.1038/nature11028.

Llinás, R.R. (2003) 'The contribution of Santiago Ramón y Cajal to functional neuroscience', *Nature Reviews. Neuroscience*, 4(1), pp. 77–80. doi:10.1038/nrn1011.

Lock, J.T., Parker, I. and Smith, I.F. (2015) 'A comparison of fluorescent $Ca^{2+}$ indicators for imaging local $Ca^{2+}$ signals in cultured cells', *Cell Calcium*, 58(6), pp. 638–648. doi:10.1016/j.ceca.2015.10.003.

Logothetis, N.K. *et al.* (2001) 'Neurophysiological investigation of the basis of the fMRI signal', *Nature*, 412(6843), pp. 150–157. doi:10.1038/35084005.

Logothetis, N.K. (2003) 'The underpinnings of the BOLD functional magnetic resonance imaging signal', *The Journal of Neuroscience: The Official Journal of the Society for Neuroscience*, 23(10), pp. 3963–3971.

Logothetis, N.K. and Wandell, B.A. (2004) 'Interpreting the BOLD signal.', *Annual review of physiology*, 66, pp. 735–769. doi:10.1146/annurev.physiol.66.082602.092845.

Lohani, S. *et al.* (2017) 'Unexpected global impact of VTA dopamine neuron activation as measured by opto-fMRI', *Molecular Psychiatry*, 22(4), pp. 585–594. doi:10.1038/mp.2016.102.

Lovejoy, L.P. and Krauzlis, R.J. (2010) 'Inactivation of primate superior colliculus impairs covert selection of signals for perceptual judgments', *Nature Neuroscience*, 13(2), pp. 261–266. doi:10.1038/nn.2470.

Lovick, T.A. (1993) 'The periaqueductal gray-rostral medulla connection in the defence reaction: efferent pathways and descending control mechanisms', *Behavioural Brain Research*, 58(1–2), pp. 19–25. doi:10.1016/0166-4328(93)90087-7.

Lu H, van Zijl PC. A review of the development of Vascular-Space-Occupancy (VASO) fMRI. Neuroimage. 2012 Aug 15;62(2):736-42. doi: 10.1016/j.neuroimage.2012.01.013. Epub 2012 Jan 8. PMID: 22245650; PMCID: PMC3328630.

Macé, E. *et al.* (2011) 'Functional ultrasound imaging of the brain.', *Nat Methods*, 8(8), pp. 662–664. doi:10.1038/nmeth.1641.

Mace, E. *et al.* (2013) 'Functional ultrasound imaging of the brain: theory and basic principles.', *IEEE transactions on ultrasonics, ferroelectrics, and frequency control*, 60(3), pp. 492–506. doi:10.1109/TUFFC.2013.2592.

Macé, É. *et al.* (2018) 'Whole-Brain Functional Ultrasound Imaging Reveals Brain Modules for Visuomotor Integration', *Neuron*, 100(5), pp. 1241-1251.e7. doi:10.1016/j.neuron.2018.11.031.

Madisen, L. *et al.* (2010) 'A robust and high-throughput Cre reporting and characterization system for the whole mouse brain', *Nature Neuroscience*, 13(1), pp. 133–140. doi:10.1038/nn.2467.

Madisen, L., Mao, T., Koch, H., Zhuo, J., Berenyi, A., Fujisawa, S., Hsu, Yun-Wei A., *et al.* (2012) 'A toolbox of Cre-dependent optogenetic transgenic mice for light-induced activation and silencing', *Nature Neuroscience*, 15(5), pp. 793–802. doi:10.1038/nn.3078.

Malach, R. *et al.* (1995) 'Object-related activity revealed by functional magnetic resonance imaging in human occipital cortex', *Proceedings of the National Academy of Sciences of the United States of America*, 92(18), pp. 8135–8139. doi:10.1073/pnas.92.18.8135.

de Malmazet, D., Kühn, N.K. and Farrow, K. (2018) 'Retinotopic Separation of Nasal and Temporal Motion Selectivity in the Mouse Superior Colliculus', *Current biology: CB*, 28(18), pp. 2961-2969.e4. doi:10.1016/j.cub.2018.07.001.

Mandeville JB, Marota JJ, Kosofsky BE, Keltner JR, Weissleder R, Rosen BR, Weisskoff RM. Dynamic functional imaging of relative cerebral blood volume during rat forepaw stimulation. Magn Reson Med. 1998 Apr;39(4):615-24. doi: 10.1002/mrm.1910390415. PMID: 9543424.

Maren, S. and Quirk, G.J. (2004) 'Neuronal signalling of fear memory', *Nature Reviews. Neuroscience*, 5(11), pp. 844–852. doi:10.1038/nrn1535.

Maresca, D. *et al.* (2020) 'Acoustic biomolecules enhance hemodynamic functional ultrasound imaging of neural activity', *NeuroImage*, 209, p. 116467. doi:10.1016/j.neuroimage.2019.116467.

Martersteck, Emily M *et al.* (2017) 'Diverse Central Projection Patterns of Retinal Ganglion Cells', *Cell Reports*, 18(8), pp. 2058–2072. doi:10.1016/j.celrep.2017.01.075.

Masland, R.H. (2004) 'Neuronal cell types', *Current Biology*, 14(13), pp. R497–R500. doi:10.1016/j.cub.2004.06.035.

Masterson, S.P. *et al.* (2019) 'Ultrastructural and optogenetic dissection of V1 corticotectal terminal synaptic properties', *The Journal of Comparative Neurology*, 527(4), pp. 833–842. doi:10.1002/cne.24538.

Masullo, L. *et al.* (2019) 'Genetically Defined Functional Modules for Spatial Orienting in the Mouse Superior  Colliculus.', *Current biology : CB*, 29(17), pp. 2892-2904.e8. doi:10.1016/j.cub.2019.07.083.

Maturana, H.R. *et al.* (1960) 'Anatomy and Physiology of Vision in the Frog (Rana pipiens)', *The Journal of General Physiology*, 43(6), pp. 129–175.

May, P.J. (2006) 'The mammalian superior colliculus: laminar structure and connections', *Progress in Brain Research*, 151, pp. 321–378. doi:10.1016/S0079-6123(05)51011-2.

May, P.J. *et al.* (2009) 'Tectonigral projections in the primate: a pathway for pre-attentive sensory input to midbrain dopaminergic neurons', *The European Journal of Neuroscience*, 29(3), pp. 575–587. doi:10.1111/j.1460-9568.2008.06596.x.

May, P.J. and Hall, W.C. (1984) 'Relationships between the nigrotectal pathway and the cells of origin of the predorsal bundle', *The Journal of Comparative Neurology*, 226(3), pp. 357–376. doi:10.1002/cne.902260306.

McCormick, C. and Maguire, E.A. (2021) 'The distinct and overlapping brain networks supporting semantic and spatial constructive scene processing', *Neuropsychologia*, 158, p. 107912. doi:10.1016/j.neuropsychologia.2021.107912.

McCulloch, W.S. and Pitts, W. (1943) 'A logical calculus of the ideas immanent in nervous activity', *The bulletin of mathematical biophysics*, 5(4), pp. 115–133. doi:10.1007/BF02478259.

McDonald, I. (2005) 'A HISTORY OF NERVE FUNCTIONS: FROM ANIMAL SPIRITS TO MOLECULAR MECHANISMS Sidney Ochs  2004. Cambridge: Cambridge University Press  Price £65.00.  ISBN 052124742X', *Brain*, 128(1), pp. 227–231. doi:10.1093/brain/awh359.

McFarland, J.L. and Fuchs, A.F. (1992) 'Discharge patterns in nucleus prepositus hypoglossi and adjacent medial vestibular nucleus during horizontal eye movement in behaving macaques', *Journal of Neurophysiology*, 68(1), pp. 319–332. doi:10.1152/jn.1992.68.1.319.

McHaffie, J.G. *et al.* (2005) 'Subcortical loops through the basal ganglia', *Trends in Neurosciences*, 28(8), pp. 401–407. doi:10.1016/j.tins.2005.06.006.

McHaffie, J.G. and Stein, B.E. (1982) 'Eye movements evoked by electrical stimulation in the superior colliculus of rats and hamsters', *Brain Research*, 247(2), pp. 243–253. doi:10.1016/0006-8993(82)91249-5.

McKeefry, D.J. *et al.* (2009) 'The noninvasive dissection of the human visual cortex: using FMRI and TMS to study the organization of the visual brain', *The Neuroscientist: A Review Journal Bringing Neurobiology, Neurology and Psychiatry*, 15(5), pp. 489–506. doi:10.1177/1073858409334424.

McNaughton, B.L., O'Keefe, J. and Barnes, C.A. (1983) 'The stereotrode: A new technique for simultaneous isolation of several single units in the central nervous system from multiple unit records', *Journal of Neuroscience Methods*, 8(4), pp. 391–397. doi:10.1016/0165-0270(83)90097-3.

McPeek, R.M. and Keller, E.L. (2004) 'Deficits in saccade target selection after inactivation of superior colliculus', *Nature Neuroscience*, 7(7), pp. 757–763. doi:10.1038/nn1269.

Meenakshi, P., Kumar, S. and Balaji, J. (2021) 'In vivo imaging of immediate early gene expression dynamics segregates neuronal ensemble of memories of dual events', *Molecular Brain*, 14(1), p. 102. doi:10.1186/s13041-021-00798-3.

Mendes-Gomes, J. *et al.* (2020) 'Defensive behaviors and brain regional activation changes in rats confronting a snake', *Behavioural Brain Research*, 381. doi:10.1016/j.bbr.2020.112469.

Michaiel, A.M., Abe, E.T. and Niell, C.M. (2020) 'Dynamics of gaze control during prey capture in freely moving mice', *eLife*. Edited by M. Spering et al., 9, p. e57458. doi:10.7554/eLife.57458.

Miller, J.K. *et al.* (2014) 'Visual stimuli recruit intrinsically generated cortical ensembles', *Proceedings of the National Academy of Sciences of the United States of America*, 111(38), pp. E4053-4061. doi:10.1073/pnas.1406077111.

Miller, J.K., Miller, B.R. and Yuste, R. (2018) *An increase in spontaneous activity mediates visual habituation*, p. 507814. doi:10.1101/507814.

Mink, J.W. (1996) 'The basal ganglia: focused selection and inhibition of competing motor programs', *Progress in Neurobiology*, 50(4), pp. 381–425. doi:10.1016/s0301-0082(96)00042-1.

# References

Mitchell, A.S. *et al.* (2018) 'Retrosplenial cortex and its role in spatial cognition', *Brain and Neuroscience Advances*, 2, p. 2398212818757098. doi:10.1177/2398212818757098.

Mitchell, I.J., Dean, P. and Redgrave, P. (1988) 'The projection from superior colliculus to cuneiform area in the rat', *Experimental Brain Research*, 72(3), pp. 626–639. doi:10.1007/BF00250607.

Miyamoto, K. *et al.* (2013) 'Functional differentiation of memory retrieval network in macaque posterior parietal cortex', *Neuron*, 77(4), pp. 787–799. doi:10.1016/j.neuron.2012.12.019.

Miyawaki, A. *et al.* (1997) 'Fluorescent indicators for Ca2+ based on green fluorescent proteins and calmodulin', *Nature*, 388(6645), pp. 882–887. doi:10.1038/42264.

Mize, R.R. (1992) 'The organization of GABAergic neurons in the mammalian superior colliculus', *Progress in Brain Research*, 90, pp. 219–248. doi:10.1016/s0079-6123(08)63616-x.

Moeller, S. *et al.* (2010) 'Multiband multislice GE-EPI at 7 tesla, with 16-fold acceleration using partial parallel imaging with application to high spatial and temporal whole-brain fMRI', *Magnetic Resonance in Medicine*, 63(5), pp. 1144–1153. doi:10.1002/mrm.22361.

Moeller, S., Freiwald, W.A. and Tsao, D.Y. (2008) 'Patches with links: a unified system for processing faces in the macaque temporal lobe', *Science (New York, N.Y.)*, 320(5881), pp. 1355–1359. doi:10.1126/science.1157436.

Moeyaert, B. *et al.* (2018) 'Improved methods for marking active neuron populations', *Nature Communications*, 9(1), pp. 1–12. doi:10.1038/s41467-018-06935-2.

Mohan, Akansha *et al.* (2016) 'The Significance of the Default Mode Network (DMN) in Neurological and Neuropsychiatric Disorders: A Review', *The Yale Journal of Biology and Medicine*, 89(1), pp. 49–57.

Molnár, Z. and Brown, R.E. (2010) 'Insights into the life and work of Sir Charles Sherrington', *Nature Reviews. Neuroscience*, 11(6), pp. 429–436. doi:10.1038/nrn2835.

Monavarfeshani, A., Sabbagh, U. and Fox, M.A. (2017) 'Not a one-trick pony: Diverse connectivity and functions of the rodent lateral geniculate complex', *Visual Neuroscience*, 34, p. E012. doi:10.1017/S0952523817000098.

Mongeau, R. *et al.* (2003) 'Neural correlates of competing fear behaviors evoked by an innately aversive stimulus', *Journal of Neuroscience*, 23(9), pp. 3855–3868. doi:10.1523/jneurosci.23-09-03855.2003.

Montaldo, G. *et al.* (2009) 'Coherent plane-wave compounding for very high frame rate ultrasonography and transient elastography', *IEEE transactions on ultrasonics, ferroelectrics, and frequency control*, 56(3), pp. 489–506. doi:10.1109/TUFFC.2009.1067.

Moon, H.S. *et al.* (2021) 'Contribution of Excitatory and Inhibitory Neuronal Activity to BOLD fMRI', *Cerebral Cortex (New York, N.Y.: 1991)*, 31(9), pp. 4053–4067. doi:10.1093/cercor/bhab068.

Morgan, J.I. *et al.* (1987) 'Mapping patterns of c-fos expression in the central nervous system after seizure', *Science (New York, N.Y.)*, 237(4811), pp. 192–197. doi:10.1126/science.3037702.

Morgan, J.I. and Curran, T. (1991) 'Stimulus-transcription coupling in the nervous system: Involvement of the inducible proto-oncogenes fos and jun', *Annual Review of Neuroscience*. Annu Rev Neurosci, pp. 421–451. doi:10.1146/annurev.ne.14.030191.002225.

Mori, S. *et al.* (1989) 'Site-specific postural and locomotor changes evoked in awake, freely moving intact cats by stimulating the brainstem', *Brain Research*, 505(1), pp. 66–74. doi:10.1016/0006-8993(89)90116-9.

Morin, L.P. and Studholme, K.M. (2014) 'Retinofugal projections in the mouse', *Journal of Comparative Neurology*, 522(16), pp. 3733–3753. doi:10.1002/cne.23635.

Morita, T. *et al.* (2004) 'The neural substrates of conscious color perception demonstrated using fMRI', *NeuroImage*, 21(4), pp. 1665–1673. doi:10.1016/j.neuroimage.2003.12.019.

Moro, E. *et al.* (2020) 'Visual Dysfunction of the Superior Colliculus in De Novo Parkinsonian Patients', *Annals of Neurology*, 87(4), pp. 533–546. doi:10.1002/ana.25696.

Morozov, A., Sukato, D. and Ito, W. (2011) 'Selective Suppression of Plasticity in Amygdala Inputs from Temporal Association Cortex by the External Capsule', *Journal of Neuroscience*, 31(1), pp. 339–345. doi:10.1523/JNEUROSCI.5537-10.2011.

Morris, J.S., DeBonis, M. and Dolan, R.J. (2002) 'Human amygdala responses to fearful eyes', *NeuroImage*, 17(1), pp. 214–222. doi:10.1006/nimg.2002.1220.

Moschovakis, A.K., Scudder, C.A. and Highstein, S.M. (1996) 'The microscopic anatomy and physiology of the mammalian saccadic system', *Progress in Neurobiology*, 50(2), pp. 133–254. doi:10.1016/S0301-0082(96)00034-2.

Motta, P.S. and Judy, J.W. (2005) 'Multielectrode microprobes for deep-brain stimulation fabricated with a customizable 3-D electroplating process', *IEEE Transactions on Biomedical Engineering*, 52(5), pp. 923–933. doi:10.1109/TBME.2005.845225.

Mountcastle, V.B. (1957) 'Modality and topographic properties of single neurons of cat's somatic sensory cortex', *Journal of Neurophysiology*, 20(4), pp. 408–434. doi:10.1152/jn.1957.20.4.408.

Münch, T.A. *et al.* (2009) 'Approach sensitivity in the retina processed by a multifunctional neural circuit', *Nature Neuroscience*, 12(10), pp. 1308–1316. doi:10.1038/nn.2389.

Myhrvold, C. (2013) *In a Frog's Eye*, *MIT Technology Review*. Available at: https://www.technologyreview.com/2013/01/02/180819/in-a-frogs-eye/ (Accessed: 3 December 2021).

Nagel, G. *et al.* (2003) 'Channelrhodopsin-2, a directly light-gated cation-selective membrane channel', *Proceedings of the National Academy of Sciences of the United States of America*, 100(24), pp. 13940–13945. doi:10.1073/pnas.1936192100.

Nagy, A. *et al.* (2003) 'Visual receptive field properties of neurons in the caudate nucleus', *European Journal of Neuroscience*, 18(2), pp. 449–452. doi:10.1046/j.1460-9568.2003.02764.x.

Najafi, K. and Wise, K.D. (1986) 'An implantable multielectrode array with on-chip signal processing', *IEEE Journal of Solid-State Circuits*, 21(6), pp. 1035–1044. doi:10.1109/JSSC.1986.1052646.

Nakai, J., Ohkura, M. and Imoto, K. (2001) 'A high signal-to-noise Ca(2+) probe composed of a single green fluorescent protein', *Nature Biotechnology*, 19(2), pp. 137–141. doi:10.1038/84397.

Nakamura, Yuki *et al.* (2020) 'fMRI detects bilateral brain network activation following unilateral chemogenetic activation of direct striatal projection neurons.', *NeuroImage*, 220, p. 117079. doi:10.1016/j.neuroimage.2020.117079.

Nasr, S. *et al.* (2011) 'Scene-selective cortical regions in human and nonhuman primates', *The Journal of Neuroscience: The Official Journal of the Society for Neuroscience*, 31(39), pp. 13771–13785. doi:10.1523/JNEUROSCI.2792-11.2011.

Nayak, R. *et al.* (2021) 'Imaging the response to deep brain stimulation in rodent using functional ultrasound', *Physics in Medicine and Biology*, 66(5), p. 05LT01. doi:10.1088/1361-6560/abdee5.

Nelissen, K., Vanduffel, W. and Orban, G.A. (2006) 'Charting the lower superior temporal region, a new motion-sensitive region in monkey superior temporal sulcus', *The Journal of Neuroscience: The Official Journal of the Society for Neuroscience*, 26(22), pp. 5929–5947. doi:10.1523/JNEUROSCI.0824-06.2006.

Netser, S., Zahar, Y. and Gutfreund, Y. (2011) 'Stimulus-Specific Adaptation: Can It Be a Neural Correlate of Behavioral Habituation?', *The Journal of Neuroscience*, 31(49), pp. 17811–17820. doi:10.1523/JNEUROSCI.4790-11.2011.

Nguyen, T.V. *et al.* (1992) 'Differential expression of c-fos and zif268 in rat striatum after haloperidol, clozapine, and amphetamine', *Proceedings of the National Academy of Sciences of the United States of America*, 89(10), pp. 4270–4274. doi:10.1073/pnas.89.10.4270.

Niranjan, A. *et al.* (2016) 'fMRI mapping of the visual system in the mouse brain with interleaved snapshot GE-EPI', *NeuroImage*, 139, pp. 337–345. doi:10.1016/j.neuroimage.2016.06.015.

Nunez-Elizalde, A.O. *et al.* (2021) 'Neural basis of functional ultrasound signals'. bioRxiv, doi:10.1101/2021.03.31.437915.

O'Doherty, J.P., Hampton, A. and Kim, H. (2007) 'Model-based fMRI and its application to reward learning and decision making', *Annals of the New York Academy of Sciences*, 1104, pp. 35–53. doi:10.1196/annals.1390.022.

Oh, S.W. *et al.* (2014) 'A mesoscale connectome of the mouse brain', *Nature*, 508(7495), pp. 207–214. doi:10.1038/nature13186.

Ohayon, S. *et al.* (2013) 'Saccade modulation by optical and electrical stimulation in the macaque frontal eye field', *The Journal of Neuroscience: The Official Journal of the Society for Neuroscience*, 33(42), pp. 16684–16697. doi:10.1523/JNEUROSCI.2675-13.2013.

O'Herron, P. *et al.* (2016) 'Neural correlates of single-vessel haemodynamic responses in vivo', *Nature*, 534(7607), pp. 378–382. doi:10.1038/nature17965.

O'Keefe, J. and Dostrovsky, J. (1971) 'The hippocampus as a spatial map. Preliminary evidence from unit activity in the freely-moving rat', *Brain Research*, 34(1), pp. 171–175. doi:10.1016/0006-8993(71)90358-1.

Okuno, H. (2011) 'Regulation and function of immediate-early genes in the brain: beyond neuronal activity markers', *Neuroscience Research*, 69(3), pp. 175–186. doi:10.1016/j.neures.2010.12.007.

Ólafsdóttir, H.F., Bush, D. and Barry, C. (2018) 'The Role of Hippocampal Replay in Memory and Planning', *Current Biology*, 28(1), pp. R37–R50. doi:10.1016/j.cub.2017.10.073.

Olgiati, V.R. *et al.* (1980) 'The central GABAergic system and control of food intake under different experimental conditions', *Psychopharmacology*, 68(2), pp. 163–167. doi:10.1007/BF00432135.

Olivé, I. *et al.* (2018) 'Superior colliculus resting state networks in post-traumatic stress disorder and its dissociative subtype', *Human Brain Mapping*, 39(1), pp. 563–574. doi:10.1002/hbm.23865.

Omlor, W. *et al.* (2019) 'Context-dependent limb movement encoding in neuronal populations of motor cortex', *Nature Communications*, 10(1). doi:10.1038/s41467-019-12670-z.

Optican, L.M. (2008) 'The role of omnipause neurons', *Progress in brain research*, 171, pp. 115–121. doi:10.1016/S0079-6123(08)00615-8.

References

Osiro, S. *et al.* (2012) 'August Forel (1848-1931): a look at his life and work', *Child's Nervous System: ChNS: Official Journal of the International Society for Pediatric Neurosurgery*, 28(1), pp. 1–5. doi:10.1007/s00381-011-1659-7.

Osmanski, B.F. *et al.* (2014a) 'Functional ultrasound imaging of intrinsic connectivity in the living rat brain with high spatiotemporal resolution', *Nature Communications*, 5, p. 5023. doi:10.1038/ncomms6023.

Osmanski, B.F. *et al.* (2014b) 'Functional ultrasound imaging reveals different odor-evoked patterns of vascular activity in the main olfactory bulb and the anterior piriform cortex', *NeuroImage*, 95, pp. 176–184. doi:10.1016/j.neuroimage.2014.03.054.

Osterhout, J.A. *et al.* (2015) 'Contactin-4 mediates axon-target specificity and functional development of the accessory optic system', *Neuron*, 86(4), pp. 985–999. doi:10.1016/j.neuron.2015.04.005.

Overton, P.G. (2008) 'Collicular dysfunction in attention deficit hyperactivity disorder', *Medical Hypotheses*, 70(6), pp. 1121–1127. doi:10.1016/j.mehy.2007.11.016.

Owen, S.F., Liu, M.H. and Kreitzer, A.C. (2019) 'Thermal constraints on in vivo optogenetic manipulations', *Nature Neuroscience*, 22(7), pp. 1061–1065. doi:10.1038/s41593-019-0422-3.

Oyama, K. *et al.* (2021) 'Chemogenetic dissection of the primate prefronto-subcortical pathways for working memory and decision-making', *Science Advances*, 7(26), p. eabg4246. doi:10.1126/sciadv.abg4246.

Oyster, C.W. and Takahashi, E.S. (1975) 'Responses of rabbit superior colliculus neurons to repeated visual stimuli', *Journal of Neurophysiology*, 38(2), pp. 301–312. doi:10.1152/jn.1975.38.2.301.

Palay, S.L. (1956) 'Synapses in the central nervous system', *The Journal of Biophysical and Biochemical Cytology*, 2(4 Suppl), pp. 193–202. doi:10.1083/jcb.2.4.193.

Palay, S.L. and Palade, G.E. (1955) 'THE FINE STRUCTURE OF NEURONS', *The Journal of Biophysical and Biochemical Cytology*, 1(1), pp. 69–88.

Parkes, L.M. *et al.* (2009) 'Multivoxel fMRI analysis of color tuning in human primary visual cortex', *Journal of Vision*, 9(1), p. 1.1-13. doi:10.1167/9.1.1.

Pascoli, V., Turiault, M. and Lüscher, C. (2012) 'Reversal of cocaine-evoked synaptic potentiation resets drug-induced adaptive behaviour', *Nature*, 481(7379), pp. 71–75. doi:10.1038/nature10709.

Pasupathy, A. and Connor, C.E. (2001) 'Shape representation in area V4: position-specific tuning for boundary conformation', *Journal of Neurophysiology*, 86(5), pp. 2505–2519. doi:10.1152/jn.2001.86.5.2505.

Pearce, J.M.S. (2003) 'Sir David Ferrier MD, FRS', *Journal of Neurology, Neurosurgery, and Psychiatry*, 74(6), p. 787. doi:10.1136/jnnp.74.6.787.

Pearce, J.M.S. (2009) 'Marie-Jean-Pierre Flourens (1794-1867) and cortical localization', *European Neurology*, 61(5), pp. 311–314. doi:10.1159/000206858.

Pearce, J.M.S. (2018) 'Lord Adrian, MD, PRS, OM', *European Neurology*, 79(1–2), pp. 64–67. doi:10.1159/000485615.

Penaud-Budloo, M. *et al.* (2008) 'Adeno-Associated Virus Vector Genomes Persist as Episomal Chromatin in Primate Muscle', *Journal of Virology* [Preprint]. doi:10.1128/JVI.00649-08.

Pessoa, L. (2019) 'Embracing integration and complexity: placing emotion within a science of brain and behaviour', *Cognition & Emotion*, 33(1), pp. 55–60. doi:10.1080/02699931.2018.1520079.

Pfeffer, C.K. *et al.* (2013) 'Inhibition of inhibition in visual cortex: the logic of connections between molecularly distinct interneurons', *Nature Neuroscience*, 16(8), pp. 1068–1076. doi:10.1038/nn.3446.

Piccolino, M. (2008) 'Visual images in Luigi Galvani's path to animal electricity', *Journal of the History of the Neurosciences*, 17(3), pp. 335–348. doi:10.1080/09647040701420198.

Pickard, R.S. (1979) 'Printed circuit microelectrodes', *Trends in Neurosciences*, 2, pp. 259–261. doi:10.1016/0166-2236(79)90101-2.

Pinsk, M.A. *et al.* (2009) 'Neural representations of faces and body parts in macaque and human cortex: a comparative FMRI study', *Journal of Neurophysiology*, 101(5), pp. 2581–2600. doi:10.1152/jn.91198.2008.

Polimeni, J.R. *et al.* (2018) 'Analysis strategies for high-resolution UHF-fMRI data', *NeuroImage*, 168, pp. 296–320. doi:10.1016/j.neuroimage.2017.04.053.

Popivanov, I.D. *et al.* (2012) 'Stimulus representations in body-selective regions of the macaque cortex assessed with event-related fMRI', *NeuroImage*, 63(2), pp. 723–741. doi:10.1016/j.neuroimage.2012.07.013.

Pretegiani, E. *et al.* (2019) 'Evidence From Parkinson's Disease That the Superior Colliculus Couples Action and Perception', *Movement Disorders: Official Journal of the Movement Disorder Society*, 34(11), pp. 1680–1689. doi:10.1002/mds.27861.

Provost, J. *et al.* (2018) 'Simultaneous positron emission tomography and ultrafast ultrasound for hybrid molecular, anatomical and functional imaging', *Nature Biomedical Engineering*, 2(2), pp. 85–94. doi:10.1038/s41551-018-0188-z.

Rabut, C. *et al.* (2019) '4D functional ultrasound imaging of whole-brain activity in rodents', *Nature Methods*, 16(10), pp. 994–997. doi:10.1038/s41592-019-0572-y.

Rabut, C. *et al.* (2020) 'Pharmaco-fUS: Quantification of pharmacologically-induced dynamic changes in brain perfusion and connectivity by functional ultrasound imaging in awake mice', *NeuroImage*, 222, p. 117231. doi:10.1016/j.neuroimage.2020.117231.

Raducanu, B.C. *et al.* (2017) 'Time Multiplexed Active Neural Probe with 1356 Parallel Recording Sites', *Sensors*, 17(10), p. 2388. doi:10.3390/s17102388.

Rafiee, F. *et al.* (2021) 'Brain MRI in Autism Spectrum Disorder: Narrative Review and Recent Advances', *Journal of magnetic resonance imaging: JMRI* [Preprint]. doi:10.1002/jmri.27949.

Ragan, T. *et al.* (2012) 'Serial two-photon tomography for automated ex vivo mouse brain imaging', *Nature Methods*, 9(3), pp. 255–258. doi:10.1038/nmeth.1854.

Rahal, L. *et al.* (2020) 'Ultrafast ultrasound imaging pattern analysis reveals distinctive dynamic brain states and potent sub-network alterations in arthritic animals', *Scientific Reports*, 10(1), p. 10485. doi:10.1038/s41598-020-66967-x.

Ramirez, S. *et al.* (2013) 'Creating a False Memory in the Hippocampus', *Science* [Preprint]. doi:10.1126/science.1239073.

Ramon y Cajal, S. (1899) *Die Structur des Chiasma opticum : nebst einer allgemeinen Theorie der Kreuzung der Nervenbahnen*. Leipzig : Johann Ambrosius Barth. Available at: http://archive.org/details/b22384753 (Accessed: 19 January 2022).

Ramsey, J.D. *et al.* (2010) 'Six problems for causal inference from fMRI', *NeuroImage*, 49(2), pp. 1545–1558. doi:10.1016/j.neuroimage.2009.08.065.

Rau, R. *et al.* (2018) '3D functional ultrasound imaging of pigeons', *NeuroImage*, 183, pp. 469–477. doi:10.1016/j.neuroimage.2018.08.014.

Rauch, A., Rainer, G. and Logothetis, N.K. (2008) 'The effect of a serotonin-induced dissociation between spiking and perisynaptic activity on BOLD functional MRI', *Proceedings of the National Academy of Sciences of the United States of America*, 105(18), pp. 6759–6764. doi:10.1073/pnas.0800312105.

Redgrave, P. *et al.* (1981) 'Gnawing and changes in reactivity produced by microinjections of picrotoxin into the superior colliculus of rats', *Psychopharmacology*, 75(2), pp. 198–203. doi:10.1007/BF00432187.

Redgrave, P. *et al.* (1988) 'The projection from superior colliculus to cuneiform area in the rat. I. Anatomical studies', *Experimental Brain Research*, 72(3), pp. 611–625. doi:10.1007/BF00250606.

Redgrave, P. *et al.* (2010) 'Interactions between the Midbrain Superior Colliculus and the Basal Ganglia', *Frontiers in Neuroanatomy*, 4, p. 132. doi:10.3389/fnana.2010.00132.

Redgrave, P., Marrow, L.P. and Dean, P. (1992) 'Anticonvulsant role of nigrotectal projection in the maximal electroshock model of epilepsy--II. Pathways from substantia nigra pars lateralis and adjacent peripeduncular area to the dorsal midbrain', *Neuroscience*, 46(2), pp. 391–406. doi:10.1016/0306-4522(92)90060-f.

Redgrave, P., Prescott, T.J. and Gurney, K. (1999) 'The basal ganglia: a vertebrate solution to the selection problem?', *Neuroscience*, 89(4), pp. 1009–1023. doi:10.1016/s0306-4522(98)00319-4.

Redgrave, P., Vautrelle, N. and Reynolds, J.N.J. (2011) 'Functional properties of the basal ganglia's re-entrant loop architecture: selection and reinforcement', *Neuroscience*, 198, pp. 138–151. doi:10.1016/j.neuroscience.2011.07.060.

Rees, A. (1996) 'Aligning maps of visual and auditory space. Sensory maps', *Current biology: CB*, 6(8), pp. 955–958. doi:10.1016/s0960-9822(02)00637-1.

Reig, R. and Silberberg, G. (2014) 'Article Multisensory Integration in the Mouse Striatum', *Neuron*, 83, pp. 1200–1212. doi:10.1016/j.neuron.2014.07.033.

Reijmers, L.G. *et al.* (2007) 'Localization of a stable neural correlate of associative memory', *Science (New York, N.Y.)*, 317(5842), pp. 1230–1233. doi:10.1126/science.1143839.

Rein, M.L. and Deussing, J.M. (2012) 'The optogenetic (r)evolution', *Molecular Genetics and Genomics*, 287(2), pp. 95–109. doi:10.1007/s00438-011-0663-7.

Reinhard, K. *et al.* (2019) 'A projection specific logic to sampling visual inputs in mouse superior colliculus.', *eLife*, 8. doi:10.7554/eLife.50697.

Renier, N. *et al.* (2014) 'iDISCO: a simple, rapid method to immunolabel large tissue samples for volume imaging', *Cell*, 159(4), pp. 896–910. doi:10.1016/j.cell.2014.10.010.

Renshaw, B., Forbes, A. and Morison, B.R. (1940) 'ACTIVITY OF ISOCORTEX AND HIPPOCAMPUS: ELECTRICAL STUDIES WITH MICRO-ELECTRODES', *Journal of Neurophysiology* [Preprint]. doi:10.1152/jn.1940.3.1.74.

Rickgauer, J.P., Deisseroth, K. and Tank, D.W. (2014) 'Simultaneous cellular-resolution optical perturbation and imaging of place cell firing fields', *Nature Neuroscience*, 17(12), pp. 1816–1824. doi:10.1038/nn.3866.

Ringer, S. (1883) 'A further Contribution regarding the influence of the different Constituents of the Blood on the Contraction of the Heart', *The Journal of Physiology*, 4(1), pp. 29-42.3. doi:10.1113/jphysiol.1883.sp000120.

# References

Rios, G. *et al.* (2016) 'Nanofabricated Neural Probes for Dense 3-D Recordings of Brain Activity', *Nano Letters*, 16(11), pp. 6857–6862. doi:10.1021/acs.nanolett.6b02673.

Rispoli, V., Schreglmann, S.R. and Bhatia, K.P. (2018) 'Neuroimaging advances in Parkinson's disease', *Current Opinion in Neurology*, 31(4), pp. 415–424. doi:10.1097/WCO.0000000000000584.

Robles, E., Filosa, A. and Baier, H. (2013) 'Precise lamination of retinal axons generates multiple parallel input pathways in the tectum', *The Journal of Neuroscience: The Official Journal of the Society for Neuroscience*, 33(11), pp. 5027–5039. doi:10.1523/JNEUROSCI.4990-12.2013.

Roe, D. and Finger, S. (1996) 'Gustave Dax and his fight for recognition: an overlooked chapter in the early history of cerebral dominance', *Journal of the History of the Neurosciences*, 5(3), pp. 228–240. doi:10.1080/09647049609525672.

Rogan, S.C. and Roth, B.L. (2011) 'Remote control of neuronal signaling', *Pharmacological Reviews*, 63(2), pp. 291–315. doi:10.1124/pr.110.003020.

van Rooij, S.J.H. *et al.* (2021) 'Defining focal brain stimulation targets for PTSD using neuroimaging', *Depression and Anxiety* [Preprint]. doi:10.1002/da.23159.

Roy, D.S. *et al.* (2019) 'Brain-wide mapping of contextual fear memory engram ensembles supports the dispersed engram complex hypothesis', *BioRxiv* [Preprint]. doi:10.1101/668483.

Rubin, J.M. *et al.* (1994) 'Power Doppler US: a potentially useful alternative to mean frequency-based color Doppler US.', *Radiology*, 190(3), pp. 853–856. doi:10.1148/radiology.190.3.8115639.

Rubin, J.M. *et al.* (1995) 'Fractional moving blood volume: estimation with power Doppler US.', *Radiology*, 197(1), pp. 183–190. doi:10.1148/radiology.197.1.7568820.

Rungta, R.L. *et al.* (2017) 'Light controls cerebral blood flow in naive animals', *Nature Communications*, 8. doi:10.1038/ncomms14191.

Sagar, S.M., Sharp, F.R. and Curran, T. (1988) 'Expression of c-fos protein in brain: metabolic mapping at the cellular level', *Science (New York, N.Y.)*, 240(4857), pp. 1328–1331. doi:10.1126/science.3131879.

Sahibzada, N., Dean, P. and Redgrave, P. (1986) 'Movements resembling orientation or avoidance elicited by electrical stimulation of the superior colliculus in rats', *Journal of Neuroscience*, 6(3), pp. 723–733. doi:10.1523/JNEUROSCI.06-03-00723.1986.

Sakurai, K. *et al.* (2016) 'Capturing and Manipulating Activated Neuronal Ensembles with CANE Delineates a Hypothalamic Social-Fear Circuit', *Neuron*, 92(4), pp. 739–753. doi:10.1016/j.neuron.2016.10.015.

Salay, L.D. and Huberman, A.D. (2021) 'Divergent outputs of the ventral lateral geniculate nucleus mediate visually evoked defensive behaviors', *Cell Reports*, 37(1), p. 109792. doi:10.1016/j.celrep.2021.109792.

Salay, L.D., Ishiko, N. and Huberman, A.D. (2018) 'A midline thalamic circuit determines reactions to visual threat', *Nature*, 557(7704), pp. 183–189. doi:10.1038/s41586-018-0078-2.

Sandrone, S. and Zanin, E. (2014) 'David Ferrier (1843-1928)', *Journal of Neurology*, 261(6), pp. 1247–1248. doi:10.1007/s00415-013-7023-y.

Sans-Dublanc, A. *et al.* (2021) 'Optogenetic fUSI for brain-wide mapping of neural activity mediating collicular-dependent behaviors', *Neuron*, 109(11), pp. 1888-1905.e10. doi:10.1016/j.neuron.2021.04.008.

Savjani, R.R. *et al.* (2018) 'Polar-angle representation of saccadic eye movements in human superior colliculus', *NeuroImage*, 171, pp. 199–208. doi:10.1016/j.neuroimage.2017.12.080.

Schaefer, K.P. (1970) 'Unit analysis and electrical stimulation in the optic tectum of rabbits and cats', *Brain, Behavior and Evolution*, 3(1), pp. 222–240. doi:10.1159/000125475.

Scheffer, L.K. *et al.* (2020) 'A connectome and analysis of the adult Drosophila central brain', *eLife*, 9, p. e57443. doi:10.7554/eLife.57443.

Schenberg, L.C. *et al.* (2005) 'Functional specializations within the tectum defense systems of the rat', *Neuroscience and Biobehavioral Reviews*, 29(8), pp. 1279–1298. doi:10.1016/j.neubiorev.2005.05.006.

Schiller, P.H. and Stryker, M. (1972) 'Single-unit recording and stimulation in superior colliculus of the alert rhesus monkey', *Journal of Neurophysiology*, 35(6), pp. 915–924. doi:10.1152/jn.1972.35.6.915.

Schiller, P.H. and Tehovnik, E.J. (2005) 'Neural mechanisms underlying target selection with saccadic eye movements', *Progress in Brain Research*, 149, pp. 157–171. doi:10.1016/S0079-6123(05)49012-3.

Schmid, F. *et al.* (2017) 'True and apparent optogenetic BOLD fMRI signals', *Magnetic Resonance in Medicine*, 77(1), pp. 126–136. doi:10.1002/mrm.26095.

Schmitt, C. *et al.* (2020) 'A Causal Role of Area hMST for Self-Motion Perception in Humans', *Cerebral Cortex Communications*, 1(1), p. tgaa042. doi:10.1093/texcom/tgaa042.

Schmued, L.C. and Fallon, J.H. (1986) 'Fluoro-Gold: a new fluorescent retrograde axonal tracer with numerous unique properties', *Brain Research*, 377(1), pp. 147–154. doi:10.1016/0006-8993(86)91199-6.

Scholvin, J. *et al.* (2016) 'Close-Packed Silicon Microelectrodes for Scalable Spatially Oversampled Neural Recording', *IEEE Transactions on Biomedical Engineering*, 63(1), pp. 120–130. doi:10.1109/TBME.2015.2406113.

Schulz, J.M. *et al.* (2009) 'Short-latency activation of striatal spiny neurons via subcortical visual pathways', *Journal of Neuroscience*, 29(19), pp. 6336–6347. doi:10.1523/JNEUROSCI.4815-08.2009.

Scudder, C.A. *et al.* (1996) 'Anatomy and physiology of saccadic long-lead burst neurons recorded in the alert squirrel monkey. II. Pontine neurons', *Journal of Neurophysiology*, 76(1), pp. 353–370. doi:10.1152/jn.1996.76.1.353.

Scudder, C.A., Fuchs, A.F. and Langer, T.P. (1988) 'Characteristics and functional identification of saccadic inhibitory burst neurons in the alert monkey', *Journal of Neurophysiology*, 59(5), pp. 1430–1454. doi:10.1152/jn.1988.59.5.1430.

Seidl, K. *et al.* (2011) 'CMOS-Based High-Density Silicon Microprobe Arrays for Electronic Depth Control in Intracortical Neural Recording', *Journal of Microelectromechanical Systems*, 20(6), pp. 1439–1448. doi:10.1109/JMEMS.2011.2167661.

Sestieri, C., Shulman, G.L. and Corbetta, M. (2017) 'The contribution of the human posterior parietal cortex to episodic memory', *Nature Reviews. Neuroscience*, 18(3), pp. 183–192. doi:10.1038/nrn.2017.6.

Seyfarth, E.-A. (2006) 'Julius Bernstein (1839-1917): pioneer neurobiologist and biophysicist', *Biological Cybernetics*, 94(1), pp. 2–8. doi:10.1007/s00422-005-0031-y.

Sgambato, V. *et al.* (1999) 'Effect of a functional impairment of corticostriatal transmission on cortically evoked expression of c-Fos and zif 268 in the rat basal ganglia', *Neuroscience*, 93(4), pp. 1313–1321. doi:10.1016/s0306-4522(99)00267-5.

Shang, C. *et al.* (2015) 'A parvalbumin-positive excitatory visual pathway to trigger fear responses in mice', *Science*, 348(6242), pp. 1472–1477. doi:10.1126/science.aaa8694.

Shang, C. *et al.* (2018) 'Divergent midbrain circuits orchestrate escape and freezing responses to looming stimuli in mice', *Nature Communications*, 9(1), p. 1232. doi:10.1038/s41467-018-03580-7.

Shang, C. *et al.* (2019) 'A subcortical excitatory circuit for sensory-triggered predatory hunting in mice', *Nature Neuroscience*, 22(6), pp. 909–920. doi:10.1038/s41593-019-0405-4.

Sheffield, J.M. and Barch, D.M. (2016) 'Cognition and resting-state functional connectivity in schizophrenia', *Neuroscience and Biobehavioral Reviews*, 61, pp. 108–120. doi:10.1016/j.neubiorev.2015.12.007.

Shen, T. *et al.* (1993) 'Monocrystalline iron oxide nanocompounds (MION): physicochemical properties', *Magnetic Resonance in Medicine*, 29(5), pp. 599–604. doi:10.1002/mrm.1910290504.

Shi, X. *et al.* (2017) 'Retinal origin of direction selectivity in the superior colliculus', *Nature Neuroscience*, 20(4), pp. 550–558. doi:10.1038/nn.4498.

Shiba, Y. *et al.* (2017) 'Converging Prefronto-Insula-Amygdala Pathways in Negative Emotion Regulation in Marmoset Monkeys', *Biological Psychiatry*, 82(12), pp. 895–903. doi:10.1016/j.biopsych.2017.06.016.

Shih, Y.-Y.I. *et al.* (2009) 'A new scenario for negative functional magnetic resonance imaging signals: endogenous neurotransmission', *The Journal of Neuroscience: The Official Journal of the Society for Neuroscience*, 29(10), pp. 3036–3044. doi:10.1523/JNEUROSCI.3447-08.2009.

Shih, Y.-Y.I. *et al.* (2011) 'Striatal and cortical BOLD, blood flow, blood volume, oxygen consumption, and glucose consumption changes in noxious forepaw electrical stimulation', *Journal of Cerebral Blood Flow and Metabolism: Official Journal of the International Society of Cerebral Blood Flow and Metabolism*, 31(3), pp. 832–841. doi:10.1038/jcbfm.2010.173.

Shin, L.M., Rauch, S.L. and Pitman, R.K. (2006) 'Amygdala, medial prefrontal cortex, and hippocampal function in PTSD', *Annals of the New York Academy of Sciences*, 1071, pp. 67–79. doi:10.1196/annals.1364.007.

Shipley, F.B. *et al.* (2014) 'Simultaneous optogenetic manipulation and calcium imaging in freely moving C. elegans', *Frontiers in Neural Circuits*, 8, p. 28. doi:10.3389/fncir.2014.00028.

Sieu, L.-A. *et al.* (2015) 'EEG and functional ultrasound imaging in mobile rats', *Nature Methods*, 12(9), pp. 831–834. doi:10.1038/nmeth.3506.

Silvanto, J. and Pascual-Leone, A. (2012) 'Why the assessment of causality in brain-behavior relations requires brain stimulation', *Journal of Cognitive Neuroscience*, 24(4), pp. 775–777. doi:10.1162/jocn_a_00193.

Simons-Weidenmaier, N.S. *et al.* (2006) 'Synaptic depression and short-term habituation are located in the sensory part of the mammalian startle pathway', *BMC Neuroscience*, 7(1), p. 38. doi:10.1186/1471-2202-7-38.

Simpson, J.I. (1984) 'The accessory optic system', *Annual Review of Neuroscience*, 7, pp. 13–41. doi:10.1146/annurev.ne.07.030184.000305.

Sirotin, Y.B. and Das, A. (2009) 'Anticipatory haemodynamic signals in sensory cortex not predicted by local neuronal activity', *Nature*, 457(7228), pp. 475–479. doi:10.1038/nature07664.

Smith, R.H. (2008) 'Adeno-associated virus integration: virus versus vector', *Gene Therapy*, 15(11), pp. 817–822. doi:10.1038/gt.2008.55.

# References

Smitha, K.A. *et al.* (2017) 'Resting state fMRI: A review on methods in resting state connectivity analysis and resting state networks', *The Neuroradiology Journal*, 30(4), pp. 305–317. doi:10.1177/1971400917697342.

Soddu, A. *et al.* (2011) 'Resting state activity in patients with disorders of consciousness', *Functional Neurology*, 26(1), pp. 37–43.

Sokoloff, L. *et al.* (1977) 'The [14C]deoxyglucose method for the measurement of local cerebral glucose utilization: theory, procedure, and normal values in the conscious and anesthetized albino rat', *Journal of Neurochemistry*, 28(5), pp. 897–916. doi:10.1111/j.1471-4159.1977.tb10649.x.

Sotelo, C. (2003) 'Viewing the brain through the master hand of Ramón y Cajal', *Nature Reviews. Neuroscience*, 4(1), pp. 71–77. doi:10.1038/nrn1010.

Sparks, D.L. (1999) 'Conceptual issues related to the role of the superior colliculus in the control of gaze', *Current Opinion in Neurobiology*, 9(6), pp. 698–707. doi:10.1016/S0959-4388(99)00039-2.

Sparks, D.L. (2002) 'The brainstem control of saccadic eye movements', *Nature reviews. Neuroscience*, 3(12), pp. 952–964. doi:10.1038/nrn986 [doi]; nrn986 [pii].

Sparks, D.L. and Hartwich-Young, R. (1989) 'The deep layers of the superior colliculus', *Reviews of Oculomotor Research*, 3, pp. 213–255.

Sprague, J.M. and Meikle, T.H. (1965) 'THE ROLE OF THE SUPERIOR COLLICULUS IN VISUALLY GUIDED BEHAVIOR', *Experimental Neurology*, 11, pp. 115–146. doi:10.1016/0014-4886(65)90026-9.

Stachniak, T.J., Ghosh, A. and Sternson, S.M. (2014) 'Chemogenetic synaptic silencing of neural circuits localizes a hypothalamus→midbrain pathway for feeding behavior', *Neuron*, 82(4), pp. 797–808. doi:10.1016/j.neuron.2014.04.008.

Stahnisch, F.W. (2015) 'Joseph von Gerlach (1820-1896)', *Journal of Neurology*, 262(5), pp. 1397–1399. doi:10.1007/s00415-015-7735-2.

Stamatakis, A.M. *et al.* (2016) 'Lateral Hypothalamic Area Glutamatergic Neurons and Their Projections to the Lateral Habenula Regulate Feeding and Reward', *The Journal of Neuroscience*, 36(2), pp. 302–311. doi:10.1523/JNEUROSCI.1202-15.2016.

Stauffer, W.R. *et al.* (2016) 'Dopamine Neuron-Specific Optogenetic Stimulation in Rhesus Macaques', *Cell*, 166(6), pp. 1564-1571.e6. doi:10.1016/j.cell.2016.08.024.

Steenland, H.W. and McNaughton, B.L. (2015) 'Techniques for Large-Scale Multiunit Recording', in Tatsuno, M. (ed.) *Analysis and Modeling of Coordinated Multi-neuronal Activity*. New York, NY: Springer (Springer Series in Computational Neuroscience), pp. 3–39. doi:10.1007/978-1-4939-1969-7_1.

Stein, B.E., Magalhães-Castro, B. and Kruger, L. (1976) 'Relationship between visual and tactile representations in cat superior colliculus', *Journal of Neurophysiology*, 39(2), pp. 401–419. doi:10.1152/jn.1976.39.2.401.

Steinmetz, N.A. *et al.* (2017) 'Aberrant Cortical Activity in Multiple GCaMP6-Expressing Transgenic Mouse Lines', *eNeuro*, 4(5), p. ENEURO.0207-17.2017. doi:10.1523/ENEURO.0207-17.2017.

Steinmetz, N.A. *et al.* (2018) 'Challenges and opportunities for large-scale electrophysiology with Neuropixels probes', *Current Opinion in Neurobiology*, 50, pp. 92–100. doi:10.1016/j.conb.2018.01.009.

Steinmetz, N.A. *et al.* (2019) 'Distributed coding of choice, action and engagement across the mouse brain', *Nature*, 576(7786), pp. 266–273. doi:10.1038/s41586-019-1787-x.

Steinmetz, N.A. *et al.* (2021) 'Neuropixels 2.0: A miniaturized high-density probe for stable, long-term brain recordings', *Science (New York, N.Y.)*, 372(6539), p. eabf4588. doi:10.1126/science.abf4588.

Stirman, J.N. *et al.* (2016) 'Wide field-of-view, multi-region, two-photon imaging of neuronal activity in the mammalian brain', *Nature Biotechnology*, 34(8), pp. 857–862. doi:10.1038/nbt.3594.

Stoeckel, K., Schwab, M. and Thoenen, H. (1977) 'Role of gangliosides in the uptake and retrograde axonal transport of cholera and tetanus toxin as compared to nerve growth factor and wheat germ agglutinin', *Brain Research*, 132(2), pp. 273–285. doi:10.1016/0006-8993(77)90421-8.

Storace, D.A. *et al.* (2015) 'Monitoring brain activity with protein voltage and calcium sensors', *Scientific Reports*, 5, p. 10212. doi:10.1038/srep10212.

Strassman, A., Highstein, S.M. and McCrea, R.A. (1986) 'Anatomy and physiology of saccadic burst neurons in the alert squirrel monkey. I. Excitatory burst neurons', *The Journal of Comparative Neurology*, 249(3), pp. 337–357. doi:10.1002/cne.902490303.

Stringer, C. *et al.* (2019) 'Spontaneous behaviors drive multidimensional, brainwide activity', *Science*, 364(6437). doi:10.1126/science.aav7893.

Stuphorn, V., Bauswein, E. and Hoffmann, K.P. (2000) 'Neurons in the primate superior colliculus coding for arm movements in gaze-related coordinates', *Journal of Neurophysiology*, 83(3), pp. 1283–1299. doi:10.1152/jn.2000.83.3.1283.

Stuphorn, V., Hoffmann, K.P. and Miller, L.E. (1999) 'Correlation of primate superior colliculus and reticular formation discharge with proximal limb muscle activity', *Journal of Neurophysiology*, 81(4), pp. 1978–1982. doi:10.1152/jn.1999.81.4.1978.

Sugita, S. *et al.* (1983) 'Laminar origin of the tecto-thalamic projections in the albino rat', *Neuroscience Letters*, 43(2–3), pp. 143–147. doi:10.1016/0304-3940(83)90178-7.

Sun, L.O. *et al.* (2015) 'Functional Assembly of Accessory Optic System Circuitry Critical for Compensatory Eye Movements', *Neuron*, 86(4), pp. 971–984. doi:10.1016/j.neuron.2015.03.064.

Suzuki, D.G. *et al.* (2019) 'The role of the optic tectum for visually evoked orienting and evasive movements', *Proceedings of the National Academy of Sciences*, 116(30), pp. 15272–15281. doi:10.1073/pnas.1907962116.

Sweeney, P. and Yang, Y. (2016) 'An Inhibitory Septum to Lateral Hypothalamus Circuit That Suppresses Feeding', *The Journal of Neuroscience: The Official Journal of the Society for Neuroscience*, 36(44), pp. 11185–11195. doi:10.1523/JNEUROSCI.2042-16.2016.

Syka, J. and Radil-Weiss, T. (1971) 'Electrical stimulation of the tectum in freely moving cats', *Brain Research*, 28(3), pp. 567–572. doi:10.1016/0006-8993(71)90068-0.

Tafreshiha, A. *et al.* (2021) 'Visual stimulus-specific habituation of innate defensive behaviour in mice', *Journal of Experimental Biology*, 224(6), p. jeb230433. doi:10.1242/jeb.230433.

Tainaka, K. *et al.* (2014) 'Whole-body imaging with single-cell resolution by tissue decolorization', *Cell*, 159(4), pp. 911–924. doi:10.1016/j.cell.2014.10.034.

Takada, M. *et al.* (1985) 'Topographical projections from the posterior thalamic regions to the striatum in the cat, with reference to possible tecto-thalamo-striatal connections', *Experimental Brain Research*, 60(2), pp. 385–396. doi:10.1007/BF00235934.

Takahashi, T. (1985) 'The organization of the lateral thalamus of the hooded rat', *Journal of Comparative Neurology*, 231(3), pp. 281–309. doi:10.1002/cne.902310302.

Takakusaki, K. *et al.* (2004) 'Role of basal ganglia-brainstem pathways in the control of motor behaviors', *Neuroscience Research*, 50(2), pp. 137–151. doi:10.1016/j.neures.2004.06.015.

Takata, N. *et al.* (2015) 'Optogenetic activation of CA1 pyramidal neurons at the dorsal and ventral hippocampus evokes distinct brain-wide responses revealed by mouse fMRI', *PloS One*, 10(3), p. e0121417. doi:10.1371/journal.pone.0121417.

Talbot, S.A. and Marshall, W.H. (1941) 'Physiological Studies on Neural Mechanisms of Visual Localization and Discrimination*', *American Journal of Ophthalmology*, 24(11), pp. 1255–1264. doi:10.1016/S0002-9394(41)91363-6.

Talbot, W.H. *et al.* (1968) 'The sense of flutter-vibration: comparison of the human capacity with response patterns of mechanoreceptive afferents from the monkey hand', *Journal of Neurophysiology*, 31(2), pp. 301–334. doi:10.1152/jn.1968.31.2.301.

Taniguchi, H. *et al.* (2011) 'A resource of Cre driver lines for genetic targeting of GABAergic neurons in cerebral cortex.', *Neuron*, 71(6), pp. 995–1013. doi:10.1016/j.neuron.2011.07.026.

Tasaka, G. *et al.* (2020) 'The Temporal Association Cortex Plays a Key Role in Auditory-Driven Maternal Plasticity', *Neuron*, 107(3), pp. 566-579.e7. doi:10.1016/j.neuron.2020.05.004.

Tayler, K.K. *et al.* (2013) 'Reactivation of Neural Ensembles during the Retrieval of Recent and Remote Memory', *Current Biology*, 23(2), pp. 99–106. doi:10.1016/j.cub.2012.11.019.

Taymans, J.-M. *et al.* (2007) 'Comparative analysis of adeno-associated viral vector serotypes 1, 2, 5, 7, and 8 in mouse brain', *Human Gene Therapy*, 18(3), pp. 195–206. doi:10.1089/hum.2006.178.

Terpou, B.A. *et al.* (2019) 'The Innate Alarm System and Subliminal Threat Presentation in Posttraumatic Stress Disorder: Neuroimaging of the Midbrain and Cerebellum', *Chronic Stress*, 3, p. 247054701882149. doi:10.1177/2470547018821496.

Thanos, P.K. *et al.* (2013) 'Mapping brain metabolic connectivity in awake rats with μPET and optogenetic stimulation', *The Journal of Neuroscience: The Official Journal of the Society for Neuroscience*, 33(15), pp. 6343–6349. doi:10.1523/JNEUROSCI.4997-12.2013.

Thompson, R.F. and Spencer, W.A. (1966) 'Habituation: A model phenomenon for the study of neuronal substrates of behavior', *Psychological Review*, 73(1), pp. 16–43. doi:10.1037/h0022681.

Tian, L. *et al.* (2009) 'Imaging neural activity in worms, flies and mice with improved GCaMP calcium indicators', *Nature Methods*, 6(12), pp. 875–881. doi:10.1038/nmeth.1398.

Tiran, E. *et al.* (2017) 'Transcranial Functional Ultrasound Imaging in Freely Moving Awake Mice and Anesthetized Young Rats without Contrast Agent', *Ultrasound in Medicine & Biology*, 43(8), pp. 1679–1689. doi:10.1016/j.ultrasmedbio.2017.03.011.

Tischmeyer, W. and Grimm, R. (1999) 'Activation of immediate early genes and memory formation', *Cellular and molecular life sciences: CMLS*, 55(4), pp. 564–574. doi:10.1007/s000180050315.

# References

Tolhurst, D.J. and Movshon, J.A. (1975) 'Spatial and temporal contrast sensitivity of striate cortical neurones', *Nature*, 257(5528), pp. 674–675. doi:10.1038/257674a0.

Tootell, R.B. *et al.* (1982) 'Deoxyglucose analysis of retinotopic organization in primate striate cortex', *Science (New York, N.Y.)*, 218(4575), pp. 902–904. doi:10.1126/science.7134981.

Tovote, P. *et al.* (2016) 'Midbrain circuits for defensive behaviour', *Nature*, 534(7606), pp. 206–212. doi:10.1038/nature17996.

Tsien, J.Z. *et al.* (1996) 'Subregion- and cell type-restricted gene knockout in mouse brain', *Cell*, 87(7), pp. 1317–1326. doi:10.1016/s0092-8674(00)81826-7.

Tsien, R.Y. (1980) 'New calcium indicators and buffers with high selectivity against magnesium and protons: design, synthesis, and properties of prototype structures', *Biochemistry*, 19(11), pp. 2396–2404. doi:10.1021/bi00552a018.

Tsien, R.Y. (1981) 'A non-disruptive technique for loading calcium buffers and indicators into cells', *Nature*, 290(5806), pp. 527–528. doi:10.1038/290527a0.

Tye, K.M. *et al.* (2011) 'Amygdala circuitry mediating reversible and bidirectional control of anxiety', *Nature*, 471(7338), pp. 358–362. doi:10.1038/nature09820.

Tye, K.M. *et al.* (2013) 'Dopamine neurons modulate neural encoding and expression of depression-related behaviour', *Nature*, 493(7433), pp. 537–541. doi:10.1038/nature11740.

Uhlirova, H. *et al.* (2016) 'Cell type specificity of neurovascular coupling in cerebral cortex', *eLife*. Edited by S.B. Nelson, 5, p. e14315. doi:10.7554/eLife.14315.

Ukai, H., Kiyonari, H. and Ueda, H.R. (2017) 'Production of knock-in mice in a single generation from embryonic stem cells', *Nature Protocols*, 12(12), pp. 2513–2530. doi:10.1038/nprot.2017.110.

Urban, A. *et al.* (2014) 'Chronic assessment of cerebral hemodynamics during rat forepaw electrical stimulation using functional ultrasound imaging', *NeuroImage*, 101, pp. 138–149. doi:10.1016/j.neuroimage.2014.06.063.

Urban, A. *et al.* (2015) 'Real-time imaging of brain activity in freely moving rats using functional ultrasound', *Nature Methods*, 12(9), pp. 873–878. doi:10.1038/nmeth.3482.

Urban, A. *et al.* (2017) 'Understanding the neurovascular unit at multiple scales: Advantages and limitations of multi-photon and functional ultrasound imaging', *Advanced Drug Delivery Reviews*, 119, pp. 73–100. doi:10.1016/j.addr.2017.07.018.

Van Keuren, M.L. *et al.* (2009) 'Generating Transgenic Mice from Bacterial Artificial Chromosomes: Transgenesis Efficiency, Integration and Expression Outcomes', *Transgenic research*, 18(5), pp. 769–785. doi:10.1007/s11248-009-9271-2.

Vanduffel, W. *et al.* (2001) 'Visual motion processing investigated using contrast agent-enhanced fMRI in awake behaving monkeys', *Neuron*, 32(4), pp. 565–577. doi:10.1016/s0896-6273(01)00502-5.

Vanni, M.P. *et al.* (2017) 'Mesoscale Mapping of Mouse Cortex Reveals Frequency-Dependent Cycling between Distinct Macroscale Functional Modules', *The Journal of Neuroscience: The Official Journal of the Society for Neuroscience*, 37(31), pp. 7513–7533. doi:10.1523/JNEUROSCI.3560-16.2017.

Venkatakrishnan, A.J. *et al.* (2013) 'Molecular signatures of G-protein-coupled receptors', *Nature*, 494(7436), pp. 185–194. doi:10.1038/nature11896.

Vetere, G. *et al.* (2017) 'Chemogenetic Interrogation of a Brain-wide Fear Memory Network in Mice', *Neuron*, 94(2), pp. 363-374.e4. doi:10.1016/j.neuron.2017.03.037.

Vianna, D.M.L. *et al.* (2003) 'Fos-like immunoreactive neurons following electrical stimulation of the dorsal periaqueductal gray at freezing and escape thresholds', *Brain Research Bulletin*, 62(3), pp. 179–189. doi:10.1016/j.brainresbull.2003.09.010.

Villalobos, C.A. *et al.* (2018) 'Parvalbumin and GABA Microcircuits in the Mouse Superior Colliculus', *Frontiers in Neural Circuits*, 12, p. 35. doi:10.3389/fncir.2018.00035.

Viswanathan, A. and Freeman, R.D. (2007) 'Neurometabolic coupling in cerebral cortex reflects synaptic more than spiking activity', *Nature Neuroscience*, 10(10), pp. 1308–1312. doi:10.1038/nn1977.

Wallace, M.T., Wilkinson, L.K. and Stein, B.E. (1996) 'Representation and integration of multiple sensory inputs in primate superior colliculus', *Journal of Neurophysiology*, 76(2), pp. 1246–1266. doi:10.1152/jn.1996.76.2.1246.

Wang, F. *et al.* (2021) 'OFF-transient alpha RGCs mediate looming triggered innate defensive response', *Current biology: CB*, 31(11), pp. 2263-2273.e3. doi:10.1016/j.cub.2021.03.025.

Wang, L. *et al.* (2020) 'A Causal Role for Mouse Superior Colliculus in Visual Perceptual Decision-Making', *The Journal of Neuroscience: The Official Journal of the Society for Neuroscience*, 40(19), pp. 3768–3782. doi:10.1523/JNEUROSCI.2642-19.2020.

Wang, L. and Krauzlis, R.J. (2018) 'Visual Selective Attention in Mice', *Current biology: CB*, 28(5), pp. 676-685.e4. doi:10.1016/j.cub.2018.01.038.

Wang, N. *et al.* (2013) 'Anatomical Evidence that the Superior Colliculus Controls Saccades through Central Mesencephalic Reticular Formation Gating of Omnipause Neuron Activity', *Journal of Neuroscience*, 33(41), pp. 16285–16296. doi:10.1523/JNEUROSCI.2726-11.2013.

Wang, Q. and Burkhalter, A. (2013) 'Stream-related preferences of inputs to the superior colliculus from areas of dorsal and ventral streams of mouse visual cortex', *The Journal of Neuroscience: The Official Journal of the Society for Neuroscience*, 33(4), pp. 1696–1705. doi:10.1523/JNEUROSCI.3067-12.2013.

Wang, Y.C. *et al.* (2020) 'Ultra High Field fMRI of Human Superior Colliculi Activity during Affective Visual Processing', *Scientific Reports*, 10(1), p. 1331. doi:10.1038/s41598-020-57653-z.

Wank, I. *et al.* (2021) 'Central amygdala circuitry modulates nociceptive processing through differential hierarchical interaction with affective network dynamics', *Communications Biology*, 4(1), p. 732. doi:10.1038/s42003-021-02262-3.

Wei, P. *et al.* (2015) 'Processing of visually evoked innate fear by a non-canonical thalamic pathway', *Nature Communications*, 6, p. 6756. doi:10.1038/ncomms7756.

Wei, Z. *et al.* (2020) 'A comparison of neuronal population dynamics measured with calcium imaging and electrophysiology', *PLoS computational biology*, 16(9), p. e1008198. doi:10.1371/journal.pcbi.1008198.

Weitz, A.J. *et al.* (2015) 'Optogenetic fMRI reveals distinct, frequency-dependent networks recruited by dorsal and intermediate hippocampus stimulations', *NeuroImage*, 107, pp. 229–241. doi:10.1016/j.neuroimage.2014.10.039.

Werner, W., Hoffmann, K.P. and Dannenberg, S. (1997) 'Anatomical distribution of arm-movement-related neurons in the primate superior colliculus and underlying reticular formation in comparison with visual and saccadic cells', *Experimental Brain Research*, 115(2), pp. 206–216. doi:10.1007/pl00005691.

White, B.J. *et al.* (2017) 'Superior colliculus neurons encode a visual saliency map during free viewing of natural dynamic video', *Nature Communications*, 8(1), p. 14263. doi:10.1038/ncomms14263.

White, J.G. *et al.* (1986) 'The structure of the nervous system of the nematode Caenorhabditis elegans', *Philosophical Transactions of the Royal Society of London. Series B, Biological Sciences*, 314(1165), pp. 1–340. doi:10.1098/rstb.1986.0056.

Whyland, K.L., Slusarczyk, A.S. and Bickford, M.E. (2020) 'GABAergic cell types in the superficial layers of the mouse superior colliculus', *Journal of Comparative Neurology*, 528(2), pp. 308–320. doi:10.1002/cne.24754.

Wilson, J.S., Hull, C.D. and Buchwald, N.A. (1983) 'Intracellular studies of the convergence of sensory input on caudate neurons of cat', *Brain Research*, 270(2), pp. 197–208. doi:10.1016/0006-8993(83)90593-0.

Wilson, M.A. and McNaughton, B.L. (1993) 'Dynamics of the hippocampal ensemble code for space', *Science (New York, N.Y.)*, 261(5124), pp. 1055–1058. doi:10.1126/science.8351520.

Wilson, Y. *et al.* (2002) 'Visualization of functionally activated circuitry in the brain', *Proceedings of the National Academy of Sciences of the United States of America*, 99(5), pp. 3252–3257. doi:10.1073/pnas.042701199.

Winder, A.T. *et al.* (2017) 'Weak correlations between hemodynamic signals and ongoing neural activity during the resting state', *Nature Neuroscience*, 20(12), pp. 1761–1769. doi:10.1038/s41593-017-0007-y.

Winnubst, J. *et al.* (2019) 'Reconstruction of 1,000 Projection Neurons Reveals New Cell Types and Organization of Long-Range Connectivity in the Mouse Brain', *Cell*, 179(1), pp. 268-281.e13. doi:10.1016/j.cell.2019.07.042.

Wise, K.D., Angell, J.B. and Starr, A. (1970) 'An Integrated-Circuit Approach to Extracellular Microelectrodes', *IEEE Transactions on Biomedical Engineering*, BME-17(3), pp. 238–247. doi:10.1109/TBME.1970.4502738.

Wolters, A.F. *et al.* (2019) 'Resting-state fMRI in Parkinson's disease patients with cognitive impairment: A meta-analysis', *Parkinsonism & Related Disorders*, 62, pp. 16–27. doi:10.1016/j.parkreldis.2018.12.016.

Wurtz, R.H. (1969) 'Visual receptive fields of striate cortex neurons in awake monkeys', *Journal of Neurophysiology*, 32(5), pp. 727–742. doi:10.1152/jn.1969.32.5.727.

Wurtz, R.H. (2009) 'Recounting the impact of Hubel and Wiesel', *The Journal of Physiology*, 587(Pt 12), pp. 2817–2823. doi:10.1113/jphysiol.2009.170209.

Wurtz, R.H. and Goldberg, M.E. (1971) 'Superior colliculus cell responses related to eye movements in awake monkeys', *Science (New York, N.Y.)*, 171(3966), pp. 82–84. doi:10.1126/science.171.3966.82.

Wurtz, R.H. and Goldberg, M.E. (1972) 'Activity of superior colliculus in behaving monkey. 3. Cells discharging before eye movements', *Journal of Neurophysiology*, 35(4), pp. 575–586. doi:10.1152/jn.1972.35.4.575.

Wurtz, R.H. and Optican, L.M. (1994) 'Superior colliculus cell types and models of saccade generation', *Current Opinion in Neurobiology*, 4(6), pp. 857–861. doi:10.1016/0959-4388(94)90134-1.

Xiao, D. *et al.* (2017) 'Mapping cortical mesoscopic networks of single spiking cortical or sub-cortical neurons', *eLife*, 6, p. e19976. doi:10.7554/eLife.19976.

Xiong, W. and Jin, X. (2012) 'Optogenetic field potential recording in cortical slices', *Journal of Neuroscience Methods*, 210(2), pp. 119–124. doi:10.1016/j.jneumeth.2012.07.019.

# References

Xiu, J. *et al.* (2014) 'Visualizing an emotional valence map in the limbic forebrain by TAI-FISH', *Nature Neuroscience*, 17(11), pp. 1552–1559. doi:10.1038/nn.3813.

Yamagata, M. *et al.* (2006) 'Labeled lines in the retinotectal system: markers for retinorecipient sublaminae and the retinal ganglion cell subsets that innervate them', *Molecular and Cellular Neurosciences*, 33(3), pp. 296–310. doi:10.1016/j.mcn.2006.08.001.

Yang, B. *et al.* (2014) 'Single-cell phenotyping within transparent intact tissue through whole-body clearing', *Cell*, 158(4), pp. 945–958. doi:10.1016/j.cell.2014.07.017.

Yang, Y. *et al.* (2018) 'Improved calcium sensor GCaMP-X overcomes the calcium channel perturbations induced by the calmodulin in GCaMP', *Nature Communications*, 9(1), p. 1504. doi:10.1038/s41467-018-03719-6.

Ye, L. *et al.* (2016) 'Wiring and Molecular Features of Prefrontal Ensembles Representing Distinct Experiences', *Cell*, 165(7), pp. 1776–1788. doi:10.1016/j.cell.2016.05.010.

Yilmaz, M. and Meister, M. (2013) 'Rapid innate defensive responses of mice to looming visual stimuli', *Current Biology*, 23(20), pp. 2011–2015. doi:10.1016/j.cub.2013.08.015.

Yin, W. *et al.* (2020) 'A petascale automated imaging pipeline for mapping neuronal circuits with high-throughput transmission electron microscopy', *Nature Communications*, 11, p. 4949. doi:10.1038/s41467-020-18659-3.

Yizhar, O. *et al.* (2011) 'Optogenetics in Neural Systems', *Neuron*, 71(1), pp. 9–34. doi:10.1016/j.neuron.2011.06.004.

Yoshida, K. *et al.* (1982) 'Morphological and physiological characteristics of inhibitory burst neurons controlling horizontal rapid eye movements in the alert cat.', *Journal of Neurophysiology*, 48(3), pp. 761–784. doi:10.1152/jn.1982.48.3.761.

Yu, Y. and Bradley, A. (2001) 'Engineering chromosomal rearrangements in mice', *Nature Reviews. Genetics*, 2(10), pp. 780–790. doi:10.1038/35093564.

Yuste, R. (2015) 'From the neuron doctrine to neural networks', *Nature Reviews Neuroscience*, 16(8), pp. 487–497. doi:10.1038/nrn3962.

Yuste, R. and Katz, L.C. (1991) 'Control of postsynaptic Ca2+ influx in developing neocortex by excitatory and inhibitory neurotransmitters', *Neuron*, 6(3), pp. 333–344. doi:10.1016/0896-6273(91)90243-s.

Zahler, S.H. *et al.* (2021) 'Superior colliculus drives stimulus-evoked directionally biased saccades and attempted head movements in head-fixed mice', *eLife*. Edited by M. Vinck and T. Moore, 10, p. e73081. doi:10.7554/eLife.73081.

Zangenehpour, S. and Chaudhuri, A. (2001) 'Neural activity profiles of the neocortex and superior colliculus after bimodal sensory stimulation', *Cerebral Cortex (New York, N.Y.: 1991)*, 11(10), pp. 924–935. doi:10.1093/cercor/11.10.924.

Zatka-Haas, P. *et al.* (2021) 'Sensory coding and the causal impact of mouse cortex in a visual decision', *eLife*, 10, p. e63163. doi:10.7554/eLife.63163.

Zeng, H. and Sanes, J.R. (2017) 'Neuronal cell-type classification: challenges, opportunities and the path forward.', *Nature reviews. Neuroscience*, 18(9), pp. 530–546. doi:10.1038/nrn.2017.85.

Zerbi, V. *et al.* (2019) 'Rapid Reconfiguration of the Functional Connectome after Chemogenetic Locus Coeruleus Activation', *Neuron*, 103(4), pp. 702-718.e5. doi:10.1016/j.neuron.2019.05.034.

Zhang, F. *et al.* (1994) 'Distribution of immediate early gene zif-268, c-fos, c-jun and jun-D mRNAs in the adult cat with special references to brain region related to vision', *Neuroscience Letters*, 176(2), pp. 137–141. doi:10.1016/0304-3940(94)90067-1.

Zhang, F. *et al.* (2007) 'Multimodal fast optical interrogation of neural circuitry', *Nature*, 446(7136), pp. 633–639. doi:10.1038/nature05744.

Zhang, Q. *et al.* (2018) 'Use of TAI-FISH to visualize neural ensembles activated by multiple stimuli', *Nature Protocols*, 13(1), pp. 118–133. doi:10.1038/nprot.2017.134.

Zhang, X., Pan, W.-J. and Keilholz, S.D. (2020) 'The relationship between BOLD and neural activity arises from temporally sparse events', *NeuroImage*, 207, p. 116390. doi:10.1016/j.neuroimage.2019.116390.

Zhang, Y. *et al.* (2020) *jGCaMP8 Fast Genetically Encoded Calcium Indicators*, *figshare*. Janelia Research Campus. doi:10.25378/janelia.13148243.v4.

Zhang, Z., Liu, W.Y., *et al.* (2019) 'Superior Colliculus GABAergic Neurons Are Essential for Acute Dark Induction of Wakefulness in Mice', *Current Biology*, 29(4), pp. 637-644.e3. doi:10.1016/j.cub.2018.12.031.

Zhang, Z., Liu, W.-Y., *et al.* (2019) 'Superior Colliculus GABAergic Neurons Are Essential for Acute Dark Induction of Wakefulness in Mice', *Current Biology*, 29(4), pp. 637-644.e3. doi:https://doi.org/10.1016/j.cub.2018.12.031.

Zhao, X., Liu, M. and Cang, J. (2014) 'Visual cortex modulates the magnitude but not the selectivity of looming-evoked responses in the superior colliculus of awake mice', *Neuron*, 84(1), pp. 202–213. doi:10.1016/j.neuron.2014.08.037.

Zhivotovsky, B. and Orrenius, S. (2011) 'Calcium and cell death mechanisms: a perspective from the cell death community', *Cell Calcium*, 50(3), pp. 211–221. doi:10.1016/j.ceca.2011.03.003.

Zhou, C. *et al.* (2015) 'Central neural circuitry mediating courtship song perception in male Drosophila', *eLife*. Edited by M. Ramaswami, 4, p. e08477. doi:10.7554/eLife.08477.

Zhou, N. *et al.* (2018) 'The Mouse Pulvinar Nucleus Links the Lateral Extrastriate Cortex, Striatum, and Amygdala', *Journal of Neuroscience*, 38(2), pp. 347–362. doi:10.1523/JNEUROSCI.1279-17.2017.

Zhou, N.A. *et al.* (2017) 'The mouse pulvinar nucleus: Organization of the tectorecipient zones', *Visual Neuroscience*, 34, p. E011. doi:10.1017/S0952523817000050.

Zhou, Z. *et al.* (2019) 'A VTA GABAergic Neural Circuit Mediates Visually Evoked Innate Defensive Responses', *Neuron*, 103(3), pp. 473-488.e6. doi:10.1016/j.neuron.2019.05.027.

Zingg, B. *et al.* (2017) 'AAV-Mediated Anterograde Transsynaptic Tagging: Mapping Corticocollicular Input-Defined Neural Pathways for Defense Behaviors', *Neuron*, 93(1), pp. 33–47. doi:10.1016/j.neuron.2016.11.045.

van der Zwaag, W. *et al.* (2018) 'High spatio-temporal resolution in functional MRI with 3D echo planar imaging using cylindrical excitation and a CAIPIRINHA undersampling pattern', *Magnetic Resonance in Medicine*, 79(5), pp. 2589–2596. doi:10.1002/mrm.26906.

# Publications derived from this project

Brunner C, Grillet M, Sans-Dublanc A, Farrow K, Lambert T, Macé E, Montaldo G, Urban A. A Platform for Brain-wide Volumetric Functional Ultrasound Imaging and Analysis of Circuit Dynamics in Awake Mice. Neuron. 2020 Dec 9;108(5):861-875.e7. doi: 10.1016/j.neuron.2020.09.020. Epub 2020 Oct 19. PMID: 33080230.

Sans-Dublanc A*, Chrzanowska A*, Reinhard K, Lemmon D, Nuttin B, Lambert T, Montaldo G, Urban A, Farrow K. Optogenetic fUSI for brain-wide mapping of neural activity mediating collicular-dependent behaviors. Neuron. 2021 Jun 2;109(11):1888-1905.e10. doi: 10.1016/j.neuron.2021.04.008. Epub 2021 Apr 29. PMID: 33930307.

# Presentations at international conferences

**Posters:**

Sans-Dublanc A., Chrzanowska A., Montaldo G., Urban A., Farrow K. (2018). Mapping the projectome of the Superior Colliculus to understand visually guided innate behaviors. Presented at 11th FENS Forum of Neuroscience, Berlin, Germany, Jul 7-11, 2018.

Sans-Dublanc A., Chrzanowska A., Montaldo G., Urban A., Farrow K. (2019). Mapping the projectome of the superior colliculus to understand visually guided innate behaviors. Presented at Berntein Conference, Sep 19, 2019.

**Oral presentations:**

Sans-Dublanc A. Chrzanowska A., Reinhard K., Lemmon D., Montaldo G., Urban A., Farrow K. (2020). opto-fUSI reveals the downstream networks governing distinct aversive behaviors driven by individual cell-types of the superior colliculus. Presented at Cold Spring Harbor Laboratory 2020: Neuronal Circuits Virtual Meeting. Mar 18, 2020.

Sans-Dublanc A. Chrzanowska A., Reinhard K., Lemmon D., Montaldo G., Urban A., Farrow K.(2020). Brain-wide mapping of neural activity evoked by different superior colliculus cell-types. Presented at Neuromatch 3.0 virtual conference. Oct 27, 2020